Not-so-Dark Matter: strategies for indirect detection and identification of Dark Matter

Mattia Fornasa

Dipartimento di fisica "G.Galilei" dell'Università degli studi di Padova & Istituto Nazionale di Fisica Nucleare (sezione di Padova), via Marzolo 8, 35131 Padova

E-mail: `mfornasa@pd.infn.it`

Abstract.

Abstract

The existence of Dark Matter (DM) is supported by multiple evidences, achieved by means of very different experimental strategies. Its energy density today has been measured to account for almost a quarter of the total energy density in the Universe. DM is mainly sensible to gravity and it interacts only weakly through nuclear and electromagnetic interactions. Under the assumption that a DM particle is its own anti-particle, annihilation products can be searched for in order to obtain informations about DM distribution and, more generally, to infer some of its properties. This is the idea beyond DM *indirect detection*. In this Ph.D. thesis I will focus only on DM annihilation into gamma-rays and discuss the possibility of obtaining clear DM signatures from the analysis of gamma-rays signals. Being the annihilation flux proportional to the DM density squared, natural targets for indirect searches are the Galactic Center (due to its vicinity and its large amount of DM) and the near dwarf spheroidal galaxies (due to their large mass-to-light ratio). Experimental data from both these classes of sources have not found any clear DM signal, being able only to provide upper limits on the annihilation flux. I will present here two alternative strategies for which DM signatures may be detected and a signal from annihilation may be disentagled from the gamma-ray background. In the first case I will focus on the effect that Black Holes (BHs) can have on the distribution of DM producing overdensities. The most efficent mechanism is the adiabatic contraction around SuperMassive Black Holes, able to create large enhancements called *spikes*. However, the scenario of *mini-spikes* around Intermediate Mass Black Holes is more realistic and I will present prospects of detecting DM from mini-spikes in our Galaxy and in the Andromeda Galaxy. I will move then to the analysis of the angular power spectrum of anistropies in the gamma-ray emission. After that the galactic foreground (due to cosmic rays interacting with the Galactic interstellar medium) is subtructed from a map of the gamma-ray sky, a residual isotropic background remains, called Extra-galactic Cosmic Gamma-ray Background (EGB) and measured by EGRET. The Fermi LAT satellite will soon provide a more precise measurement of the EGB and I will present here predictions showing that the DM can contribution to the EGB flux and that its presence can be detected in the analysis of the angular power spectrum of the EGB. Both Galactic and extra-galactic DM substructures are taken into account, the first dominating the angular spectrum at low multipoles. This thesis is based on the projects I have been involved in during my Ph.D. and I will mainly present results already discussed in those papers where I am among the authors.

Abstract

L'esistenza della Materia Oscura (MO) è sostenuta da molteplici evidenze, ottenute con l'utilizzo di tecniche sperimentali diversificate e complementari. La densità energetica della MO risulta spiegare quasi un quarto della densità di energia dell'intero Universo. Essa risente prevalentemente della gravità interagendo solo debolmente tramite interazioni nucleari ed elettromagnetiche. Seguendo l'ipotesi che la particella di MO sia anche la sua stessa anti-particella, una strategia per ottenere informazioni su come è distribuita la MO e, più in generale per dedurre alcune delle sue proprietà, è quella di cercare i suoi prodotti di annichilazione. È questa l'idea che sta alla base della *rivelazione indiretta* di MO. Nella presente tesi di dottorato mi limiterò all'annichilazione della MO in raggi gamma e verranno discusse le previsioni per ottenere una chiara segnatura della presenza della MO dall'analisi dei segnali gamma. Essendo il flusso di annichilazione proporzionale alla densitaà di MO al quadrato, gli obiettivi principali della rivelazione indiretta sono il Centro Galattico (a causa della sua vicinanza e della grande quantità di MO stimata) e le galassie sferoidali nane presenti all'interno della Via Lattea (a causa del loro alto rapporto massa su luce). Gli dati sperimentali attuali provenienti da queste due classi di oggetti, non sono stati in grado di rivelare un chiaro segnale della presenza della MO, ma solamente di fornire dei limiti superiori al flusso di annichilazione. Presenterò in questa tesi due strategie alternative in grado di identificare delle segnature piuttosto chiare della presenza della MO attraverso le quali sarà possibile distinguere il segnale di annichilazione dal fondo gamma. Nel primo caso mi focalizzerò sull'effetto che i buchi neri possono avere sulla distribuzione di MO portando alla formazione di sovra-densità. Il meccanismo più efficente è quello della contrazione adiabatica attorno ai Buchi Neri SuperMassici, capace di produrre grandi innalzamenti nella densità di MO chiamate *spikes*. D'altro canto, lo scenario più plausibile è quello delle *mini-spikes* attorno ai Buchi Neri di Massa Intermedia e verranno presentate previsioni per la rivelazione della MO nelle mini-cuspidi della Via Lattea e della galassia di Andromeda. Mi focalizzerò poi sulla seconda alternativa, lo studio dello spettro angolare di potenza per le anisotropie nell'emissione gamma. Dopo che il contributo Galattico (dovuto all'interazione dei raggi cosmici con il mezzo interstellare Galattico) è stato sottratto dai dati di EGRET, un fondo isotropo residuo rimane, chiamato Fondo Extra-galattico Gamma (FEG). Il satellite Fermi LAT fornirà nell'immediato futuro una nuova stima del FEG ed io mosterò, negli ultimi capitoli, come la MO possa contribuire al flusso del FEG e come la sua presenza possa essere rivelata nell'analisi dello spettro angolare del FEG. Verranno considerate allo stesso tempo sottostrutture Galattiche ed extra-galattiche, dove le prime constituiscono la componente principale dello spettro angolare a bassi multipoli. Questa tesi è basata sui progetti nei quali sono stato coinvolti durante il mio dottorato e presenterò risultati già discussi in quei lavori per i quali figuro tra gli autori.

Abstract

L'existence de la Matière Noire (MN) est supportée par des nombreuses preuves, obtenues à travers des techniques expérimentales différentes et complémentaires. La densité d'énergie de la MN est supposé expliquer presque un quart de la densité d'énergie de l'Univers entier. Elle ressent principalement de l'effet de la gravité et elle interagit seulement faiblement à travers les interactions nucléaire et electromagnétique. Sous l'hypothese que la particule de MN soit sa propre anti-particule, une façon d'obtenir des informations sur la distribution de la MN ou, en general, de déduire quelques caractéristiques, est de rechercher ses produits d'annihilation. Il s'agit de l'idée sur laquelle est basée la détection indirecte de MN. Dans cette thése je vais me concentrer seulement sur l'annihilation de la MN en rayons gamma et je vais examiner les perspectives pour obtenir une claire signature de la présence de la MN par l'analyse de l'émission gamma. Comme le flux d'annihilation est proportionnel au carré de la densité de MN, les plus naturelles objectives pour la détection indirecte de MN sont le Centre Galactique (à cause de sa proximité et de l'abondance de MN estimeé) et les galaxies spirales naines de la Voie Lactée (a cause du grand rapport lumière sur masse). Les données expérimentales actuelles de ces classes des objets ne peuvent pas fournir une preuve de le présence de la MN, mais ils ont seulement fixé des limites supérieures au flux d'annihilation. Dans cette thése je vais présenter deux stratégies alternatives capables d'identifier des claires signatures de la présence de la MN, à travers lesquelles il sera possible de distinguer le signal d'annihilation du fond gamma. Dans le premier cas, je vais me concentrer sur l'effet que les trous noirs peuvent avoir sur la distribution de la DM en formant des sur-densités. Le mécanisme plus efficace est la contration adiabatique autour des Trous Noirs SuperMassifs, capables de produire des grands augmentations de la densité de MN appelées *spikes*. D'un autre coté, le cas le plus vraisemblable est celui des *mini-spikes* autour des Trous Noirs de Masse Intermédiaire et je vais presenter des perspectives pour la détection de MN dans le mini-cuspides de la Voie Lactée et de la Galaxie d'Andromède. Ensuite je m'occuperai de la deuxième alternative: l'étude du spectre angulaire de puissance pour les anisotropies de l'émission gamma. Après la soustraction de la contribution Galactique aux données EGRET (en raison de l'interaction des rayons cosmiques avec le moyen interstellaire Galactique), un fond isotrope restera, appelé Fond Extra-galactique Gamma (FEG). Le satellite Fermi LAT fournira bientôt une nouvelle estimation du FEG et, dans le derniers chapitres, je vais montrer comment la MN peut contribuer au flux du FEG et comment sa présence peut être detectée à travers l'analyse du spectre angulaire du FEG. Au même temps les sous-structures Galactiques et extra-galactiques seront considérées, en constituant, les premiéres, le composant principal du spectre angulaire aux multipôles inférieurs. Cette thése est fondée sur les projets où j'ai travaillé pendant mon doctorat et les résultats que je vais présenter sont déjà discutés dans le papiers dont je suis co-auteur.

Introduction

The pages you are about to read form the final thesis for my Ph.D. in Theoretical Physics at the Physics Department of the University of Padova. Prof. Antonio Masiero has been my supervisor and I also had the opportunity of working with Gianfranco Bertone in Padova and at the Institut d'Astrophysique de Paris.

The main topic of this work is the detection and identification of Dark Matter (DM), mainly through what is called *indirect detection*, i.e. the search for the particles produced by DM annihilation and the attempt of using a possible detection to infer the properties of the DM itself.

During the three years of my Ph.D., I was involved on different projects related to indirect DM detection that gave me the possibility of collaborate with many physicists from different countries and to see some papers with my name published on the arXiv (http://arxiv.org/) and on international journals. The arguments that will be presented in this thesis are essentialy the subjects of my previous works. So, except for the introduction on standard Cosmology and evidences DM, this is just an attempt to unify all my papers written during the Ph.D. years in a more compact and complete essay.

They are the following:

- Paper I: Fornasa M, Taoso M and Bertone G, 2007, *Gamma-rays from DM mini-spikes in M31*, published in Physics Review **D** 76:043517, preprint astro-ph/0703757.

- Paper II: Fornasa M and Bertone G, 2008, *Black Holes as annihilation Boosters*, published in International Journal of Modern Physics **D** 17:1125, preprint 0711.3148.

- Paper III: Bringmann T, Doro M and Fornasa M, 2008, *Dark Matter signals from Draco and Willman 1: Prospects for MAGIC II and CTA*, published in Journal of Cosmology and Astrophysics 01:16, preprint 0809.2269.

- Paper IV: Fornasa M, Pieri L, Bertone G and Branchini E, 2009, *Anisotropy probe of galactic and extra-galactic Dark Matter annihilations*, submitted to Physical Review **D**, preprint 0901.2921.

The thesis is organized as follows: Chapter I introduces the framework in which DM indirect detection and are located. It is a very brief overview of the standard model of Cosmology, where I also try to present some experimental evidences on the existence of DM. The attention, then, focuses on some of the best-motivated and widely-used DM candidates. A particular attention is reserved to the neutralino and I will summarize the very basic notions of SuperSymmetry, too.

Chapter II deals more in detail with indirect DM detection, defining the annihilation flux and the terms to which it depends. The case of DM annihilations in the Galactic Center (GC) will be then considered: it represents a natural source for indirect DM detection and I will present the results of some papers predicting the annihilation flux coming from that particular direction in the sky. From an experimental point of view, gamma-rays have been detected from the GC, both by EGRET (http://www.cossc.gsfc.nasa.gov/cossc/egret/) and by Air Cherenkov Telescopes (ACTs). I will discuss these data and motivate the reasons of why

they are not usually interpreted as DM signals. The topics of these first two chapters have not been subjects of my work during the Ph.D., thus I will simply present results in the literature that I believe to be important in order to fully understand the following chapters.

On the other hand, starting from Chapter III, some of the results from my papers will be discussed: in Chapter III the attention will move to another optimal target to detect the presence of DM, the dwarf Spheroidal galaxies (dSphs) of the MW. In Paper III, Torsten Bringmann, Michele Doro and I computed the prospects for the detection of DM from the halos of two reference dSphs, Draco and Willman I. Our aim was to provide an update on the possibility for ACTs to detect DM from dSphs and, in this contest, we summarized the principal characteristics of an ACT, emphasizing the expected improved performances of the next generation of ACTs, MAGIC II and CTA. Moreover, for the first time in an analysis of this kind, we included the contribution of Virtual Internal Bremsstrahlung which was recently proved (Bringmann et al. 2008) to be useful in the identification of DM from the analysis of the energy annihilation spectrum.

In Chapter IV and V, I will write about Black Holes and their property of being *Annihilation Boosters*, i.e. the effect that they may have on the distribution of DM creating overdensities and hence boosting up the annihilation flux. This has been also the subject of Paper II (by Gianfranco Bertone and I), on which these two chapters are based. In particular Chapter IV will be dedicated to the case of SuperMassive Black Holes (SMBHs) hosted at the center of galaxies and clusters of galaxies. The largest boosting effect will be due to the so-called *adiabatic compression* producing density enhancements called *spikes* that result to be very delicate and sensitive to the evolution of the halo.

On the other hand, Chapter V studies the effect of Intermediate Mass Black Holes (IMBHs): in this case adiabatic compression lead to the formation of smaller, *mini-spikes*. The detection of a DM signal from mini-spikes will be discussed, also referring to Paper I, where, with Marco Taoso and Gianfranco Bertone, we studied the prospects of detecting IMBHs from the Andromeda galaxy.

Finally, in the last chapter (Chapter VI), I will present the results of my most recent paper (Paper IV) written in collaboration with Lidia Pieri, Gianfranco Bertone and Enzo Branchini. It is based on an alternative approach to the detection of DM since it is proposed to detect a DM signature from the analysis of the angular power spectrum of the anisotropies in the gamma-ray emission. Annihilations within the Galactic halo and its subhalos will be considered and also the contribution of extra-galactic DM structures. We will see that the DM presence can be detected over the contribution of the astrophysical background from the analysis of the angular spectrum as it will measured by the soon-available data of the Fermi LAT telescope (http://www-glast.stanford.edu).

This thesis is not going to represent a conclusive discussion on indirect DM detection: the subject is quite vast, touching different disciplines on which I am not an expert. Anyway, the organization of this essay is thought to follow a precise path and I will try to motivate the different steps that form this path, giving you at least a look on what the indirect detection of DM is.

Table of Contents

Chapter I:
Dark Matter as an
AstroParticle issue

1. Overview of Standard Cosmology

In Standard Cosmology, one of the key ingredient for the description of our Universe and its evolution is the metric $g_{\mu\nu}$, which, following the prescriptions by Friedmann, Robertson and Walker for an homogeneous and isotropic Universe, can be written as follows

$$ds^2 = -c^2 dt^2 + a^2(t)[dx^2 + dy^2 + dz^2]. \tag{1}$$

c is the velocity of light and $a(t)$ is called the *scale factor* and has the dimension of a length, so that the spatial coordinates (dx, dy, dz) have no dimensions at all. The scale factor depends on the time variable dt and accounts for the expansion of the metric: a particle (a star, for example) can move with respect to the coordinate grid (proper motion) or can simply follow the evolution of the grid (*covariant* motion). In that case its spatial coordinates remain the same.

The expansion of the metric has been introduced to match the fact that the Universe itself is in an expansion phase as it was suggested by the Hubble law: apart for a handful of near objects, the light that we receive from all stars and galaxies is redshifted proportionally to the distance d of the particular object from us, distant stars exhibit larger redshifts than nearer stars. The redshift is a consequence of the Doppler effect so that larger redshifts correspond to larger velocities v. Finally we end up with the Hubble law:

$$d = H_0 v. \tag{2}$$

H_0 is the Hubble constant, parametrized as $100\,h\,\mathrm{km\,s^{-1}Mpc^{-1}}$. The most recent estimate of h comes from Komatsu et al. (2008) and is equal to (0.705 ± 0.013). The correlation between velocity and distance can be seen in Figure 1, taken from the original paper by Hubble (Hubble 1929).

Instead of the actual velocity, the redshift z itself is often used in Equation (2):

$$1 + z = \frac{a_0}{a}, \tag{3}$$

being a_0 the scale factor today. The Hubble law can be derived, in the simplest form of Equation (2), assuming that stars move with the comoving grid of the Friedmann-Robertson-Walker (FRW) metric so that, being r the comoving distance costant with time, $v = \dot{d} = \dot{a}r = (\dot{a}/a)d = H(t)d$. $H(t)$ is called the Hubble parameter being H_0 its value today.

Besides its metric, one should also define the shape of the Universe. As stated by the theory of General Relativity, the shape depends on the amount of matter present in the Universe. More precisely the Universe is flat if the average energy density is equal to the critical value $\rho_{crit,0}$, close (or positively curved) if it is more dense than $\rho_{crit,0}$ and open (or negatively curved) if it is less dense. The critical density is equal to $1.38 \times 10^{-7} M_\odot \mathrm{pc}^{-3}$ today and, since the measurements of the total energy density indicate a value very close to $\rho_{crit,0}$ (Komatsu et al. 2008), the Universe results to be flat.

The evolution of the scale factor is governed by the Einstein equations which, in their most general form, are

$$G_{\mu\nu} = 8\pi T_{\mu\nu}. \tag{4}$$

Figure 1. Velocities of distant galaxies (units should be km s^{-1}) plotted vs. distance. Solid (dashed) line is the best fit to the filled • (open ○) points which are corrected (uncorrected) for the motion of the Sun. Taken from Hubble (1929).
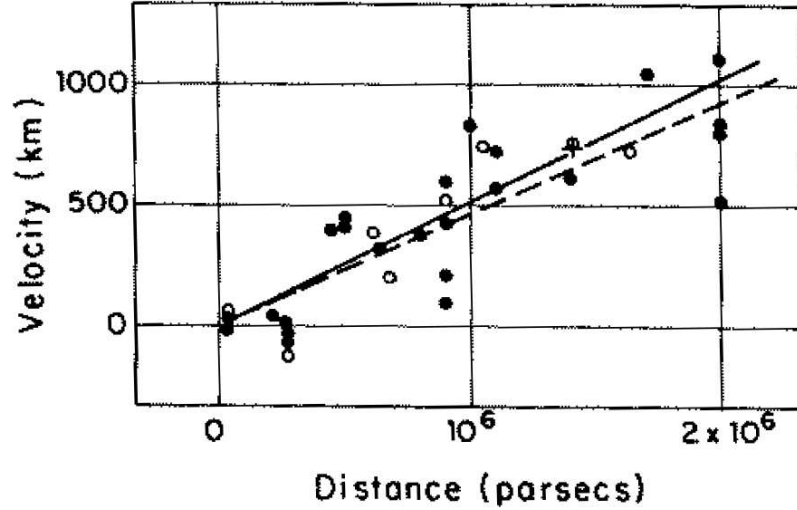
$G_{\mu\nu}$ is called the Einstein tensor and can be derived from the metric, while $T_{\mu\nu}$ is the energy-momentum tensor and depends on the matter components present in the Universe. The fact that the metric and the energy (or matter) content are related through Equation (4) is one of the most relevant fact of General Relavity. In the early Universe all matter components (photons, electrons, Dark Matter particles, etc.) are supposed to be in thermodynamical equilibrium one with the other, so that they are described by homogeneous and isotropic fluids with energy densities that only depend on the time. In this simple scenario, Equation (4) becomes

$$\frac{\dot{a}}{a} = \frac{8\pi G}{3}\rho, \tag{5}$$

$$\frac{\ddot{a}}{a} = -\frac{4\pi G}{3}(\rho + 3p), \tag{6}$$

for which we assumed a flat geometry for the Universe and fundamental units are used (I will keep using fundamental units for which $\hbar = c = k_B = 1$ if not differently indicated). G is the fundamental Newton constant and ρ and p are, respectively, the average energy density and pressure. Three different types of matter can be distinguished based on the way their energy densities evolve with the expansion of the Universe:

- photons and all massless particles, whose energy density evolves as $\rho_\gamma(t) \propto a^{-4}(t)$ due to the fact that, while the Universe expands (and the unit volume goes as $a^3(t)$), also the photon frequency evolves with $\propto 1/a$.

- all the remaining massive particles, with energy density going as $\rho_m(t) \propto a^{-3}(t)$.

- Dark Energy remains constant with time $\rho_\Lambda = $ const.

In Equation (5) and Equation (6), when the energy ρ or the pressure p are present, the sum over these three forms of matter should be considered.

The different evolution behaviours of the components of the Universe imply that it is possible to determine an epoch where the total energy density was dominated by photons (also called generically *radiation*) and all other forms of matter were less relevant. Such epoch ended when the radiation energy density was so diluited to match the value for massive particles (here called generally *matter*). This happened at the *equality* a_{eq} (around $z \sim 10^4$), after that the matter was the main component in the Universe till very recently when even the matter density was overcome by Dark Energy, which accounts today for almost three quarters of the energy budget.

From simple thermodynamical considerations (for more details see, e.g., Dodelson 2003), a fluid of relativistic particles in thermodynamical equilibrium has an energy density proportional to the fourth power of the temperature (actually this can be thought as a definition of the temperature of the fluid). The expansion of the scale factor and the decrease in the energy density are therefore accompained by the Universe becoming cooler. Back in the radiation-dominated phase, the energy density was so high (we can also re-phrase this last sentence, simply saying that the Universe was so much hotter) that all particles were relativistic. Collisions among particles were able to maintain thermodynamical equilibrium, but as the temperature decreased, the cross section for collisions became so low that thermal equilibrium could not be maintained any longer. It is the so-called *freeze-out* and, as an example, let me consider the case of the reaction between electrons and neutrinos $e^- + \nu_e \leftrightarrow e^- + \nu_e$: with the temperature going down, also the cross section for this reaction decreased to a point that equilibrium could not be maintained anymore between the two species. They freezed-out and continued separately their evolution. Another way of considering this, is thinking that the Universe was expanding too fast so that collisions were not frequent enough to keep the two species in equilibrium. In fact, it is usually considered as a criterion to understand when freeze-out happens, determining the moment when the expansion rate equals the collision rate: $n\sigma v \sim H$, n is the number density and $H(t)$, being defined as $\dot{a}/a$, is the expansion rate. σ and v indicate respectively the cross section and the relative velocity of the interaction.

I described the freeze-out (or decoupling) in the case of the interaction between electrons and neutrinos, but the same happens for all the fundamental species that are initially in thermodynamical equilibrium. One of the most relevant decoupling is the one between electrons and photons, which is also called *recombination*. It happens when the scale factor is equal to $a_\star$, around $z \sim 10^3$ in the matter-dominated epoch. After $a_\star$, photons are completely decoupled from all others species and simply travel undisturbed without interacting with anything, becoming cooler and cooler as the Universe expands. The radiation emitted at recombination is what we saw when the Cosmic Microwave Background (CMB) Radiation was detected for the first time in 1964: it is precisely the black-body radiation predicted for the photon fluid which has expanded and cooled till reaching today a temperature of $T = 2.725$ K.

The detection of an isotropic radiation coming from opposite directions in the sky, as it is for the CMB, led to the *horizon problem*: how can regions what have been in causal contact only recently exhibit the same black-body spectrum for the CMB? A possible solution for the horizion problem (sketched in Figure 2) is a very early epoch of accelerated expansion called

Figure 2. left panel: the shaded area indicates the region within the comoving horizon, with the Earth at the center. Points inside the comoving horizon are in causal contact. The CMB emerges from the Last Scattering Surface (LSS) at the recombination epoch and travels till reaching the Earth. Two different regions from the LSS, therefore, can have entered the comoving horizon only today (or recently). The horizon problem is the fact that these two regions exhibit the same black-body spectrum for the CMB. right panel: a very early epoch of accelerated expansion (marked *inflation*) with a consequently enlarged comoving horizon, can solve the problem. Taken from Dodelson (2003).
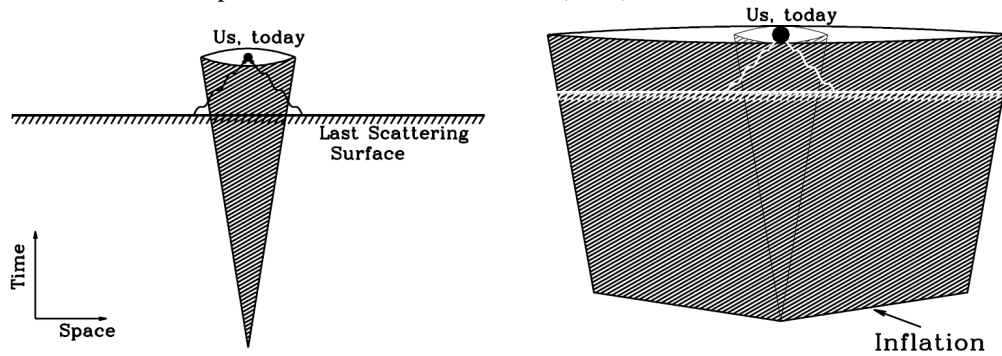
inflation: during this phase, regions that were in causal contact exit the comoving horizon (the maximal distance traveled by the light till today), rentering only recently, after inflation is finished and the Universe has followed the evolution I described before. Therefore, the reason why these regions are characterized by the same temperature for the CMB resides in the fact that they have been in causal contact long ago, before inflation.

We do not have conclusive evidences for the theory of inflation. Nonetheless much attention has been dedicated to it with many groups working on theories of inflation all around the world. In fact, inflation not only represents a solution to the horizon problem but also provides us with a mechanism to account for the perturbations that have been detected in the temperature of the CMB. Its isotropy, in fact, is precise but small perturbations, of the order of one part over 10^6 have been detected. A full-sky map of the CMB radiation, as it has been measured by the Wilkinson Microwave Anistropy Probe (WMAP http://map.gsfc.nasa.gov/news/), is presented in Figure 3.

The overview I made for the evolution of the Universe, starting with the FRW metric in Equation (1), is based on hypothesis that the Universe is homogeneous and isotropic, which works well, above all for the early stages. Beyond this approximation there are fluctuations in the matter density (which cannot longer be considered as an homogeneous fluid described only by its energy density $\rho(t)$) and in the metric, being these two connected one with the other. Understanding the evolution of fluctuations is a very interesting and well-developed field. Inflation is able to provide initial conditions to this scenario: anisotropies in the radiation temperature field, produced in the inflation epoch, will evolve till today and what we see in Figure 3 is an image of these fluctuations at the moment of recombination when photons decoupled from electrons.

Figure 3. Image of the anisotropies of the CMB radiation as measured by WMAP (5 year release). Taken from http://map.gsfc.nasa.gov/media/080997/index.html
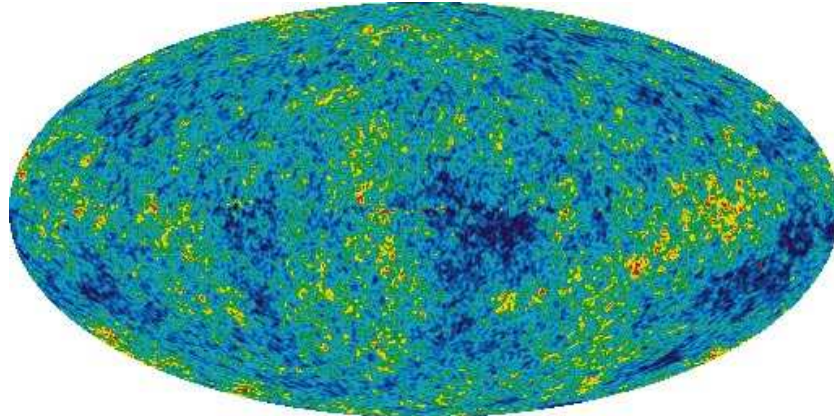
In the matter density (meaning now, everything that is not radiation or Dark Energy) the fluctuations produced during inflation started to grow due to gravitational attraction when the Universe became matter-dominated ($a > a_{eq}$), they soon left the linear regime, becoming larger and larger and being responsible from the highly non-linear structures that we detect now in the Universe as galaxies and clusters of galaxies.

2. Dark Matter evidences

In the previous section, I briefly reviewed the history of the Universe, always assuming that the matter density $\rho_m(t)$ plays a significant role in the evolution of the cosmos and that a big part of what we called "matter" is due to DM.

However, only recently the community reached a quite large consensus on the existence of this fundamental component of the Universe, a fact that is undoubtedly due to some strong evidences coming from different research areas and obtained with different experimental techniques (for a recent review, see Bertone, Hooper & Silk 2005).

The first time that the existence of DM was proposed (and the word "Dark Matter" was used with the modern meaning) was by F. Zwicky in the study of the Coma cluster (also known as Abell 1656 (Zwicky 1933, Zwicky 1937)). He argued that infering the mass of clusters of galaxies from the detection of the luminous component and internal rotation, can only lead to a lower limit on the mass of the cluster. On the contrary he proposed a strategy based on the virial theorem so that, from a measurement of the velocity dispersion of the galaxies belonging to the cluster, it is possible to infer the value of its total mass. This approach remains valid (at least as an order of magnitude estimate) even if the hypothesis of equilibrium for the cluster is relaxed. The value Zwicky found for the mass of the Coma cluster was ~ 200 times larger than what usually assumed considering only the luminous component. Therefore he claimed the existence of a new form of non-luminous matter able to explain the large value he had found for the mass of Coma.

Nowadays additional evidences have accumulated, favouring the presence of DM at all

scales, from cosmological distances and all the way down to galactic scales. In the remaining part of this section, I am going to present some of these evidences, obtained by the analysis of the CMB radiation, gravitational lensing or the study of the rotation curves of galaxies.

However, a conclusive evidence for DM (and hopefully the first determination of its characteristics) will be asserted when an incontrovertible signal will be produced in one of the three "classic" channels for DM detection:

- production of the DM particle at colliders. It has been predicted that the recently activated Large Hadron Collider (http://public.web.cern.ch/Public/fr/LHC/LHC-fr.html) may be able to produce some of the most studied DM candidates. These particles, due to their very low cross section, will soon leave the detector, revealing themselves only through unbalanced, missing energy. In this case, it will be really hard to pin down the presence of DM, since missing energy is the typical signature of many scenarios for physics beyond the Standard Model.

- direct detection of DM. When a DM particle passes through the Earth, it can interact with the nuclei of a detector and deposit a small amount of energy of the order of the keV. Cryogenically controlled, underground experiments as Xenon10 (http://xenon.astro.columbia.edu/) or COUPP (http://www-coupp.fnal.gov/) can detect such small deposits of energy and potentially infer DM properties. The italian DAMA collaboration (www.lngs.infn.it/lngs/htexts/dama/) recently published results for a detection of DM by the DAMA/Libra experiment (confirming and extending their previous results in Bernabei et al. 2008) sensitive to the annual modulation of the DM flux on the Earth. Their claim still remains controversial due to the fact that other collaborations tested the region in the parameters space (or at least a large fraction of it) where the DAMA collaboration detected a signal, wihout finding a correspondent detection.

- indirect detection of DM. The topic of this Ph.D. thesis: DM is revealed through the detection of the products of its annihilation, mainly gamma-rays, positrons, anti-protons and neutrinos. In this case large attention should be reserved to the analysis of the background since one has to be able to distinguish a DM signal from other astrophysical, less exotic sources. This is why, in order to use indirect detection as an evidence for DM, particularly characteristic signatures have to be found, as e.g., a class of gamma-ray sources with the same cut-off in the energy spectrum or a clear feature in the angular power spectrum of gamma-ray emissivity.

2.1. Angular spectrum of anisotropies in the CMB radiation

The analysis of the angular spectrum of anisotropies of the CMB radiation (see Figure 3) is one of the most striking result of physics for, at least, the last decade. In particular, it provides us with a value for $\Omega_\chi h^2$, the ratio of the average DM density ρ_χ to the critical energy density $\rho_{\text{crit},0}$, so that it can be considered one of the strongest evidence for the existence of DM (for the latest release of WMAP data, see Komatsu et al. 2008).

As we have already mentioned, the CMB radiation was emitted at the moment of recombination when the primordial plasma of photons (in thermal equilibrium and, therefore, radiating as a black-body) decoupled from the electrons and positrons and propagates till us becoming cooler and cooler. In fact today, the photons of the CMB exhibit a black-body radiation spectrum with a very low temperature of $T = 2.725$ K. Little fluctuations in the temperature of the CMB, around the isotropic value of $T = 2.725$ K, have also being detected, so that, photons are hotter when arriving from some regions in the sky with respect to other regions. These fluctuations are very small (of the order of one part over 10^6) and they can be seen in Figure 3 as they have been measured by WMAP.

Following the standard explanation, these little anisotropies are produced, as quantum fluctuations, during the inflationary epoch and are usually decomposed in their Fourier modes, so that the wave vector $\vec{k}$ is used to characterize fluctuations with wavelength equal to $\lambda = 2\pi/k$. During inflation the Universe expands so quickly that all fluctuation waves of cosmological interest fall outside the horizon, i.e. are characterized by a wavelength that is larger than the comoving horizon. Modes larger that the horizon are freezed and cannot evolve until inflation ends and the comoving horizon starts slowly to increase again so that the mode will finally re-enter the horizon. The exact moment when the perturbation re-enters the horizon depends, of course, on the wavelength of the perturbations: large scale modes (smaller k) re-enter later than small scale modes (large k). When causality is recovered and the perturbation is within the horizon, it can start to evolve, following prescriptions that depend on the particular epoch of the history of the Universe (e.g. if the perturbations re-enters the horizon before or after recombination, or if the Universe is in its radiation- or matter-dominated era).

The amplitude of a sub-horizon perturbation in the density of photons (and consequently in their temperature) oscillates during matter domination ($z \lesssim 10^4$) so that the power spectrum of fluctuations at recombination $a_\star$ ($z \sim 10^3$) will be a series of peaks and valleys (see Figure 4) as a consequence of the different moments that different modes re-entered the horizon (for a more detailed description on the evolution of primordial fluctuations, see, e.g., Dodelson 2003). More precisely, instead of the wavevector k, the multipole ℓ is present in Figure 4, since the temperature map is considered in its decomposition in spherical harmonics. Each mode will then correspond to a fluctuation of *angular* scale equal to $2\pi/\ell$.

At a first approximation the height of the peaks in the angular spectrum should be constant. But two additional effects have to be considered:

- first of all the presence of DM: at recombination DM is already decoupled from radiation and it is characterized, as radiation, by small perturbations with respect to the homogeneous energy density. These pertubations, which them-selves evolve, gravitationally influence the fluctuations in the radiation temperature. One can think that taking DM into consideration corresponds to "strengthen" the effect of gravity. The odd peaks in the angular spectrum of Figure 4 refer to regions where the photons are overdense: considering DM will make the potential wells deeper so that these overdensities tend to be even denser. On the other hand, even peaks indicates regions where the density of photon is suppressed (one should remember that the

Figure 4. Angular power spectrum of anisotropies in the CMB radiation. Data refers to the 5th data release from WMAP. Taken from http://map.gsfc.nasa.gov/news/index.html
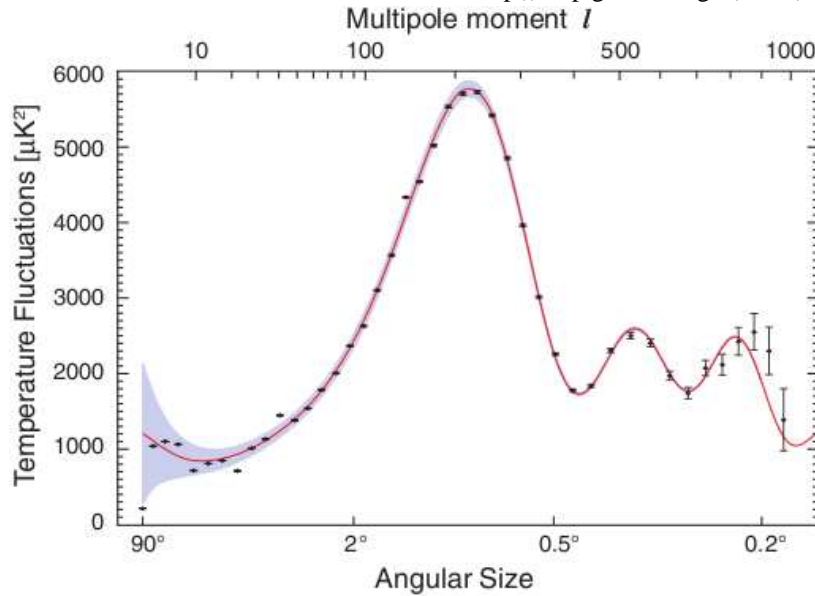
angular spectrum gives the fluctuation amplitude squared so both positive and negative fluctuations appears as peaks): gravitational attraction of DM will contrast the smearing effect of pressure radiation with the consequence that these underdensities are somewhat mitigated. The net effect of introducing DM is that odd peaks result to be higher and even peaks lower, as it can be easily seen it Figure 4.

- thermodynamical equilibrium in the photons is maintained by collisions. Between two collisions a photon, on average, covers a distance equal to the *mean free path* λ_{MFP} which depends from the baryon density (a larger baryon density corresponds to a smaller λ_{MFP}). As a consequence a density fluctuation with a wavelength smaller that the photon mean free path cannot propagate and its amplitude will be suppressed. This is why all scales larger than a certain multipole in Figure 4 are damped.

With this brief and incomplete description of the CMB angular spectrum, I simply want to stress that the physics of CMB perturbations depends on different effects and in particular is very sensitive to the composition and the properties of the early Universe. The curve in Figure 4, therefore, represents a very rich source of informations. The most important to us are the density ratio $\Omega_\chi h^2$ for DM and for baryons, being equal, respectively to $\Omega_\chi h^2 = (0.1099 \pm 0.0062)$ and $\Omega_b h^2 \sim 0.0023$ ‡, proving that DM is a large component of the Universe and that it has a non-baryonic nature. The value of the baryonic density agrees from what predicted by Big Bang nucleosynthesis (Yao et al. 2006).

‡ these values at taken from Table 1 of Komatsu et al. (2008) and represent the result to a fit only to the WMAP data, in contrast with the case where data from the matter power spectrum, as e.g. from SDSS (see Section 2.2), are considered.

2.2. Large Scale Structure

Maybe the strongest evidence in favour of DM is the fact that baryonic structures (from the large scales of clusters of galaxies to the smaller scales of solar systems) exist. This would have not been possible without DM.

During the matter-dominated epoch before recombination, the fluctuations in the DM density grows proportionally to the scale factor $\delta_\chi \propto a$. In the meanwhile radiation perturbations oscillate forcing the perturbations in the baryon density to do the same since photons and baryons are tightly coupled before recombination. This coupling comes to an end at the moment of recombination and the baryons, free from radiation pression, are free to grow. Gravitationally affected by the potential wells created by DM (which have become deeper and deeper), the amplitude of their fluctuations will experience a rapid growth in order to match the amplitudes of DM fluctuations and they will then follow the evolution of DM.

From $a_\star$ and $z \sim 1$, baryonic perturbations (starting with an amplitude that is what we detect in the CMB) have just enough time to become non-linear and form collapsed structures as we see now everywhere in the Univere around us. Without DM, there would have been nothing driving the rapid growth phase just after recombination and baryonic fluctuations would not have time to grow (by themselves) till reaching non-linearity.

Therefore, cosmological informations can be extracted by the analysis of the matter fluctuations too, as it has been done for the CMB radiation. The Sloan Digital Sky Survey (www.sdss.org/) extensively scanned the sky and detected almost 1 million of galaxies (over more 300 millions of objects) at different redshifts (Abazajian et al. 2008). The survey can be used to extract the three-dimensional power spectrum of matter fluctuations (see Figure 5).

The theory of inflation predicts that the power spectrum should be a Harrison-Zel'dovich-Peebles one, proportional to the third power of the wavevector ($P(k) \propto k^3$) at small scales and exhibit a turn-over at large scales in correspondence of the scale of the fluctuation that re-enters the comoving horizon exactly at the moment of equality a_{eq} (Dodelson 2003). The exact location in time of a_{eq} depends on the components of the Universe so that fitting the galaxy power spectrum and determining the position of the turn-over, one can estimate the cosmological parameters in an independent way than with the analysis of the CMB (Tegmark et al. 2004*a*, Tegmark et al. 2004*b*). Usually these two sources of informations are combined to narrow down the uncertainty on the determination of the cosmological parameters.

2.3. Gravitational weak lensing: the bullet cluster

After a cluster of galaxies has reached a well-relaxed configuration, all its components, namely the luminous galaxies, the interstellar medium and the DM halo, are characterized by a distribution that peaks in the same point at the center of the cluster. This is not true in the case that two clusters are colliding: in that case the galaxies population and the DM halo would react in a similar way as a collissionless fluid, almost not influenced by the collision, while, on the contrary, the interstellar medium (hot plasma that emits X-rays) experiences ram pressure and its distribution is strongly influenced by the collision. An example is the famous *bullet cluster* 1E0657-558 at redshift $z = 0.296$. In the right panel of Figure 6 an optical image

Figure 5. Data indicate the three-dimension power spectrum of galaxies as measured by the Sloan Digital Sky Survey (SDSS). The inner blue error band indicate the 1σ error on the spectrum estimated with a Monte Carlo Markov Chain technique implementing also constraints from WMAP. See Tegmark et al. (2004a) for additional informations. Taken from Tegmark et al. (2004a).
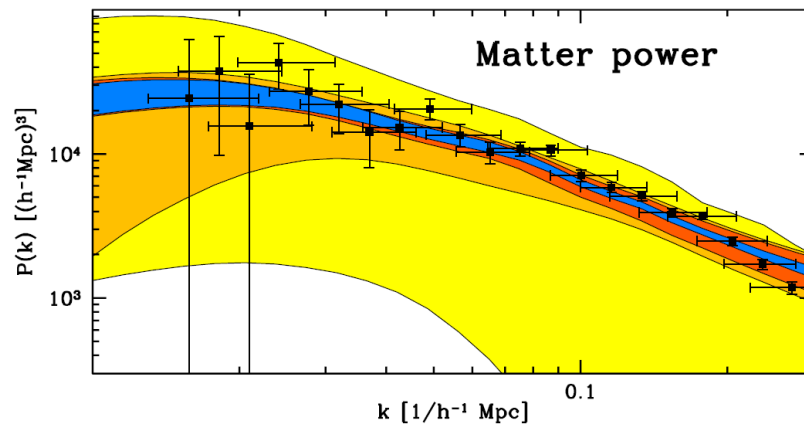
Figure 6. right panel: color image from the Magellan images of the 1E0657-558 cluster. left panel: a 500 ks Chandra image of the same cluster. Shown in green contours in both panels are the weak lensing κ reconstruction contours with the outer contour level at $\kappa = 0.16$ and increasing in steps of 0.07. The white contours show the errors on the positions on the κ peaks and correspond to 68.3%, 95.5% and 99.8% confidence levels. The white line on the right bottom indicates 200 kpc at the distance of the cluster. Taken from Clowe et al. (2006).
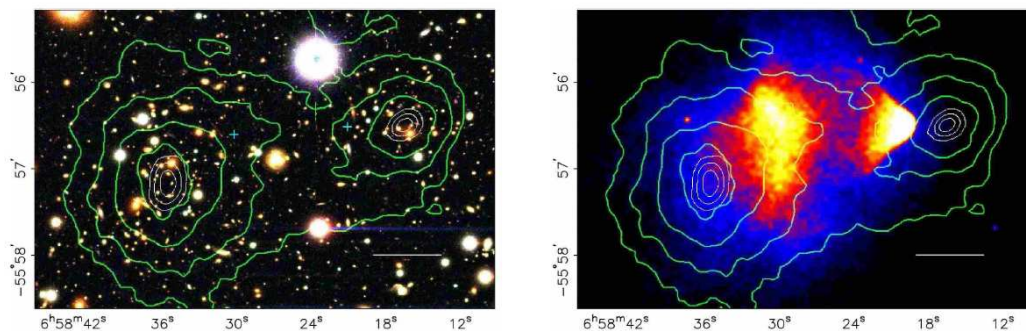
of the cluster can be seen, while, in left panel, the Chandra /http://chandra.harvard.edu/) image shows the distribution of the interstellar hot medium. The main feature of this second image is the shock wave in the western side (on the right in the figure) of the plasma, a clear evidence in favour of the on-going collision between two sub-units: a smaller cluster passing through a more massive structure (on the left). From the analysis of the temperature gradient near the shock is possible to estimate that the smaller subcluster in moving away from the larger companion at a velocity of 4700 km s^{-1}.

Recent observations of clusters suggest that their mass is made of $\sim$ 1% of baryons observable in optical and infrared data, $\sim$ 11% of baryons observable in X-ray and the remaining $\sim$ 88% is accounted by the DM (Allen et al. 2002). On the contrary, if there is

not DM, the hot plasma would be responsible for the majority of the mass in the cluster. As a consequence, if it was possible to obtain data on the distribution of the total mass of the cluster, we would see it peaked at the same position of the luminous matter in the case that DM is there (DM, as galaxies, is collisionless and their distributions should be similar) while, on the contrary, if there is not DM, the total mass of the cluster should track the X-ray emitting plasma, being distributed as the right panel of Figure 6.

Gravitational lensing can provide this kind of information, being sensitive to mass independently on the its nature. The idea comes from General Relativity and is based on the fact that light coming from a distant source is deflected if passing close to a massive object so that, when it arrives at us, the image of the original source can be displaced respect to its true position and also distorted (stretched towards the center of the deflecting object) and enlarged (preserving it surface brightness). The deflector acts on the light in the same way of a lens, and both displacements and deflections on the path of the light that passes close to it, can be used to infer properties on its mass.

The effect can be large with the formation of multiple images or evident arcs, but also very small as in the case of weak gravitational lensing, for which a significant signal can be obtained only statistically from the analysis of a large number of images.

In Clowe et al. (2004) and Clowe et al. (2006), the authors considered a population of vary far away elliptical galaxies and analyzed the images of these galaxies in the region near the bullet cluster. The alignement and the size of the ellipticity in these images (once corrected for smearing by the Point Spread Function) can be connected to the gravitational potential that causes the lensing effect (i.e. the gravitational potential of the cluster). In particular the observable is the reduced shear $\vec{g}$:

$$\vec{g} = \frac{\vec{\gamma}}{1 - \kappa},\tag{7}$$

with $\vec{\gamma}$ (called *shear*) being the amount of anisotropic stretching detected in the images and κ (called *convergence*) describes how the image of the galaxy is increased in size due to the gravitational effect and it is directly related to the surface density of the lens. The final results, therefore, are κ maps (as the green contours in Figure 6) indicating the distribution of the gravitational potential in the cluster.

As it can be seen, the convergence κ does not follow the hot plasma and the peaks (detected by a significance of 8 and 12σ for the two subclusters) are almost coincident with the luminous matter, providing a strong evidence in favour of the DM scenario.

2.4. Rotation curves of galaxies

A *rotation curve* indicates the velocity of a star orbiting in a galaxy vs. its distance to the center of the galaxy itself. The analysis of rotation curves have been used as a DM evidence since long time (Faber & Gallagher 1979, Begeman et al. 1991). Galaxies are examined through the detection of the 21-cm line of hydrogen and selection criteria are applied discarding all objects that show evidences for a non-spherical configuration so that, with remaining objects,

the velocity can be fully considered as a tracker of the radial gravitational force through the simple Newtonian relation

$$v(r) = \sqrt{\frac{GM(r)}{r}}, \tag{8}$$

with G the Newton constant of gravitation and $M(r)$ the mass of the galaxy enclosed within a distance r from the center. If only luminous matter is present in galaxies, in the outer region, outside the radius within which this luminous contribution is distributed, the velocity should decrease as $v(R) \propto r^{-1/2}$ since moving to larger distances does not include more mass. On the contrary, measurements clearly show that rotation curves stay flat even very far away from the center (Begeman et al. 1991).

A constant rotation curve suggests that the galaxy is embedded in a larger distribution of matter that is not visible and that should roughly follows a radial distribution of $\rho_\chi(r) \propto r^{-2}$. In fact, isothermal models (with a constant DM density in the central region and decreasing at larger distances as r^{-2}) are the first proposed modelizations for *DM halos* around galaxies. Modern N-body simulations (Navarro et al. 2004, Diemand et al. 2006), instead, seem to indicate that the halo is better described by a Navarro-Frank-White (NFW) profile (Navarro et al. 1997):

$$\rho_\chi(r) = \rho_s \left(\frac{r}{r_s}\right)^{-1} \left(1 + \frac{r}{r_s}\right)^{-2}, \tag{9}$$

with a logaritmic slope equal to -1 in the central region, monotonically decreasing to -3 in the outer region. The -2 behaviour is reached more or less at distances examined by the rotation curves so that the NFW profile is in accord with data from rotation curves. In Equation (9), r_s is called the *scale radius* and is the distance where the slope is equal to -2 and ρ_s is linked to the DM density at the center.

More recently large attention was reserved to the Einasto profile:

$$\frac{d \ln \rho_\chi(r)}{d \ln \rho_{-2}} = \left(-\frac{2}{\alpha}\right) \left[\left(\frac{r}{r_{-2}}\right)^\alpha - 1 \right], \tag{10}$$

which seems to provide a better fit to galaxy-sized DM halos (Merritt et al. 2005, Springel et al. 2008*b*). r_{-2} is the distance where the logaritmic slope of the profile is equal to -2 and α, called the *Einasto index*, ranges from ~ 0.1 to 0.25.

3. Dark Matter candidates

3.1. A large zoo

Larger and larger attention has been devoted to the issue of DM, with the consequence that a wide range of DM candidates can be found in the literature, each of them proposed to solve the DM problem or at least some issues related to it. Some candidates are part of a larger theory, created for reasons that are not directly related to DM and for which the existence of a good candidate is a welcome by-product. On the contrary, others proposed particles are thought explicitly to explain the current DM abundance.

Different candidates can have very different characteristics, with masses that go from the sub-eV scale to values larger than the TeV, and formation mechanisms that can be different from the thermal production that I assumed in the previous sections summarizing the evolution of the Universe.

Experimental data and phenomenological considerations are available, that can constrain to some extent the properties of a good DM candidate. In particular this has been studied in the recent review by Taoso, Bertone & Masiero (2008), where the authors propose a list of 10 characteristics that a good DM candidate should have: e.g. it should be stable, neutral (both for electrical charge and color), it should be within the limits posed by astrophysics and so on.

Throughout the rest of the thesis, I am going to concentrate mainly on a particular class of DM candidtes, the so-called Weakly Interacting Massive Particles (WIMPs). The characteristics of WIMPs are summarized in the next section, where I will also describe how to obtain an estimate of the WIMP relic density today.

Other non-WIMP candidates will not be described here, even if they pass all the requirements imposed by Taoso, Bertone & Masiero (2008) and they should be considered, at all means, good DM candidates. That will be the case of the axion A (or its supersymmetric partner, the axino $\tilde{a}$) (Sikivie 2006, Raffelt 2007).

Therefore, after having briefly described the WIMP class, I will only present those WIMP candidates that pass the 10 point test in Taoso, Bertone & Masiero (2008): the lightest neutralino $\tilde{\chi}$ (whose section will be preceded by a quick overview on SuperSymmetry, Section 3.3 and Section 3.4), the first Kaluza-Klein states for the photon $\gamma^{(1)}$ in theories with Unified Extra-Dimensions (Section 3.5), the bosonic WIMP predicted by Little Higgs theories (Section 3.6), and very briefly Inert DM H_0 (Section 3.7) and the sneutrino $\tilde{\nu}$ (Section 3.8). I will not talk about the possibility of a gravitino DM candidate $\tilde{G}$ (Pagels & Primack 1982, Berezinsky 1991, Feng et al. 2003).

3.2. *Weakly Interacting Massive Particles WIMPs*

A WIMP is a generic, stable particle with a mass of the order of the GeV-TeV and a very weak cross section with Standard Model particles ($\sigma v \sim 10^{-24} - 10^{-28} \mathrm{cm}^3 \mathrm{s}^{-1}$) that has been in thermal equilibrium with the primordial photons at some epoch of the evolution of the Universe.

Many DM candidates are WIMPs and this is by far the most used assumption about DM. The reason is the fact that, quite naturally, without any further details on the theory of particle physics that can lie behind a WIMP, the three characteristics that I mentioned (a thermally produced, weakly interacting, GeVish particle) can account for the current DM abundance and can provide a candidate that may soon be detectable with the use of colliders or both direct and indirect techniques.

More precisely, a WIMP (I will generically call it $\tilde{\chi}$ which will refer in next section to the supersymmetric neutralino) is supposed to be in thermal equilibrium with photons in the early Universe. It follows the same evolution phases described in Section 1 and thus the homogenous and isotropic fluid of WIMPs cools down as the Universe expands. When the

temperature is too low to maintain a relativistic regime ($m_\chi \ll T$), WIMPs enter their non-relativistic phase, their number density n_χ^{eq} suppressed (and at the same time a corresponding quantity of energy from WIMP annihilations is transferred to the photons) and WIMPs are described by a Maxwell-Boltzmann distribution:

$$n_\chi^{\text{eq}} = g \left(\frac{m_\chi T}{2\pi} \right)^{3/2} e^{-m_\chi/T}, \tag{11}$$

where g is the number of degrees of freedom. n_χ^{eq} continues to decrease as the temperature goes down with the evolution of the Universe, until WIMPs freeze-out when the expansion rate becomes larger than the collision rate $H \gtrsim n_\chi^{\text{eq}} \sigma_{\text{ann}} v$, with $\sigma_{\text{ann}} v$ being the annihilation cross section between two WIMPs and v their relative velocity in the annihilation. After freeze-out WIMPs evolve completely decoupled by other particle species until they reach the value for energy density measured today (Komatsu et al. 2008). Analytically the evolution of the WIMP number density is determined by the Boltzmann equation, which can be sintetically expressed as:

$$\mathbf{L}[f^\chi] = \mathbf{C}[f^\chi]. \tag{12}$$

The left hand side is the Loiuville operator acting on the WIMP phase space density f^χ and it describes how f^χ evolves in the case of collisionless WIMPs. The right hand side, on the contrary, takes into account the effect of collisions. For the FRW metric in Equation (1), the Boltzmann equation becomes

$$\frac{dn_\chi}{dt} + 3Hn_\chi = -\langle \sigma_{\text{ann}} v \rangle [n_\chi^2 - (n_\chi^{\text{eq}})^2], \tag{13}$$

where the term proportional to H accounts for the fact that evolution occours in an expanding Universe, brackets $\langle \cdot \rangle$ denote thermal average and the equilibrium distribution (which is the phase space density integrated over all phase space coordinates but time) is that of Equation (11).

Following Kolb & Turner (1990) the number density is rescaled to the comoving entropy density s and the x variable is preferred to the temperature T according to the following definitions:

$$Y_\chi = n_\chi / s, \tag{14}$$

$$s = \frac{2\pi^2 g_\star T^3}{45}, \tag{15}$$

$$x = m_\chi / T, \tag{16}$$

where $g_\star$ is a slightly different definition of the number of degrees of freedom (for details, see Kolb & Turner 1990). Using the conservation of entropy density per comoving volume (sa^3=constant), Equation (13) becomes:

$$\frac{dY_\chi}{dx} = -\frac{\langle \sigma_{\text{ann}} v \rangle s}{Hx} [Y_\chi^2 - (Y_\chi^{\text{eq}})^2]. \tag{17}$$

Another change of variable ($\Delta_\chi = Y_\chi - Y_\chi^{\mathrm{eq}}$) and the expansion of the thermally-averaged annihilation cross section in terms of the relative velocity $\langle \sigma_{\mathrm{ann}} v \rangle = a + b\langle v^2 \rangle + O(v^4) = a + b/x + O(x^{-2})$ make the equation as follows:

$$\frac{d\Delta_\chi}{dx} = -\frac{dY_\chi^{\mathrm{eq}}}{dx} - f(x)\Delta_\chi(2Y_\chi^{\mathrm{eq}} + \Delta_\chi), \tag{18}$$

with

$$f(x) = \sqrt{\frac{\pi g_\star}{45}} m_{\mathrm{Pl}} m (a + 6b/x) x^{-2}. \tag{19}$$

From Equation (18) it is now clear that the solution can be analytically obtained for the after freeze-out regime $x \gg x_F = m_\chi/T_F$, assuming that the terms proportional to Y_χ^{eq} and dY_χ^{eq}/dx are negligible:

$$\frac{d\Delta_\chi}{dx} = f(x)\Delta_\chi^2 \tag{20}$$

Integrating this last equation from the freeze-out epoch x_F to today, the modern value of Y_χ (assuming $\Delta_\chi(\infty) \ll \Delta_\chi(x_F)$) is

$$Y_\chi^{-1}(\infty) = \sqrt{\frac{\pi g_\star}{45}} m_{\mathrm{Pl}} m x_F^{-1} (a + 3b/x_F), \tag{21}$$

from which the ratio of the DM density to the critical one results to be

$$\Omega_\chi h^2 = \frac{1.07 \times 10^9 \text{ GeV}^{-1}}{m_{\mathrm{Pl}}} \frac{x_F}{\sqrt{g_\star}} \frac{1}{a + b/x_F}. \tag{22}$$

In Equation (22) I use the fact that, being non-relativistic, the energy density of DM is equal to $\rho_\chi = n_\chi m_\chi$ and that $s_0 = 2889.2 \text{ cm}^{-3}$. The Planck mass m_{Pl} is equal to $G^{-1/2}$ and the number of degrees of freedom is evaluated at the freeze-out temperature.

Thus, to determine the today relic density of a WIMP, one should just determine the total annihilation cross section (computing the branching ratios to all possible channels) and obtain the values for the a and b parameters in the expansion of the annihilation cross section. The freeze-out temperature can be estimated remembering that decoupling occurs when the collision rate becomes smaller than the expansion rate, which translates in the following equation to be solved:

$$e^{x_F} = c(c + 2) \sqrt{\frac{45}{8}} \frac{g}{2\pi^3} \frac{m_{\mathrm{Pl}} m (a + 6b/x_F)}{\sqrt{g_\star x_F}}, \tag{23}$$

c is a constant that can be determined in the matching between the after freeze-out and before freeze-out solution.

From Equation (22) one can also see that the relic density is proportional to the mass of the WIMP and inversely proportional to its cross section (both these dependences are not exact but valid only as a rule of thumb): a larger annihilation cross section translates in a later decoupling and a consequent smaller relic density today as it can be seen in Figure 7.

Since we are interested in describing the properties of WIMPs, assuming a mass of the order of GeV, the relic density results to be

$$\Omega_\chi h^2 = \frac{3 \times 10^{-27} \text{cm}^{-3}\text{s}^{-1}}{\langle \sigma_{\mathrm{ann}} v \rangle}, \tag{24}$$

Figure 7. Comoving number density for a generic WIMP n_χ as a function of the temperature (encoded in the $x = m_\chi/T$ parameter). Before freeze-out the number density decreases as the Universe expands following the behaviour of primordial photons. After freeze-out WIMPs do not interact anymore and the comoving number density remains constant. Increasing the thermally averaged WIMP annihilation cross section $\sigma_{\text{ann}}v$ the freeze-out is retarded and, consequently, fewer WIMPs are left and the actual relic density is lower. Taken from Kolb & Turner (1990).
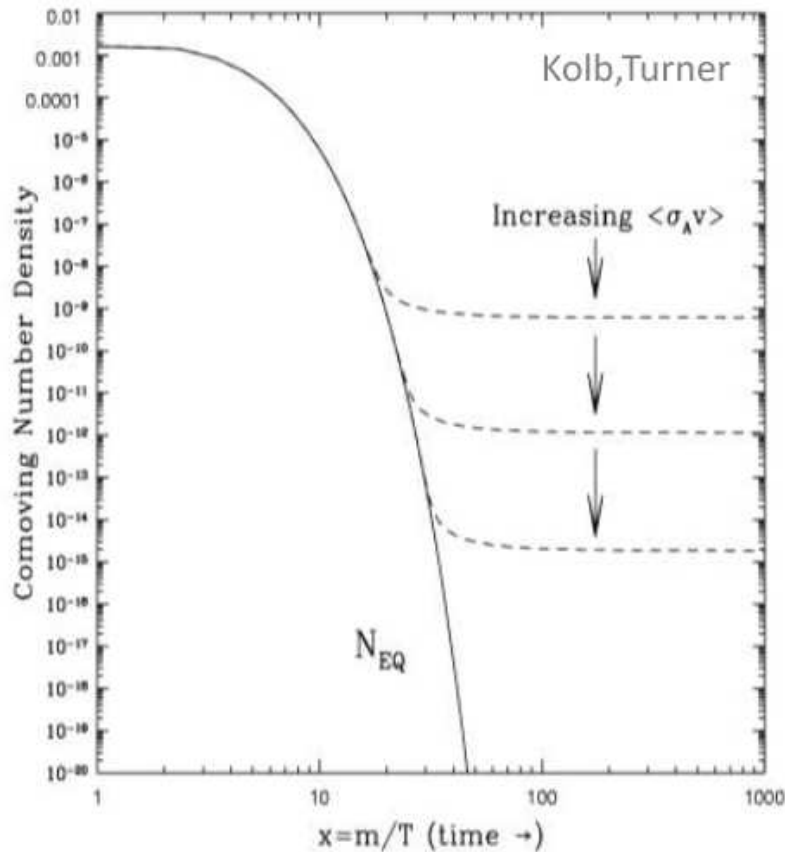
making explicit the so-called *WIMP miracle*, i.e. the fact that, in order to obtain the exact DM relic density predicted today, the particle should have a cross section of the order of the weak interactions, making this scenario experimentally accessible to the present and future generation of experiments that are looking for DM. Moreover this approach suggests the existence of a particle that share the same characteristics of what other theories not related to the DM problem (as SuperSymmetry or models with UEDs) are able to predict.

There are situations in which the scenario can strongly deviate from the standard computation of the DM relic density as depicted before and the final result can substantially change. This is the case, e.g., of coannihilations: if other particles $X_1, X_2, ...$ beyond the standard model are predicted with a mass quite close to m_χ, interactions with these more massive particles are open and kinetically accessible for the WIMP (Griest & Seckel 1991). The Boltzmann equation in Equation (13) will be affected from these extra terms and, in the hypothesis that all these X_i particles will sooner or later decay in the WIMP, the final result

will depend also on the number density n_{X_i}.

In this case one should carefully compute not only the cross sections for all the WIMP annihilation channels but also the possible interactions with these higher mass X_i. This will lead to the definition of effective a_{eff} and b_{eff} parameters, as in Equation (22). Then, one can derived the relic density following the same path as before, finding a resulting density that can be either enhanced or damped with respect to the case in which coannihilations are neglected.

In particular, this contribution is very important both in the case of SUSY and for models with Unified Extra Dimensions (UEDs). For SUSY, the DM role is played by the lightest neutralino $\tilde{\chi}$: the relic density computed following Equation (22) results to be usually too high respect to the current measurements and additional mechanisms should be looked for in order to reduce the prediction for $\Omega_\chi h^2$. There are regions in the supersymmetric parameters space where coannihilations are important (the superpartner of the top quark $\tilde{t}$ or of the tau lepton $\tilde{\tau}$ being the supersymmetric particle slightly more massive than $\tilde{\chi}$) and their effect is exactly that of reducing the value of the neutralino relic density to the value predicted by Komatsu et al. (2008).

On the other hand, in the case of UEDs (see Section 3.4), coannihilations (and loops diagrams) are important to remove the mass degeneracy among Kaluza-Klein states, determining the mass spectrum for the model and the reactions that are kinetimatically allowed.

3.3. SuperSymmetry

The standard model of particle physics, in the formulation by Glashow, Weinberg and Salam (for extensive description see Peskin & Schroeder 1995) with the introduction of massive neutrinos, is a theory that received excellent confirmations from decades of experimental data. However it is also well known that the standard model should be considered as an effective low-energy theory.

The main issue remains the *hierarchy problem* for the corrections to the mass of the Higgs boson (Martin 1997): in fact, radiative loop corrections to the mass of this fundamental scalar field are sensitive to some power of the high-energy cut-off Λ_{UV} of the theory, which represents the energy scale at which new physics enters to alterate the high-energy behaviour of the standard model. As an example, if the Higgs boson H interacts with a Dirac fermion f of mass m_f through a Lagrangian three-bodies interaction term like $-\lambda_f \bar{f} f H$ where λ_f is the coupling constant, the correction to the Higgs boson mass due to loops where the fermion f propagate, starts with a terms like:

$$\delta m_H^2 = -\frac{|\lambda_f|^2}{8\pi^2}\Lambda_{\mathrm{UV}}^2 + ... \tag{25}$$

Since the high-energy cut-off can be as high as the Planck mass, this correction can completely destabilize the Higgs mass, shifting its value up to the same scale of Λ_{UV}, out of the experimental window around $\sim 114\,\mathrm{GeV}$. This problem only concerns the Higgs boson: in fact, the mass terms for fermions and for gauge bosons are protected by the gauge

symmetry ensuring that all corrections will vanish in the limit that the spontaneously-broken gauge symmetry is restored.

The same kind of ultraviolet divergences to the Higgs boson mass appear if the scalar is assumed to interact with a vector field. This suggests one possible way out of the hierarchy problem: imposing a symmetry, the SuperSymmetry (SUSY), that links fermions and bosons so that the corrections like in Equation (25) from fermions exactly cancel with those due to bosons at all perturbative orders.

SUSY generators are spinors $Q, Q^\dagger$ that transform a fermion to a boson and viceversa. Re-phrased in a different way, the irreducible representations of the supersymmetric algebra will be multiplets with both fermionic and bosonic components (the number of bosonic degrees of freedom in a SUSY multiplet has to be the same of the fermionic degrees of freedom). Moreover SUSY generators commutates with the operators of linear momentum ($[Q, P^\mu] = [Q^\dagger, P^\mu] = 0$) and with the generators of gauge symmetries so that the different components of a multiplet share the same mass (which is simply $P^\mu P_\mu$) and the same gauge interactions.

All the standard model fermions, that, written as Weyl spinors, are characterized by 2 fermionic degrees of freedom, belong to SUSY multiplets called *chiral multiplets* for which the additional two bosonic degrees of freedom are accounted by a complex scalar field that will be the so-called *superpartner* of the fermion. On the contrary, standard model vector bosons (which, by now, are massless) are described by *vector multiplets*. A massless vector boson has two degrees of freedom so that its SUSY partner will be a Weyl fermion.

This completely determines the Lagrangian, at least for the Minimal SuperSymmetric Model (MSSM), where only the superpartners of the standard models fields are introduced, and in the case that SUSY is conserved. Since superpartners share the same gauge interactions and masses of the original standard model fields, no additional parameters are needed and the whole range of new supersymmetric interactions can be described with the same parameters that define the standard model. Table 1 summarizes the names and quantum numbers of all the fields (both SUSY or not) predicted in a MSSM.

The only non-trivial feature is the fact that, even after the electroweak symmetry breaking which gives the Higgs boson a vacuum expectation value different from zero, it is not possible in the MSSM to give mass to all Standard Model fermions. The MSSM needs two Higgs bosons $H_u = (H_u^+, H_u^0)$ and $H_d = (H_d^0, H_d^-)$ (see Table 1), both receiving vacuum expecation values. The first scalar field will be responsible for the masses of all up-like quarks and the second to the masses of down-like quarks and leptons. $v_u = \langle H_u^0 \rangle$ and $v_d = \langle H_d^0 \rangle$ are, respectively, the values of the vacua, even if it is more common to use the variables v and $\tan \beta$:

$$v_u^2 + v_d^2 = v^2 \sim (174 \text{ GeV})^2, \tag{26}$$

$$\tan \beta = v_u / v_d. \tag{27}$$

SUSY cannot remains unbroken since it would predict the existence, e.g., of a scalar with the same mass of the electron, which it has never been detected. Thus, terms that explicitly break SUSY have to be added to the Lagrangian. These can only be *soft SUSY breaking*

Table 1. MSSM particle fields. The first row indicates if the multiplet is chiral or vector. The second row gives the name of the field and the third its symbol. Note that the convention of showing symbols for left-handed particles is followed, thus the right-handed electron, e.g., is written as $\bar{e}^\dagger$ since the name of the field is assigned to the left-handed $\bar{e}$. In the following two rows the multiplet is separated in its bosonic and fermionic components. The last row indicates the quantum numbers of the multiples under the gauge groups. For quarks and leptons the content of the lines should be repeated three times accounting for the three families. When a sfermion is referred to as left- or right-handed, what it is meant is that it is the superpartner of a left or right-handed fermion.

	Name		Bosons	Fermions	$(U(1)_Y, SU(2), SU(3))$
Chiral	(squarks, quarks)	Q	$(\tilde{u}, \tilde{d})$	(u, d)	$(1/6, \mathbf{2}, \mathbf{3})$
Chiral	(squarks, quarks)	$\bar{u}$	$\tilde{\bar{u}}^*$	$\bar{u}^\dagger$	$(-2/3, \mathbf{1}, \bar{\mathbf{3}})$
Chiral	(squarks, quarks)	$\bar{d}$	$\tilde{\bar{d}}^*$	$\bar{d}^\dagger$	$(1/3, \mathbf{1}, \bar{\mathbf{3}})$
Chiral	(sleptons, leptons)	L	$(\tilde{\nu}_e, \tilde{e})$	(ν_e, e)	$(-1/2, \mathbf{2}, \mathbf{1})$
Chiral	(sleptons, leptons)	$\bar{e}$	$\tilde{\bar{e}}^*$	$\bar{e}^\dagger$	$(1, \mathbf{1}, \mathbf{1})$
Chiral	(Higgs, Higgsino)	H_u	(H_u^+, H_u^0)	$(\tilde{H}_u^+, \tilde{H}_u^0)$	$(1/2, \mathbf{2}, \mathbf{1})$
Chiral	(Higgs, Higgsino)	H_d	(H_d^0, H_d^-)	$(\tilde{H}_d^0, \tilde{H}_d^-)$	$(-1/2, \mathbf{2}, \mathbf{1})$
Vector	(B boson, Bino)	B_μ	B_μ	$\tilde{B}$	$(0, \mathbf{1}, \mathbf{1})$
Vector	(W^i boson, Winos)	W_μ^i	W_μ^i	$\tilde{W}^i$	$(0, \mathbf{3}, \mathbf{1})$
Vector	(gluons, gluinos)	$g_{\alpha\beta}$	$g_{\alpha\beta}$	$\tilde{g}_{\alpha\beta}$	$(0, \mathbf{0}, \mathbf{3})$

terms, since we still want to maintain the cancellation of the divergences in the corrections to the Higgs boson mass. If m_{soft} is the largest term with the dimension of a mass in the soft SUSY breaking part of the Lagrangian, the corrections that this soft breaking part induce to the Higgs mass go like

$$\delta m_H^2 = m_{\mathrm{soft}}^2 \left[\frac{\lambda}{16\pi^2} \ln(\Lambda_{\mathrm{UV}}/m_{\mathrm{soft}}^2) + ... \right]. \tag{28}$$

The splitting between the mass of a standard model field and its superpartner is encoded in the SUSY breaking part and therefore depends on m_{soft}. It follows that a superpartner cannot be much more massive (meaning large m_{soft}) than its standard model companion, otherwise this would induce, again, large corrections to the Higgs mass, spoiling the very motivation for SUSY.

That is why SUSY is supposed to predict the existence of new particles around the TeV scale, not far from the scale of the standard model and within the reach of new experiments as the LHC.

Apart from the fact that it represents a cure for the hierarchy problem and that it is a testable theory, another good feature of SUSY is the possibility of mediating the Grand Unification of gauge couplings: in Figure 8 the evolution of the coupling costants α_i for three fundamental interactions can be seen. Their behaviour depends on the Renormalization Group Equations (RGEs) that, from the computation of all the radiative corrections for the coupling constants, fix the their dependence from the energy. Corrections involving all the particles in the theory should be taken into account and, as a consequence, the evolution predicted within a MSSM will be slightly different than the standard model. In particular, it appears that all

Figure 8. Renormalization Group evolution of the inverse gauge couplings $\alpha_a^{-1}(Q)$ in the standard model (dashed lines) and the MSSM (solid lines). In the MSSM case, the sparticles mass thresholds are varied between 250 GeV and 1 TeV and $\alpha_3(m_Z)$ between 0.113 and 0.123. Two-loop effects are included. Taken from Martin (1997).
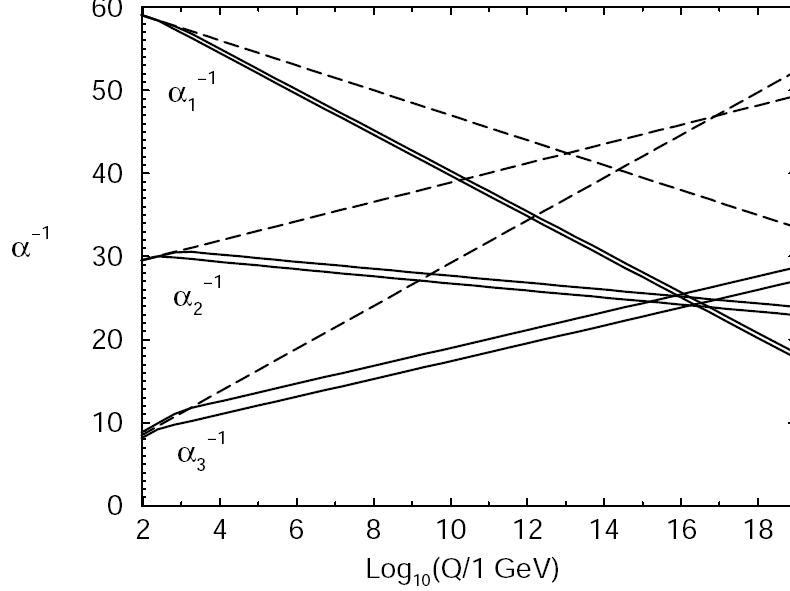
couplings unify at a scale of $M_U \sim 2 \times 10^{16}$GeV improving that non-perfect unification that was predicted by the standard model and that can be seen in the dashed lines of Figure 8. Of course only the MSSM is taken into accout, while more complicated SUSY models can again alter the precise convergence of the couplings. Anyway, this result stands as a strong hint in favour of the unification of fundamental interactions.

Going back to the SUSY Lagrangian, the non-gauge interactions are described by the superpotential W, which is still part of the SUSY-conserving Lagrangian, and by the soft SUSY-breaking terms. In the case of the MSSM, the superpotential can be written as:

$$W_{\mathrm{MSSM}} = \bar{u}\mathbf{Y_u}QH_u - \bar{d}\mathbf{Y_d}QH_d - \bar{e}\mathbf{Y_e}LH_d + \mu H_u H_d. \tag{29}$$

All the fields in Equation (29) are multiplets as indicated in Table 1 so that interactions can be obtained expanding the superfields in their components. The $\mathbf{Y_i}$ matrices are 3×3 matrices in the generation space and depend on the same Yukawa couplings of the Standard Model. The only new parameter is μ.

There is not a full consensus on the mechanism that breaks SUSY, neither on how the SUSY breaking is communicated to the low-energy scales where we live. On the contrary, the soft breaking terms in the Lagrangian are quite commonly written as:

$$
\begin{aligned}
\mathcal{L}_{\mathrm{MSSM}}^{\mathrm{soft}} = {} & \frac{1}{2}(M_1\tilde{B}\tilde{B} + M_2\tilde{W}^i\tilde{W}^i + M_3\tilde{g}\tilde{g} + \text{c.c.}) + \\
& - \tilde{Q}^\dagger\mathbf{m_Q^2}\tilde{Q} - \tilde{L}^\dagger\mathbf{m_L^2}\tilde{L} - \tilde{u}\mathbf{m_u^2}\tilde{u}^\dagger - \tilde{d}\mathbf{m_d^2}\tilde{d}^\dagger - \tilde{e}\mathbf{m_e^2}\tilde{e}^\dagger \\
& - m_{H_u}^2 H_u^* H_u - m_{H_d}^2 H_d^* H_d - (bH_uH_d + \text{c.c.}), \\
& - (\tilde{\bar{u}}\mathbf{a_u}\tilde{Q}H_u - \tilde{\bar{d}}\mathbf{a_d}\tilde{Q}H_d - \tilde{\bar{e}}\mathbf{a_e}\tilde{L}H_d + \text{c.c.})
\end{aligned}
\tag{30}
$$

where c.c. indicates complex conjugation and the different terms are, in order, masses for the gauginos, for all the sfermions, for the Higgs, a mixed mass term between the two Higgs and an additional set of Yukawa interactions.

With the introduction of the terms in Equation (30) the Lagrangian depends now on a much larger set of parameters, that have nothing to do with standard model masses or couplings and should be fixed by the experiment. In particular, assuming that all new parameters in Equation (30) are free parameters will have the consequence of opening up interactions through Flavour Changing Neutral Current (FCNC, which are forbidden in the standard model) and will introduce a larger amount of *CP* violation respect to what has been measured for the standard model. In order to keep under control these undesidered features and to reduce the number of free parameters, commonly a particular, simplifying structure is assumed for the matrices in the soft-breaking terms. E.g., a particularly well-studied case is that of *mSUGRA*, a MSSM in which SUSY is broken at high-energy and this is communicated to the lower energy scales by gravitational interactions. At the SUSY-breaking energy scale the terms in Equation (30) are assumed to be universal so that they result to depend only by 4 remaining parameters $(m_{1/2}, m_0, A_0, B_0)$, respectively the common mass of gauginos, the common mass of scalars, the universal Yukawa coupling and the coeffecient of the mixed mass term for Higgs:

$$M_1 = M_2 = M_3 = m_{1/2}, \tag{31}$$

$$\mathbf{m}_Q^2 = \mathbf{m}_L^2 = \mathbf{m}_u^2 = \mathbf{m}_d^2 = \mathbf{m}_e^2 = m_0\mathbf{1}, \tag{32}$$

$$\mathbf{a}_u = A_0\mathbf{Y}_u \qquad \mathbf{a}_d = A_0\mathbf{Y}_d \qquad \mathbf{a}_e = A_0\mathbf{Y}_e, \tag{33}$$

$$b = B_0\mu. \tag{34}$$

This gets rid of undesired FCNC interactions and *CP* violation. The determination of the effective masses and couplings at the low-energy scale around the TeV where the particles are hoped to be detected, is based on the RGEs: in Figure 9 a particular example is shown in order to see how the evolution to low scales of the parameters defining a mSUGRA model can account for the different values for the masses of all supersymmetric particles. Note in particular the evolution of the $\mu^2 + m_{H_u}^2$ combination, which it has to go negative at low energy in order to account for electroweak symmetry breaking. This requirement permits to determine the B_0 parameter and the modulus of μ as functions of the remaining variables. So finally a mSUGRA model is defined only by 5 quantities: $(m_0, m_{1/2}, A_0)$ from the soft breaking part, the sign of μ from the superpotential and the ratio of the vacua $\tan\beta$.

A large phenomenolgy is possible varying those 5 parameters. In Trotta et al. (2008), the authors studied if the precision tests to the standard model can constrain these 5 mSUGRA parameters. Considering, among others, precision measurements on the mass of top m_t, mixing data fixing the ΔM_{B_s} for B_s mesons, informations about the anomalous magnetic momentum of the muon a_μ and assuming that the Lightest Supersymmetric Particle (LSP) is a neutralino which, interpreted as DM, provides the exact relic DM density measured by WMAP, the tightest constraints can be seen in Figure 10. The main unresolved issue in these plots (obtained as results of a Monte Carlo Markov Chain (de Austri et al. 2006)) is

Figure 9. Renormalizatin Group evolution of scalar and gaugino mass parameters (defined at 2.5×10^{26} GeV) in a mSUGRA model. It should be notice that the quantity $\mu^2 + m^2_{H_u}$ runs negative, provoking at low scale the electroweak symmetry breaking. Taken from Martin (1997).
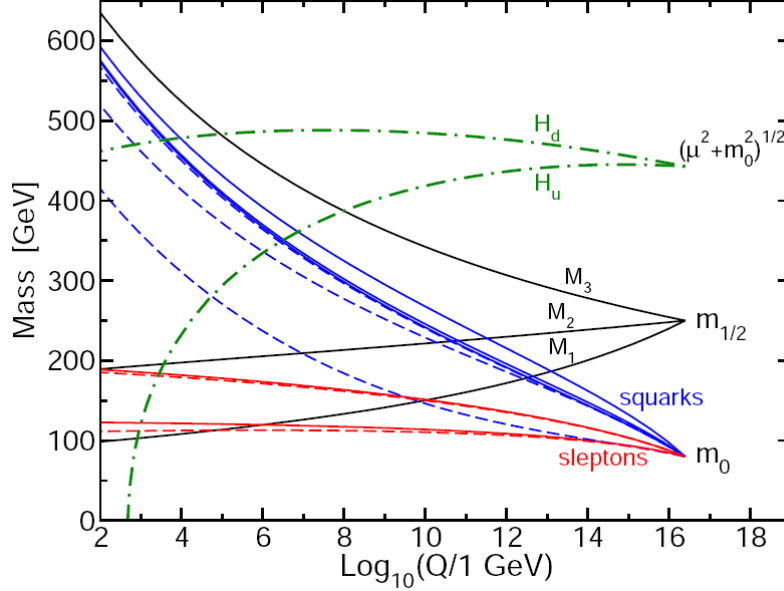
the dependence on how SUSY variables are parametrized before the constraints are taken into account, the so-called *prior dependence*. The fact that Figure 10 shows some prior dependence is a clear sign that the experimental constraints that are considered are not constraining.

3.4. The lightest neutralino $\tilde{\chi}$

When I wrote down the superpotential in Equation (29), I neglected some terms that can be included since permitted by the theory and that, consequently, should appear in the final Lagrangian. These interactions are characterized by the fact that they violate leptonic number L (as the term $LL\bar{e}$) or baryonic number B (as $\bar{u}\bar{d}\bar{d}$), and are able to mediate the decay of the proton with a half-time of less than seconds in the case that the couplings of these baryon-violating interactions are of the order of unity.

A theory that includes such terms would be highly unphysical. A possible solution would simply be imposing L and B conservation as fundamental symmetries: this would be a step back respect to the standard model where conservation of leptonic and baryonic number arise as by-products. Moreover such symmetries are known to be radiatively violated by quantum effects.

Instead what can be done is introducing a less constraining symmetry, called *R*-parity, assumed to be an exact symmetry of Nature. This *R*-parity is able to get rid of all the baryonic and leptonic violating terms so that now the only allowed interactions are the ones that I have already written for the superpotential in Equation (29).

Figure 10. Posterior probability function for flat priors (top row) and log priors (bottom row) for a scan including all the constrains in Table 3 of Trotta et al. (2008). The inner and outer contours include, respectively, 68% and 95% joint regions for both statistics. The posterior pdf has been smoothed with a Gaussian kernel of 1 bin width for display purposes. The cross point ($\otimes$) gives the best-fit point and the filled point ($\bullet$) the posterior mean. Taken from Trotta et al. (2008).
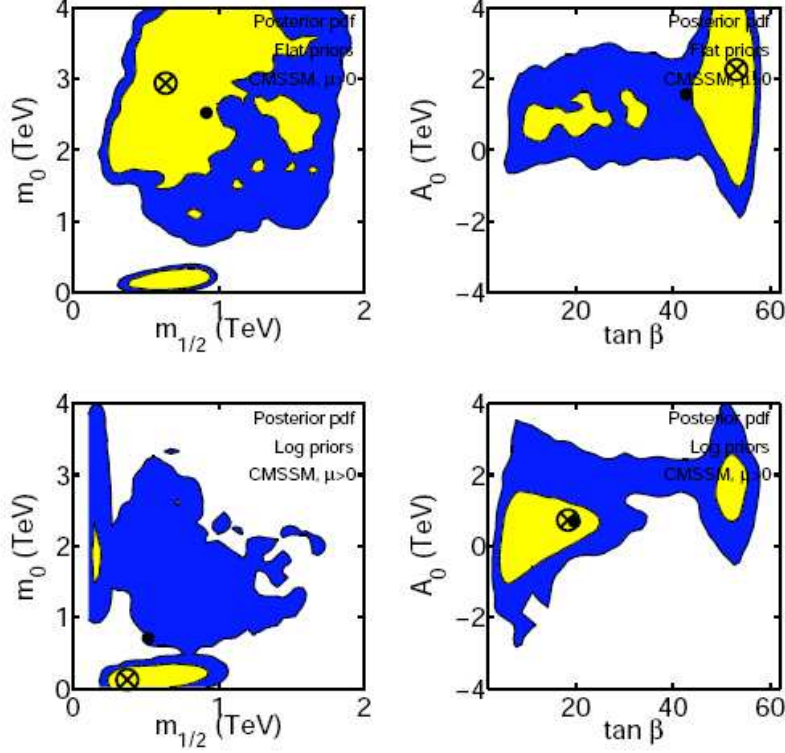
If not differently indicated, if a SUSY model is proposed as a description of the constituents of Nature and of its interactions, *R*-parity is always assumed. Without it, our model would suffer from strong problems as the stability of the proton. Moreover, *R*-parity is a key ingredient also for the DM issue: in fact *R*-symmetry belongs to the class of Z_2 trasformations, and it assigns a multiplicative quantum number equal to +1 to all standard model particles and equal to −1 to all SUSY particles. Thus standard model particles can interact only with couples of SUSY particles (otherwise *R*-parity would be violated) and the LSP will be a stable particle since it will be forbidden to it to decay but only to annihilate. In many SUSY models, the LSP is the first neutralino.

Neutralinos are the mass eigenstates obtained as linear combinations of the superpartners of the neutral gauge bosons and of the neutral Higgsinos (Jungman et al. 1996, Martin 1997). If $\tilde{\psi}_0 = (\tilde{B}, \tilde{W}^3, \tilde{H}_d^0, \tilde{H}_u^0)$, the mass term in the Lagrangian results $-1/2(\tilde{\psi}_0)^T \mathbf{M}_{\tilde{N}} \tilde{\psi}_0$ + c.c., with

$$
\mathbf{M}_{\tilde{N}} = \begin{pmatrix} M_1 & 0 & -g'v_d/\sqrt{2} & g'v_u/\sqrt{2} \\ 0 & M_2 & gv_d/\sqrt{2} & gv_u/\sqrt{2} \\ -g'v_d/\sqrt{2} & gv_d/\sqrt{2} & 0 & -\mu \\ g'v_u/\sqrt{2} & gv_u/\sqrt{2} & -\mu & 0 \end{pmatrix}. \tag{35}
$$

The M_1 and M_2 entries depend on the SUSY breaking part of the Lagrangian, the μ terms comes from the superpotential, while the other non-zero entries are gauge interactions with the Higgs bosons receiving vacuum expectation values after electroweak symmetry breaking. That is why they depend on g and g' (the coupling constants of the electroweak symmetry group). From the diagonalization of the mass matrix, the four neutralinos can be defined. Therefore the lightest neutralino $\tilde{\chi}_1$ (or simply the neutralino $\tilde{\chi}$) is:

$$\chi = N_{11}\tilde{B} + N_{12}\tilde{W}^3 + N_{13}\tilde{H}_d + N_{14}\tilde{H}_u, \tag{36}$$

where **N** is the diagonalizing matrix. $Z_g = |N_{11}|^2 + |N_{12}|^2$ and $Z_H = |N_{13}|^2 + |N_{14}|^2$ are called the *gaugino* and *Higgsino fraction*, respectively and indicate how the neutralino is aligned towards the different interaction eigenstates. It is a WIMP since it is stable, with a mass of the order of the GeV-TeV scale and a weak cross section becoming, by far, the most studied candidate for DM.

The theory that predicts the existence of the neutralino is well-defined and one can proceed in the calculation of its annihilation channels, obtaining an estimate for its today relic density, as described in Section 3.2 (see Equation (22)). Of course, the calculation will depend on some unknown parameters. In the case of mSUGRA these parameters are defined at high-energy and then the RGEs are used to evolve masses and couplings to the electroweak scale where it can be checked if the particular model predicts the right relic density for the neutralino DM (Battaglia et al. 2001, Battaglia et al. 2004).

In the largest region of the SUSY parameters space the relic density results to be higher than the value of WMAP: in Figure 11 the cyan area indicates the region when $0.1 \leq \Omega_\chi h^2 \leq 0.3$, overestimating the error in the most recent measurement by WMAP. As it can be seen, the neutralino provides the right DM adundance only in narrow regions where some particular features in the mass spectrum of SUSY particles step in enhancing the annihilation cross section and, consequently reducing the relic density to the desired value (it should be noted that Figure 11 refers to a particular set of mSUGRA parameters and that in other configurations the colored region would change their shape). In particular, Battaglia et al. (2001) and Battaglia et al. (2004) defined a collection of benchmark models inside the cyan area and indicated by the purple stars in Figure 11. For each of these models they studied the signatures that SUSY particles would leave in a collider, in the hope that future measurements with Tevatron or the LHC will be able to detect the DM particle.

From Figure 11 five regions are usually singled out, each of them with a different mechanism able to assign the desired value to $\Omega_\chi h^2$:

- the *bulk region* at low m_0 and $m_{1/2}$, where the mass spectrum contains light sleptons $\tilde{l}$ and, as a consequence, the relic density is mainly determined by annihilation processes $\tilde{\chi}\chi \rightarrow l^+l^-$ in the early Universe (through a *t*-channel exchange of $\tilde{l}$),

- the *funnel region* at intermediate values for m_0 and $m_{1/2}$, where $m_A \approx 2m_\chi$ and annihilations in the early Universe are thus enhanced by the presence of the near-resonant pseudoscalar Higgs boson A,

- the hyperbolic branch or *focus point region*, where $m_0 \gg m_{1/2}$ and the neutralino becomes an almost pure Higgsino, with large annihilation rates into gauge bosons,

Figure 11. Qualitative overview of the location of the benchmark models proposed by Battaglia et al. (2001) in a generic $(m_{1/2}, m_0)$ plane. The other parameters defining mSUGRA are $\tan\beta$, $\text{sign}(\mu)$ and A_0 which is supposed to be 0. The light cyan region is the cosmologically preferred region with $0.1 \leq \Omega_\chi h^2 \leq 0.3$, whose exact shape depends on the value of $\tan\beta$ and, to some extent on the standard model inputs, as m_t, m_b and α_S. In the dark, brick red region at bottom right, the LSP is the charged $\tilde{\tau}_1$ (the first mass eigenstate of the $\tilde{\tau}$) so that this region is excluded. Electroweak symmetry breaking is not possible in the pink region at top left. The proposed benchmark models are marked with purple stars. The lines indicate experimental constraints (for more details see Battaglia et al. 2001). Taken from Battaglia et al. (2001).
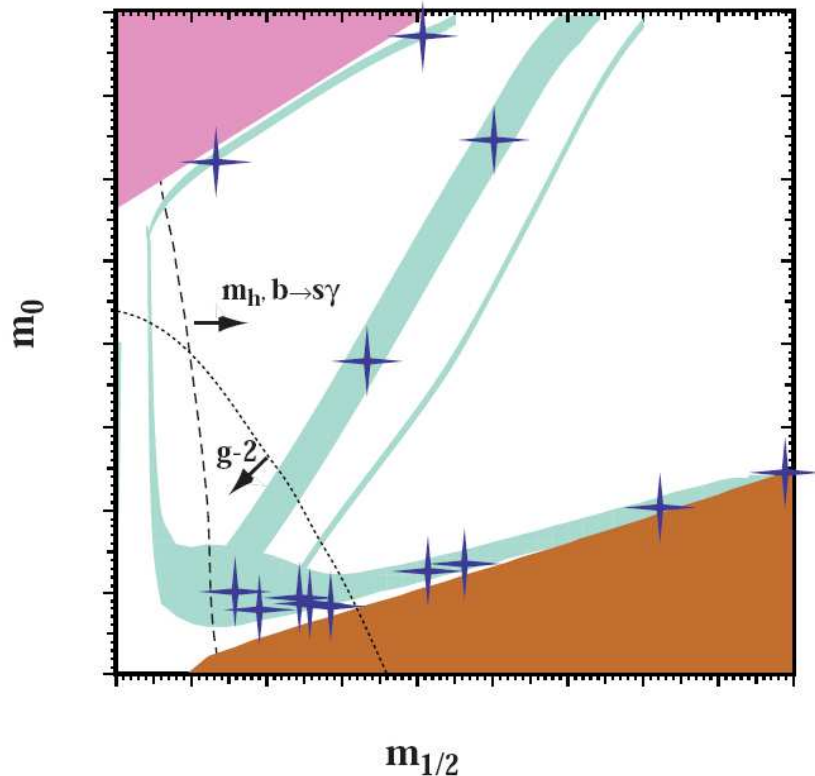
- the *stau coannihilation region* at large $m_{1/2}$ but small m_0, where $m_\chi \approx m_{\tilde{\tau}}$ and coannihilations with staus $\tilde{\tau}$ (and usually other sleptons as well) are important in determining the relic density,

- the *stop coannihilation region* (arising when $A_0 \neq 0$ and thus not visible in Figure 11) where $m_\chi \approx m_{\tilde{t}}$.

3.5. The first Kaluza-Klein excitation of the photon $\gamma^{(1)}$

Many theories and models have been built on the hypothesis of the existence of hidden extra-dimension beyond the usual four. The case of Unified Extra-Dimensions (UEDs) is the only one I am going to talk about. In UEDs (Appelquist et al. 2001, Hooper & Profumo 2007) all standard model quantum fields can propagate in the extended space-time (also called the *bulk*). The d extra-dimensions y^a (with $a \in (1, ..., d)$), opposite to the usual x^μ (with $\mu \in (1, 2, 3, 4)$), are compactified over a manifold which is usually assumed to be a multidimensional torus

$[(S^1 \times S^1)/Z_2]^k$ if k is even or $[(S^1 \times S^1)/Z_2]^k \times (S^1/Z_2)$ if k is odd, where $d = 2k$ if d is even or $d = 2k + 1$ if d is odd.

The gamma matrices in (4+d) dimensions are anti-commuting $2^{k+2} \times 2^{k+2}$ matrices. Chiral fermions exist only when d is even, or equivalently, the chiral projection operators $P_L^{(4+d)}$ and $P_R^{(4+d)}$ can be constructed only if d is even. In any case, the Lagrangian can be defined in the bulk and, in order to derive the 4-dimensional effective theory, it simply has to be integrated over the extra-dimensions.

It is also very important to define how a field transforms under the Z_2 orbifold projection that transforms the extra-dimensions from $\{y^a\}$ to $\{-y^a\}$. E.g. let Q be a generic spinor in a 6-dimensional bulk, designed to reproduced, in the 4-dimensional effective theory, a left-handed fermion (the fermionic $SU(2)$ doublet $Q = (u, d)$ for instance). Applying the 6-dimensional chiral projection operators, I can re-write Q as Q_R and Q_L. I assign different trasformation properties to the two fields assuming that Q_L is even while Q_R is odd under orbifold trasformation. In this way Q can finally be written as

$$Q(x^\mu, y^1, y^2) = \frac{1}{\sqrt{\pi R}} \left\{ Q_L^0(x^\mu) + \sqrt{2} \sum_{n,m} \left[P_L Q_L^{(n,m)}(x^\mu) \cos\left(\frac{ny^1 + my^2}{R}\right) + \right. \right. \quad (37)$$
$$\left. \left. P_R Q_R^{(n,m)}(x^\mu) \sin\left(\frac{ny^1 + my^2}{R}\right) \right] \right\},$$

so that the zero-order field Q_L^0 that will represent the standard model doublet will have the right chirality, and the undesired states (like a zero mode for Q_R) will be excluded by the assumed transformation propriety under the orbifold projection. The decomposition in Equation (37) (R indicates the dimension of the extra-dimensions) shows that a whole collection of states called *Kaluza-Klein states* is predicted, one for each couple of integers (n, m).

The same decomposition is possible for a spinor that is supposed to represent a right-handed fermion, like e.g. u, assuming u_R to be even under Z_2 and u_L to be odd:

$$u(x^\mu, y^1, y^2) = \frac{1}{\sqrt{\pi R}} \left\{ u_R^0(x^\mu) + \sqrt{2} \sum_{n,m} \left[P_R u_R^{(n,m)}(x^\mu) \cos\left(\frac{ny^1 + my^2}{R}\right) + \right. \right. \quad (38)$$
$$\left. \left. P_L u_L^{(n,m)}(x^\mu) \sin\left(\frac{ny^1 + my^2}{R}\right) \right] \right\},$$

or for the Higgs boson:

$$H(x^\mu, y^1, y^2) = \frac{1}{\sqrt{\pi R}} \left[H^0(x^\mu) + \sqrt{2} \sum_{n,m} H^{(n,m)}(x^\mu) \cos\left(\frac{ny^1 + my^2}{R}\right) \right], \quad (39)$$

for which there are not problems related to chirality and which is assumed to be even under orbifold projection. In the case of gauge bosons, their Lorentz index runs also over the additional dimensions. In order to avoid zero state associate to the polarization along the extra-dimensions, those modes are assumed to be odd under orbifold projection, while the remaining four are even. Thus:

$$A_\nu(x^\mu, y^1, y^2) = \frac{1}{\sqrt{\pi R}} \left[A_\nu^0(x^\mu) + \sqrt{2} \sum_{n,m} A_\nu^{(n,m)}(x^\mu) \cos\left(\frac{ny^1 + my^2}{R}\right) \right], \quad (40)$$

with $\nu \in (1, 2, 3, 4)$ and

$$A_a(x^\mu, y^1, y^2) = \sqrt{\frac{2}{\pi R}} \sum_{n,m} A_a^{(n,m)}(x^\mu) \sin\left(\frac{ny^1 + my^2}{R}\right), \tag{41}$$

with $a \in (5, 6)$.

The Lagrangian of UED is the same one of the standard model but now, once each field is expanded in its decomposition as shown in the previous equations, new interactions involving KK states appear, for which the Kaluza-Klein number (the index over which it was summed in the previous equations) is conseved. The zero mode Higgs boson assumes a vacuum expectation value in the same way it does in the standard model. Then in general a (n, m) state (always in the case of 2 extra-dimensions) gets a mass equal to:

$$m^2_{(n,m)} = m^2_0 + \frac{n^2 + m^2}{R}, \tag{42}$$

meaning that the theory will have as many degenerate states with mass $m^2_{(n,m)}$ as many couples of integer numbers are solutions of Equation (42). Moreover, since experimentally $1/R$ is bound to be ≥ 600 GeV (considering the standard model precision test of the inclusive $\bar{B} \to X_s\gamma$ in Haisch & Weiler (2007)), the zero order mass m^2_0 is usually negligeble, thus the UED theory is characterized by a high amount of degeneracy.

Beyond the usual interactions, one should include additional Lagrangian terms that are localized at the fixed points of the orbifold projection and are due to breaking of momentum conservation along the extra-dimensions caused by the orbifold projection itself. E.g. the following Equation (43) indicates possible boundary kinetic terms:

$$\frac{\delta^{(2)}(y^1, y^2) - \delta^{(2)}(y^1 - \pi R, y^2 - \pi R)}{\Lambda}[G_4(F_{\mu,\nu})^2 + F_4\bar{\psi}i\slashed{D}\psi + \tag{43}$$
$$F_5\bar{\psi}\Gamma_5\partial_5\psi + F_6\bar{\psi}\Gamma_6\partial_6\psi].$$

The coupling in front of these additional contributions to the total Lagrangian are free parameters not connected to the standard model. This can jeopardize the predictive power of our theory: however it should be remembered that, since the wave functions of the quantum fields are spread out over the extra-dimensions, these new couplings are volume suppressed (Cheng et al. 2002). We can get estimates of these corrections assuming that they are strong at the high-energy cut-off Λ of the theory. The result is that their amplitude is at the same order of magnitude of the amplitude of usual corrections from loops.

As a consequence, boundary terms and loops corrections in UEDs play a fundamental role, breaking mass degeneracy and determining the hierarchy in the mass spectrum and which channels are kinematically open. Typical corrections are shown in the following equations (for only one extra-dimension, Hooper & Profumo 2007):

$$\delta m^2_{B^{(n)}} = \frac{g'^2}{16\pi^2 R^2}\left(\frac{-39}{2}\frac{\zeta(3)}{\pi^2} - \frac{n^2}{3}\ln\Lambda R\right), \tag{44}$$

$$\delta m_{W^{(n)}} = \frac{g'^2}{16\pi^2 R^2}\left(\frac{-5}{2}\frac{\zeta(3)}{\pi^2} + 15n^2\ln\Lambda R\right), \tag{45}$$

$$\delta m_{Q^{(n)}} = \frac{n}{16\pi^2 R}\left(6g_3^2 + \frac{27}{8}g^2 + \frac{1}{8}g'^2 \ln \Lambda R\right),$$ (46)

where $\zeta(3)$ is the zeta function. The terms proportional to $\ln \Lambda R$ comes from the boundary terms while the others proportional to $\zeta(3)$ are usual loops corrections. In the first equation for the mass of the KK-states of the B vector boson, both kinds of corrections are negative, thus we have reasons to believe that the $B^{(1)}$ will be the Lightest Kaluza-Klein Particle (LKP). Indeed, after mixing with the first level of the third W boson, the first Kaluka-Klein state of the photon $\gamma^{(1)}$ is usually the LKP (another possibility is that the LKP is the $\nu^{(1)}$ (Servant & Tait 2003)).

As I already pointed out, orbifold projection breaks momentum conservation over extra-dimensions (which, on the 4-dimensional effective theory implies conservation of KK number). A residual symmetry remains, called *K-parity*. More precisely, a complete analysis of the ultra-violet behaviour of the theory is needed in order to state if the residual K-parity is a symmetry or not, but under common assumptions, this is the case. Z_2 is very similar to *R*-parity in SUSY, since it characterized, again, each standard model field with a multiplicative quantum number equal to $+1$ and each new KK-states with -1. As a consequence the LKP is a stable particle becoming a good WIMP DM candidate as it was the case for the lightest neutralino in SUSY. On the other hand, in comparison to SUSY, UEDs is a theory which needs much less parameters in order to completely determine the model (basically only the number of extra-dimensions, their dimensions R and the cut-off scale Λ). Moreover, in contrast to the fermionic neutralino, the DM candidate is, in this case, a boson (Cheng et al. 2002).

3.6. Little Higgs theories with T-parity

As in the case of SUSY, the introduction of interactions with new massive particles not predicted by the standard model is able to solve the problem related to the divergences in the corrections of the Higgs boson mass. In particular loop corrections where particles with a mass around the TeV scale run around the loops are able to fully remove the divergences and "heal" the theory (Cheng & Low 2003). On the other hand, precision tests of the standard model and measurements of rare events (like mixing and *CP* violation) indirectly excluded the existence of new particles up to $5 - 7$ TeV (Barbieri & Strumia 1999), creating some tension with the previous requirement so that one has to fine-tune the model to some extent.

The lower limit of $5-7$ TeV for the mass of new particles permitted by the standard model is based on the assumption that these particles interact directly with usual standard model particles, through tree level diagrams. On the contrary, the cancellation of the divergences in the Higgs mass occurs through loops. Therefore it is possible to relax the lower limit of few TeV in the case that a symmetry is present to forbid the tree level interactions but allows the loops that cure the Higgs mass, so that ~ 1 TeV are compatible with electroweak data.

This is what the *R*-parity in SUSY does, forbidding a particular set of operators in the Lagrangian that would have disastrous consequences for the phenomenology of the theory (predicting, first of all, a too low decay time for the proton), still correcting the Higgs mass. The same is true in the case of UEDs for what we called *K*-parity. It has been

therefore proposed to introduce the aforementioned symmetry in the framework of little Higgs theories: he existence of this new *T-symmetry*, will have important consequences from the phenomenology of little Higgs theories at colliders. From the point of view of DM searches, *T*-symmetry makes the Lightest *T*-odd Particle (LTP) a stable, good WIMP DM candidate.

3.7. Inert Dark Matter H_0

The particle physics model behind Inter DM is simply the usual standard model with an additional Higgs boson H_2 (the usual Higgs boson is now called H_1) and a discrete Z_2 symmetry under which all the fields are even except the new Higgs boson H_2 which is odd $H_2 \rightarrow -H_2$ (Lopez Honorez et al. 2007, Ma 2006, Barbieri et al. 2006). This second Higgs, in principle, share the same interactions than the original Higgs, but the exact Z_2 symmetry forbids all interactions leading to FCNCs.

The complete scalar potential results to be

$$V = \mu_1^2|H_1|^2 + \mu_2^2|H_2|^2 + \lambda_1|H_1|^4 + \lambda_2|H_2|^4 + \tag{47}$$
$$\lambda_3|H_1|^2|H_2|^2 + \lambda_4|H_1^\dagger H_2|^2 + \frac{\lambda_5}{2}\Re\left[(H_1^\dagger H_2)^2\right].$$

H_1 gets its usual vacuum expectation value v in contrast with the second Higgs for which $\langle H_2 \rangle = 0$. The four degrees of freedom of H_2 are the charged H^+, the neutral *CP*-even H_0 and the *CP*-odd A_0 for which the masses can be written as

$$m_{H^\pm}^2 = \mu_2^2 + \frac{\lambda_3 v^2}{2}, \tag{48}$$

$$m_{H_0}^2 = \mu_2^2 + \frac{(\lambda_3 + \lambda_4 + \lambda_5)v^2}{2} \tag{49}$$

$$m_{A_0}^2 = \mu_2^2 + \frac{(\lambda_3 + \lambda_4 - \lambda_5)v^2}{2} \tag{50}$$

and are around the TeV scale. Such model does not represent a cure for the hierarchy problem, but the new scalars are able to stabilize the electroweak scale up to energies beyond the reach of future colliders.

Moreover, in absence of any violation of the Z_2 under which H_2 is odd, the lightest between H_0 and A_0 is a stable and good WIMP DM candidate. Assuming that H_0 is the lighter, the right relic density is obtained (being consistent with electroweak constraints) for $m_{H_0} = 10 - 80$ GeV in the low mass limit and above 500 GeV in the high mass limit (Lopez Honorez et al. 2007). In the first case, annihilations occurs mainly to Z and W bosons and to h pairs.

The H_0 candidate is characterized by a low cross section with nucleons (so that current direct detection experiments have still a too low sensitivity) but a quite large annihilation cross section into gamma-rays, being very promising for indirect searches (Gustafsson et al. 2007).

3.8. The sneutrino $\tilde{\tilde{\nu}}$

Within SUSY framework, there are some regions of the parameters space where the LSP is the (left-handed) sneutrino $\tilde{\nu}_e$. However, its large coupling to the Z boson, leads to a too large annihilation cross section, or, equivalently, a too low relic density (Ibanez 1984, Hagelin et al. 1984). Moreover, direct detection experiments have already excluded the values for nucleon-LSP interaction in the case of the sneutrino (Falk et al. 1994).

There remains the possibility, favored by the recent discoveries about ν oscillations, to introduce a right-handed neutrino in the standard model, and a corresponding right-handed sneutrino $\tilde{\tilde{\nu}}$ as its superapartner. In this way the coupling to the Z boson can be reduced considering a mixture between right-handed and left-handed sneutrino or simply a purely right-handed sneutrino as LSP. Both these cases seem to have some difficulties: for the mixture between the right-handed and left-handed sector a large soft SUSY-breaking trilinear term is need which is not possible in the standard framework of SUSY-breaking mediated by gravity. On the other hand, the coupling of a right-handed sneutrino to matter is extremely reduced since it is proportional to the neutrino Yukawa matrix (Cerdeno et al. 2008).

Thus, in order to explain DM using sneutrinos, one is pushed to move to a Next-to-Minimal SuperSymmetric Model (NMSSM) in which a new scalar singlet S is added which can interact with the right-handed sneutrino. The full superpotential can be written as:

$$W_{\text{NMSSM}} = W_{\text{MSSM}} + \tilde{\tilde{\nu}}\mathbf{Y}_\nu LH_u - \lambda S \cdot H_u H_d + \frac{1}{3}\kappa S^3 + \lambda_\nu S \cdot \tilde{\tilde{\nu}}\tilde{\tilde{\nu}}, \tag{51}$$

where W_{MSSM} is the usual superpotential of Equation (29), the following term $\tilde{\tilde{\nu}}\mathbf{Y}_\nu LH_u$ generalizes the usual Yukawa coupling for the neutrinos and the last one indicates the trilinear interaction between sneutrinos and the S superfield.

In the electroweak-breaking phase, the two Higgs H_u and H_d acquire their vacuum expectation values v_u and v_d. Also S breaks down being v_s its expectation value. As a consequence, the right-handed neutrinos get a mass equal to $m_\nu = 2\lambda_\nu v_s$ and the left-handed ones obtain a smaller mass through the see-saw mechanism of the order to $\mathbf{Y}_\nu^2 v_u^2 / m_\nu$, which implies a Yukawa coupling of the order of 10^{-6} like for the electron. The sneutrino mass terms can be deduced by the superpotential but also soft SUSY breaking terms have to be considered.

Finally the right-handed sneutrino, having a mass of the order of the electroweak scale, may be the LSP for particular choices of the SUSY parameters and represents a good WIMP DM candidate, compatible with current direct detection experiments and in the reach of next-generation ones (Cerdeno et al. 2008).

Chapter II:
The Galactic Center

4. Annihilation flux

Among the products of DM annihilation, I am going to focus only on gamma-rays. They are particularly interesting since they are able, moving on geodesics through the Universe, to track the source where they are produced. Assuming that emission of photons is isotropic, the annihilation flux per steradiant is defined as the number of gamma-rays with energy between E and $E + dE$ that can be detectable, per solid angle, on Earth by a detector with an effective area dA over a time interval dt:

$$\frac{d\Phi}{dEd\Omega} = \frac{dN}{dAdtdEd\Omega} = \frac{1}{8\pi}\frac{\langle\sigma_{\text{ann}}v\rangle}{m_\chi^2}\sum_f B_f\frac{dN_\gamma^f}{dE}\int_{\Delta\Omega}\int_{\text{l.o.s.}}\frac{\rho_\chi^2(l,\psi)}{d^2(l)}dld\Omega, \quad (52)$$

and, thus, it is measured in $\text{cm}^{-2}\text{s}^{-1}\text{GeV}^{-1}\text{sr}^{-1}$. Two different factors are usually distinguished in Equation (52): the first is the *particle physics factor* $d\Phi^{\text{PP}}/dEd\Omega$ which depends on the mass m_χ, the (thermally averaged) cross section $\langle\sigma_{\text{ann}}v\rangle$ of the DM particle and its annihilation channels, while being independent on the way DM is distributed in the source:

$$\frac{d\Phi^{\text{PP}}}{dEd\Omega} = \frac{1}{8\pi}\frac{\langle\sigma_{\text{ann}}v\rangle}{m_\chi^2}\sum_f B_f\frac{dN_\gamma^f}{dE}. \quad (53)$$

The sum is over all the annihilation channels $\chi\chi \to f\bar{f}$, where χ stands for the generic DM candidate which is assumed to be a Majorana particle. B_f is the branching ratio of the particular annihilation channel and dN_γ^f/dE the number of photons (with energy within E and $E + dE$) produced through that particular channel. More details on the particle physcis factor will be given in Section 5.

The remaining part of Equation (52) is called the *cosmological factor* and, on the contrary, does not depend on the particular DM candidate:

$$\Phi^{\text{cosmo}} = \int_{\Delta\Omega}\int_{\text{l.o.s.}}\frac{\rho_\chi^2(l,\psi)}{d^2(l)}dld\Omega = \bar{J}_{\Delta\Omega}\frac{\Delta\Omega}{d^2}. \quad (54)$$

The second integration is over the line-of-sight pointing to the direction ψ and the first one is over the solid angle $\Delta\Omega$ which is usually chosen to match the angular resolution of a gamma-ray telescope, so that (being $d(l)$ the distance from the detector) Equation (54) results to be proportional to the number of DM annihilations that a telescope can see pointing to the direction Ψ at the center of the solid angle $\Delta\Omega$, with an angular resolution equal to $\Delta\Omega$.

In the case of a point-like annihilation source at a distance d, it can be assumed that all annihilations occur inside $\Delta\Omega$. It is under this assumption that the second equality in Equation (54) holds and that the quantity $\bar{J}_{\Delta\Omega}$ is defined, representing the integrated squared DM density over the solid angle.

As it evident from Equation (52), the annihilation flux is proportional to the DM density squared, thus most natural targets for DM indirect searches are overdense, near regions in the sky. The optimal source would be the center of the Milky Way DM halo, the Galactic Center (GC), due to its proximity and the predicted large amount of DM that it hosts. That is the reason why this second chapter is dedicated to gamma-rays detections from the GC and their possible interpretation as coming from DM annihilation.

5. The particle physics factor

A complete analysis of the annihilation characteristics of the DM candidate is needed to determine the particle physics factor in Equation (53), assigning a value both to the total annihilation cross section $\langle \sigma_{\text{ann}} v \rangle$ and to the set of annihilation multeplicities dN_γ^f/dE and branching ratios B_f. Three different mechanisms for photons production are usually distinguished:

- monochromatic lines: monoenergetic photons can be directly produced from DM annihilations by processes like $\chi\chi \rightarrow \gamma\gamma$ and $\chi\chi \rightarrow Z\gamma$, if kinematically allowed (Bergstrom et al. 1998, Bergstrom et al. 2005*c*). The energy of the lines will be $E = m_\chi hi$ in the first case and $E \cong m_\chi(1 - m_Z^2/4m_\chi^2)$. The corresponding diagrams, however, contain loops and, therefore, the branching ratios result to be suppressed. Values around 10^{-3} are common (Bergstrom et al. 1998, Gondolo et al. 2004) in the case of a SUSY DM. The importance of annihilation monochromatic photons is very model-dependent, i.e. it strongly depends on which particle physics model is assumed to account for DM and on the particular set of parameters chosen to define that model. The presence of clear lines in the energy spectrum of a gamma-ray source in the sky would be a smoking-gun signature for DM annihilation, and, moreover, would provide the first measurement of the mass of the particle. This scenario, however, is obstacled by the not-so-good energy resolution of current gamma-rays telescopes (Bringmann et al. 2009) that would smear out the nice and clear feature of lines.

- emission from neutral pions: neutral pions are a very common product of hadronization of the quarks directly produced by DM annihilation or obtained as secondary decay products from the directly produced W or Higgs bosons. Also τ leptons can produce neutral pions through semi-hadronic decays. Gamma-rays are then emitted through the channel $\pi^0 \rightarrow \gamma\gamma$. Contrary of the previous case of monochromatic lines, this contribution is quite model-independent, i.e. it does not depend much on the specifics of the DM candidate. For a SUSY neutralino, e.g., photons coming from the decay of neutral pions have all a similar spectrum, no matter which channels were responsible for the pion production. The energy spectrum is a continuum and quite soft, being very roughly described by a power-law $dN/dE \propto (E/m_\chi)^{-1.5}$ and a cut-off at the mass of the DM particle (Fornengo et al. 2004)for a more description of annihilation spectra from neutral pions see. This would provide an additional smoking-gun signature for DM signal: in fact, the detection of a handful of gamma-ray sources all with the same energy cut-off can hardly be mistaken for less exotic, astrophysical sources whose energy spectra are usually bare power-laws with no cut-off. Again such signature is obstacled by the fact that the energy spectrum is quite soft. Moreover the mass of the DM particle can be too high or too low for detectors to actually detect the cut-off: telescopes like EGRET detecting photons till ~ 10 GeV would not be able to detect the cut-off while, on the contrary Air Cherenkov Telescopes (ACTs) like MAGIC (wwwmagic.mppmu.mpg.de) or H.E.S.S. (http://www.mpi-hd.mpg.de/hfm/HESS/) with an energy threshold of tens of GeV may not be able to detect the annihilation products of light DM particles at all.

Examples of annihilation spectra can be seen in Figure 12.

- in the case of annihilation to light leptons, gamma-rays can be emitted through bremsstrahlung by the final leptonic legs of the diagrams. These gamma-rays are characterized by an harder energy spectrum than the case of neutral pion decay, with a consequent more pronounced cut-off at the mass of the DM particle. For a neutralino DM, the annihilation to light leptons is helicity-suppressed so that these contributions are normally subleading and the energy spectrum is dominated by the second mechanism in this list. The helicity suppression is not active, e.g., in the case of UEDs, where radiative gamma-rays from light leptons constitute an important contribution to the energy spectrum (Bergstrom et al. 2005*b*, Bergstrom et al. 2005*c*), above all at the high energies, near the mass of the DM candidate (the tree-level Feynman diagrams can be see in Figure 13). Moreover the detection of an energy spectrum with an hard cut-off would be a strong indication in favour of a non-SUSY interpretation for DM (see the long-dashed line in Figure 12). This peculiarity of non-helicity-suppressed models has been recently proved to be not so strong: in fact Bringmann et al. (2008) have proved that new contributions to the photon yield should be included, for which gamma-rays are emitted by a virtual charged particle (see Section 10.2). This new contribution has been called *Virtual Internal Bremsstrahlung* (VIB) and can be present also for a SUSY DM candidate. It a very model-dependent, leading to large enhancements in the photon multeplicity but only for particular model configurations. In such cases VIB will appear as pronounced bumps at high-energies near the mass cut-off, hardening the spectrum also for neutralino annihilations and making it more similar to the case of KK DM. About VIB, see Bringmann et al. (2008), Bringmann et al. (2009) and Section 10.2.

6. The cosmological factor

Regarding the density profiles used to describe the DM halos around galaxies, a common class of models is the so-called (α, β, γ) models (Zhao 1996):

$$\rho_\chi(r) = \rho_0 \left(\frac{r_0}{r}\right)^\gamma \frac{1}{[1 + (r/r_0)^\alpha]^{(\beta-\gamma)/\alpha}}, \qquad (55)$$

that reduces to $\rho_\chi \propto r^{-\gamma}$ ($\rho_\chi \propto r^{-\beta}$) in the limit of small (large) distance and α characterizes the sharpness of the change in the logarithmic slope. The NFW profile (see Equation (9)) is recovered for $(\alpha, \beta, \gamma) = (1, 3, 1)$ and the Moore profile for $(\alpha, \beta, \gamma) = (1, 3, 1.5)$ (Moore, Quinn, Governato, Stadel & Lake 1999):

$$\rho_\chi(r) = \rho_s \left(\frac{r}{r_s}\right)^{-1.5} \left(1 + \frac{r}{r_s}\right)^{-1.5}. \qquad (56)$$

The NFW is undoubtefully the most widely used since *N*-body simulations proved it to be quite universal, being a well fit to DM halos over a large wide in mass, from the halos of dSphs dwarf Spheroidal galaxies ($\sim 10^{10} M_\odot$) to those of clusters of galaxies ($\sim 10^{15} M_\odot$) (Navarro et al. 2004, Reed et al. 2005). It defines the *shape* of the halo while the two parameters,

Figure 12. Energy spectra of photons for different annihilation channels. The solid and dotted line both correspond to the $b\bar{b}$ annihilation, the differences are due to different parametrizations for quark fragmentations and a different mass for the DM particle. The solid line shows the parametrization of Fornengo et al. (2004) with $m_\chi = 1$ TeV, while the dotted line shows that of Bertone et al. (2003) with $m_\chi = 100$ GeV. The short-dashed line corresponds to the spectra for annihilations through the *WW* and the *ZZ* channels. In particular we show the fit from Bergstrom et al. (1998). Finally the long-dashed line shows the spectrum, summed over contributing channels, for annihilating Kaluza-Klein DM from Bergstrom et al. (2005*b*). Taken from Bertone, Zentner & Silk (2005).
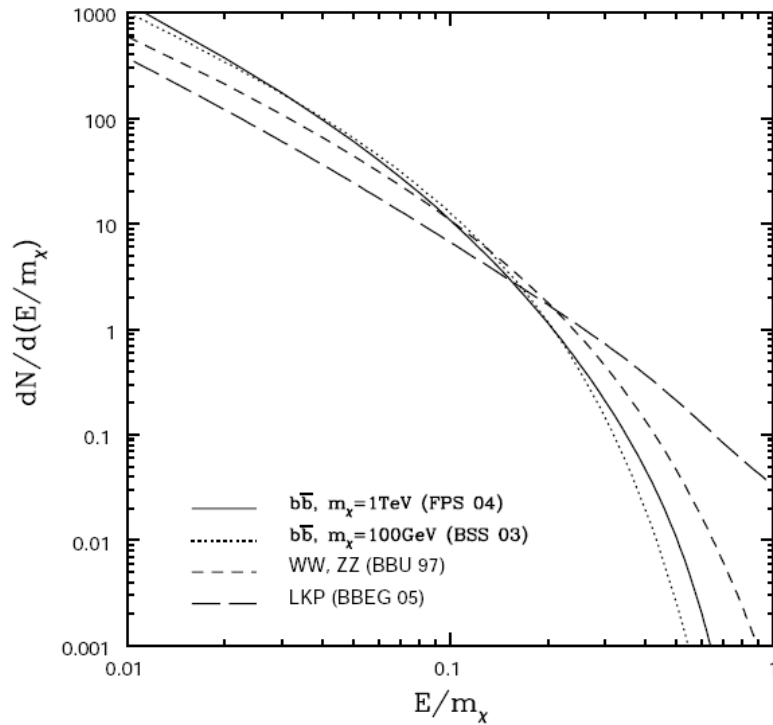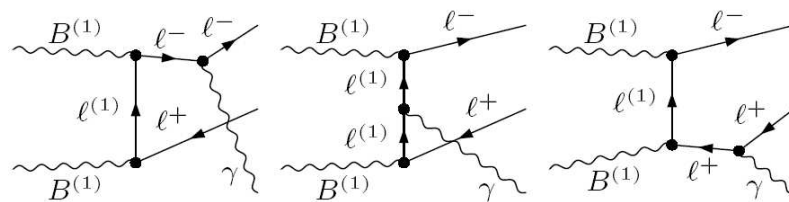

Figure 13. Tree-level contributions to the $\gamma^{(1)}\gamma^{(1)} \to l^+l^-\gamma$ annihilation. Taken from Bergstrom et al. (2005*b*).

the scale radius r_s (the distance where the slope $\gamma = -d \ln \rho_\chi / d \ln r$ is equal to -2) and the normalization ρ_s depend on the mass and the size of the halo.

More precisely one usually starts from the virial mass $M_{\rm vir}$ and the concentration $c_{\rm vir}$ of a halo. The virial mass is defined as the mass contained in a spherical region than encloses $\Delta_{\rm vir}$ times the average DM density today, with $\Delta_{\rm vir}$ being (Bryan & Norman 1998):

$$\Delta_{\rm vir}(z) = \frac{18\pi^2 - 82(\Omega_\chi(z) - 1) - 39(\Omega_\chi(z) - 1)^2}{\Omega_\chi(z)}. \tag{57}$$

$\Omega_\chi(z)$ is the ratio between the DM density and the critical density today.

The radius of the sphere which enclosed the virial mass is the virial radius $r_{\rm vir}$, while the concentration is simply the ratio between the virial and the scale radius $c_{\rm vir} = r_{\rm vir}/r_s$. Alternatively, the mass of the halo can also be defined as M_{200} as the mass of the sphere (with a radius r_{200}) that encloses 200 times the critical density. The corresponding concentration results to be $c_{200} = r_{200}/r_s$ (Navarro et al. 1996, Navarro et al. 1997).

No matter which definition is chosen, the scale radius of the NFW profile is determined knowing the concentration and the virial radius (which itself depends on the virial mass) and finally ρ_s is obtained imposing that the integral of the density profile extended till the virial radius gives the virial mass.

N-body simulations of the clustering properties of DM, aiming at reproduce the formation of DM structures as galaxies and clusters of galaxies, showed that the NFW profile can provide a good fit to the DM halos (Navarro et al. 2004, Reed et al. 2005). Despite the success of *N*-body simulations, two main problems have emerged on the scale of individual galaxies and their central structure: the first is due to the fact that the NFW profile predicts a *cuspy* inner behaviour, with a slope equal to -1 and this seems to be in contrast with the rotation curves observed for low surface brightness galaxies (McGaugh & de Blok 1998, Hayashi & Navarro 2006). On the other hand, the second issue regards the number of subhalos predicted to populate a smooth DM halo. In the case of our Galaxy, this number is much larger than the number of satellites observed in the halo of the MW (Klypin et al. 1999, Moore et al. 1999). See Section 8 for more details on this so-called *missing-satellites problem*.

Related to these problems about the reliability of the *N*-body approach, one should remember that these massive simulations do not account for the presence of baryons, but only describe DM. Baryons can have significant effects on the DM distribution, above all in the inner region of halos, as it can be seen studying the way DM react to the presence of a SuperMassive Black Hole (SMBH) at the center of the halo: the mechanism of adiabatic compression is able to create strong DM overdensities at the center of the halo called *spikes* (I will talk more extensively about spikes in Section 14) so that this possibility is usually evoked as a *boost effect* to increase the annihilation flux (Gondolo & Silk 1999). But, if also a stellar cusp is present around the SMBH, collisions between DM and baryons are very efficent in reducing the possible overdensity (Ullio et al. 2001) so that the final DM distribution strongly depends on the interactions with the baryons (Merritt et al. 2007).

Thus, even if a NFW profile represents a fair descriptions of DM halos over 5 decades of masses, other viable possibilities cannot be excluded, above all for what regards the inner

region where the finite resolution of *N*-body simulations is reached and the presence of baryons cannot be neglected. The Moore profile in Equation (56) predicts an inner slope equal to -1.5. However this steep value can be excluded comparing, at a precise distance r, the value of $\rho_\chi(r)$ to the corresponding enclosed mass density $\bar{\rho}_\chi(r) \propto \int_0^r \rho_\chi(r')dr'/r^3$. Under the conservative assumption that the slope is monotonic with radius, the quantity $\gamma_{max}(r) = 3(1 + \rho_\chi(r))/\bar{\rho}_\chi(r)$ indicates the maximum allowed slope at distance r (steeper values would require more mass than what is available at that radius) and value as steep as in the case of a Moore profile are excluded by the simulations by Navarro et al. (2008), while a slope equal to -1 (as for the NFW case) is still compatible with the simulation.

However, the most recent simulation (the so-called *Aquarius Project*) (Springel et al. 2008*b*, Navarro et al. 2008) does not see any signs for the slope to converge to a precise value (as predicted by the NFW profile) so that the Einasto profile in Equation (10) (for which the slope describes as a power-law at smaller distance) should be preferred to the NFW (see Figure 14). The Einasto index *n* results to depend on the mass of the particular halo, losing the universality which was a appealing feature of the NFW profile. Halos simulated by the *Aquarius Project* have indexes ranging from 0.115 to 0.179.
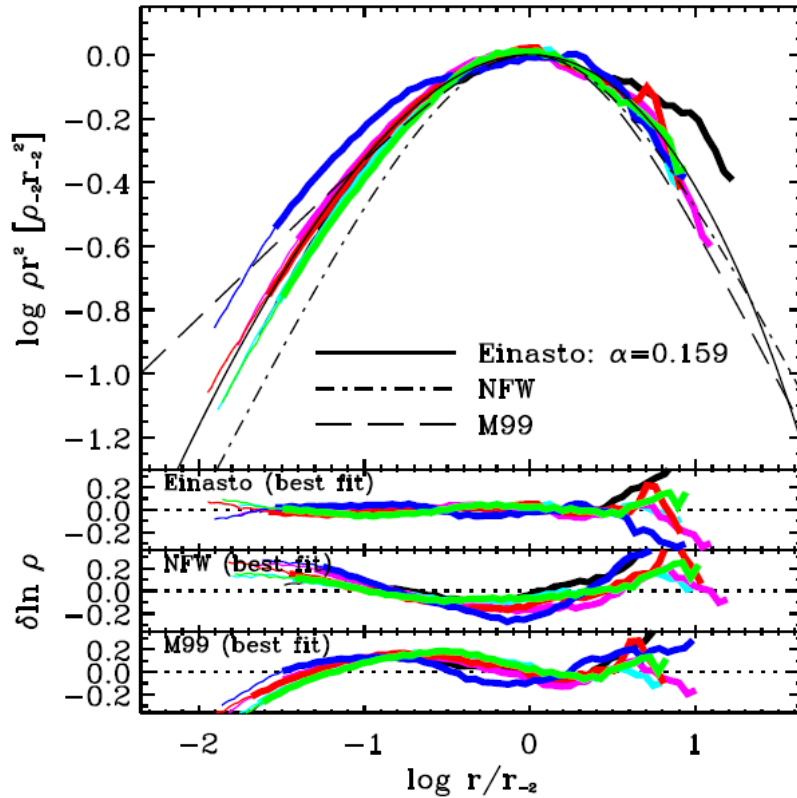
7. Detection of gamma-rays from the Galactic Center and interpretation as Dark Matter annihilation

Many authors computed the annihilation flux towards the direction of the GC (see, e.g., Fornengo et al. 2004, Bergstrom et al. 1998, Ando 2005, Cesarini et al. 2004). In Fornengo et al. (2004) a wide range of DM profiles has been considered (from a truncated isothermal profile to a NFW with a spike resulting from adiabatic contraction) showing that the integral of the squared DM density can vary of many orders of magnitude in the inner region. When the experimental angular resolution is taken into account, the uncertainty is reduced but remains quite large: with a resolution of $\Delta\Omega = 10 - 5$ sr, the cosmological factor within the $\Delta\Omega$-wide cone centered to the GC varies of a factor 10^{-6} from a Moore profile (with an inner radial cut-off of 10^{-8}kpc) to a truncated isothermal profile, and of a factor $\sim 10^{-3}$ to the NFW with the same radial cut-off. With the introduction of the particle physics factor (assuming a SUSY DM candidate) uncertainties in the cross section and the mass of the particle should also be considered, making the prediction even more difficult.

Similar studies were conducted by Bergstrom et al. (1998) where, estimating the sensitivity of ACTs and of the Fermi LAT satellite (which it has been recently launched) they conclude that these experiments should be able to access some interesting regions of the parameters space from the analysis of the GC.

From an observational point of view, the region near the GC has been observed using different detectors and a certain number of sources have been detected over a quite wide range of wavelenghts (see Figure 15). The dynamical center of the Galaxy host the X-ray and radio source Sgr A* (Pohl 1997) which has the feature of an Active Galactic Nucleus and, in fact, it is thought to be the site of the $\sim 10^6 M_\odot$ SMBH at the center of our Galaxy. Only a few parsecs away from Sgr A*, the Supernova Remnant Sg A East has been detected which is believed

Figure 14. Spherically-averaged density profiles of all level-2 *Aquarius* halos. Thick lines show the profiles from $r_{\rm conv}^{(7)}$ outward; thin lines extend inward till $r_{\rm conv}^{(1)}$. For further details on how the Aquarius runs are produced and on how the convergence radius is defined see Navarro et al. (2008). An Einasto profile with $\alpha = 0.159$, a NFW and a Moore profile are shown. The botton panels show residuals to the best fits. Note that the Einasto fits all profiles well, especially in the inner regions. The shape parameter α varies significantly from halo to halo, indicating that the profiles are not strictly self-similar. The NFW is also able to reproduce the inner region quite well, although systematic deviations are present, increading inward and are maximal at the innermost resolved point. The steeply-cusped Moore profile gives the poorest fits. Bumps and wiggles in the outer region are due to resolved substructures. Taken from Navarro et al. (2008).

to be the source of Galactic cosmic-rays. Gamma-rays have been detected from the Arches and Quintuplet star clusters, but I am going to focus, at first, on the detection by EGRET of a gamma-rays source (3EG J1746-2853) (Mayer-Hasselwander et al. 1998, Cesarini et al. 2004). The energy of the gamma-rays ranges from $\sim 30\,\mathrm{MeV}$ to $\sim 30\,\mathrm{GeV}$ and its energy spectrum and integrated flux may be explained as a DM source favouring particles with $m_\chi \sim 50\,\mathrm{GeV}$ (Cesarini et al. 2004). However, on a dedicated analysis, Hooper & Dingus (2004) proved that the preferred location of this source is not exactly the GC but instead the point with Galactocentric coordinates equal to $(l, b) = (0.19, -0.08)$. At this new location the source would be included in the EGRET unidentified sources, even if has been proposed that its emission can be explained as inverse Compton gamma-rays from the electrons produced at the Galactic radio arc (Pohl 1997).

Figure 15. A sky-map of the GC region. The solid and dashed contours correspond to the regions observed by Whipple and CANGAROO-II respectively. In these regions the observed significance is greater than 80% for Whipple and than 95% for CANGAROO-II. The 95% confidence region for the off-center source observed by EGRET (EG Ji1746-2851) is shown as a shaded region. Also shown are a number of selected objects known to be present in the region included Sgr A* (the dynamical center of the Galaxy and location of the SMBH), two supernovae remnants (SNR1 and SNR2 corresponding to Sgr A East and SNR 000.3+00.0, respectively), the Arches and Quintuplet star clusers, the low mass X-ray binary 1E 1743.1-2843 and two gamma-ray sources observed by INTEGRAL (G1 and G2). Taken by Hooper et al. (2004).
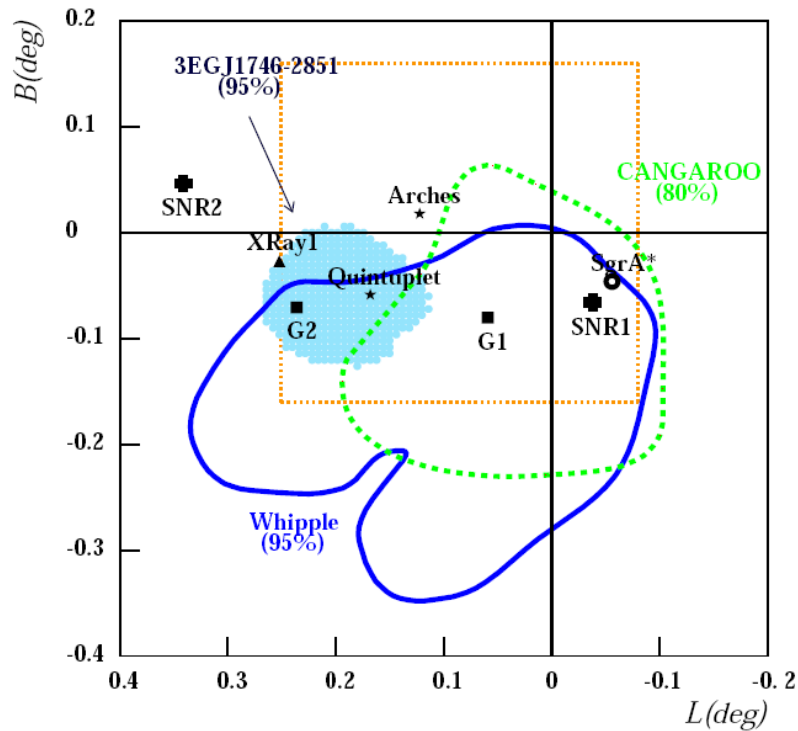
The precise estimate of the source location as in Hooper & Dingus (2004) relies on a detailed knownledge of the gamma-ray background which is present in the GC region. It also has been measured by EGRET and interpreted as a gamma-ray flux originated by interactions of Galactic cosmic-ray electrons and protons with the interstellar medium, and therefore it is not isotropic (Hunter et al. 1997). EGRET data on this diffuse gamma-rays emission, in fact, can be used to determine properties about the cosmic-rays distribution. The emission is mostly concentrated on the Galactic Plane and rapidly decreasing with latitude. The energy spectrum of background photons is well fitted by a power-law with slope equal to -2.7 even if some dependence of the slope on the Galactic location has been detected.

More precisely, the full-sky gamma-ray maps of EGRET, once privated from the point sources, receive contributions not only by the diffuse background due to the interaction between the interstellar medium and the cosmic rays. An additional contribution has been identified as an isotropic background with an power-law energy spectrum with a -2.1 slope

(Sreekumar et al. 1998) called the *Extra-galactic Gamma-ray Background* (EGB). The EGB is usually interpreted as emission from an unresolved population of extra-galactic blazars. Many authors also proposed the possibility that DM annihilations, both from the halo of the MW and from extra-galactic halos, can contribute to some extent to the EGB (see Section 18).

Assuming that the 3EG J1746-2853 is not at the GC, EGRET is able to put only upper limits on the gamma-ray flux from the GC in the 30 MeV − 30 GeV. Fermi LAT will soon release its first data. Its lower sensitivity and better angular resolution should be able to provide us with more precise informations about the location of 3EG J1746-2853 and on the gamma-ray flux from the GC.

In the meanwhile, many ACTs have looked at the GC, detecting high-energy gamma-rays emission. The first detection by the Whipple telescope (Kildea et al. 2007) has been confirmed (Hooper et al. 2004) by CANGAROO-II (http://icrhp9.icrr.u-tokyo.ac.jp/) and, basically by all the ACTs (Aharonian et al. 2006*b*, Albert et al. 2006). The H.E.S.S. collaboration (Aharonian et al. 2006*b*) reported an integrated flux above 1 TeV of (1.87 ± 0.10(stat.) ± 0.30(syst.)) × 10^{-12}cm^{-2}s^{-1} over a total of 33.5 hours of exposure. This is the detection which reported the largest energy range and conducted with the better experimental condition (the position of the source in the sky can affect both the effective area and the energy threshold of the telescope and since the GC is located in the Southern emisphere, the H.E.S.S. telescopes are in a privileged position). The source location is estimated to be at $(l, b) = (359°56'33.3'' ± 9.7'', −0°2'40.6'^{prime} ± 10'')$ consistent within the H.E.S.S. Point Spread Function (PSF) of 0.1° with the position of Sgr A*.

The distribution of the angle θ between the gamma-ray direction and the position of Sgr A*, after subtraction of the diffuse background emission (whose contribution is 16% of the integrated flux) is shown in Figure 16 and is consistent with the PSF so that the source can be assumed to be point-like. The energy spectrum is shown in Figure 17 and be characterized as a power-law with slope equal to $\Gamma = (2.25 ± 0.04(stat.) ± 0.10(syst.))$, without any sign of cut-off. It is not straight-forward to interpret this spectrum as a result of DM annihilations since it would require a particularly high DM mass: Profumo (2005) determined with a Monte Carlo Markov Chain (MCMC) approach the preferred set of branching ratios B_f (see Equation (52)) for a SUSY DM candidate and the preferred range in mass compatible with the H.E.S.S. data. The results point at masses between 6 TeV and 30 TeV, higher than what is permitted by a MSSM with neutralino DM compatible with WMAP data. Thus the author proposed to extend the SUSY model beyond the minimal setup and, in particular, to anomaly and gauge mediated soft SUSY-breaking models, showing that, in such cases, the DM candidate would be characterized by the mass value required to match the H.E.S.S. energy spectum but would provide a too low annihilation flux requiring thus a boost factor to reproduce the data (Profumo 2005). Other non-MSSM interpretations have been proposed (Hooper & March-Russell 2005).

Fitting H.E.S.S. data with annihilation spectra from KK DM, it is possible to bring down the value of the predicted DM mass around 10 TeV. This is due to the fact that, including channels like $l^+l^-\gamma$ the total spectrum has a different shape than in the case of neutralino DM (Bergstrom et al. 2005*b*, Bergstrom et al. 2005*c*). However, to provide the right relic density

Figure 16. Distribution of the angle ϑ between the gamma-ray direction and the position of Sgr A*. Circles •: all detecting events. Open triangles: △: central object after subtraction of the gamma-ray diffuse emission model (Aharonian et al. 2006*a*). Line: calculated PSF normalized to the number of gamma-rays within 0.1° after subtraction. The distribution of events after subtraction matches the calculated PSF while the initial distribution shows a significant tail. Insert: same distribution for the point-like source PKS 2155-304 (Aharonian et al. 2005). The calculated PSF (red line) also matches the data. Taken from Aharonian et al. (2006*b*).
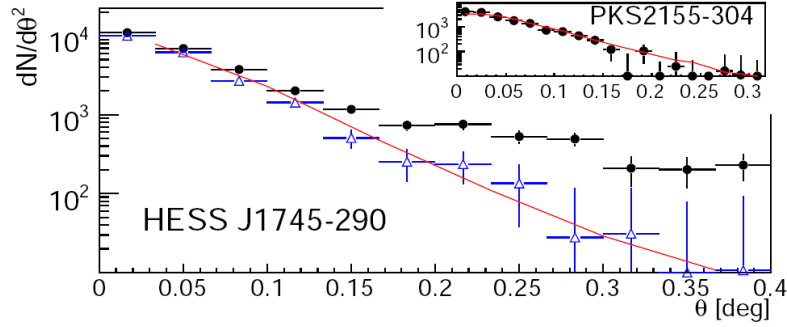

Figure 17. Spectral energy density $E^2 \times dN/dE$ for gamma-rays from the GC source, for the 2004 data (•) and the 2003 data (○). Upper limits are 95% C.L. The shaded area shows the power-law fit $dN/dE \sim E^{-\Gamma}$. The dashed line illustrated typical spectra of phenomelogical MSSM DM annihilation for best fit neutralino masses of 14 TeV. The dotted line shows the distribution predicted for KK DM with a mass of 5 TeV. The solid line gives the spectrum of a 10 TeV DM partilcle annihilating into $\tau^+\tau^-$ (30%) and $b\bar{b}$ (70%). Taken from Aharonian et al. (2006*b*).
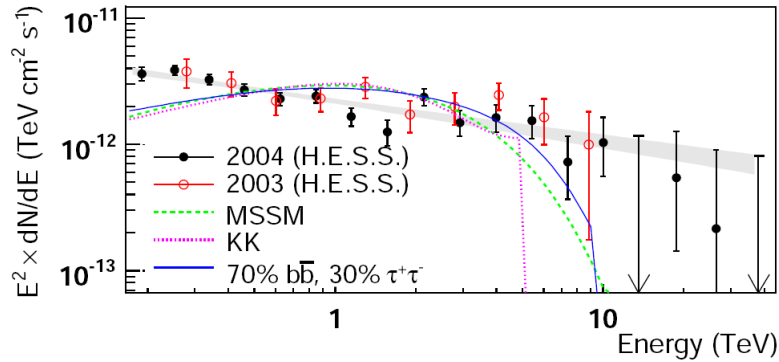
still lower values ($m_{\gamma^{(1)}} \sim 0.5 - 1$ TeV) are needed (one can always move to a non minimal UEDs scenario in order to alleviate this problem (Dienes et al. 1998)).

Even assuming the more conservative point of view that DM accounts only for a fraction of the gamma-ray signal detected by H.E.S.S. and that an astrophysical signal is present as well, the result of the fit points to a negligeble DM contribution. Finally the H.E.S.S. collaboration claims that the GC source is not compatible with a DM interpretation. In principal, this is nonetheless interesting, since it may provide usefull upper limits on the

annihilation flux. For a NFW profile for the MW, the limit on the annihilation cross section are still to large, excluded values above $10^{-23} - 10^{-24}\mathrm{cm}^{-3}\mathrm{s}^{-1}$. On the contrary, if a spike is present at the GC, the limits are reduced about two orders of magnitude and this can exclude interesting regions of the parameters space (WIMP cross section is assumed around $3 \times 10^{-26}\mathrm{cm}^{-3}\mathrm{s}^{-1}$ in order to provide the desired relic density).

GC upper limit can be very usefull if used together with another source of information. Ando (2005) proposed the idea that DM annihilations in unresolved, extra-galactic halos can account for (at least part of) the EGB (see also Section 18). Assuming a NFW profile for extra-galactic halos, a boost factor is again needed to match EGRET data for the EGB. Considering the effect that such boost factor would have to the emission of the GC, a maximal value for the boost factor can be derived in order not to overcome the upper limit from the GC. Finally Ando (2005) concluded that this maximal boost factor is too low for DM to significantly contribute to the EGB, or, at least, one should assume some mechanism (as the effect of SMBHs and Intermediate Mass Black Holes) able to enhance the annihilation flux for extra-galactic halos but having almost no influence for the GC (Ahn et al. 2007, Horiuchi & Ando 2006).

To conclude: the EGRET data of the source 3EG J1746-2853 can be interpreted as a DM signal but the position of the object is not completely coincident with the GC. On the other hand, basically all the ACTs have collected high-energy data from the GC. These gamma-rays are hardly interpreted as products of DM annihilation, due both to the energy spectral shape and the global amplitude of the signal, which would require a too steep DM profile. Moreover it is not possible to explain at the same time both sources as DM sources: the EGRET excess is in the 30 MeV − 30 30 GeV while ACTs provide high-energy data above ∼ 300 GeV. A good fit to EGRET data would be obtained by a ∼ 40 − 60 GeV neutralino, that cannot be responsible for the emission presented in Figure 17. On the contrary a massive DM candidate (with the use of some boosting mechanism) can explain H.E.S.S. data but would remain a negligeble contribution for EGRET (Ando 2005).

Chapter III:
Observation of
Dwarf Spheroidal galaxies
with Air Cherenkov Telescopes

8. Dwarf Spheroidal galaxies

In the ΛCDM scenario, DM structures are supposed to form from the merging of smaller objects: the primordial fluctuations in the DM smooth distribution, grow larger and larger till becoming non-linear. These small overdensities experienced gravitational attraction and collisions lead to mergings and the consequent formation of largers and larger structures. *N*-body simulations are aimed exactly at understanding how DM halos (from sub-galaxy size to the super-halos embedding clusters of galaxies) form from the fluctuations described by the matter power spectrum in Figure 5.

A certain number of DM objects are supposed to survive the merging with a larger structure and remain as a gravitationally-bound structures orbiting in the gravitational well of the larger body. That is why large DM halos are supposed to be populated by smaller wandering subhalos. The dwarf Spheroidal galaxies (dSphs) of the MW can be interpreted as the largest of these Galactic subhalos. In fact, from the analysis of their stellar component it appears that they are embedded within a large DM halo, so that their mass-to-light ratio is very large. dSphs result to be one of the most DM dominated class of objects in the sky (Gilmore et al. 2007). As a consequence, next to the GC, they also are natural and optical candidates for indirect DM searches, both for the large DM component and for the absence of a known astrophysical background (for recent studies, see, e.g., Bergstrom & Hooper 2006, Strigari et al. 2007*b*, Colafrancesco et al. 2007, Sanchez-Conde et al. 2007, Strigari et al. 2007*a*).

It is not clear which is the minimal mass of DM subhalos, depending mainly on the chosen DM candidate: for warm DM this value results to be around $10^4 - 10^5 M_\odot$ while for cold DM, Earth-sized substructures $\sim 10^{-6} M_\odot$ are predicted. *N*-body simulations indeed found subhalos harbored in large DM halos even if the low mass scale of $10^{-6} M_\odot$ is still far away from their mass resolution (Diemand et al. 2005, Springel et al. 2008*b*, Bullock et al. 2001*b*).

Moreover, it is also uncertain how many DM subhalos should be present as satellite galaxies within a larger halo. In the case of the MW this is known as the *missing satellite problem*: i.e. the fact that the number of structures predicted by *N*-body simulations highly overcomes the number of dwarf Spheroidal galaxies (dSphs) detected as satellites of our Galaxy (Klypin et al. 1999, Moore et al. 1999, Strigari et al. 2007*b*) (see Figure 18). While many interpretations have been suggested, including the effect of decaying DM (see, e.g., Cembranos et al. 2005, Kaplinghat 2005, Borzumati et al. 2008), the most natural explanation would be that the missing dSphs have so far simply escaped detection. In fact, it has been proposed that dSphs below a certain mass cannot efficiently accrete baryons, which would explain the intrinsic faintness of these objects (Strigari et al. 2007*b*). The claimed discrepancy has recently also been mitigated considerably by the discovery of a bunch of new ultra-faint galaxies in the SDSS data (Simon & Geha 2007).

So far, almost all detected dSphs are located in the Local Group, a fact that is most likely related to the low luminosity of these objects, ranging from $330 L_\odot$ to $3 \times 10^7 L_\odot$ (Mateo 1998, Da Costa 1999, Simon & Geha 2007, Geha et al. 2008).

Observations of their stars is translated to informations about the stellar velocity

Figure 18. The mass within 600 pc of the MW satellites and dark subhalos in the Via Lactea (Diemand et al. 2005, Diemand et al. 2006) simulation. The red, short-dashed curve is the total subhalo mass function from the simulation. The solid, black curve is the median of the observed satellite mass function. For the interpretation of the error bars see Strigari et al. (2007*b*). Taken from Strigari et al. (2007*b*).
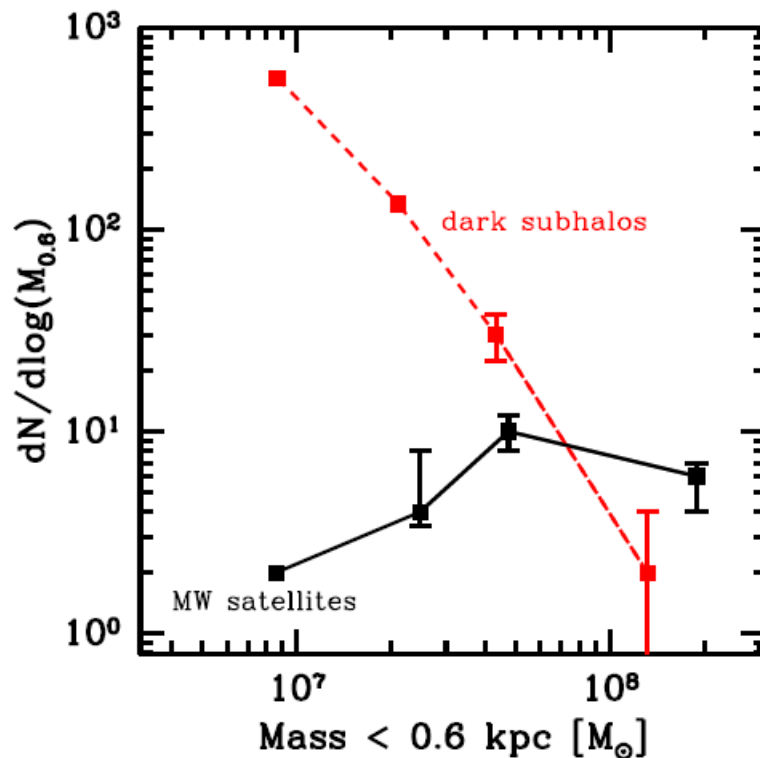
dispersion profile that, with the use of the Jeans equation, can be used to infer properties on the gravitational potential and, in particular, on the total mass of the dSph or on the profile of the DM halo (Lokas et al. 2005, Mashchenko et al. 2006). The procedure is based on the assumption that the galaxy is spherical and in equilibrium. The knownledge of the stellar velocity anisotropy (i.e. the ratio between the circular and tangential velocity of the stars) is also assumed. The kinematical equilibrium of a dSph is guaranteed from the comparison of its internal gravitational energy to the external interaction energy with the MW. The results indicates that the internal force is usually ~ 100 times larger than the external one (Strigari et al. 2008, Strigari et al. 2007*c*): even if this does not exclude the possibility that tidal interactions have been important in some phases of the evolution of the dSph and that the galaxy may have been stripped by the stars in the outer region (see, e.g., Munoz et al. 2005, McConnachie et al. 2006)), this allows us to proceed with the assumption that the object is in equilibrium and the remaining stars trace the gravitational potential of the dwarf.

However, it has to be noticed that one of the main obstacle in this kind of analysis is the uncertainty in the criteria to be used in order to determine if a star belong to the dSph or not (Martin et al. 2007).

Figure 19. The integrated mass of the MW dwarf satellites, in units of $M_\odot$, within the inner 300 pc as a function of their total luminosity, in units of $L_\odot$. The circle red points on the left ($\circ$) refer to the newly discovered SDSS satellites, while the squares, blue points on the right ($\square$) refer to the classical dwarf satellites discovered pre-SDSS. The error bars refer to the points where te likelihood function falls off to 60.6% of its peak value. Taken from Strigari et al. (2008).
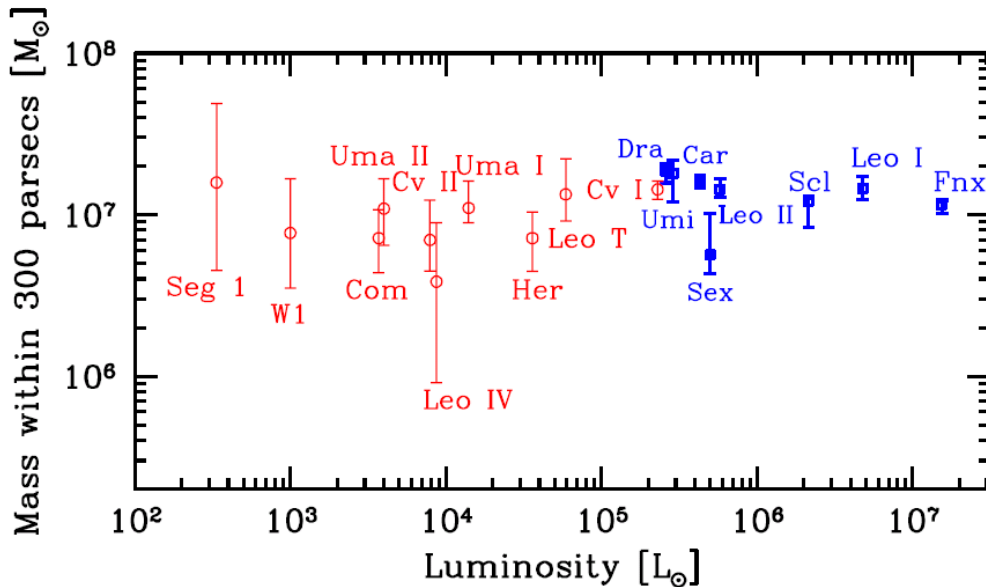
Accounting for a quite large range of possibilities, both for the DM density profile and for the velocity anisotropy profile, Strigari et al. (2007*c*) and Strigari et al. (2008) used a likelihood analysis to demonstrate that, despite the very different luminosities (ranging over 4 orders of magnitude), all the dSphs detected in the MW seem to be embedded in a DM halo with the same mass scale (see Figure 19) of the order of $10^7 M_\odot$. As a consequence the very faint, recently-discovered dwarfs on the left side of Figure 19 will be characterized by a mass-to-light ratio of the order of 1000, being very promising for indirect DM searches.

This is the reason why in this chapter I will focus on the study of possible DM signals from dSphs, mainly reporting the results of Bringmann et al. (2009) which I also signed. In that paper, we computed the annihilation flux from two reference dSphs, Draco and Willman 1. While the choice of Draco is supported by the large set of available data, Willman 1 has been discussed as a very promising target for future detection. In particular, we considered the prospect for detecting a DM signal with ACTs, focusing on the case of the next-generation telescopes like MAGIC II and the Cherenkov Telescope Array CTA. The more relevant characteristics of an ACT for DM detection were also presented and will be described here in Section 9. Finally in Bringmann et al. (2009), we included for the first time the contribution of Virtual Internal Bremsstrahlung (VIB) in the prospect for the detection of a DM signal from dSphs (see Section 10.2).

8.1. Draco

Draco is located at a distance of (80 ± 7) kpc from the Earth (Mateo 1998) and is one of the best known and most often studied dSph. Discovered by Wilson (1954), the first estimation of its DM content was performed only 30 years later by Aaronson (1983) from the analysis of the stellar velocity dispersion. Nowadays, a large set of data is available for Draco (Shetrone et al. 2001, Aparicio et al. 2002, Piatek et al. 2002, Segall et al. 2007, Walker et al. 2007). Even though the formation of the DM halo cannot be traced back with great precision, it can be inferred that the system is composed of very old, low-metallicity stars, without any significant sign of star formation in the last 2 Gyrs. At its short distance from the MW center, Draco has likely been stripped off its outermost stars in the past; today, however, no signs of tidal interactions are observed (Segall et al. 2007). From a kinematical analysis of a sample of 200 stellar line-of-sight velocities (with radii that range from 50 pc to 1 kpc), one can infer the DM profile: the result of the fit (assuming a NFW profile) indicates a virial mass of the order of $10^9 M_\odot$ (Walker et al. 2007), with a corresponding mass-to-light ratio of $M/L \gtrsim 200 \, M_\odot/L_\odot$ that characterizes Draco as highly DM dominated.

Many groups have analysed the available data for Draco and modelized its DM profile (Colafrancesco et al. 2007, Sanchez-Conde et al. 2007, Tyler 2002, Kazantzidis et al. 2004, Lokas et al. 2005, Mashchenko et al. 2006). I am going to follow Bringmann et al. (2009) and discuss here only the two extreme cases of a cusp profile and a core profile, which span the range of possible configurations. It should be underlined that core profiles are not compatible with current CDM simulations: recent results predict DM halos well-fitted by an Einasto profile without converging to a precise value for the inner slope (Springel et al. 2008*b*). For comparison with previous studies, however, we chose to still include core profiles in the analysis.

For the cusp profile we assumed a NFW profile, while for the core one, a Burkert profile (Burkert 1996, Salucci & Burkert 2000):

$$\rho_{\text{Burkert}}(r) = \rho_s \left(1 + \frac{r}{r_s}\right)\left(1 + \left(\frac{r}{r_s}\right)^2\right). \tag{58}$$

For the scale radius r_s and the normalization density ρ_s, we used the values summarized in Table 2 (taken from Mashchenko et al. (2006)). Note that both profiles produce good fits to the velocity dispersion profiles, down to the pc scales where the innermost stars are observed. No direct observational information is available for distances even closer to the center, where the two profiles differ significantly.

Possible DM annihilation signals from Draco have already been searched for in the past: after the CACTUS experiment had claimed the detection of an excess of ~ 7000 high-energy photons in only 7 hours (Chertok et al. 2006), almost all IACTs tried to reproduce the result, but the claim was not confirmed (Driscoll et al. 2007, Wood et al. 2008). MAGIC observed Draco for 7.8 hours in 2007 above 140 GeV (Albert et al. 2008). Within a 2σ confidence limit, the collaboration reported an upper limit for the integral flux of $\Phi^{u.l.}(E \geq 40 \text{ GeV}) \leq 1.1 \times 10^{-11} \text{cm}^{-2}\text{s}^{-1}$.

Table 2. Scale radius (in kpc) and normalization density (in $M_\odot/\text{kpc}^3$) that appear in the DM density profiles. The NFW and the Burkert profiles in the case of Draco represent models N3 and B2, respectively, from Mashchenko et al. (2006). In the case of Willman 1, the NFW fit is taken from Strigari et al. (2007c). In addition, the semi-aperture of the solid angle corresponding to 90% of emission θ_{90} (in degrees) is reported together with the target distance D (in kpc).

	Draco (Burkert)	Draco (NFW)	Willman 1 (NFW)
r_s	0.35	0.50	0.18
ρ_s	3.6×10^8	1.3×10^8	4.0×10^8
θ_{90}	0.52°	0.35°	0.20°
D		80 ± 7	38 ± 7

8.2. Willman 1

Willman 1 (SDSS J1049+5103) is a very peculiar object, located at a distance of (38 ± 7) kpc from the Earth in the constellation of Ursa Major. Discovered by Willman et al. (2005) (see also Willman et al. 2006), using data from the Sloan Digital Sky Survey (York et al. 2000), it was then further observed with Keck/DEIMOS (Martin et al. 2007) and more recently by Siegel et al. (2008). Recently the MAGIC collaboration reported an upper limit on the observation of Willman 1 of the order of 10^{-12}ph cm^{-2}s^{-1} above 100 GeV using the analysis method described in Aliu et al. (2008). With an absolute magnitude of $M_V \sim -2.5$ and a half-light radius (i.e. the radius of a cylinder, pointing to the earth, that encloses half of the luminosity of the object) of (21 ± 7) pc, it looks very similar to a globular cluster, even if its narrow distribution of stellar velocities and the large spread in stellar metallicities suggests that it is indeed the smallest dSph ever observed.

The object may show evidence for tidal disruption from its tri-axial stellar distribution (Willman et al. 2006). On the other hand, the difference in the stellar luminosity function between the central and outermost stars reveals a strong mass segregation. With a luminosity of 855 $L_\odot$, and a mass of the order of $5 \times 10^5 M_\odot$ (Martin et al. 2007), Willman 1 could feature a mass-to-light ratio in the range $500 - 700$ $M_\odot/L_\odot$, or even more, making it one of the most DM dominated objects in the Universe (Strigari et al. 2007c).

The small number of stars that belong to this dSph hinders, however, an accurate determination of the DM density profile. Following Strigari et al. (2007c), we parametrize its DM halo with a NFW profile, as specified in Table 2, although these parameters are subject to somewhat larger uncertainties than in the case of Draco.

9. Observation with ACTs: MAGIC II and CTA

When entering into the atmosphere, cosmic gamma-rays (as well as the many orders of magnitude more frequent background charged cosmic rays) quickly lose energy through interactions with the nuclei of atmospheric molecules, dominantly by pair production of electrons and positrons. Bremsstrahlung photons radiated by these highly energetic electrons

and positrons in turn lead to the production of secondary electron-positron pairs, thus triggering the subsequent development of a particle shower. When the electron-positron energy falls below $E_c \approx 83$ MeV in the atmosphere, the dominant mechanism of energy loss becomes ionization and the shower rapidly dies off. This takes place at an altitude of $8 - 12$ km, depending on the energy of the primary gamma-ray. This cascade of highly relativistic particles causes a flash of UV-blue Cherenkov light, with the greatest emission coming from the shower maximum (i.e. where the number of free electrons and positrons is maximal), lasting a few nanoseconds and propagating in a cone with an opening angle of $\sim 1°$, slightly depending on the primary energy. The resulting circle of projected light at 2000 m asl (the MAGIC telescope altitude) has a radius of about ~ 120 m. If a telescope is located inside this Cherenkov-light pool, the light can be reflected from the collecting mirrors and focused onto a multi-pixel recording camera. An image reconstruction algorithm (Hillas 1985) then allows the recovery of the energy and direction of the primary particle, and determines whether it was more likely a hadron or a photon. In this way, it is possible to reject up to 99% of the background, constituted mainly by sub-showers generated by charged cosmic ray particles, by muons and by the night sky background light.

This technique was pioneered by the Whipple telescope, followed by several successors currently under operation as e.g. MAGIC, H.E.S.S., CANGAROO-III and VERITAS (http://veritas.sao.arizona.edu/). In Bringmann et al. (2009) we only considered observational prospects for the upcoming MAGIC II telescope system and for the future generation of ACTs, focusing on the case of CTA. MAGIC II is a stereoscopic system of telescopes, composed of MAGIC and a second telescope currently under commissioning on the island of La Palma, which will start operation in 2009. The stereoscopic view of two telescopes (pioneered by HEGRA (Pulhofer et al. 2003)), together with the improved technical characteristics of the second detector, will allow a general improvement in the overall performance of the experiment, in particular in terms of energy and angular resolution, as well as energy threshold. The performance of the MAGIC II array was simulated with Monte Carlo tools by Carmona et al. (2007). CTA, on the other hand, is the result of an effort for a next generation Cherenkov observatory with increased capabilities: normally, one single telescope can cover 1.5-2 orders of magnitude in energy range. With the combined use of many telescopes of 2-3 different sizes, CTA should be able to extend the energy range to almost 4 orders of magnitude, from roughly ~ 30 GeV to ~ 100 TeV. The experiment is still in the early design phase and the final layout of the array is thus far from defined yet; the performance, therefore, is still subject to changes (I will refer mainly to the work of Bernloehr et al. (2007)). The CTA prototype construction could start in 2010, at least for some of the main components, and the final installation is foreseen in 2012-15.

The performance of an ACT in terms of its prospects to detect a DM annihilation signal can generally be characterized by a small number of basic parameters, which are described in the following (see also Table 3 for a summary of the characteristics for MAGIC II and CTA):

- *Energy threshold:* The energy threshold of an ACT can take slightly different values according to the definition. In Bringmann et al. (2009) we considered it to be the peak of the reconstructed MC energy distribution (other definitions being analysis threshold,

trigger threshold, etc.). This value depends mainly on the reflector area of the telescope: a larger mirror area allows, in particular, to collect more photons from the showers and thus increases the chance of discrimination against the night sky background light, in particular for low energy showers. The use of a stereoscopic system also plays an important role because it enhances the gamma/hadron (g/h) discrimination power which is weaker at low energy. The energy threshold changes with the zenith angle of observation, and sources culminating high in the sky are preferred. Reaching a low energy threshold is an important feature for DM studies with ACTs, both because of the increased number of photons and because of the enhanced possibility to observe the spectral cut-off even for low-mass neutralinos. Making use of stereoscopic observations, MAGIC II will have an energy threshold of $60 - 70$ GeV (Carmona et al. 2007), with possible extension to even lower energies with improved analysis techniques and new trigger systems currently under development. This value will be further lowered to at least 30 GeV for CTA. The telescope acceptance for gamma-rays around 30 GeV starts to decrease rapidly, but a very strong gamma-ray signal could probably even be detected at energies as low as about 10 GeV.

- *Energy resolution:* The true energy of the primary gamma-ray E' is reconstructed on the basis of a comparing analysis between the shower image parameters and MC events. The probability to assign, after the analysis, an energy E to the primary gamma-ray can be approximated by

$$R_\epsilon(E - E') \approx \frac{1}{\sqrt{2\pi}E} \cdot \exp\left(-\frac{(E - E')^2}{2\epsilon^2 E^2}\right). \tag{59}$$

Typical values for the energy resolution ϵ are of the order of 10-30% for ACTs, depending on the energy. The reason for such large uncertainties is the combined effect of many sources of uncertainties (for a more detailed discussion, see Albert et al. 2008)). The energy resolution is an important parameter when observing spectral features as bumps and cut-offs that can provide clear signatures for a DM signal. MAGIC II will have an energy resolution of 15% above 300 GeV (up to 20% at 70 GeV); for the CTA, this situation could radically improve. Finally, let me note that further systematic errors might hide in the absolute energy calibration; the recent MAGIC observation of a clear cut-off in the Crab Nebula spectrum (the Crab Nebula is a supernova remnant that is conventionally taken as reference source for cross-calibrations in gamma-ray astronomy due to its very stable and intense flux), when compared to a corresponding future observation by Fermi LAT (Gehrels & Michelson 1999), may allow for the first robust calibration of gamma-ray energies (Biland 2008).

- *Angular resolution:* The reconstruction of the direction of a primary gamma-ray is performed through image analysis. As a result, a gamma-ray coming from a direction ψ' will be reconstructed to a direction ψ in the sky with a probability distribution that can be fitted to a Gaussian function:

$$B_{\vartheta_r}(\psi' - \psi) = \frac{1}{2\pi\vartheta_r^2} \cdot \exp\left(-\frac{(\psi' - \psi)^2}{2\,\vartheta_r^2}\right). \tag{60}$$

The standard deviation ϑ_r of the Gaussian corresponds to the telescope PSF. As a consequence, any source will appear somewhat blurred. The stereoscopic system exploited in MAGIC-II will improve the PSF, allowing values as low as 0.05°, while for CTA we expect an even smaller PSF. It is hard to predict an exact value given the current lack of knowledge of the CTA design, but a realistic value that has been used in Bringmann et al. (2009) is 0.02° (see also Hofmann 2006). For extended sources, as in the case of dSphs, the PSF plays an important role in the reconstruction of the DM density profile, as discussed in the next section.

- *Flux sensitivity:* The sensitivity of an ACT is usually defined as the minimum flux for a 5σ detection over the background, after 50 hours of observation time and based on at least 10 collected photons. For operating experiments, the sensitivity can be computed by using real data and following Equation 17 of Li & Ma (1983), while for planned experiments the sensitivity has to be estimated on the basis of MC simulations and is therefore subject to larger uncertainties. The procedure is as follows: a full data analysis is performed on two samples of MC simulations, one for gamma-ray events and one for background events (basically protons and helium), during which a number of parameters ("cuts") is optimised to maximize the analysis quality factor $Q = \epsilon_\gamma / \sqrt{\epsilon_h}$, i.e. the ratio between the efficiency for gamma-rays and the square root of the hadron efficiency ("efficiency" refering here to the ratio between the number of events passing the analysis cuts and the number of events at MC, input, level). After the optimisation, one can estimate the number of hadrons $N_h(> E)$ above some energy E. Given the Poissonian distribution of events, a 5σ detection is obtained whenever the number of gamma-rays detected is larger than $5\sqrt{N_h(> E)}$. The integrated sensitivity above E is thus given by:

$$\Phi^{\min}(> E) = \frac{5\sqrt{N_h(> E)}}{A \cdot t_{50}} \frac{1}{\epsilon_\gamma}, \tag{61}$$

where A is the MC gamma-ray simulation area and t_{50} is the time interval corresponding to 50 hours.

$N_h(> E)$ and ϵ_γ, and thus the sensitivity, are usually determined assuming a featureless power-law spectrum of MC gamma-ray events of index -2.6. This corresponds approximately to the spectrum of the Crab. For this reason, the sensitivity is often also expressed in terms of "Crab" units (C.U). In the case of the benchmark neutralinos under study (see next section), the gamma-ray spectra are usually harder than that of the Crab and no longer featureless; it is therefore natural to ask how much this would change the sensitivity.

To address this question, let us note that the sensitivity mainly depends on the g/h discrimination power. The g/h separation, however, is very efficient at intermediate and large energies, where the shower parameters are firmly distinguishable between hadronic and gamma events. At energies below $\sim 30\,\mathrm{GeV}$, on the other hand, the differences are more subtle and the sensitivity *is* affected. Hence we expect that the differential sensitivity does not depend too strongly on the spectrum of the source, unless in the case of rather low energies. An exact treatment of this effect would require dedicated studies with MC simulations, which is beyond the aim of this work. Based on a preliminary

Table 3. Comparison of the performance of the MAGIC, MAGIC II and CTA* telescopes. E_0 (in GeV) is the energy threshold, ϵ the energy resolution and ϑ_r (in degrees) the angular resolution. The sensitivity $S(> E_0)$ (in cm^{-2}s^{-1}) is given for a Crab-like spectrum above the energy threshold.
*For CTA, the numbers have to be taken as placeholders because the telescope design is not yet fixed.

	MAGIC	MAGIC II	CTA*
E_0 (in GeV)	100	70	30
ϵ	30-20%	20-10%	10%
ϑ_r (in degrees)	0.10°	0.05°	0.02°
$S(> E_0)$ (in cm^{-2}s^{-1})	5×10^{-11}	1.4×10^{-11}	1.5×10^{-11}

MC analysis, however, we generally expect that the sensitivity at a given energy will not change by more than a factor of two compared to that defined for the Crab.

10. Computation of the annihilation flux

10.1. The cosmological factor

Following Equation (52), I consider separately the cosmological and the particle physics factor. The former is discussed in the present section and the latter is the subject of next section.

The cosmological factor depends on the source distance and geometry (as well as the PSF of the telescope), but for a given DM profile it does not depend on the particular DM candidate. As a consequence, the discussion here remains valid for any generic WIMP candidate. Pointing the telescope towards a direction ψ in the sky, and taking into account its finite angular resolution, the cosmological factor depends on the quantity:

$$J(\psi) = \frac{1}{4\pi} \int d\Omega' \int d\lambda \left[\rho^2(r(\lambda, \psi)) \cdot B_{\vartheta_r}(\psi, \psi') \right], \tag{62}$$

where the angular integration $d\Omega' = d\varphi' d(\cos \theta')$ extends over a cone centered around ψ, with an opening angle a few times the PSF ϑ_r. The integration over λ is along the line-of-sight, in the direction ψ, so that $r = \sqrt{\lambda^2 + D^2 - 2D\lambda \cos(\Psi)}$, where D is the distance of the source from the Earth and $\cos(\Psi) \equiv \cos(\theta') \cos(\psi) - \cos(\varphi') \sin(\theta') \sin(\psi)$. Defined as above, $J(\psi)$ is conventionally expressed in units of $M_\odot^2$kpc^{-5}sr^{-1} or GeV^{2}cm^{-5}sr^{-1}. In order to translate it to the dimensionless quantity $J(\psi)$ as defined in Bergstrom et al. (1998), one simply has to multiply it by 5.32×10^{-21}GeV^{-2}cm^{5}sr ($= 2.37 \times 10^{-14} M_\odot^{-2}$ kpc^{5}sr).

Integrating Equation (62) over the full angular extension of the source gives:

$$\widetilde{J} \equiv \int \frac{\Phi^{\text{cosmo}}}{4\pi} = d\Omega_\psi J(\psi) \simeq \frac{1}{4\pi D^2} \int dV \rho^2(r), \tag{63}$$

where the second integral is over the *spatial* extent of the source. Note that this expression is expressed now in $M_\odot^2$kpc^{-5} or GeV^{2}cm^{-5} and no longer depends on the telescope PSF.

Figure 20. The $J(\psi)$ factor in the case of Draco (upper plot) and Willman 1 (lower plot). Core profiles are shown in blue, cusp profiles in red. Thick solid (dashed) lines represent profiles smeared with the MAGIC II (CTA) angular resolution. Thin solid lines represent the profiles without smearing. The upper right panel in each figure shows a zoom-in of the region close to the center. For comparison, we also show the profiles for a hypothetical, infinite angular resolution. Taken from Bringmann et al. (2009).
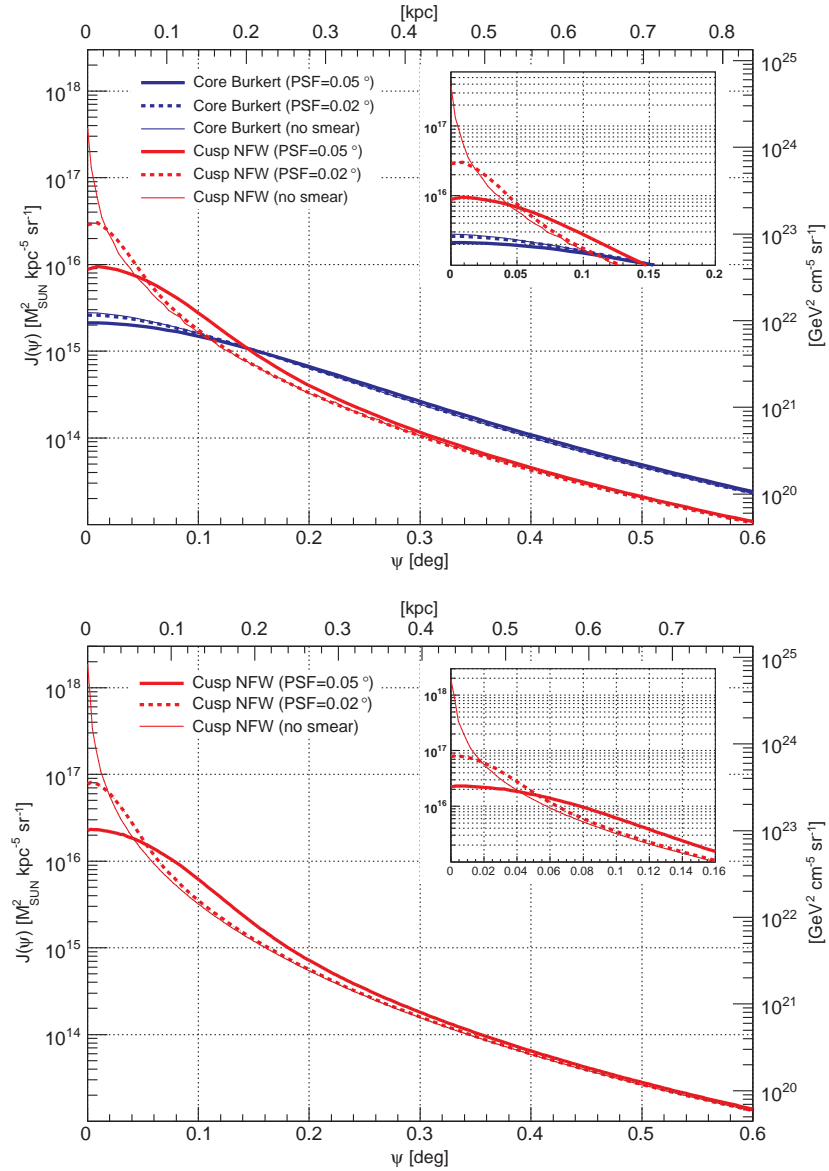
Table 4. Comparison of the integrated quantity $\widetilde{J}$ (related to the cosmological factor) for Draco and Willman 1, for the profiles specified in Table 2.

$\widetilde{J}$	Draco-Burkert	Draco-NFW	Willman 1–NFW
(GeV^{2}cm^5)	3.84×10^{17}	4.71×10^{17}	9.55×10^{17}
($M_\odot$/kpc^5)	8.63×10^{10}	1.06×10^{11}	2.15×10^{11}

Using the DM profile parameters of Table 2, in Figure 20 the quantity $J(\psi)$ for Draco and Willman 1 is displayed. While the two sources, from this plot, appear similar in terms of their angular size ψ, I recall that their spatial extension is quite different: by comparing, e.g., their respective scale radii for an NFW profile, one sees that Willman 1 ($r_s = 0.18$ kpc) is considerably smaller than Draco ($r_s = 0.50$ kpc). In the case of Draco, the cusp and core profiles are almost identical (up to an overall normalization factor of ~ 2) for angular distances larger than about $\psi \sim 0.3°$, below which the cusp profile starts to increase more rapidly. At the center, the two profiles differ by around one order of magnitude, the difference increasing with decreasing PSF. Whenever an extended emission would be observed, one could thus in principle be able to discriminate between different profiles by comparing the flux at different distances from the center. As it becomes obvious from Figure 20, and as already stressed by Sanchez-Conde et al. (2007), the angular resolution of the telescope would play an important role in this case. Taking into account the full range of profiles consistent with the observational data (Strigari et al. 2007c), the astrophysical factor for dSphs is far better constrained than for, e.g., the GC, where the uncertainty in the inner part spans several orders of magnitude (Fornengo et al. 2004).

Given a telescope PSF of the order of $0.1°$, and the expected feebleness of the signal, however, the capability of reconstructing the morphology of extended sources is very limited. This is particularly true in the case of non-stereo ACTs where the shower direction is reconstructed with less precision. Even when making the rather optimistic assumption that a signal could be discriminated against the background out to a distance where the annihilation flux is a factor of 3 less than from the direction towards the center, the source would appear at a size of only roughly twice the PSF for both Draco and Willman 1, in the case of a cuspy profile. For a core profile, the same measure would indicate an apparent extension out to $\lesssim 0.2°$, still well contained in a normal ACT camera ($\sim 3°$ aperture). As we will see, the expected annihilation fluxes are rather low and we find it therefore premature to discuss in depth the possibilities to distinguish between different profiles in the way indicated above; rather, we will in the following focus on the total, i.e. integrated, flux.

Table 4 reports the calculation of the *integrated* quantity $\widetilde{J}$ for the two dSphs studied here. For Willman 1, the uncertainty in the DM profile translates into a 95% confidence interval of about $8 \times 10^{17} \text{GeV}^2/\text{cm}^5 \lesssim \widetilde{J} \lesssim 4 \times 10^{19} \text{GeV}^2/\text{cm}^5$ (Strigari et al. 2007c). In the case of Draco, the astrophysical factor lies in the range $10^{17} \text{GeV}^2/\text{cm}^5 \lesssim \widetilde{J} \lesssim 2 \times 10^{18} \text{GeV}^2/\text{cm}^5$ (Strigari et al. 2007a). Again, these astrophysical uncertainties are rather small when compared to other potential sources of DM annihilation signals, but one should keep in mind that our choices

Figure 21. Type of diagrams that contribute to the first order QED corrections to a WIMP annihilation into a pair of charged particle final states. The leading contributions to diagrams (a) and (b) are universal, referred to as *final state radiation*, with a spectrum which only depends slightly on the final state particle spin. VIB as in diagram (c), on the other hand, is strongly dependent on the details of the short-distance physics such as helicity properties of the initial state and masses of intermediate particles. Taken from Bringmann et al. (2008).
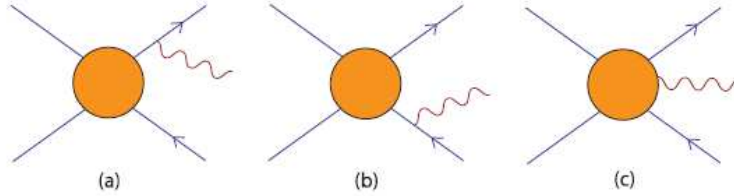
of DM profiles are actually quite conservative: taking into account the above quoted range of possible values for $\widetilde{J}$ that are consistent with current observations of velocity dispersions in the dwarfs, one could thus win a factor up to about 4 (in the case of Draco) or 40 (in the case of Willman 1) in the annihilation flux. I will get back to this in Section 11.

10.2. Particle Physics factor and Virtual Internal Bremsstrahlung

The particle physics factor in Equation (52) is given by:

$$\frac{d\Phi^{\mathrm{PP}}}{dE} = \frac{\sigma_{\mathrm{ann}}v}{2m_\chi^2} \cdot \sum_i B^i \int dE' \frac{dN_\gamma^i(E')}{dE'} R_\epsilon(E - E'), \tag{64}$$

where the integration over $R_\epsilon(E - E')$ (see Equation (59)), takes into account the finite energy resolution of the instrument. The *total* number of photons above some energy E_0 of course no longer depends on the energy resolution (as long as $1 - E_0/M_\chi \gg \epsilon$) and is given by:

$$N_\gamma(> E_0) \simeq \sum_i B^i \int_{E_0}^{m_\chi} \frac{dN_\gamma^i(E)}{dE} dE. \tag{65}$$

In Section 5, I have already discussed the different contributions to the annihilation channels dN_γ^i/dE. Here I only what to stress the important of the Internal Bremsstrahlung: in the case of charged annihilation products, the contribution of bremsstrahlung photons emitted by the charged final legs is taken into account. As already pointed out, such contribution results to play an important role for KK DM. Bringmann et al. (2008) noted that photons can be emitted also by the virtual particles exchanged in the annihilation (VIB) so that the complete set of Feynman diagrams responsible for bremsstrahlung emission can be seen in Figure 21.

There are two notable situations in which the contribution of VIB results to be releavant:

- for DM annihilating in charged particles the annihilation energy yield is enhanced by a logaritmic term of the form $\sim \log(2E_\gamma \sqrt{s}/m_X)$, where $\sqrt{s}$ is the energy in the center of

Figure 22. Gamma-ray spectra for model BM2 and BM3 of Bringmann et al. (2008). Contributions from internal bremsstrahlung and from secondary particles are shown separately. Taken from Bringmann et al. (2008).
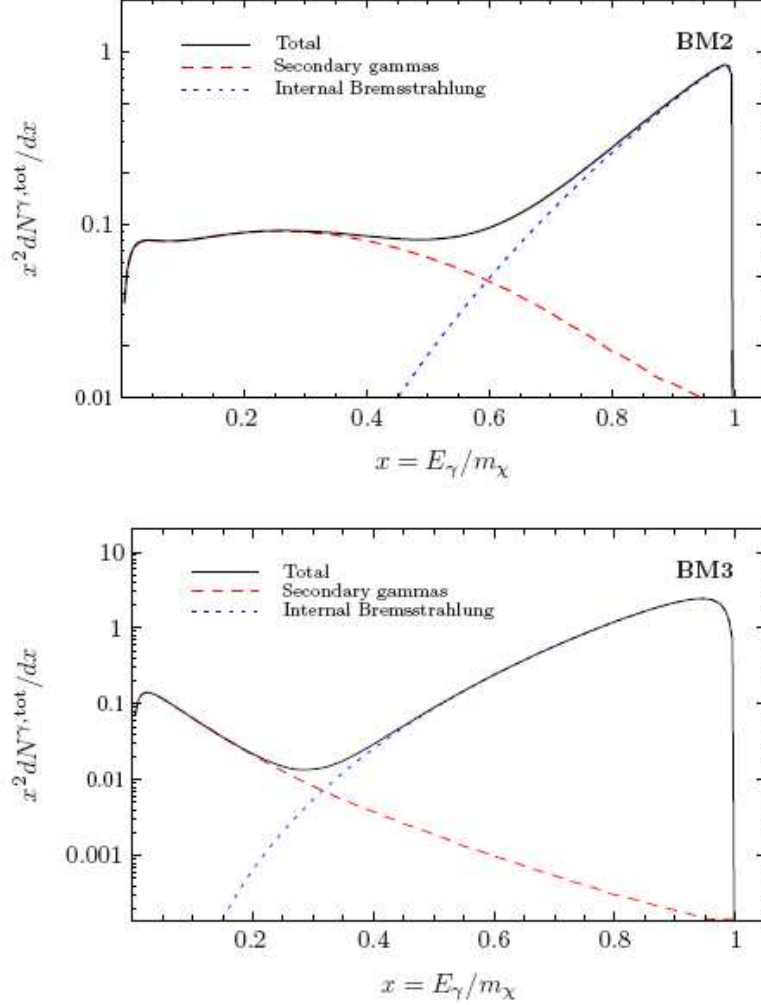
mass and m_X is the mass of the charged particle produced in the annihilation $\chi\chi \to X\bar{X}$. Such term is larger in the case of production of light leptons, but in that case an additional factor proportional to m_X^2/m_χ^2 has to be included due to the helicity property of a highly non-relativistic Majorana particle (as it is for a DM neutralino annihilating today), with the net result of suppressing this channel. On the other hand, helicity suppression is lifted for VIB photons so that this new contribution dominates the bremsstrahlung emission and, in some cases, the whole annihilation flux.

- in the case that the particle produced in the annihilation $\chi\chi \to X\bar{X}$ is a boson and the annihilation proceeds through a t-channel. The propagator results to be proportional to $\propto ((l-p)^2 - m_{\bar{X}})^{-1} \sim (m_\chi^2 - m_{\bar{X}}^2 + M_X^2 + 2m_\chi E_X)^{-1}$, where l is quadrimomentum of the ingoing DM particle and p the quadrimomentum of the exchanged particle $\bar{X}$ over

Table 5. Parameters defining the benchmark models and some relevant quantities related to the annihilation spectrum. $m_{1/2}$ and m_0 (expressed in GeV) are the uniform masses of gauginos and scalars, respectively. $\tan\beta$ is the ratio between the vacuum expectation values of the two Higgs bosons. A_0 (in GeV) is the coefficient of the trilinear scalar term and μ is the coefficient of the mass term in the Higgs potential. m_χ (in GeV) is the neutralino mass, $\Omega_\chi h^2$ its relic density and $\sigma_{ann} v|_{v=0}$ (expressed in cm^3s^{-1}) its annihilation rate today. r is the ratio of IB photons over secondary photons (above $0.6 m_\chi$) and $\sigma_{ann}v|_{\gamma\gamma}$, $\sigma_{ann}v|_{Z\gamma}$ are the annihilation rates for the γ lines. Φ^{PP} (expressed in $cm^3s^{-1}GeV^{-2}$), finally, is defined in Equation (53) and given for MAGIC II ($E_0 = 70$ GeV) and CTA ($E_0 = 30$ GeV) energy thresholds, respectively.

BM	$m_{1/2}$	m_0	$\tan\beta$	A_0	$\text{sign}(\mu)$	m_χ	$\Omega_\chi h^2$	$\sigma_{ann}v|_{v=0}$
I'	350	181	35.0	0	+	141	0.12	3.6×10^{-27}
J'	750	299	35.0	0	+	316	0.11	3.2×10^{-28}
K'	1300	1001	46.0	0	–	565	0.09	2.6×10^{-26}
F^*	7792	22100	24.0	17.7	+	1926	0.11	2.6×10^{-27}
J^*	576	108	3.8	28.3	+	233	0.08	9.2×10^{-29}

BM	r	$2\sigma_{ann}v|_{\gamma\gamma}$	$\sigma_{ann}v|_{Z\gamma}$	$\Phi^{PP}_{\geq 70\,\text{GeV}}$	$\Phi^{PP}_{\geq 30\,\text{GeV}}$
I'	4	7.9×10^{-30}	8.5×10^{-31}	1.6×10^{-33}	9.9×10^{-33}
J'	34	3.4×10^{-30}	4.1×10^{-31}	2.2×10^{-34}	1.1×10^{-33}
K'	≤ 0.1	1.8×10^{-31}	2.2×10^{-32}	1.5×10^{-32}	7.5×10^{-32}
F^*	11	5.8×10^{-30}	1.6×10^{-29}	9.6×10^{-34}	2.4×10^{-33}
J^*	2300	5.5×10^{-30}	1.8×10^{-30}	7.9×10^{-34}	8.9×10^{-34}

which it will integrated on. If $\tilde\chi$ and X are almost degenerate in mass, one thus find an enhancement for small E_X that corresponds to large photon energies E_γ. This second possibility is more relevant for neutralino DM in the coannihilation regions.

While the effect of IB is largely model dependent, it appears in general as a pronounced "bump" at energies close to the kinematic cut-off at the neutralino mass. The importance of this effect is two–fold: first, the flux at high energies, where ACTs are most sensitive, is significantly increased; secondly, the introduction of spectral features allows an easier discrimination of a DM source from potential astrophysical sources located in the vicinity, whose spectrum is usually a featureless power-law. Figure 22 shows how the introduction of VIB can modify the energy spectrum.

In Bringmann et al. (2009) we considered, for the first time, the effect of VIB in the computation of the prospects for DM detection from dSphs. We focused only to mSUGRA models (see, e.g., Chamseddine A. H. & P. 1982). For the calculation of the low-energy features of mSUGRA models (i.e. mass spectra etc.), version 4.01 of DarkSUSY were used (Gondolo et al. 2004) that relies on the public code Isajet 7.69 (Paige et al. 2003). As a marginal note, let me stress that these calculations are highly sensitive to how the renormalization group equations are implemented and different codes, or even different versions of the same code, may give rather different results (see, e.g., Battaglia et al. 2001, Battaglia et al. 2004). Typically, the *qualitative* low-energy features of a given

model can still easily be reconstructed by allowing for slight shifts in the parameter space (defined at high energies). From a practical point of view, this situation therefore does not constitute a severe problem as one may always regard a set of low-energy quantities like the mass spectrum, annihilation cross section and branching ratios as a valid *effective* definition of the model.

Even if highly constrained, mSUGRA permits a rich phenomenology, as summarized by the five regions enlisted in Section 3.4 able to provide the right relic density. In Bringmann et al. (2009) we worked with a set of benchmark models, representative of these five different regions in the SUSY parameter space. From an experimental point of view, the advantage of benchmark models is that they allow a direct comparison between data from different experiments (most of the benchmarks that we used have already been extensively studied in other contexts) and, in general, a more detailed *per case* analysis than for, e.g., parameter scans. Our particular choice of benchmark models is summarised in Table 5.

The features of these models that are important in our context are the following:

- I': This model (like the following two) was introduced by Battaglia et al. (2004), where also its phenomenology at colliders was extensively studied. It is a typical example of a model in the *bulk region*. While the annihilation into lepton pairs is strongly suppressed for neutralinos with the small velocities they exhibit today (unlike in the early Universe), annihilation into $\ell^+\ell^-\gamma$, which does not suffer from helicity suppression (Bergström 1989), gives a considerable contribution due to the lightness of the sleptons.

- J': This model lies in the *coannihilation tail*. The sleptons being close to degenerate with the neutralino, IB from lepton final states gives even higher enhancements to the flux than in the previous case.

- K': A representative model for the *funnel region*, where the annihilation dominantly occurs through an *s*-channel pseudo-scalar Higgs boson. Consequently, the additional emission of a photon does not lift the helicity suppression in this case and therefore IB contributions have to be subdominant.

- F^*: Introduced in Bringmann et al. (2008) as BM4, this model exhibits a large neutralino mass, as typical in the *focus point* region. In this regime, the chargino is close to degenerate with the neutralino (in this case an almost pure Higgsino) and large IB contributions result from charged gauge boson final states (Bergström et al. 2005*a*).

- J^*: Introduced in Bringmann et al. (2008) as BM3, this is another example of a neutralino in the coannihilation region, characterized by a particularly large IB contribution.

We used DarkSUSY, which in its most recent public release 5.0.1 (Gondolo et al. 2005), contains a full implementation of the IB contributions focused on here, to compute the annihilation spectra for the benchmark models defined above. Line signals are also taken into account, but they turn out to be completely subdominant in the cases studied here (except for model F^*). The resulting spectra are plotted in Figure 23, both before taking into account the finite energy resolution of the detector and for the case of an energy resolution of 10%. The main characteristics of these spectra are also summarized in Table 5.

Figure 23. The particle physics factor $d\Phi^{\rm PP}/dE$, as defined in Equation (64), for the benchmarks models introduced in Section 10.2. The upper panel shows the case of a hypothetical detector with perfect energy resolution, and a line width of $\epsilon \sim v \sim 10^{-3}$, while the lower case shows the more realistic example of $\epsilon = 10\%$. For comparison, we also show the spectrum of the Crab Nebula, taken from Albert et al. (2008) with an arbitrary normalization. Taken from Bringmann et al. (2009).
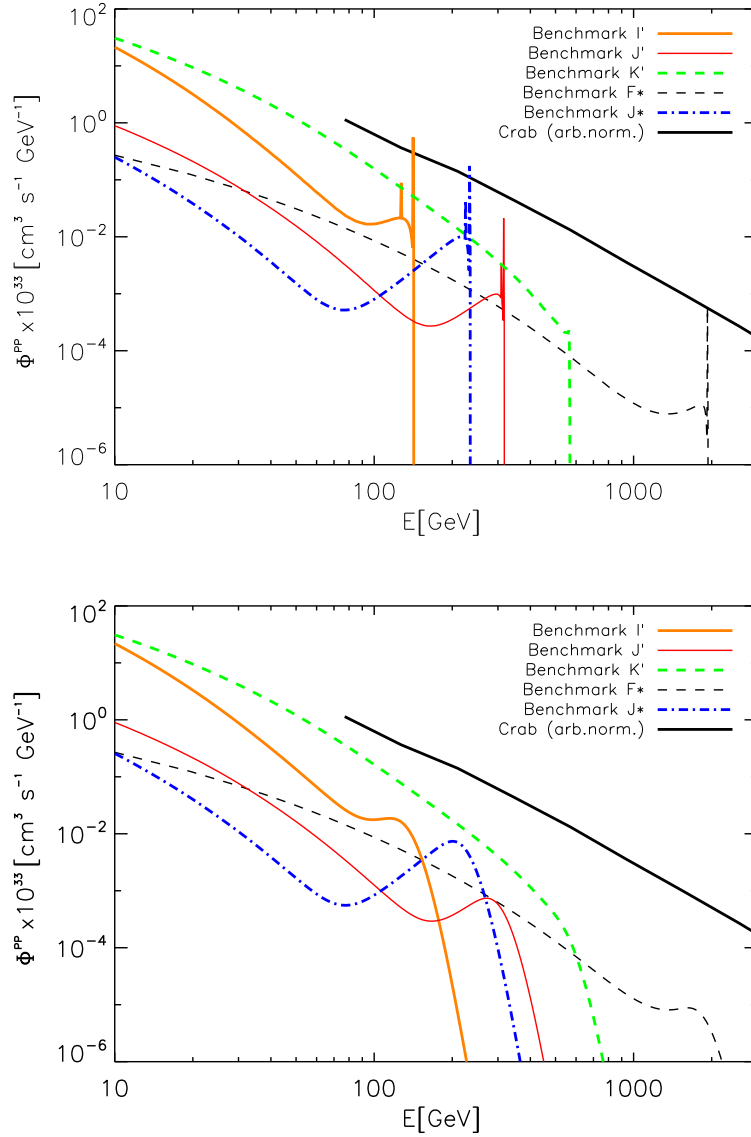
Table 6. Expected integrated flux $\Phi(E > E_0)$ for the neutralino benchmark models in Table 5 (in units of $10^{-15}\mathrm{cm}^{-2}\mathrm{s}^{-1}$), where we used the experimental parameters listed in Table 3. In parentheses, we state the increase in the signal that would be needed for a 5σ detection as (B1,*B2*,**B3**). Here, B1 is the often cited increase that is needed when simply comparing the sensitivity and annihilation fluxes above the telescope energy threshold E_0. *B2* is more realistic in that it gives the corresponding quantity *above a certain energy* E^*, depending on the benchmark, where the integrated flux to sensitivity ratio is greatest and **B3** is the same as *B2*, yet for the most favourable halo profile consistent with current observations (still not taking into account the effect of substructures, however). See text for further details.

		Draco-NFW		
		MAGIC II		CTA$_{30}$
I'	0.75	$(1.9 \times 10^4,\ 1.3 \times 10^4,\ \mathbf{2900})$	4.7	$(3100,\ 2100,\ \mathbf{490})$
J'	0.10	$(1.4 \times 10^5,\ 3.2 \times 10^4,\ \mathbf{7600})$	0.52	$(2.8 \times 10^4,\ 4900,\ \mathbf{1200})$
K'	7.0	$(2000,\ 2000,\ \mathbf{470})$	35	$(410,\ 260,\ \mathbf{61})$
F^*	0.45	$(3.1 \times 10^4,\ 1.6 \times 10^4,\ \mathbf{3800})$	1.1	$(1.3 \times 10^4,\ 2800,\ \mathbf{670})$
J^*	0.37	$(3.8 \times 10^4,\ 7400,\ \mathbf{1700})$	0.42	$(3.4 \times 10^4,\ 1200,\ \mathbf{290})$

		Willman 1		
		MAGIC II		CTA$_{30}$
I'	1.5	$(9200,\ 6200,\ \mathbf{150})$	9.4	$(1500,\ 1000,\ \mathbf{25})$
J'	0.21	$(6.9 \times 10^4,\ 1.6 \times 10^4,\ \mathbf{380})$	1.1	$(1.4 \times 10^4,\ 2400,\ \mathbf{58})$
K'	14	$(990,\ 990,\ \mathbf{24})$	71	$(200,\ 130,\ \mathbf{3})$
F^*	0.92	$(1.5 \times 10^4,\ 8100,\ \mathbf{190})$	2.2	$(6500,\ 1400,\ \mathbf{34})$
J^*	0.76	$(1.9 \times 10^4,\ 3700,\ \mathbf{88})$	0.85	$(1.7 \times 10^4,\ 610,\ \mathbf{15})$

11. Results and discussion

Combining the values in Table 4 with the particle physics factor from Table 5, we finally made predictions about the expected gamma-ray flux above the telescope energy threshold E_0. A summary of the results from Bringmann et al. (2009) is reported in Table 6, where we also quoted the increase in the overall flux normalization that would be necessary to meet the required sensitivity for a 5σ detection (referred to as B1 in the table). While it is customary to quote sensitivities and actual fluxes above E_0 in this kind of analysis, we recalled that DM annihilation spectra are rather hard, in particular when taking into account possible spectral features at photon energies close to the spectral cut-off at the mass of the DM particle. On the other hand, the sensitivity of ACTs is considerably better at energies somewhat larger than the telescope energy threshold. We therefore considered the projected sensitivities for the integrated flux above some energy $E^* > E_0$, using the sensitivity curves as provided by Bernloehr et al. (2007) for CTA and by Carmona et al. (2007) for MAGIC II and, by comparing those to the annihilation spectra, we then computed the *minimal* increase in the normalization that is required to see at least part of the DM annihilation spectrum above E^*. This is referred to as the quantity *B2* in Table 6; finally, we also stated as **B3** the corresponding

value for the most favourable *smooth* halo profile that is consistent with the observational data (i.e. here we took the upper limit on $\tilde{J}$ as discussed in Section 10.1).

So far, only smooth DM distributions were discussed. On the other hand, it is well known from both theory (Green et al. 2005) and numerical *N*-body simulations (Diemand et al. 2005) that cold DM is expected to cluster and thereby to form substructures with masses all the way down to the small-scale cut-off in the spectrum of matter density fluctuations, which can be determined to a great accuracy from the underlying DM model (Bringmann & Hofmann 2007); if surviving until today, such inhomogeneities in the DM distribution would greatly enhance the DM annihilation rate (Bergström et al. 1999). For the case of typical dSphs, this could result in an additional boost of the signal by a factor of 10-100 (Strigari et al. 2007*a*). Another considerable boost in the annihilation flux could also result from the existence of a hypothetical black hole at the center of the dwarfs (Colafrancesco et al. 2007). In the most optimistic astrophysical configuration, the required increase stated as **B3** in Table 6, would thus further be *reduced* by up to two orders of magnitude.

Some comments can be made about these results:

- *Sources.* For Draco, the model-dependent fluxes for the Burkert and NFW profiles are very similar, and therefore we presented only the latter in Table 6. For the astrophysical benchmark profiles introduced in Section 10.1, detectional prospects for Draco and Willman 1 only differ by a factor of around 2, and are obviously not very encouraging. When considering the most optimistic astrophysical configurations, adopting the highest observationally allowed value for $\tilde{J}$, things change considerably and Willman 1 becomes an interesting and indeed very promising target for DM searches. Allowing for an additional, in fact well-motivated, boost due to the presence of DM substructures in the dwarfs, this may give at least CTA the chance to see also Draco in some cases.

- *Telescopes.* Depending on the DM model, the ability of CTA to detect gamma-rays from DM annihilation is a factor of $6 - 8$ better than for MAGIC II. Focusing on Willman 1, and assuming very favourable astrophysical conditions, CTA would in principle be able to see *all* the benchmark models considered here, while MAGIC II should be able to see at least some of them. We recall that the flux enhancements needed for a 5σ detection, as states in Table 6, are calculated with respect to an observation time of $t_{obs} = 50$ hrs and scale like $t_{obs}^{-1/2}$. For prolonged observation times, one could thus win a factor of a few for both telescopes. Furthermore, as the CTA parameters are still quite preliminary, an additional factor of 2 in the sensitivity of the operating instrument seems quite feasible.

- *Benchmark models.* The best prospects for detection are found for the neutralino in the funnel region (model K'), the reason simply being a rather large annihilation rate. The second-best prospects are found for model J^* in the coannihilation region. Recalling from Table 5 that J^* is actually the model with the *smallest* annihilation rate, this may come as some surprise and nicely illustrates the importance of including IB contributions when estimating the flux from DM annihilation. The model F^* is yet another example with rather pronounced IB contributions; a mass of almost 2 TeV, however, efficiently suppresses the annihilation flux (in this case, the required boost

actually depends significantly on the details of the - so far not sufficiently well known - integrated sensitivity of CTA for TeV photons and could thus eventually be significantly improved).

When compared to previous work, these results are considerably more optimistic than the conclusions reached by Sanchez-Conde et al. (2007) for the analysis of present-day gamma-ray telescopes - not the least due to our fully taking into account all the contributions to the expected annihilation spectrum. On the other hand, we find the conclusions of Strigari et al. (2007*c*) overly optimistic, a fact that we traced back to the very large particle physics factor of $\Phi^{\mathrm{PP}} = 5 \times 10^{-29} \mathrm{cm}^3 \mathrm{s}^{-1} \mathrm{GeV}^{-2}$ that the authors assumed as a fiducial value (this should be compared to Table 5 and the corresponding values for our benchmark models, which represent typical neutralino DM candidates). While it may indeed be possible to find DM models with higher gamma-ray yields than considered here, we recall that there exist rather tight general bounds on the allowed annihilation cross section and the number of high-energy photons that are produced (Mack et al. 2008).

It has been proved that taking realistic DM spectra has an important impact on the analysis and, although common practice, *it can be a rather bad approximation to simply assume a featureless DM spectrum like from $b\bar{b}$ fragmentation and/or to only focus on the total flux above a given energy threshold E_0* in these kind of studies. The basic underlying reason for this is that *realistic DM annihilation spectra show a harder energy dependence than the sensitivity of ACTs*. Once detected, clear spectral features would, of course, have the additional advantage of providing a rather fool-proof way of discriminating DM spectra against astrophysical background sources - which is even more important in view of the still rather large astrophysical uncertainties involved.

Although these effects do provide a considerable enhancement of the detectional prospects, the expected flux from dSphs remains at a level that, for conservative scenarios, will be challenging to detect with the next generation of ACTs. This, rather than the angular resolution of these instruments, is the reason why the potential of ACTs to discriminate between different DM profiles in dSphs is limited even in the case of the detection of an annihilation signal; the eventual disentanglement between cored and cuspy profiles is probably more promising to perform at other wavelengths (Colafrancesco et al. 2007, Jeltema & Profumo 2008).

On the other hand, if one adopts the most optimistic astrophysical configurations that are compatible with current observational data of Willman 1, i.e. a favourable DM profile and an $\mathcal{O}(10-100)$ flux enhancement due to the existence of substructures, *all* of our benchmark models approach the reach of at least the CTA which, for the models studied here, is a factor of $6-8$ more sensitive to the annihilation signal than MAGIC II (this is, of course, independent of the source). The most promising case of our analysis turns out to be a neutralino in the funnel region, characterized by no sizeable IB contributions to its spectrum but a rather large annihilation rate; the second best case is a neutralino from the coannihilation region, making up for its small annihilation rate with enormously large radiative corrections.

Having demonstrated that the prospects of indirect DM detection through gamma-rays *do* depend on the details of the annihilation spectrum, and thus the underlying particle nature,

it would be interesting to perform similar analyses also for other targets of potential DM annihilation. Another further direction of extending the present analysis would be to perform a full scan over the parameter space of viable models. I also want to stress that the very concept of sensitivity of an ACT depends on the spectrum that is observed; in the context of DM searches, this is particularly important as DM annihilation spectra can significantly deviate from the usually assumed Crab-like spectrum. While in Bringmann et al. (2009) a first estimate of how to proceed in such a case is provided, it would be warranting to perform a dedicated analysis, using the full power of state-of-the-art Monte Carlo tools, in order to accurately determine the importance of this effect.

Even in the case of negative detection, ACTs could in principle put interesting upper limits on the flux which in turn would translate into constraints on the combined space of astrophysical and particle physics parameters. Though much smaller than for other sources like, e.g., the GC, the main uncertainty in this case lies in the overall scale of the flux as determined by the details of the DM distribution. This, unfortunately, will therefore greatly obstacle any stringent constraint from null searches on the particle physics nature of DM for quite some time ahead.

To conclude, nearby dwarf galaxies - and in particular Willman 1 - are very interesting and promising targets for DM searches with the next generation of ACTs. An excellent performance of these experiments, in particular in terms of the sensitivity at energies slightly below the DM particle mass, will be of paramount importance in such searches. In fact, given the low level of fluxes involved, a factor of 2 in sensitivity might decide whether a signal will be seen or not. Complementary to such demanding requirements on the experiments, the above discussion should also have made clear that it will be very important to collect more astrophysical data and to improve the theoretical understanding of how DM is distributed in order to reduce the still unpleasantly large astrophysical uncertainties involved.

Chapter IV:
Black Holes as
Annihilation Boosters

12. Black Holes as Annihilation Boosters

In the previous two chapters, I discussed indirect DM searches towards those that can be considered the most natural targets for detecting a DM annihilation signal: the GC, due to its nearness and its large amount of DM, and the dSphs hosted by the MW, due to their large mass-to-light ratio. In both cases there are no data which reveal a clear DM signal: observing the GC region, the detected gamma-rays are hardly interpreted as coming from DM annihilation, whether for the shape of the energy spectrum or for the uncertainty on the source of emission. On the other hand, in the case of dSphs, current experiments have only been able to put upper limits and new telescopes like Fermi LAT or the next generation of ACTs have to be waited to probe interesting regions of the paramters space. Clear features in the annihilation spectrum, as lines or bumps, are very useful in the discrimination of a DM signal with respect of the astrophysical background, but their contribution is model dependent and their detection is obstacled by the not-so-precise energy resolution (at least for ACTs).

In the remaining of this thesis, I am going to present two alternative strategies able to improve the possibility of a detection. Firstly, I am going to consider under which circumstances the DM profile can be modified in order to increase the cosmological factor in Equation (54). In particular the effect of Super Massive Black Holes (SMBHs) is going to be the subject of this chapter, while Intermediate Mass Black Holes (IMBHs) will be treated in next chapter.

Then the last chapter of the thesis my attention will turn to a completely different approach, considering the analysis of the angular power spectrum of anisotropies in the gamma-ray emissivity. Again, the aim will be the identification of clear singatures able to reveal the the contribution of DM.

Going back to the idea of studying the effect of Black Holes (BHs), two classes of astrophysical objects of particular interest are SMBHs (Ferrarese & Ford 2004, Kormendy & Ho 2000), with masses from 10^6 to $10^9 M_\odot$ and the more speculative IMBHs, with a mass from $20 M_\odot$ to $10^6 M_\odot$ (see, e.g., Miller & Colbert 2004, Koushiappas, Bullock & Dekel 2004, Bertone, Zentner & Silk 2005) and references therein. Both these classes of compact objects can influence the distribution of DM in which they are embedded, leading to strong overdensities: I am going to follow Fornasa & Bertone (2008) and review here our study on the impact of the formation and growth of BHs on the surrounding distribution of matter, and the consequences for indirect DM searches. Being the annihilation flux proportional to the integral of the DM density squared, scenarios where the density is *boosted* by the presence, or the growth, of a central BH, are very promising for indirect searches. BHs can thus be considered as *DM Annihilation Boosters*.

12.1. Dark Matter profiles without Black Holes

There is strong evidence in favour of the presence of SMBHs at the center of every galaxy with a substantial bulge component (Kormendy & Ho 2000, Ferrarese & Ford 2004, Merritt 2006*a*) and it has been suggested that even globular clusters can harbor IMBHs (Miller & Colbert

2004). Throughout the chapter, I will generically refer to large gravitationally bound systems like globular clusters, galaxies and clusters of galaxies, as *galaxies*, and I will refer to their central region as the *nucleus*, which may host BHs. Such compact objects account roughly for 10^{-3}% of the baryonic mass of the galaxy, which is composed of stars, intergalactic dust and DM. Again I will focus only on a generic WIMP scenario, with an annihilation cross section of order $\sigma v \approx 10^{-26}$cm^{3}s^{-1} and a mass ranging between the GeV and the TeV scale.

Since we want to characterize how BHs influence the surrounding distribution of matter, we need to specify how DM is distributed *before* the BHs form, and use this information as initial condition for the problem at hand. Profiles without any central object also receive particular attention *per se*, since the cuspiness of a DM halo without BH can give informations about the "coldness" of the DM candidate (Tremaine & Gunn 1979). I have already presented some profiles that fairly describe the distribution of DM around galaxies (see Section 2.4 and Section 6). Let me stress again that till recently, *N*-body simulations of galaxies were in favour of power-law profiles (with slope from -1 to -1.5) for the nuclear region, emphasizing the contrast with direct observations, such as rotation curves of Low Surface Brightness galaxies (LSBs) (de Blok 2005, de Blok & Bosma 2002, Gentile et al. 2005) and X-ray imaging, which suggest instead the presence of flat DM cores.

In particular Navarro et al. (2004) and Reed et al. (2005) used *N*-body techniques to simulate the high resolution evolution of galaxies with masses that go from dwarf galaxies ($10^{10}M_\odot$) to clusters of galaxies ($10^{15}M_\odot$). They fitted the final density profiles with a NFW profile finding that simulated data are well approximated by such a profile, that is, hence, "universal", in the sense that the same analytical form successfully captures the shape of halos at different masses. However, the logarithmic slope $\beta(r) = d\ln\rho(r)/d\ln r$ of the density profile decreases faster in the simulated data than does in the NFW profile at small radii. Moreover, *N*-body simulations do not exhibit any indications that $\beta(r)$ converges to a central value β_0, as should happen for a NFW profile ($\beta_0 = -1.0$) or for a Moore profile ($\beta_0 = -1.5$). This can be due to the finite resolution of numerical simulations, which can be trusted down to the resolution radius r_{min}, usually taken to be around 0.5% of the virial radius, depending on the total number of particles in the simulation ($r_{min} \approx$ kpc, for MW-sized halos). The structure of the inner region therefore were not clear, and the value of the central slope β_0 could only be inferred by extrapolation. Since the region near r_{min} is where the deviations from the NFW profile are stronger, the extrapolation procedure can lead to significant errors.

The new generation of *N*-body simulations (Navarro et al. 2008, Springel et al. 2008*b*), with reduced resolution radius, excluded the steep Moore profile (see Section 6) and confirmed that the NFW still provide a good fit to the simulated halos. I am going to consider the NFW value for the inner slope ($\beta_0 = -1$ as the lower limit for this quantity in the case of a DM nucleus in absence of a BH.

As already suggested in Navarro et al. (2004) (but found also in Merritt et al. (2005)), the new results of Navarro et al. (2008) show that the best fit to the simulated data for high-resolution ΛCDM halos is obtained with profiles inspired from the so-called Sérsic law (Sersic 1968)

$$\ln(\Sigma/\Sigma_e) = -b(X^{1/n} - 1). \tag{66}$$

Such a relation provides the best description of the luminosity profiles of elliptical galaxies and the bulges of disk galaxies (Graham & Guzman 2003): Σ is the projected density, $X = R/R_e$, and R is the projected radius. The parameter n, called Sérsic index, defines the shape of the profile, and b is a function of n, usually chosen so that the radius R_e contains half of the luminosity of the galaxy.

Equation (66) can be re-written as

$$\frac{d \ln \Sigma}{d \ln R} = -\frac{b}{n}\left(\frac{R}{R_e}\right)^{1/n}, \tag{67}$$

making explicit the power-law behaviour of the logarithm slope. Parametrizing the spatial DM profile in a similar way, the Einasto profile is obtained that can be written as in Equation (10) or as $\rho_\chi(r) \approx \exp(-Ar^{1/n})$ (see Figure 14). In order to emphasize the difference from the Sérsic law, it should be noted that now spatial and not projected quantities are been used. Equation (10) was tested fitting the density of the DM halos simulated by Navarro et al. (2008), providing better results than a NFW profile (see Figure 14 and also Merritt et al. (2005)).

The values of the Einasto index, left as a free parameter in the fit, depends on the mass of the halo, losing the universality that was a good feature of the NFW profile. If the Einasto relation was confirmed as a good parametrization of the inner region of DM halos, this would suggest that a scale-free relation like Equation (10), describing both dark and luminous matter, is a characteristic feature for systems that form via gravitational clustering.

13. Particle density around already-formed Black Holes

13.1. The Fokker-Planck equation and the Bahcall-Wolf solution

A population of particles (both stars and DM particles) around a BH can be described by a distribution function $f(\mathbf{x}, \mathbf{v}, t)$, whose evolution is governed by gravitational encounters among particles (Spitzer 1987). In the small-angle approximation, such distribution function slowly diffuses in the phase space $(\mathbf{x}, \mathbf{v})$ towards a steady-state configuration. The time needed to achieve this equilibrium solution is defined as the relaxation time t_{rel}. For the stellar population, assuming that all stars have the same mass $m_\star$ (Spitzer 1987):

$$t_{rel} \approx \frac{0.34\sigma^3}{G^2 \rho m_\star \ln \Lambda} \tag{68}$$

$$\approx 0.95 \cdot 10^{10} \text{ yrs} \left(\frac{\sigma}{200 \text{ km s}^{-1}}\right)^3 \left(\frac{\rho}{10^6 M_\odot \text{pc}^{-3}}\right)^{-1} \left(\frac{m_\star}{M_\odot}\right)^{-1} \left(\frac{\ln \Lambda}{15}\right)^{-1},$$

where σ is the velocity dispersion, ρ the stellar density and $\ln \Lambda$, known as the Coulomb logarithm, comes from imposing a physical upper cut-off in the distribution of impact parameters for stellar encounters. $\ln \Lambda$ is usually related to the mass of the central BH ($M_\bullet$) expressed in units of stellar masses (Preto et al. 2004):

$$\ln \Lambda \approx \ln\left(\frac{r_h \sigma^2}{2Gm_\star}\right) = \ln\left(\frac{M_\bullet}{2m_\star}\right) = \ln(N_\bullet/2). \tag{69}$$

t_{rel} depends on the distance from the center of the galaxy but usually, as in Equation (68) and Equation (69), it is computed at the influence radius r_h, defined as the radius at which the gravitational potential due to the BH is equal to the kinetic energy:

$$r_h = \frac{GM_\bullet}{\sigma^2} \approx 11 \text{ pc} \left(\frac{M_\bullet}{10^8 M_\odot}\right)\left(\frac{\sigma}{200 \text{ km s}^{-1}}\right)^{-2}. \tag{70}$$

In the case of a singular isothermal density profile (Spitzer 1987) ($\rho(r) = \sigma/2\pi G r^2$), $M(r \leq r_h) = 2M_\bullet$; and this can be used as an alternative definition of the influence radius. For the MW, $r_h \approx 3$ pc according to both definitions. There seems to be a clear trend of relaxation times with the mass of the central BH, where smaller objects (corresponding to fainter nuclei) are associated to smaller relaxation times. It can be seen from Figure 24 using the empirical $M_\bullet - \sigma$ relation (Ferrarese & Ford 2004):

$$M_\bullet = 5.72 \cdot 10^6 M_\odot \left(\frac{\sigma}{10 \text{km s}^{-1}}\right)^{4.86}. \tag{71}$$

Nuclei can then be classified in two different categories. Those nuclei with a relaxation time larger that the Hubble time, cannot have already achieved their relaxed equilibrium configuration, so that their distribution will reflect the process of nuclear formation. They are called *collisionless nuclei*, and they are characterized by a central region with a low density of stars, since near the BH a core is present with a slope $\lesssim 0.2$ (Merritt 2006a), at least for those nuclei where the influence radius is resolved. The "mass deficit" (compared to what one expects from the Sérsic law) is up to 4 times the mass of the central BH. There are, then, galaxies, like the MW and M32 that are characterized by a relaxation time smaller than 10^{10} yrs (at resolved radii, e.g. the MW has $t_{rel} = 3.5 \times 10^9$ yrs at radius $\approx 0.1 \, r_h$). These *collisional nuclei* have already reached their steady-state configuration. Usually they are faint nuclei ($M_V \lesssim -20$) and, opposite to cores of collisionless nuclei, the innermost region exceeds the Sérsic law, establishing an inner power-law profile with slope steeper than ≈ 1.5 or a compact stellar nucleus (Cote et al. 2006).

In this section, I will focus only to the case of collisional nuclei where the relaxation time is smaller than the Hubble time and the nucleus has, today, a relaxed, steady-state equilibrium configuration for the stellar population. The diffuse evolution of an isotropic distribution f is described by the Fokker-Planck equation (Spitzer 1987, Preto et al. 2004), where gravitational collisions are taken into account and parametrized as:

$$4\pi^2 p(E)\frac{\partial f}{\partial t} = -\frac{\partial F_E}{\partial E} = \frac{\partial}{\partial E}\left[-D_{EE}\frac{\partial f}{\partial E} - D_E f\right], \tag{72}$$
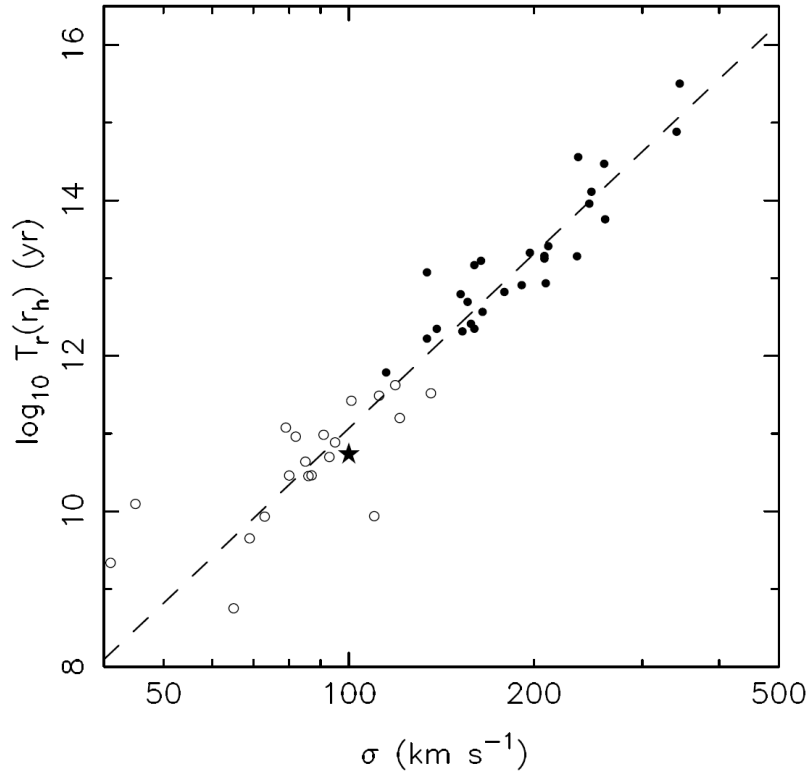
with

$$D_{EE}(E) = 64\pi^4 G^2 m^2 \ln \Lambda \left[q(E) \int_{-\infty}^{E} dE' f(E') + \int_{E}^{0} dE' q(E') f(E')\right], \tag{73}$$

$$D_E(E) = -64\pi^4 G^2 m^2 \ln \Lambda \int_{E}^{0} dE' p(E') f(E'), \tag{74}$$

$$q(E, t) = \frac{1}{3}\int_{0}^{r_{max}} v^3 r^2 dr = \frac{1}{3}\int_{0}^{r_{max}} [2(E - \phi)]^{3/2} r^2 dr, \tag{75}$$

Figure 24. Relaxation times measured at the SMBH influence radius in the ACS/Virgo sample of galaxies (see also Cote et al. 2004), versus the central stellar velocity dispersion. Filled symbols (●) are nuclei in which the influenced radius is resolved. The star is the MW. Taken from Merritt (2006*a*).

while $p(E) = -\partial q/\partial E$ is the volume of phase-space accessible to stars with energy E.

The equilibrium solution cannot be a Maxwellian distribution, since it would imply an unphysical stellar density near the BH (Shapiro & Teukolski 1983), given that stars cannot be present at radii smaller than the tidal radius r_t, inside which tidal forces tear stars apart. As a consequence, the distribution function is set to zero for $r \leq r_t$.

The physical steady-state solution was determined by Bahcall & Wolf (1976), following a previous work of Peebles (1972). They proposed that the equilibrium configuration is a zero-flux solution, and obtained a distribution function with a power-law behaviour $f(E) \propto |E|^{1/4}$, with a corresponding power-law density profile $\rho(r) = \rho_0 r^{-7/4}$. They also numerically solved a Fokker-Planck-like equation, obtaining a profile that can be very well described by the zero-flux solution, in the inner region ($r \lesssim 0.2\, r_h$, where the cusp actually forms), and a Keplerian rise in the velocity dispersion $\sigma \propto r^{-1/2}$. See Figure 25. Their solution has been confirmed by N-body simulations (Preto et al. 2004), in which the assumptions of isotropy and small-angle, characteristics of the Fokker-Planck-like formalism, had been relaxed.

The validity of Equation (72) relies on the following assumptions:

- stars are point-like masses, described by a distribution function that evolves due to gravitational interactions with the central BH and among themselves. In particular, this

Figure 25. Evolution of the stellar distribution around a SMBH due to energy exchange between stars. These curves were computed from the isotropic, orbit-average Fokker-Planck equation with boundary condition $f = 0$ at $\log|E| = 6$. *Left panel:* phase-space density f; *right panel:* configuration-space density ρ. The initial distribution (shown in bold) had $\rho \propto r^{-0.5}$ near the SMBH; thin curves show f and ρ at times of $(0.2, 0.4, 0.6, 1.0)$ in units of the relaxation time at the SMBH's initial influence radius r_h. Dashed line show the "zero-flux" solution $f \propto |E|^{1/4}$ and $\rho \propto r^{-7/4}$. The steady-state density is well approximated by the zero-flux solution at $r \lesssim 0.2\, r_h$. Taken from Merritt (2006*a*).
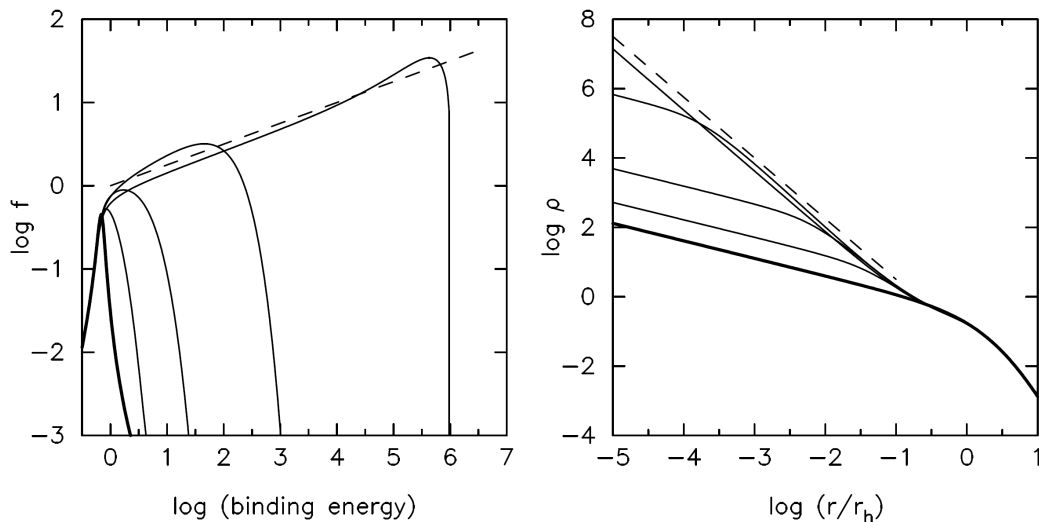
means that encounters in which stars collide with each other are neglected;

- the small-angle approximation: the gravitational potential belongs to a particular class of interactions for which the net force experienced by a test particle surrounded by a population of other bodies with which it interacts, is mainly due to cumulative, weak encounters with particles far away, rather than to strong but infrequent interactions with close particles. If we call p_0 the impact parameter for the interaction that causes a deflection of 45° in the velocity of the test particle, all the close encounters with impact parameters $p \leq p_0$ count only for 4% of the total net deflection (Spitzer 1987). Working under the small-angle approximation means that, in the study of the evolution of a test particle with a velocity **v** embedded in a larger particle population, we are considering only the encounters with those bodies far away that will produce small deflections $\mathbf{\Delta v}$ compared to the initial velocity **v**;

- the distribution function does not depends on the angular momentum and, since the gravitational potential is function only of the radial coordinate, the stellar distribution is isotropic;

- the mass of the central BH is much larger than the mass of a star and does not change with time, so that inside the influence radius, the gravitational potential is constant and Keplerian and is due only to the BH itself. Under this assumption we can (as in Equation (72)) neglect the term proportional to $\partial f/\partial E$ that would appear in a more complete

form of the Fokker-Planck equation. Moreover the BH mass has to be much smaller than the total stellar mass near the BH itself. Requiring this particular mass hierarchy (Bahcall & Wolf 1976), leads us to a consequent timescale hierarchy, i.e., the assumption $m_\star \ll M_\bullet \ll M_\star(r < r_h)$ implies that the crossing time t_{cr} (the time needed for a star to cross the nucleus) is much shorter than the relaxation time, so that in a crossing time stars do not experience any changes in the physical proprieties of the system.

All the assumptions listed above can also be satisfied in the case of a distribution of DM particles only (with a common mass m_χ), so that a Fokker-Planck formalism is appropriate also for DM. We expect the existence of a relaxed solution also in this case, but the relaxation timescale for DM is enormously larger than for stars and DM particles will never reach their steady-state solution: they can be effectively considered as collisionless objects, pratically not sensitive to the gravitational self-interactions that drive the dynamical evolution described by the Fokker-Planck equation.

The requirement of a common mass for particles (stars or DM) is not included in the list above, because in the more realistic case of a nucleus with particles of different mass, Equation (72) can be modified in order to describe a multi-mass case. For a two-component nucleus, made of stars (with a common mass $m_\star$) and DM particles with $m_\chi \ll m_\star$ the Fokker-Planck equations will be the following:

$$4\pi^2 p(E)\frac{\partial g_\star}{\partial t} = \frac{\partial}{\partial E}\left(-m_\star D_E g_\star - D_{EE}\frac{\partial g_\star}{\partial E}\right), \tag{76}$$

$$4\pi^2 p(E)\frac{\partial g_\chi}{\partial t} = \frac{\partial}{\partial E}\left(-D_{EE}\frac{\partial g_\chi}{\partial E}\right), \tag{77}$$

with

$$g_i(E, t) = \int_0^\infty f_i(E, t, m)m \, dm, \tag{78}$$

$$h_i(E, t) = \int_0^\infty f_i(E, t, m)m^2 \, dm, \tag{79}$$

with $i \in [\star, \chi]$, and the diffusion coefficents can be written as

$$D_{EE}(E) = 64\pi^4 G^2 m_\star \ln\Lambda\left[q(E)\int_{-\infty}^E dE' g_\star(E') + \int_E^0 dE' q(E')g_\star(E')\right], \tag{80}$$

$$D_E(E) = -64\pi^4 G^2 \ln\Lambda \int_E^0 dE' p(E')g_\star(E'). \tag{81}$$

$f_\star$ is the stellar distribution function, whose evolution (Equation (76)) is governed by star-star interactions, and f_χ is the distribution function for DM and in Equation (77) only DM-star encounters are considered due to the collisionless nature of DM.

The final steady-state solutions will have the usual $-7/4$ slope for stars (in fact Equation (76) is not different from Equation (72)) and a milder $-3/2$ slope for DM, that will be established in the same timescale t_{rel} (Equation (68)). The steeping of the initial profile, due to the presence of a BH, leads to an increase of the DM annihilation rate. This is why we refer

to BHs as *DM Annihilation Boosters*. The predicted profile $r^{-1.5}$ is steeper than what can be found for models without BHs (see Section 12.1) but it is more likely that the overdensity will be reduced in a couple of relaxation times (see Merritt et al. (2007) and Section 14.2), we will see cases in the next sections where BHs can provide huge boost factors.

The presence of a stellar cusp has been experimentally confirmed for the MW (Genzel et al. 2003, Schodel et al. 2007), through the detection of a profile with a slope equal to $-1.4 < \gamma < -1.3$ in the inner region ($r \lesssim 0.38$ pc) and to -2 (isothermal profile) in the outer region (see Figure 26). Our Galaxy is a collisional nucleus, since the relaxation time is shorter than the age of the Universe (3.5×10^9 yrs at $\approx 0.1 \; r_h$), so it was suggested to interpret its cusp as the Bahcall-Wolf solution to the presence of a SMBH with a mass $\approx 3.7 \times 10^6 M_\odot$ (r_h is ≈ 3 pc so that the cusp starts more or less where $r = 0.1 \; r_h$), hypothesis supported also by the luminosity of the X-ray source Sgr A*. Anyway, it is more likely that the MW experienced a merger between a redshift $z = 2$ (Merritt et al. 2002) and today, so the cusp will be the result of an *overdensity regeneration* (see Section 14.2). The actual, detected profile (Merritt & Szell 2006) is consistent with a cusp regenerated after a merger occured at a time $\gtrsim 8$ Gyr in the past.

The detected inner slope of -1.4 is not exactly what the Bahcall-Wolf solution predicts ($\gamma = -1.75$). However, the two results are considered as consistent with each other since the steeper value is derived under the simplyfing assumption of a population of stars with identical mass, and if the more realistic multi-mass formalism is introduced, the slope will become shallower, moving towards the -1.4 value. The same can be said if, as it was argued (Merritt & Szell 2006), the time required to reach a steady-state solution at the Galactic center is $\gtrsim 10^{10}$ yr.

### 13.2. Loss-cone dynamics and BH binaries

In this section, I will focus (following Fornasa & Bertone (2008) on two mechanisms that can reduce, and even completely destroy, collisional cusps.

First of all, in our paper we reviewed the basics of *loss-cone* dynamics, i.e. the effects related to the presence of a BH tidal radius or of the relativistic event horizon. This is only partially relevant for DM since it will affect mainly the stellar population, but it is relevant in this contest since we have just seen (Equation (77)) how stars and DM evolve together, so that a decrease in the stellar cusp due to loss-cone (Merritt 2006*a*) will influence the DM density, too. Moreover I want to emphasize that any enhancement in the density of DM and stars has to survive to a collection of dynamical mechanisms that can damp them.

After discussing the loss-cone, we focused on the possibility that, during the merging evolution of a nucleus, a BH binary forms. In this case, both stellar and DM distributions will be directly affected (Merritt 2006*b*), leading not only to the reduction of cusps but also to the possible destruction of spikes in models with adiabatic growth (Merritt et al. 2002) (see Section 14.1).

The loss-cone of a BH is the set of eccentric orbits populated by stars that are going to intersect the tidal radius. Such orbits are depleted in a crossing time t_{cr}, since stars are

Figure 26. Mass density profiles near the centers of the MW and M32. Dashed line is $\rho(r) \propto r^{-1.5}$. Both galaxies contain SMBHs with masses $\sim 3 \times 10^6 M_\odot$ and with influence radii $r_h \approx 3$ pc. Taken from Merritt (2006*a*).
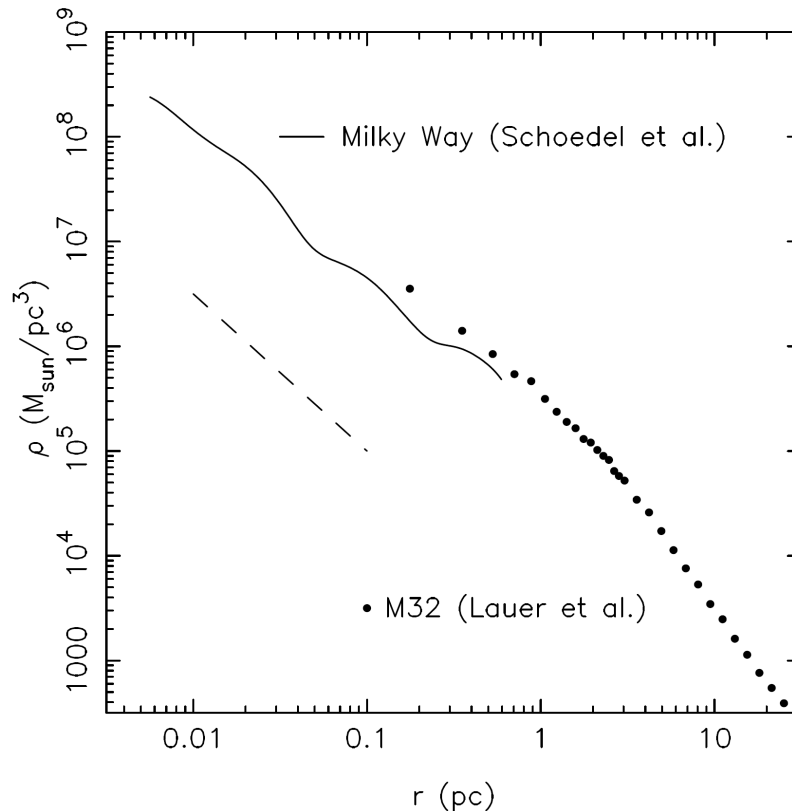
eaten up by the BH: tidal forces inside the tidal radius tear a star apart and these events are accompanied by flares, emissions of light peaked in the X or UV band with a luminosity of $\approx 10^{44}$erg s^{-1}. A handful of these flares have been observed: they have the expected signature and the number of detections is roughly consistent with theoretical estimates of the consumption rate $\dot{N}$ (Komossa et al. 2004, Komossa et al. 2004, Halpern et al. 2004, Wang & Merritt 2004)

Once depleted, loss-cone orbits can continue to contribute to the consumption rate only if they are somehow refilled with particles. Energy diffusion provides a mechanism for such a repopulation. In fact, *N*-body simulations confirmed (Merritt 2006*a*) that the zero-flux Bahcall-Wolf solution is established only approximately and that (for stars) there is a residual flux $F(E) \propto r_t^3/t_{rel}(r_t)$.

This value is too low compared to the expected $\dot{N}$ whose main contribution comes, instead, from angular momentum diffusion: the "classic loss-cone theory" (Frank & Rees 1976, Bahcall & Wolf 1976, Cohn & Kulsrud 1978) applies to globular clusters (populated with a central BH), whose relaxation time is so low that they are well-relaxed and old objects. The distribution of stars near the BH is therefore assumed to be on a steady-state, for which a Fokker-Planck-like formalism is appropriate. Resulting estimates for the consumption flux

can be introduced in the original Fokker-Planck equation (see Equation (72)) to study how particle density is affected by the presence of a tidal radius:

$$4\pi^2 p(E)\frac{\partial f}{\partial t} = -\frac{\partial F_E}{\partial E} + \rho_{lc}(E,t). \tag{82}$$

When extended to the study of galactic nuclei, the steady-state approximation may fail, at least for collisionless nuclei, and the stellar profile near the tidal radius is, in general, different from the Bahcall-Wolf one. For example, galaxies are only approximately spherical: their shape is more likely to be triaxial and there is the possibility that they are governed by centrophillic orbits, i.e. orbits that pass arbitrarily close to the BH. In the case that these chaotic orbits survive until late stages in the galactic evolution, $\dot{N}$ would increase, since more particles would fall into the tidal sphere.

Alternatively, the present galaxy can be the result of cumulative mergers of less massive mini-galaxies, each of them hosting a mini-BH: the formation of a BH binary would decrease the consumption rate, since all stars with angular momentum $L \lesssim L_{bin} = (2GM_{12}a_h)$ would be ejected (Wang & Merritt 2004) (M_{12} is the total mass of the binary and a_h the major semi-axis when the system becomes "hard"), preventing loss-cone repopulation and leading to lower rates $\dot{N}$.

Finally, in real galaxies, the diffuse mechanism of orbits refillment will cause the nucleus to expand (Merritt 2006a, Freitag et al. 2006, Murphy et al. 1991, Baumgardt et al. 2004), since the density is reduced when particles are eaten up and those particles which fall into the loss-cone transfer energy to the remaining nucleus with the same effect of a heating process. The expansion is visible in one single relaxation time, the "decay" goes on at a constant velocity and the density can be written as $\rho(r,t) = \rho_c(t)\rho^*(r)$, where $\rho^*(r)$ is the initial profile, while $\rho_c(t) \propto t^{-1}$. As a consequence, present-day collisional nuclei could have been denser in the past.

It has been suggested that also the presence of a BH binary can effectively reduce the Bahcall-Wolf cusp. The growth of a galaxy is thought to pass through the agglomeration of smaller galaxies and protogalactic fragments. If more than one of these subhalos contain a BH, the two objects will form a binary system whose dynamics can strongly affect stars and DM. This scenario has received great attention since mergers and the ultimate coalescence of the BH binary are ideal targets for the detection of gravitational waves (Thorne & B. 1976). Evidences for the presence of such binaries can be found in Komossa et al. (2003) and are based on the detection of multiple active nuclei in the same galaxy (Rodriguez et al. 2006).

Consider a compact object with mass M_2 moving, with its nucleus, around a BH with mass M_1, being $q = M_2/M_1 < 1$ the mass ratio and M_{12} the total mass. The evolution of the binary can be described by three different phases (Merritt 2006b, Merritt 2006a) (see also Figure 27): first, the smaller BH decays due to the dynamical friction with stars of the other nucleus, and the separation R_{12} between the two objects drops down. When the influence radius r_h of the more massive BH is reached, the two objects can be considered as a bound object and the first phase comes to an end. The infall time scale (Merritt 2006a) suggests that binaries are not so uncommon since, for reasonable values of q ($q \approx 10^{-3}$ and $M_1 \approx 10^8 M_\odot$), they are able to form before the Hubble time.

Figure 27. Evolution of the binary separation in 5 *N*-body simulations with the density inner slope equal to −1.5 and 2×10^5 particles. Binary mass ratios are, from left to right, 0.5, 0.25, 0.1, 0.05 and 0.025. Vertical lines show the time defined as t_{stall}. The upper horizontal line indicate the influence radius of the more massive BH in the initial model. The lower horizontal lines indicates $a_h = q/(1 + q)^2 \times r_h/4$. The rapid phase of decay continues as $a \sim a_h$ with the result that the binary binding energy at the end of this phase is nearly independent of M_2. Taken from (Merritt 2006*b*).
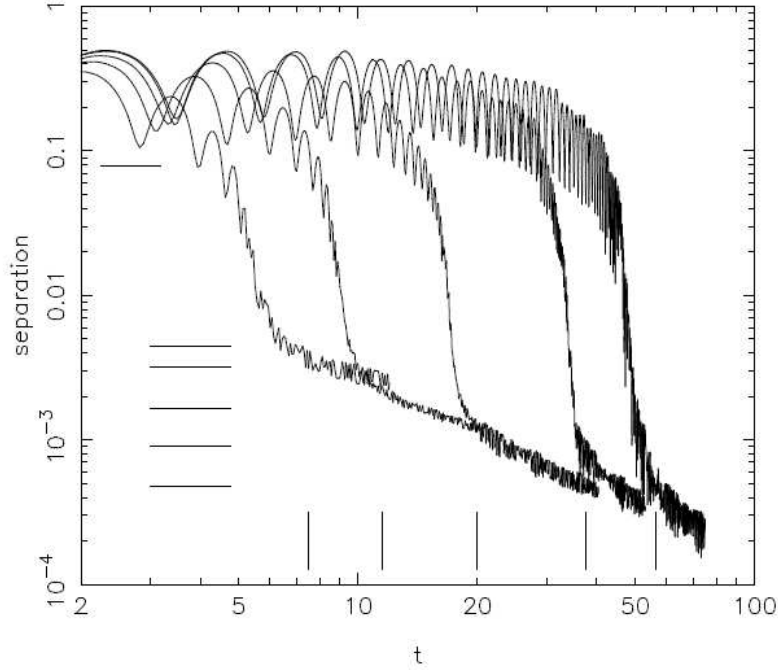
The second phase is characterized by a quick "shrinking" of the binary, until it becomes *hard*, i.e. the binding energy equals the kinetic energy, or equivalently the major semi-axis reaches $a_h = q/(1 + q)^2 \times r_h/4$ (Merritt 2006*b*). The third phase, when $a \lesssim a_h$, is the least known: a binary in a fixed background begins to harden at a constant hardening rate $s = d(1/a)/dt$, but physical binaries has already ejected almost all stars on intersecting orbits and the rate suddenly drops. These orbits need to be repopulated, usually by energy diffusion, but this effect is more likely to be only subdominant, at least in those bright galaxies where the scouring of BH binaries has been detected, characterized by a relaxation time higher than the Hubble time. In numerical simulations with finite *N*, gravitational encounters will unphysically continue to supply particles to the binary at rates roughly proportional to *N*, so experimentally it is more usefull to define the semi-major axis a_{stall} where the hardening rate goes to zero (Merritt 2006*b*). From *N*-body simulations it results

$$\frac{a_{stall}}{r'_h} = 0.2 \frac{q}{(1 + q)^2}, \tag{83}$$

r'_h is a second influence radius, defined as the radius where the total mass of particles within r'_h after the binary has stalled is equal to twice M_{12}. This values for a_{stall} is a couple of orders of magnitude higher than the distance where the binary coalescences. This is

known as the "final parsec problem", since evidence is strong that BHs binaries do eventually coalescence (Rodriguez et al. 2006, Merritt & Ferrarese 2001). Many solutions have been proposed (Gualandris & Merritt 2007*a*), e.g. that, as for loss-cone orbits, the presence of centrophillic orbits in realistic triaxial galaxies can affect the above considerations, so that the binary continues to shrink even to $a \lesssim a_h$.

Assuming that the binary does stall at a_{stall}, it will have transferred an energy

$$\Delta E \approx -\frac{GM_1M_2}{2r_h} + \frac{GM_1M_2}{2a_h} \approx -\frac{1}{2}M_2\sigma^2 + 2(M_1 + M_2)\sigma^2 \approx 2(M_1 + M_2)\sigma^2, \quad (84)$$

to the particles in the nucleus. This relation has been used to explain the mass deficit in the core of brightest galaxies since such an energy release will let stars leave the central core, with a total displacement of mass M_{def} and $0.4 \lesssim M_{def}/M_{12} \lesssim 0.6$ (Merritt 2006*b*) for $0.05 \lesssim q \lesssim 0.5$.

Strictly speaking, the observed mass deficits M_{def} reach values that are even four times larger than the mass of the binary M_{12} (that, if the coalescence occurs, is also the mass of the final BH). We can account for values as large as $M_{def}/M_{12} \lesssim 2$ if the nucleus experiences more than one merger, with more than one binary forming. The total mass displaced will be simply the sum of each M_{def} during each single merger. For even larger values, other mechanisms have to be evoked, e.g. the possibility that a third BH arrives when the first two have not coalescenced yet. In such a situation, one of the BH usually leaves the nucleus (*gravitational slingshot* effect) leading to higher values for M_{def}. Similarly one of the SMBH of a BH binary can be expelled with a high velocity, due to the so-called *gravitational-wave rocket* effect (Gualandris & Merritt 2007*b*).

14. Adiabatic growth of Black Holes

In this section the assumption of time-independent gravitational potential will be relaxed. As we will see, this can, in some cases, lead to large DM overdensities. In particular, the adiabatic growth of BHs can produce the steepest DM profiles discussed in literature.

The seed BH grows in an already-formed nucleus with a stable (stellar or DM) population. The condition of adiabaticity guarantees that the growth timescale is larger than the crossing time, but smaller than the relaxation time (for the stellar distribution). As a consequence, nuclei where a BH have grown adiabatically have not yet reached a stable, relaxed stellar configuration. Another consequence (Binney & Tremaine 1987) is that the angular momentum and the radial action (i.e. $J_r = \oint v_r dr$, where v_r is the radial velocity and the integral is over one closed orbit) are conserved. The hierarchy between the BH accretion timescale and the nuclear crossing time, that lies at the core of the adiabatic assumption, is reasonable at least for BHs with masses $M_\bullet \lesssim 10^{10}M_\odot$, as can be checked adopting the shortest timescale for the BH growth, i.e. the Salpeter time $t_s = M_\bullet/\dot{M}_{Edd}$ (where $\dot{M}_{Edd}$ is the Eddington accretion rate), and comparing it with the crossing time at the influence radius $t_{cr} \propto M_\bullet\sigma/r_h$, using the $M_\bullet - \sigma$ relation (see Equation (71)).

The first study on the impact of adiabatic growth (Young 1980) on stars, analyzed the case of a non-singular isothermal stellar profile, and predicted an overdensity extending to the same

Table 7. Different quantities computed from the adiabatic growth of the initial models proposed by Sigurdsson et al. (1994). γ and γ_{sp} are the initial and final slope in the density profile for the region closer to the BH. n indicates how the distribution function diverges as $E \to \Phi(0)$ and C is the slope of the final density profile if it were made of particles on circular orbits. The value for n in the $\gamma = 2$-model is absent since the equation used to derive n is not valid for $\gamma = 2$, but for $\gamma \to 2$ the final profile has $\gamma_{sp} \to 5/2$.

Model	γ	n	γ_{sp}	C
isothermal	0	0	3/2	9/4
γ model ($\gamma = 0$)	0	1	2	9/4
γ model ($\gamma = 1$)	1	5/2	7/3	7/3
γ model ($\gamma = 3/2$)	3/2	9/2	12/5	12/5
γ model ($\gamma = 2$)	2		5/2	5/2

size of the initial core, with a slope equal to $-3/2$. In the case of a DM halo, such overdensity has been called *spike* (Gondolo & Silk 1999), to distinguish it from the aforementioned DM cusps.

A numerical algorithm that mimic adiabatic growth was also developed, in order to confirm the creation of the overdensity (Sigurdsson et al. 1994). The method is very flexible and, in fact, it was applied to initial models other than the isothermal distribution (Sigurdsson et al. 1994). Two classes can be identified: the first includes all those profiles called "analytic cores", characterized by a density that can be expanded in a power-law series near the BH ($\rho(r) \approx \rho_0 + 1/2\rho_0'' r^2 + \ldots$), while the second describes the so-called γ models that exhibit a power-law density profile in the inner region: $\rho(r) \propto r^{-\gamma}$.

As benchmark cases, the γ models with $0 \leq \gamma \leq 2$ and the isothermal model (as an example of analytic profiles) are considered here, and results are presented in Table 7 and in Figure 28 (MacMillan & Henriksen 2002) (only for the isothermal and for $\gamma = 1$).

The spike radius r_{sp}, i.e. the distance where the slope changes due to the presence of the BH, depends on the BH mass and it is related to the influence radius as $r_{sp} \approx 0.2\, r_h$ (Merritt 2003). Inside such radius, the spike has a slope γ_{sp}, that depends on the initial γ. In the case of a model with analytic core the final slope is $-3/2$ (Young 1980), while for the γ models an analytic relation holds (Peebles 1972, Sigurdsson et al. 1994, Ullio et al. 2001):

$$\gamma_{sp} = \frac{9 - 2\gamma}{4 - \gamma}. \tag{85}$$

Such relation is valid under the following assumptions (satisfied by all the models in Sigurdsson et al. (1994)):

- the distribution function is isotropic;
- the gravitational potential can be written as $r^{2-\gamma}$ in the $r \to 0$ limit;
- f diverges as $[E - \Phi(0)]^{-n}$ in the limit $E \to \Phi(0)$ (this last requirement is what makes a model with analytic core different from a γ model).

Comparing the first two lines in Table 7, it can be seen that, even if both models start with a costant core, they develop very different final spikes, due to the different behaviour of the

Figure 28. Adiabatic growth in the isothermal (*left panel*) and for a $\gamma = 1$ (*right panel*) model for a value of $M_\bullet$ of 0.001, 0.01, 0.1 and 1.0 (mass units explained in MacMillan & Henriksen (2002)), with the mass encreasing from bottom to top in the top two panels and from top to bottom in the last panel. The density is shown in the top frame, the averaged radial velocity in the middle and the anisotropy parameter β in the last frame. $\beta = 1 - \langle v_t^2 \rangle / \langle 2v_r^2 \rangle$ where v_t (v_r) is the tangential (radial) component of velocity. Taken from MacMillan & Henriksen (2002).
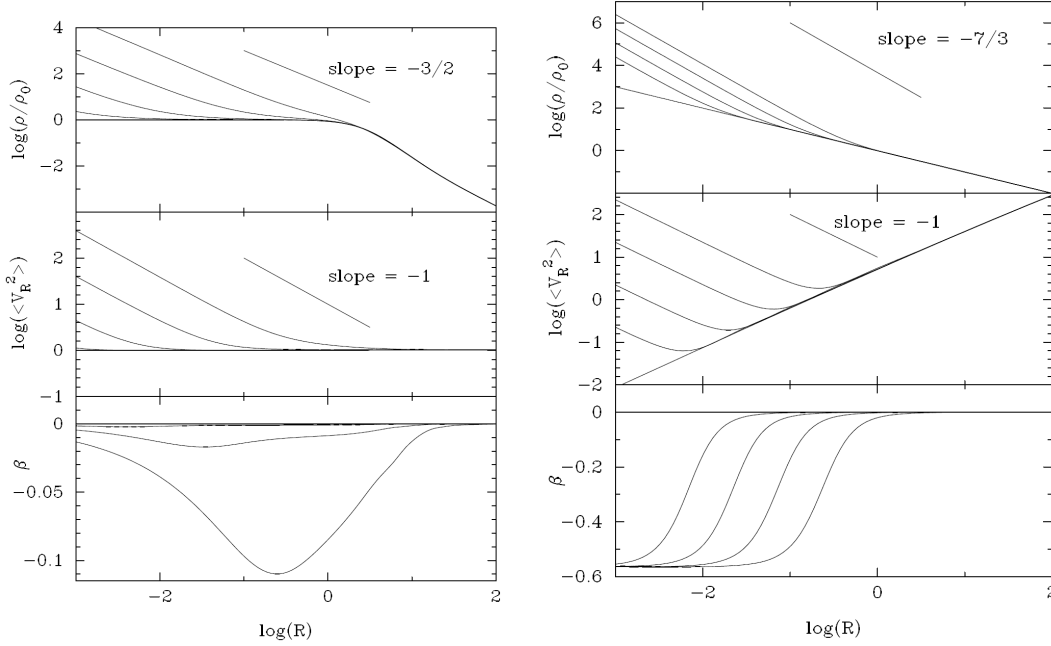
distribution functions in the $E \to \Phi(0)$ limit, suggesting that the formation of a strong spike is not a consequence of a singularity in the density profile but in the distribution function, and in particular in the way cold orbits (populated by stars with a low velocity) are arranged (see Section 14.1). We will not consider initial configurations with γ larger than 1 (see Section 12.1), so the steepest spike has a slope of $-7/3$ (when $\gamma = 1$).

The velocity dispersion reacts to the BH growth in a similar way for both classes of initial models: in fact, a Keplerian rise appears, with a slope of $-1/2$. On the contrary, the anisotropy is substantially different: analytic models exhibit a mild tangential anistropy at an intermediate distance from the BH but remains isotropic at the center; the more massive the BH is, the higher the anistropy. While for γ models, orbits are tangentially-biased in the central region and the anisotropic area increases with more massive BHs. If the hypothesis of an isotropic distributions is relaxed, a nucleus made interely by circular orbits evolves to a profile with final slope equal to C, shown in Table 7. As one can see, for γ models $\gamma_{sp} = C$, while the circular isothermal model exhibits a much steeper slope, although with a value not higher than for the γ models. Such consideration suggests that results from adiabatic growth are not very sensible to possible violations of isotropy in the initial configuration.

Even if spikes are the steepest known overdensities, they cannot be considered as signatures of BH growing adiabatically, since a simple singular isothermal profile that nothing

has to do with adiabatic growth is steeper than half of the models in Table 7. On the contrary, a rise in the σ profile is quite a robust indication of the presence of a central, compact object.

14.1. Destruction of spikes

The formation of spikes described in the previous section leads to the largest annihilation boost factors: the mechanism of adiabatic growth can, in fact, produce inner slopes as steep as -2.3 (see Table 7), for profiles that will be characterized by a large annihilation flux (which is proportional to the integral of the DM density squared), with interesting consequences for indirect DM searches.

However, it has been argued (Ullio et al. 2001, Bertone & Merritt 2005, Merritt et al. 2002) that the formation of spikes requires *ad hoc* initial conditions for the DM halo. Moreover, even if spikes do form, then, dynamical effects can reduce or even destroy them, as we considered before for collisional cusps. A spike can form even from an initial density profile that does not diverge (Ullio et al. 2001), but in order to produce a significant overdensity, the distribution function of cold orbits has to diverge in the $E \to \Phi(0)$ limit. In fact, cold orbits are those which provide the particles that will form the spike, since they are the most affected by the presence of the central BH.

But these cold orbits are more likely to be depleted due to the interactions of stars with molecular clouds or globular clusters or other bodies that can pass through a galactic nucleus. Moreover, the evolution of a galactic nucleus is thought to be characterized by the cumulative mergers of sub-nuclei and even a single merger event can have dramatic consequences on the distribution of cold orbits. In other words, one can enumerate a collection of effects that effectively heat up the particles near the BH, so that they can leave the central region obstacling the formation of the spike.

Also in the case that the spike is formed, it is unlikely that it will survive to the evolution of the nucleus and, in particular to the presence of dynamical mechanisms that would provide an additional heating source to particles on cold orbits, with the result of highly reduce of even destroy the enhancement. Numerical simulations have been performed in order to quantify these effects: for example the possibility that the BH forms slightly off the center of the nucleus was described by Ullio et al. (2001). The BH would slowly spiral in, towards the center (Nakano & Makino 1999), and then adiabatically grow to the final value. But if the initial value for the BH mass is too low, the spiraling would take too long to finally reach the center, while, if the BH is too massive, its scouring effect on the DM particles would flatten the central density, to values that can be even lower than the initial profile (see Figure 29).

Moreover, gravitational interactions of DM particles with baryons in stars modify the evolution of DM in the spike, reducing the enhancement, in the same way that stars heat the DM particles in a collisional cusp causing its damping (see Section 14.2) (Merritt et al. 2007, Ullio et al. 2001). Simulations on the effects of galactic mergers can also be found in Merritt et al. (2002). Other objections have been put forward, suggesting that spikes can form only as results of a series of accidents and, therefore, are not expected to be common in the local Universe (Ullio et al. 2001).

Figure 29. Modification of a NFW DM density profile due to the off-center formation of a BH seed of mass M^S_{BH}, its spiral in the center of the DM system and its adiabatic growth to the present-day mass of the BH M_{BH} at the GC. The cases for a few different values of the BH seed mass are plotted. ρ_{core} is the maximum WIMP density above which WIMPs are depleted by pair annihilations. Taken from Ullio et al. (2001).
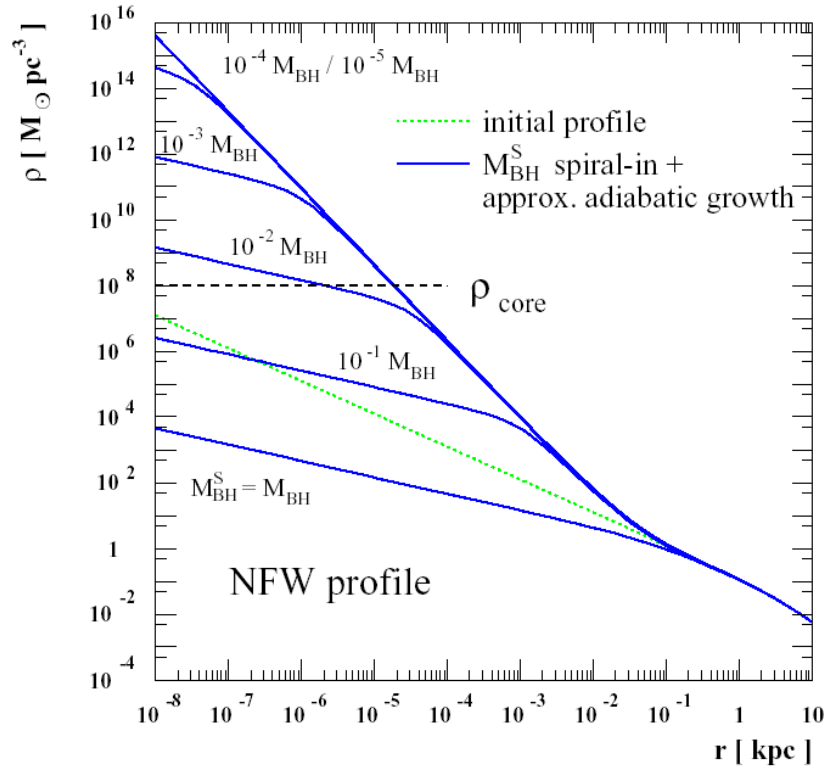
14.2. Regeneration of cusps

In the previous section I focused on the processes that can destroy overdensities (whether cusps or spikes). However, gravitational interactions among particles (during the evolution of the nucleus) can partially regenerate such structures. In a realistic nucleus populated by stars and DM, star-star collisions and star-DM collisions (given enough time) drive the evolution towards a steady-state $-7/4$ profile for the baryonic component and a $-3/2$ profile for the DM component (Merritt et al. 2007) (see Section 13.1). This is true also if the nucleus is the result of an early evolution phase in which previous enhancements were destroyed. In other words, consider a nucleus with a short t_{rel} and a steep DM and stellar profile (due to collisional relaxation or adiabatic growth of the central BH). If a merger occurs and a BH binary forms, the displaced mass will reduce or even destroy both overdensities. But, due to the short relaxation time, it can happen that the nucleus has enough time to reconstruct, from the core profile after the BHs coalescence, the collisional solutions. The new DM cusp is called CREST (Collisionally REgenerated STructure). This idea can be checked analitically, applying the two-body Fokker-Plack formalism to a core profile describing a nucleus after the scouring of a BH binary, but also with the help of numerical routines (Merritt et al. 2007).

Figure 30. Solutions of the Fokker-Planck solutions that describe the joint evolution of stars and dark matter around a BH due to star-star and star-DM gravitational encounters. Lenght unit is r_s and density is in units of initial value at r_h. Curves show the stellar (left) and DM (right) density profiles at time 0, 0.2, 0.4, 0.6, 0.8, 1.0 in units of the initial relaxation time at r_h. Dashed lines are the steady-state solutions. Taken from Merritt et al. (2007).
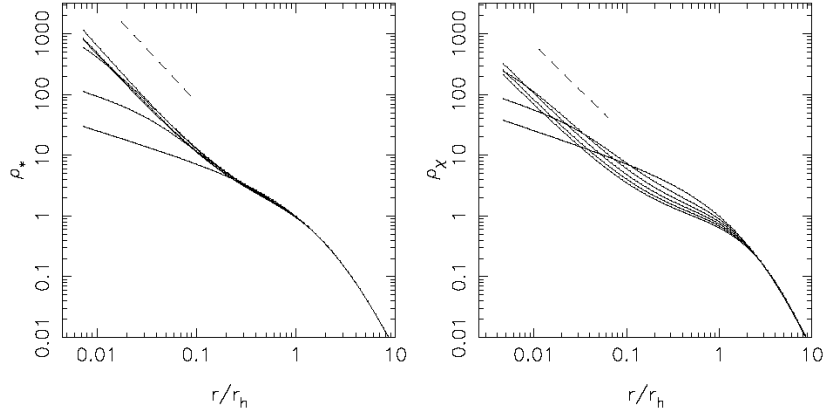
Results are summarized in Figure 30: DM CRESTs are not as steep as spikes, but they have the advantage to form from very general initial profiles, given that the (stellar) relaxation time is short enough. They need a timescale of roughly $t_{rel}(0.2\, r_h)$ to form, but then DM particles in the CREST continue to be heated by gravitational interactions with stars and the $-3/2$ solution, therefore, decays in a self-similar way

$$\rho_\chi(r,t) \approx \rho_{\chi,0}(r)G(t/t_{rel}), \tag{86}$$

with $dG/dt < 0$, so that after 4.5 $t_{rel}(r_h)$ the reduction is of a factor $1/e^2$.

The balance between the requirement that the relaxation time is short enough to let the CREST form but not too short to make the CREST not to decay too much, leaves us with a rather narrow window of galaxies where CRESTs can be present: one can detect them in galaxies with a luminosity $3 \times 10^8 L_\odot \lesssim L \lesssim 3 \times 10^9 L_\odot$. The MW is inside this range and, in fact, many proposed to interpret the cusp detected for our Galaxy (Schodel et al. 2007) as a reconstructed structure after a merger occured ~ 8 Myr ago (Merritt & Szell 2006).

Chapter V:
Intermediate Mass
Black Holes

15. Intermediate Mass Black Holes and their formation scenarios

The steep DM slopes produced by the adiabatic growth of BHs make these objects extremely interesting since they may effectively act as DM Annihilation Boosters. This circumstance encouraged many authors to look for possible ways to evade the dynamical effects causing spikes to damp.

Two possibilities have been proposed: the first is to focus on IMBHs instead than of SMBHs. IMBHs can be present within substructures of DM halos (Koushiappas, Bullock & Dekel 2004, Miller & Colbert 2004) and their evolution is such that the objections raised for spikes around SMBHs do not apply (Bertone, Zentner & Silk 2005). The second is considering the contribution of spikes and mini-spikes (i.e. DM overdensity around IMBHs) to the diffuse EGB integrating the signal from high redshift, i.e. when spikes were already formed but destruction mechanisms were not yet effective (Ahn et al. 2007, Horiuchi & Ando 2006, Ando 2005).

I am going to focus on IMBHs first, while the discussion on how compact objects can contribute to the CGB will the subject of Section 18.

IMBHs masses range from $\approx$ 20 to $10^6 M_\odot$, where the lower limit is derived in Fryer & Kalogera (2001) considering the most massive remnant of a stellar collapse and the upper limit is usually assumed as the lowest mass for a SMBH (Ferrarese & Ford 2004). There is no direct observational evidence for the existence of IMBHs but some hints come, e.g., from Ultra Luminous X-ray sources (ULXs) (Swartz et al. 2004), sources that emit in the X band with a luminosity higher than 10^{39}erg s^{-1}, and, hence, not compatible with the interpretation as BHs accreting at the Eddington limit. But, due to their positions in the host galaxy, they cannot be explained in terms of AGNs either. The hypothesis of a BH with a mass higher than $15 - 20 \ M_\odot$ and less massive than a SMBH seems to be a fair explanation, instead.

Many authors also proposed that globular clusters can host IMBHs, and a possible confirmation of such idea comes from the fact that the mass scale for an IMBH and the value of the stellar velocity dispersion measured in globular clusters, fall exactly at the extrapolation at lower values of the $M_\bullet - \sigma$ relation valid for SMBHs (Miller & Colbert 2004). From a theoretical point of view, IMBHs can also help to explain the formation of SMBHs: the Sloan Digital Survey (Fan et al. 2001, Barth et al. 2003, Willott et al. 2003) has detected quasars up to redshift $z \approx 6$ suggesting that SMBHs were already present when the Universe was ~ 1 Gyr old. One of the most natural way to understand this is that SMBHs grew, through a phase of fast accretion and mergers, starting from already massive seeds. In fact, a generic prediction of scenarios that seek to explain the properties of the observed SMBH population, is that a large number of "wandering" IMBHs exist in DM halos (Islam et al. 2003, Volonteri et al. 2003, Koushiappas, Bullock & Dekel 2004).

Despite their theoretical interest, it is difficult to obtain conclusive evidence for the existence of IMBHs. A viable detection strategy could be the search for gravitational waves produced in the mergers of the IMBHs population (Thorne & B. 1976, Flanagan & Hughes 1998*b*, Flanagan & Hughes 1998*a*, Islam et al. 2004, Matsubayashi et al. 2004, Koushiappas, Bullock & Dekel 2004), with space-based interferometers such as the Large Interferometric

Space Antenna LISA (http://lisa.nasa.gov/).

Two formation scenarios will be discussed here following Bertone, Zentner & Silk (2005). In the first (scenario A), IMBHs form from the gravitational collapse of Population III stars, that are usually heavier than local stars, since they grow in an environment with very low metallicity, for which metal line cooling can be neglected. As a consequence the Jeans mass (that scales with the temperature as $T^{3/2}$) is higher, allowing the formation of more massive structures. Such stars are characterized by very low metallicity, too, meaning that they will lose little of their mass due to winds and weak pulsations. Population III stars with masses above larger than 250 $M_\odot$ would be able to collapse directly to BHs without any explosion (Miller & Colbert 2004). The evolution timescale of these very massive stars is of the order of $1 - 10$ Myrs and it should be noticed that, in this scenario, the IMBH (which will have a mass of the order of $10^2 M_\odot$) can form not exactly at the center of the DM distribution within which the stellar collapse occurs.

I will mainly focus on the second formation scenario (scenario B) proposed by Koushiappas, Bullock & Dekel (2004). In this case the formation starts at high redshift ($z \approx 15$) where halos can be thought as overdensities made of DM and baryons, that grow by gravitational interactions. These structures can also acquire angular momentum through tidal torques. The fate of the two matter component begins to diverge when the baryonic gas cools down (cooling mechanisms can be, e.g., atomic line cooling for larger halos or molecular hydrogen cooling for smaller ones) while the DM component reaches the kinematic equilibrium forming a spheroidal distribution that embeds the baryons. At this stage of the evolution the main obstacle for BH formation is the centrifugal barrier, since the total baryonic mass centrifugally-supported is many orders of magnitude larger in size than the corresponding Schwarzschild radius. Koushiappas, Bullock & Dekel (2004) assumed that both baryons and DM are characterized by the same angular momentum distribution taken by Bullock et al. (2001a) and the effect of cooling is the formation of a pressure-supported disk made by the particles in the low-momentum tail of the angular momentum distribution.

If the original halo is massive enough, the disc will be affected by an effective viscovity, due to gravitational instabilities causing an inward mass flow and a consequent outward angular momentum flow. This process will terminate when the system experiences a major merger with another halo or the disc starts to fragmentate. The angular momentum transfer and the inward flow will allow a central massive object to form. It will be pressure-supported and short-lived and will very shortly collapse to the final BH.

Figure 31 shows the lower halo mass needed for the disc to form and for the effective viscosity to be triggered on, as a function of the redshift. We see that the values are not very sensitive to the redshift and the mass scale is around $10^7 - 10^8 M_\odot$.

The mass of the final IMBH depends on the details of the halo evolution (the angular momentum distribution, the ratio of baryons to DM in the halo, the exact redshift of formation of the halo and so on) and in particular depends on how long the viscosity is able to trasfer baryonic matter to the center of the halo: Koushiappas, Bullock & Dekel (2004) estimated that the mass of the final IMBH will be follow a log-normal distribution with a variance $\sigma_\bullet = 0.9$

Figure 31. The minimum mass M_v^{crit} of a halo capable of forming a seed BH as function of redshift. The thick solid line refers to the angular distribution assumed in Bullock et al. (2001a) (B01). The thin solid line marked $\xi = 1.3$ refers to a modification to the B01 distribution (see Koushiappas, Bullock & Dekel (2004) for more details). The dotted lines correspond to $2-8\sigma$ fluctuations in the random fluctuaction field, illustrating that the minimum masses of concern are rare systems. The short-dashed line represent the minimum mass for atomic line cooling only and the long-dashed line is an approximation for the molecular hydrogen cooling. Taken from Koushiappas, Bullock & Dekel (2004).
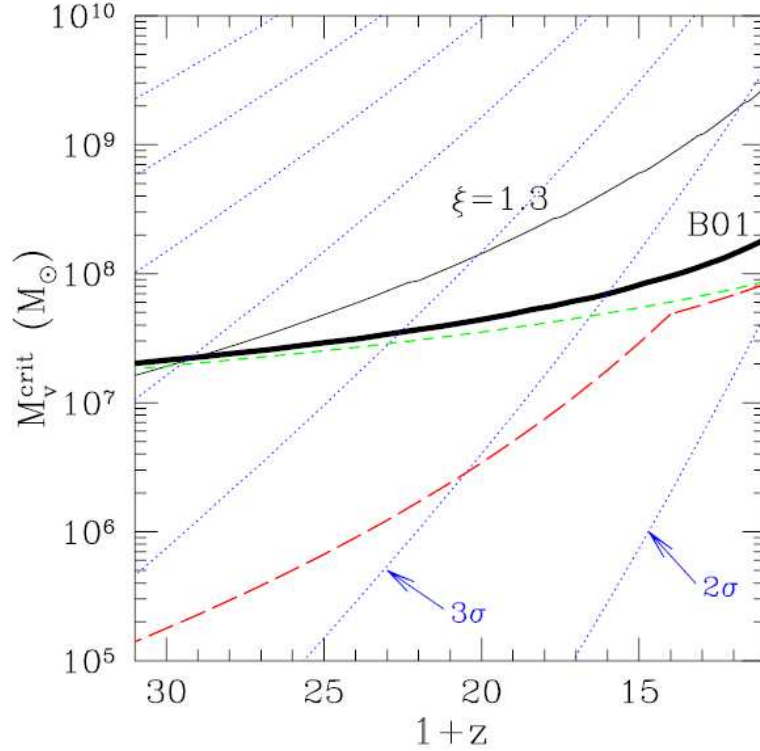
around a mean value depending on the characteristic of the system as follows:

$$M_\bullet = 3.8 \times 10^4 M_\odot \left(\frac{\kappa}{0.5}\right)\left(\frac{f}{0.03}\right)^{3/2}\left(\frac{M_{vir}}{10^7 M_\odot}\right) \times \left(\frac{1 + z_f}{18}\right)^{3/2}\left(\frac{t}{10\ \mathrm{Myr}}\right). \qquad (87)$$

f is the fraction of the total baryonic mass in the gas cloud that has cooled into the disc, κ is that fraction of the baryonic mass of the disc that forms the final BH, M_{vir} is the halo virial mass, z_f is the redshift when the formation starts from the cloud and t the timescale for the evolution of the first generation of stars which estimates the viscous timescale.

The today population of IMBHs can be estimated, as done by Bertone, Zentner & Silk (2005), in the following way:

- scenario A: the halos that correspond to a density fluctuation larger than 3σ at $z = 18$ are populated with a seed BH with a mass of $100\ M_\odot$. These halos will evolve and merge with each other forming the massive halos in which galaxies and clusters of galaxies are embedded. At the same time, the seed BH merge together forming the

Figure 32. Mass function of unmerged IMBHs in scenario B for a MW halo at $z = 0$. The distribution is based on the average of 200 realizations of a halo of virial mass $M = 10^{12.1} h^{-1} M_\odot$, roughly the size of the MW. Taken from Bertone, Zentner & Silk (2005).
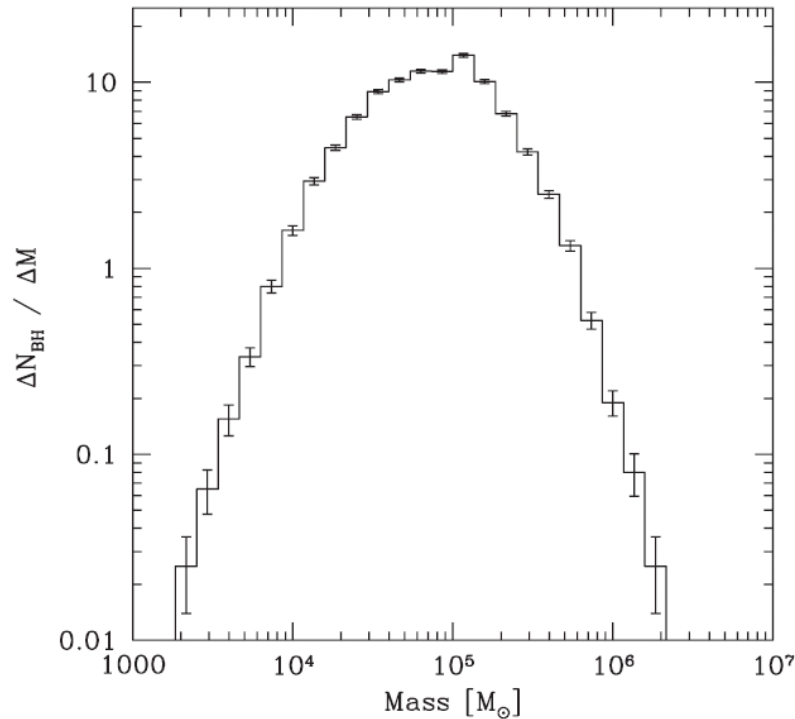
SMBH at the center of these massive structures. The halo growth and evolution models in Koushiappas & Zentner (2006), Zentner & Bullock (2003), Zentner et al. (2005) and Koushiappas, Zentner & Walker (2004) are modified to describe the formation of the MW and the primordial halos (with their seed BHs) are followed in their merging tree till the present epoch. Not all the subhalos merge: in some cases they can survive till today, appearing as wandering substructures in the MW halo and their BHs will constitute the today population of Galactic IMBHs. Bertone, Zentner & Silk (2005) evaluated the number of scenario A IMBHs in the MW to be (1027 ± 84), where the error is obtained considering 200 different realizations of the MW. All the IMBHs still have their initial mass of 200 $M_\odot$.

- scenario B: at high redshift only the halos beyond the threshold mass to host a pressure-support baryonic disc and to trigger the effective viscosity (see Figure 31) are populated with a seed BH having the corresponding mass $M_\bullet$ found using Equation (87). The same evolution procedure than with scenario A is considered and the mass spectrum of the unmerged IMBHs today is shown in Figure 32. The MW is supposed to host (101 ± 22) scenario B IMBHs.

16. Dark Matter annihilation around the IMBHs of the Milky Way

Regardless of the particular formation scenario, the mini-DM halo around the IMBH reacts to presence of the IMBH itself with the formation of a spike as described for SMBHs in Section 14. Bertone, Zentner & Silk (2005) considered the DM profile of mini-halos around IMBHs to be descrived by a NFW profile so that the mini-spikes will be characterized by a slope equal to $-7/3$ (see Equation (85)).

The mechanism of adiabatic contraction requires that the timescale for accretion is much larger than the evolution timescale: an assumption that is met for both the scenarios within r_h.

The problems that were presented in Section 14 related to the destruction of spikes, in the case of IMBHs can be evaded, at least for scenario B: IMBHs form exactly at the center of the baryonic distribution in the mini-halos, forbidding BH off-center formation. Strictly speaking, in order to avoid off-center formation, one should require that the pristine BH forms at the center of the DM distribution and this does not necessarily coincide with the center of baryons, since stars, been collisional, can experience a different evolution than the collissionless DM, resulting in a net displacement between the two distributions. But mini-halos are supposed to have a very low baryonic content, with no violent interactions able to drive the two distributions away one from the other: the fact that mini-halos are made almost entirely by DM solves the possible off-center formation and, at the same time, the problem related to stars-DM interactions. Moreover the IMBHs that are supposed to be present today in the MW halo, are those which survived the merging tree that lead to the formation of the MW and, thus, are not sensitivite to the effect of major mergings.

Similar considerations are possible for the scenario A IMBHs, with the only difference that in this case BHs are not bound to form at the center of the baryonic distribution, so that, finally, scenario B is able to circumvent all the mechanisms for spike destruction described above, while in scenario A they are reduced but still efficient: the former can be consider an optimistic description of IMBHs while, on the contrary, the latter is more conservative.

Indirect DM detection from mini-spikes around IMBHs populating the MW halo has been studied in Bertone, Zentner & Silk (2005). Equation (52) describing the annihilation flux has been re-written as:

$$\Phi = \int_{E_{\text{thr}}}^{m_\chi} dE \, \frac{d\Phi(E)}{dE} \tag{88}$$

$$= \int_{E_{\text{thr}}}^{m_\chi} dE \, \frac{1}{2} \frac{\sigma_{ann} v}{m_\chi^2} \frac{1}{d^2} \frac{dN_\gamma}{dE} \int_{r_{cut}}^{r_{sp}} \rho_{sp}^2(r) r^2 dr,$$

$$= \Phi_0 \frac{dN_\gamma}{dE} \left(\frac{\sigma_{ann} v}{10^{-26} \text{cm}^3 s^{-1}} \right) \left(\frac{m_\chi}{100 \, \text{GeV}} \right)^{-2} \left(\frac{d}{\text{kpc}} \right)^{-2} \left(\frac{\rho(r_{sp})}{10^2 \text{GeV cm}^{-3}} \right)^2$$

$$\left(\frac{r_{sp}}{\text{pc}} \right)^{14/3} \left(\frac{r_{cut}}{10^{-3}\text{pc}} \right)^{-5/3},$$

assuming that gamma-rays are detected above some energy threshold E_{thr} and that the mini-spike contribution (from r_{cut} to r_{sp}) dominates the annihilation flux of the mini-halo located at a distance d from us. The spikes extends from the *cut radius* r_{cut} to the spike radius $r_{sp} \approx 0.2 \, r_h$. The cut radius depends on the mass and the annihilation cross section of the DM

candidate, being defined as the radius where the DM density reaches an upper limit due to DM annihilations.

$\Phi_0 = 9 \times 10^{-10} \text{cm}^{-2}\text{s}^{-1}$ and indicates how large is the annihilation flux of an IMBH located at 1 kpc for a reference particle physics scenario with the DM mass equal to 100 GeV and an annihilation cross section of $10^{-26}\text{cm}^3\text{s}^{-1}$. The last line of Equation (88) is also useful to see how the flux Φ depends on the characteristics of the model: in particular, it is important to note that the dependence of the cut radius from the mass and the cross section of the DM candidate, modifies the usually behaviour $\Phi \propto \sigma_{\text{ann}} v / m_\chi^2$ so that, finally, the annihilation flux of a mini-spikes around an IMBH is proportional to $(\sigma_{\text{ann}} v)^{2/7} m_\chi^{-9/7}$ reducing the dependence from the particle physics model.

This residual dependence from the particle physics parameters combines with the dependence of the experimental energy threshold above which the gamma-rays are detected leading to a threshold effect visible in Figure 33. The figure shows the average annihilation emitted by the Galactic IMBHs in function of the mass of the DM candidate and for different values of E_{thr}: it can be seen that for values of m_χ near E_{thr} the annihilation flux results to be increase for larger values of the mass, until a maximum is reached. The threshold effect disappears for even larger values of the mass and the usual behaviour $\Phi \propto m_\chi^{-9/7}$ is recovered. As a consequence this provides us with a way to determine the *best case* particle physics scenario for indirect detection of DM around IMBHs: using ACTs to look for an annihilation signal, a conservative estimate for the energy threshold of the telescope is 100 GeV and therefore the highest flux will be obtained assuming a DM candidate with a mass around 5 TeV. On the other hand if Fermi LAT is used, it exhibits the best angular resolution of $\sim 0.1°$ above an energy threshold of 10 GeV. In that case it is more convenient to assume a DM candidate with a mass of $100 - 200$ GeV.

The prospects for the detection of IMBHs in the MW are summarized in Figure 34 where the number of point-like sources (each one associated to an IMBH) with an annihilation flux higher than Φ is plotted in function of Φ itself. Compared with the sensitivities of Fermi LAT and EGRET for a 5σ detection, the most optimistic configuration (a WIMP DM candidate with a $m_\chi = 100$ GeV and $\sigma v = 3 \times 10^{-26}\text{cm}^3\text{s}^{-1}$) corresponds to almost 100 (80) detectable sources by Fermi LAT (EGRET) in 1 year for scenario B and to 700 (5) detectable sources for scenario A.

In Aharonian et al. (2008) the IMBHs scenario was studied also by the H.E.S.S. They used ~ 400 hours of data in the region near the Galactic plane ($|b| \leq 3°$ and $-30° \leq l \leq 60°$) to construct a sensitivity map of the region for the detection of point-like sources as IMBHs. Their gamma-ray maps were used, with the reconstruction of the background and the estimated effective area and exposure time. The 90% C.L. sensitivity results to be:

$$\Phi_\gamma^{90\% \text{ C.L.}}(l,b) = \frac{N_\gamma^{90\% \text{ C.L.}}(l,b) \int_{E_{\text{thr}}}^{m_\chi} dN_\gamma(E)/dE \, dE}{\int_{t_{obs}} \int_0^{m_\chi} A_{\text{eff}}(E, z(l,b), \theta(l,b)) dN_\gamma(E)/dE d\tau}, \tag{89}$$

where dN_γ/dE is the annihilation photon energy spectrum and the effecive area A_{eff} depends on the zenith angle z and on the offset *theta* distribution of the observation livetime. Within the 2° of latitude from the Galactic plane the sensitivity results to be of order

Figure 33. Integrated flux Φ (expressed in $\mathrm{cm}^{-2}\mathrm{s}^{-1}$) above the energy threshold as a function of the neutralino mass m_χ for energy thresholds equal to 1, 10 and 100 GeV, respectively, and an annihilation cross section of $\sigma_{ann}v = 3 \times 10^{-26}\mathrm{s}^{-3}\mathrm{s}^{-1}$. The quoted error bars correspond to the r.m.s. of the integrated flux distribution. The maximum flux is obtained for masses well above the energy threshold of the experiment. Taken from Aharonian et al. (2008).
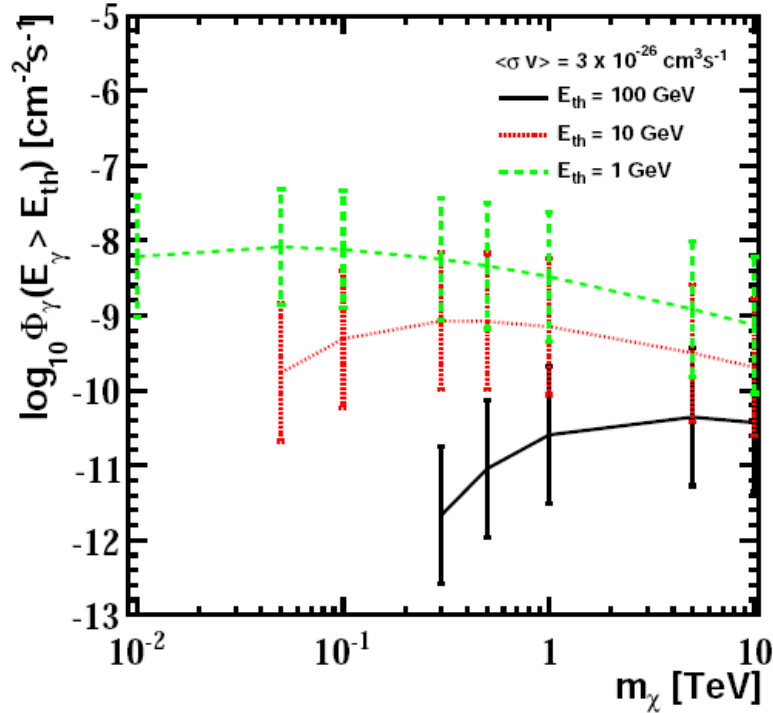
$10^{-12}\mathrm{cm}^{-2}\mathrm{s}^{-1}$ above 100 GeV and reaches $10^{-13}\mathrm{cm}^{-2}\mathrm{s}^{-1}$ near the GC, suggesting that the search for IMBHs is indeed possible. In the region of the survey around 4 IMBHs are predicted in scenario B but only 3 gamma-ray sources are detected by H.E.S.S. and all of them have been interpreted as astrophysical sources. The lack of a IMBH candidate has therefore been translated to a 90% upper limit on the annihilation flux and, in particular, on the cross section. The excluded values reach interesting portions of the parameters space for neutralino DM, excluding cross section larger than $10^{-28}\mathrm{cm}^{-3}\mathrm{s}^{-1}$ for a DM candidate with a mass of 1 TeV (Aharonian et al. 2008).

Mini-spikes around IMBHs are smaller than the enhancement that adiabatic contraction can produce at the center of galaxies, and thus associated to a lower annihilation flux. But in the case of IMBHs there are more chances that are really there and have survived till today: for SMBHs, in fact, one can enumerate a collection of mechanisms able to destroy or at least reduce the spike. All these mechanisms can be neglected for IMBHs, at least for one optimistic formation scenario and the spike or, in this case, the mini-spike is almost insensitive to the evolution of the DM mini-halo.

Moreover, compared to the case of the GC, IMBHs can be located at high latitude regions in the sky where the astrophysical background is strongly reduced. Since a mini-halo around

Figure 34. IMBHs integrated luminosity function, i.e. number of BHs producing a gamma-ray flux larger than a given flux, as a function of the flux, for scenario B (scenario A) in the left (right) panel. DM annihilations are supposed to occur only through the $b\bar{b}$ channel. The upper (lower) line corresponds to $m_\chi = 100$ GeV, $\sigma_{ann}v = 3 \cdot 10^{-26}$cm^{3}s^{-1} ($m_\chi = 1$ TeV, $\sigma_{ann}v = 10^{-29}$cm^{3}s^{-1}). For each curve we also show the 1σ scatter among different realizations of the MW DM halo. The figure can be interpreted as the number of IMBHs that can be detected from experiments with a point-source sensitivity Φ (above 1 GeV), as a function of Φ. We show for comparison the 5σ point-source sensitivity above 1 GeV of EGRET and Fermi LAT (here still marked as GLAST) for 1 year. Taken from Bertone, Zentner & Silk (2005).
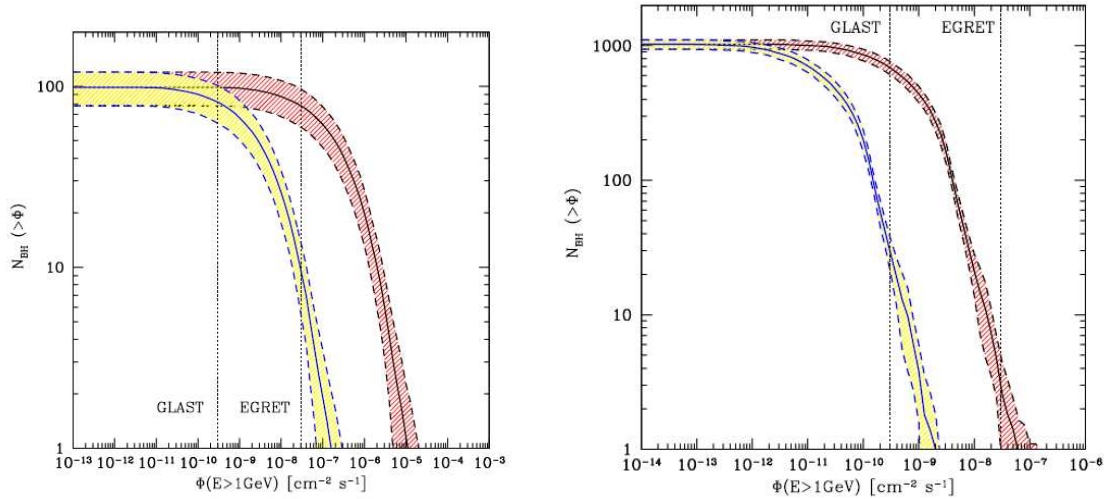

an IMBH is not characterized by an high baryon density there is also a reduced probability of having to deal with astrophysical gamma-ray sources and the indentification of a gamma-ray signal as a result of DM annihilation will be easier than, e.g., the case of the GC.

17. Dark Matter annihilation around the IMBHs of Andromeda

Since we do not know *a priori* the positions of the IMBHs in the MW halo, in order to detect DM mini-spikes a full-sky survey is needed, as the data that Fermi LAT will produce even after a single year of operation. With the full-sky map it will, hopefully, possible to determine unidentified gamma-ray source that are not associated to any of the known astrophysical mechanism of photon production. Once the locations of the candidate IMBHs are determine, one can also use ACTs to study their gamma-ray emission and investigate their nature. In particular the analysis of the gamma-ray energy spectrum plays a fundamental role as we have already seen, with bumps or sharp cut-offs representing clear indication of a DM signal.

The situation is slightly different in the case of the Andromenda galaxy M31. It is located ≈ 780 kpc away from us and thus, if the galaxy host IMBHs, they will be, in general, less bright than those of the MW. But, for M31, the sky survery is not necessary since we already know that IMBHs will be near the location of M31. ACTs can simply be pointed to that direction and, if they will detect a handful of point-like bright gamma-rays sources, it is very likely that they correspond to the brightest IMBHs of M31. In this case the detection of some

Figure 35. Luminosity function of IMBHs (fluxes are in $cm^{-2}s^{-1}$) for a DM particle with $m_\chi = 0.3, 0.5$ and 1 TeV. The energy threshold is equal to 100 GeV and $\sigma_{ann}v = 3 \times 10^{-26} cm^{-3}s^{-1}$. The vertical line shows the contribution of the smooth component of the M31 halo assuming a NFW profile and $m_\chi = 1$ TeV. Taken from Fornasa et al. (2007).
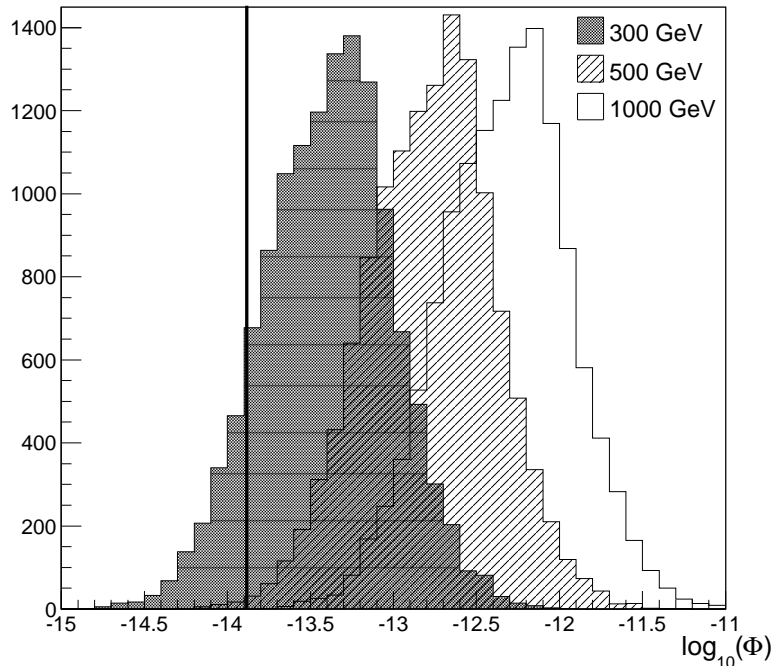
point-like source within some degrees from the center of Andromeda will represent a very strong DM signature by itself, without the need of analyzing the gamma-ray energy spectrum.

In Fornasa et al. (2007) the detection of mini-spikes around IMBHs in M31 is studied. The number of unmerged DM mini-halos is supposed to scale linearly with the mass of the host halo, as it has been checked from different realizations of DM halos over a certain mass range. Thus, the Andromeda galaxy is predicted to host (65.2 ± 14.5) mini-halos, each of them with an IMBH in the center. The mass spectrum of the IMBHs is the same as with the MW (see Figure 32) while the radial distribution is rescaled with respect to the virial radius of the hosting halo. Each mini-halo, before the growth of the mini-spike, is described by a NFW profile so that the mini-spike will be characterized by a slope equal to $-7/3$ as it was assumed for the Galactic IMBHs.

In Figure 35 the luminosity function of the IMBHs considering all the 200 statistical realizations of M31, is shown for three different particle physics setups. From the comparison to the annihilation flux of the smooth DM halo of M31 (described as a NFW profile), it results that the majority of the IMBHs are brighter than the hosting halo itself.

A sky-map around Andromeda center (as in Figure 36) is obtained computing the fluxes from the mini-spikes in a random realization of the host halo. The pixel size matches the angular resolution of an ACT or of Fermi LAT. A DM mass of 1 TeV (150 GeV) for

ACTs (Fermi LAT) and annihilation cross section of $\sigma_{ann}v = 3 \times 10^{-26} \text{cm}^{-3}\text{s}^{-1}$ is supposed. Annihilations all occur through the $b\bar{b}$ channel. The big black circle indicates the scale of the NFW Andromeda halo, while the small black circle highlights the pixels characterized by a flux larger than the experimental sensitivity, corresponding to detectable IMBHs. The experimental sensitivity (indicated by the black line in the color scale) is naively determined as the flux providing a number of photons N_γ larger than 5 times the error of the number of background photons $N_{\text{background}}$:

$$5 = \frac{N_\gamma}{\sqrt{N_{\text{background}}}} = \sqrt{t}\,\sqrt{\Delta\Omega}\,\frac{\int A_{\text{eff}}(E,\theta)\frac{d\Phi}{dEd\Omega}dEd\Omega}{\sqrt{\int A_{\text{eff}}(E,\theta)\frac{d\Phi_{\text{background}}}{dEd\Omega}dEd\Omega}}, \tag{90}$$

where t is the exposure time assumed to be 100 hours (2 months) for ACTs (Fermi LAT) , $\Delta\Omega$ is the angular binsize, A_{eff} is the effective area assumed to independent on the energy and on the angular position to a value of $3 \times 10^4 \text{cm}^2$ (8000 cm^2) for ACTS (Fermi LAT above 4 GeV). The differential energy spectrum is integrated above 100 GeV (4 GeV) for ACT (Fermi LAT). The energy threshold of 4 GeV for Fermi LAT has been chosen so that the angular resolution of the experiment can be considered equal to $0.1°$.

Regarding the background: for Fermi LAT we take into account only the EGB as measured by EGRET in the energy range between 30 MeV and 10 GeV (Sreekumar et al. 1998) and extrapolated to the energy of interest keeping the -2.1 power-law behaviour. On the contrary for ACTs the main background is due to hadrons interacting with the atmosphere and producing electromagnetic showers. Following Gaisser et al. (n.d.), we considered:

$$\frac{d\Phi_h}{dEd\Omega} = 1.5 \times \left(\frac{E}{\text{GeV}}\right)^{-2.74} \text{cm}^{-2}\text{s}^{-1}\text{GeV}^{-1}\text{sr}^{-1}. \tag{91}$$

The ratio of the number of hadrons misinterpreted as gamma-rays, over the total number of cosmic ray hadrons (ϵ_h) provides an estimate of the telescope potential to discriminate the gamma-ray signal from the hadronic background. We adopted a semplicistic value of $\epsilon_h = 0.01$. The electronic contribution to the background is typically subdominant at the energies of interest.

Although we have performed the analysis of the prospects for detection with Fermi LAT and ACTs for 2 different benchmark scenarios (essentially high DM particle mass for ACTs, low m_χ for Fermi LAT), the analysis can be easily extended to any value of the particle physics parameters of the annihilating DM particle. To explore the dependence on m_χ, we show in Figure 37 the number of objects that can be detected with the aforementioned experiments, as a function of the DM particle mass. Near the experiment threshold, fluxes increase with mass. When $m_\chi \gg E_{\text{thr}}$ this threshold effect disappears and one recovers the expected behavior (smaller fluxes for higher masses).

Similarly, one can study the number of detectable objects as a function of the angular distance from the center of M31, to estimate the region where most mini-spikes can be found. It results that the 90% of the detectable IMBHs stand within $\sim 3.3.°$ from the center of M31 for both the experiments (Fornasa et al. 2007).

Figure 36. Left (right) panel shows a map of the gamma-ray flux in units of cm^{-2}s^{-1}, from DM annihilations around IMBHs in M31, relative to one random realization of IMBHs in M31. The size of the bins is 0.1° and the energy threshold for the left (right) panel is 100 GeV (4 GeV) as appropriate for ACTs (Fermi LAT). The big circle shows, for comparison, the M31 scale radius r_s of its NFW profile and the small circles highlight IMBHs within the reach of ACTs for a 5σ detection in 100 hours (within the reach of Fermi LAT for a 5σ detection in 2 months). Taken from Fornasa et al. (2007).
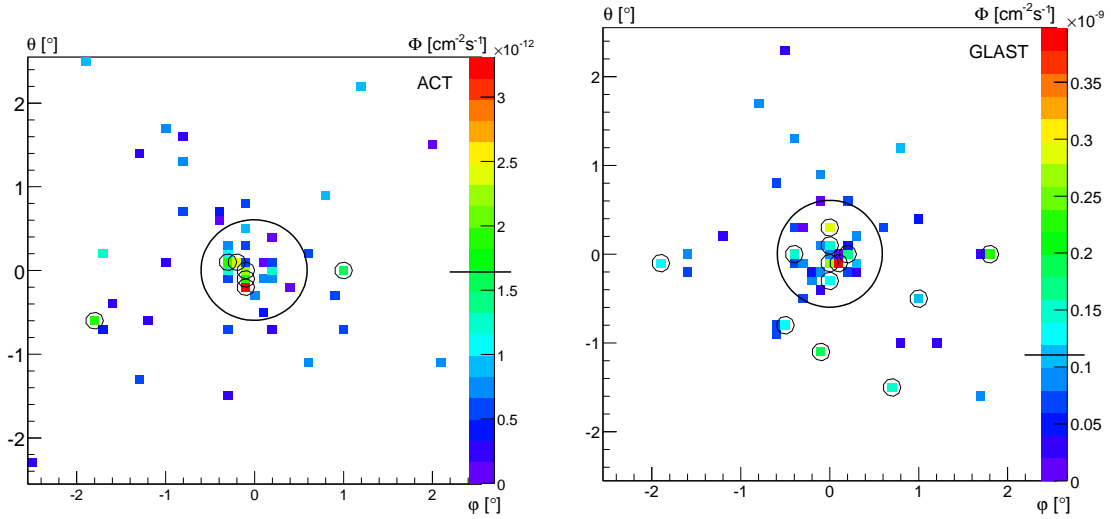
I stress again that, while in the case of Galactic IMBHs the identification of mini-spikes will require a case-by-case analysis of their spectral properties, variability and multi-wavelength counterparts, as discussed in Baltz et al. (2006), for the IMBHs around Andromeda, the detection of a cluster of sources around the center of the galaxy would *per se* provide a hint on the nature of these sources, since other astrophysical sources, e.g. gamma-ray pulsars, will tend to lie in the disk and bulge of M31, while IMBHs would be isotropically distributed around its center, within a region of $\sim 3°$.

In conclusion the obvious advantage of the proposed scenario with respect to mini-spikes in the MW, is that they are not randomly distributed over the sky, but they are contained, at 90%, within 3 degrees from the center of Andromeda, and can thus be searched for with ACTs by performing a deep scan of this small region.

The prospects for Fermi LAT appear more promising, since an exposure time of 2 months allows the detection of up to of ≈ 20 mini-spikes, that would be resolved as a cluster of point-sources with identical spectra, within a $\sim 3°$ region around the center of Andromeda. Such a distinctive prediction cannot be mimicked by ordinary astrophysical sources. As in the case of IMBHs in the MW, null searches would place very strong constraints on the proposed scenario in a wide portion of the DM parameter space.

Figure 37. Number of detectable mini-spikes in M31 with Fermi LAT (in 2 months) and with ACTs (in 100 hours) as a function of the DM particle mass. Error bars denote the 1σ scatter among different statistical realizations of M31. Taken from Fornasa et al. (2007).
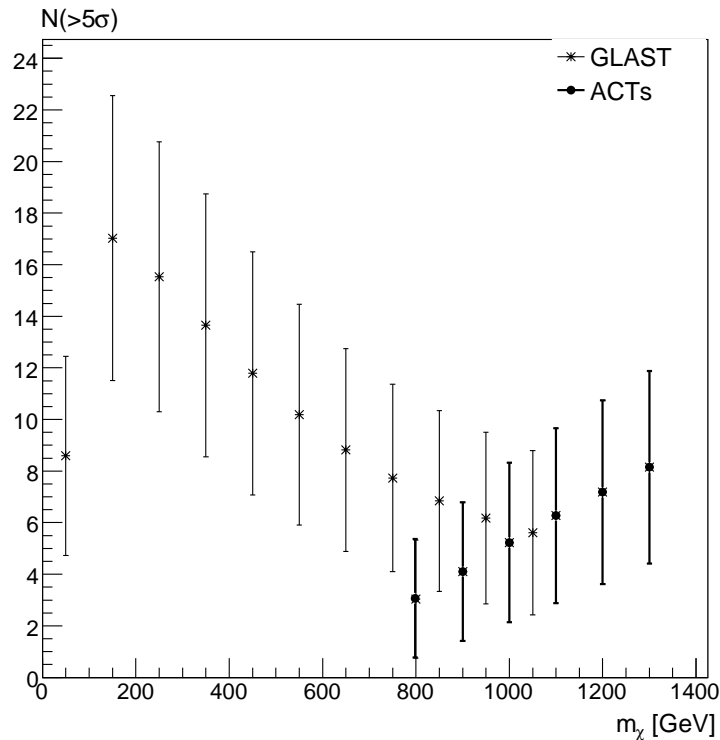
18. Contribution of SMBHs and IMBHs to the EGB

In Chapter II it was already shown how the indirect detection of DM from the GC, which appears *a priori*, to be the most natural candidate for annihilation gamma-rays, remains controversial. High-energy photons have been detected by different experimental collaborations, but their energy spectrum seems to favour an interpretation in terms of an astrophysical source, even if DM can contribute as a subdominant emission process. Moreover, at least in the case of EGRET data, the reconstruction of the location of emission, indicates that the photons may not be produced exactly at the GC.

On the other hand, the detection of gamma-rays coming from the DM halos around dSphs (Chapter III) has still not led to a detection with experimental collaborations able only to place upper limits.

These are the reasons why some authors start to look for DM signatures no more in the gamma-ray flux arriving from isolated sources but in the study of the diffure EGB. The latter results from the subtraction, from the EGRET background data, of the Galactic foreground produced by the interaction of cosmic rays with the interstellar medium of the MW. It results to be well described as an isotropic emission of photons whose energy spectrum is fitted by a power-law with index -2.1. It should be noted that also the characteristic of the EGB is the

subject of some controversy: it is a quantity which has been *inferred*, not directly measured and, moreover, Keshet et al. (2004) noted that some features at high Galactic latitudes in the EGB (which is only at a first approximation isotropic) can be explained as due to our Galaxy so that the *real* EGB, after a more detailed of the Galactic foreground, would be three orders of magnitude smaller. I am going to acknowledge this uncertainty in the subtraction procedure, but for the remaining of the thesis, I will refer to the EGRET EGB as described in Sreekumar et al. (1998). I am also going to give exstimates for the EGB that Fermi LAT will soon detect: the EGB for us will be everything that a gamma-ray telescope can detect once that the known sources have been masked and that the diffuse Galactic foreground has been subtracted. In these terms, the resulting EGB can have, partially, a Galactic origin, being contributed, e.g., by DM annihilations in the smooth Galactic halo or in the halos of DM substructures that are supposed to be present in the MW.

Usually the EGB is explained in terms of unresolved astrophysical sources, like blazars. But, as I have already anticipated, also DM annihilations can contribute to some extent and it has been studied if the DM contribution is able to account for a significant part of the EGB. Neglecting, for now, the Galactic DM, one should estimate the contribution of DM annihilations in extra-galactic halos at all redshifts. Following Ullio et al. (2002), the infinitesimal volume dV at a redshift z can be written as

$$dV = \frac{R_0^3 r^2 dr d\Omega}{(1+z)^3}, \tag{92}$$

where $d\Omega$ is the solid angle, dr is the infinitesimal comoving depth and R_0 is the scale factor at the present epoch. Assuming that the gamma-ray emission is isotropic, we can compute the number $d\mathrm{N}_\gamma$ of gamma-ray photons produced in dV in a time interval dt with an energy between E and $E + dE$ and collected by a detector with effective area dA by integrating the single halo emissivity over the halo mass function $\frac{dn}{dM}(M, z)$:

$$d\mathrm{N}_\gamma = e^{-\tau(z,E_0)} \left[(1+z)^3 \int dM \frac{dn}{dM}(M, z) \frac{d\mathcal{N}_\gamma}{dE}(E, M, z) \frac{dV dA}{4\pi R_0^2 r^2} dE_0 dt_0 \right], \tag{93}$$

where E_0 and dt_0 are, respectively, the energy and the time interval over which the photons are detected on Earth. These quantities are related to those at the redshift of emission through $E_0 = E/(1+z)$ and $dt_0 = (1+z)dt$, so that $dt_0 dE_0 = dt dE$. The halo mass function, dn/dM, represents the comoving number density of DM halos of mass M at redshift z and the factor $(1+z)^3$ converts comoving into physical volumes. In the Press-Schechter formalism (Press & Schechter 1974), the halo mass function is

$$\frac{dn}{dM}(M, z) = \frac{\rho_{\mathrm{crit},0} \Omega_{0,m}}{M^2} \nu f(\nu) \frac{d \log \nu}{d \log M}, \tag{94}$$

where $\rho_{\mathrm{crit},0}$ is the critical density, $\Omega_{0,m}$ is the mass density parameter, $\nu = delta_{sc}(z)/\sigma(M)$, $\sigma(M)$ is the r.m.s. density fluctuation on the mass scale M (normalized to the cosmological parameter σ_8) and δ_{sc} represents the critical density for spherical collapse. Refer to Ullio et al. (2002), Ahn et al. (2007) and Eisenstein & Hu (1997) for the exact computation of these quantities.

$d\mathcal{N}_\gamma/dE$ represents the number of photons with energy between E and $E + dE$ produced in a halo of mass M at redshift z. The exponential $e^{-\tau(z,E_0)}$ is an absorption coefficient that accounts for pair production due to the interaction of the gamma-ray photons with the extra-galactic background light in the optical and infrared bands. Following Bergstrom et al. (2001), the following expression that accounts for current observational constraints is adopted here: $\tau(z, E_0) = z/[3.3(E_0/10 \text{ GeV})^{-0.8}]$.

At the energies of interest, any contribution to the gamma-ray flux from sources beyond $z \sim 5$ is negligible. The mean flux is obtained by integrating Equation (93) along the line of sight:

$$\left\langle \frac{d\Phi}{dE_0 d\Omega} \right\rangle (E_0) \equiv \frac{d\mathsf{N}_\gamma}{dE_0 dt_0 dA d\Omega} \tag{95}$$

$$= \frac{1}{4\pi} \int dr R_0 e^{-\tau(z,E_0)} \int dM \frac{dn}{dM}(M, z) \frac{d\mathcal{N}_\gamma}{dE}(E_0(1 + z), M, z)$$

$$= \frac{c}{4\pi} \int dz \frac{e^{-\tau(z,E_0)}}{H_0 h(z)} \int dM \frac{dn}{dM}(M, z) \frac{d\mathcal{N}_\gamma}{dE}(E_0(1 + z), M, z),$$

where the last expression is obtained by transforming comoving distances r into redshifts z, through the introduction of the Hubble parameter $H_0 h(z) = H_0 \sqrt{\Omega_{0,m}(1 + z)^3 + \Omega_{0,\Lambda}}$, where H_0 is the Hubble constant and $\Omega_{0,i}$ the abundance in units of the critical density at $z = 0$.

The number of photons emitted in a single halo, $d\mathcal{N}_\gamma/dE$, depends on the DM density profile (NFW in our case) and on the particle physics scenario (particle mass m_χ, annihilation cross section $\sigma_{\text{ann}}v$ and differential energy spectrum per annihilation, dN_γ/dE_0). The NFW profile of a halo with mass M is completely specified by the concentration parameter and the virial overdensity Δ_{vir} of the halo. The virial radius r_{vir} is the radius of the sphere which encloses an average density $\Delta_{vir} \times \rho_m$. The way the concentration depends on the mass of the halo and on the redshift $c(M, z)$ is a key ingredient and it is usually parametrized as in Bullock et al. (2001b) that derived their relation from N-body simulations of halos with a mass between $10^{11} - 10^{14} M_\odot$. Another alternative prescription can be found in Eke et al. (2001). In Equation (93) the integration over the mass of halos should be extended over this range. Moreover, in next Chapter, I will deal with the case of DM substructures characterized by masses all the way down to $10^{-6} M_\odot$. As a consequence, the $c(M, z)$ will have to be extrapolated to lower values for the mass, since N-body simulations are not able to provide informations about structures with structures that small. They way the extrapolation is made can create large discrepancy from model and model (Pieri et al. 2008) (see Figure 38).

Bearing all this in mind, we can express $d\mathcal{N}_\gamma/dE$ as

$$\frac{d\mathcal{N}_\gamma}{dE}(E, M, z) \frac{\sigma v}{2} \frac{dN_\gamma(E)}{E} \frac{M}{m_\chi^2} \frac{\Delta_{vir}\rho_{\text{cr}}\Omega_m(z)}{3} \frac{c^3(M, z)}{I_1(x_{\min}, c(M, z))^2} I_2(x_{\min}, c(M, z)). \tag{96}$$

In the previous expression, the virial overdensity is (Ullio et al. 2002):

$$\Delta_{vir}(z) = \frac{18\pi^2 + 82(\Omega_m(z) - 1) - 39(\Omega_m(z) - 1)^2}{\Omega_m(z)}. \tag{97}$$

and the integrals I_1 and I_2 have an analytic expression:

$$I_n(x_{\min}, x_{\max}) = \int g^n x^2 dx, \tag{98}$$

Figure 38. Extrapolation of the $c(M, z = 0)$ relation to values for the mass as low as $10 \, M_\odot$. The two different lines refer to the two different prescriptions for the $c(M, z)$ relation at high masses: "Bullock et al." refers to Bullock et al. (2001*b*) while "ENS" refers to Eke et al. (2001). Taken from Ullio et al. (2002).
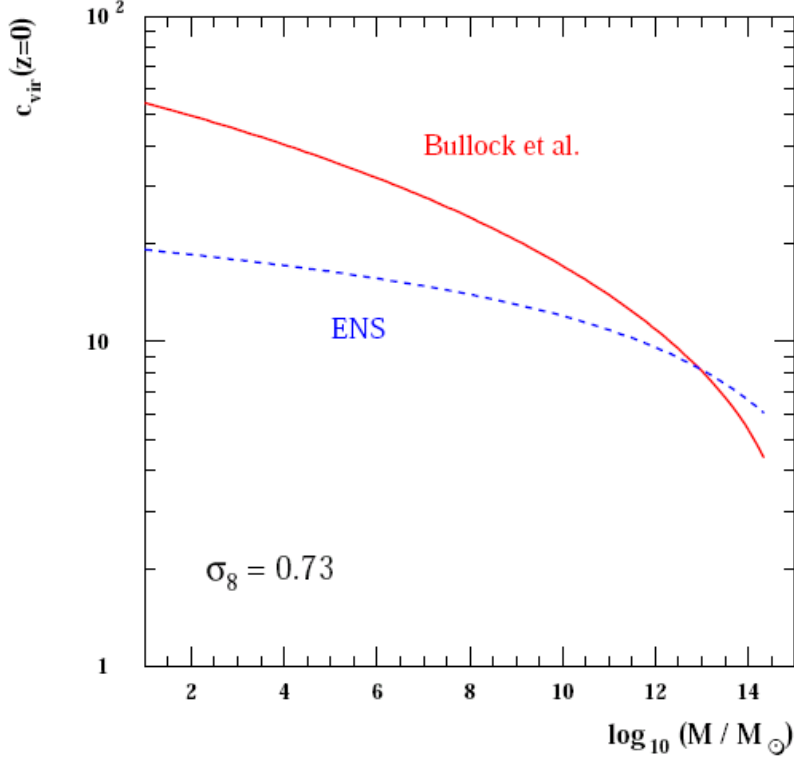
where $g(x)$ depends on the profile chosen to describe the DM density in the halos. For a NFW profile: $g(x) = x^{-1}(1 + x)^{-2}$.

In Equation (96), the lower integration limit is set at the minimum radius within which the annihilation rate equal the dynamical time: $x_{\min} = 10^{-8} \mathrm{kpc}/r_s$ (r_s is the scale radius in kpc). It has been checked that the results are not sensitive to a different choice for $x_{\min}$.

Putting Equation (95) and Equation (96) together, we obtain the expression for the isotropic gamma-ray flux from extra-galactic DM halos:

$$\left\langle \frac{d\Phi}{dE_0 d\Omega} \right\rangle (E_0) = \frac{\sigma v}{8\pi} \frac{c}{H_0} \frac{\rho_{\mathrm{cr}}^2 \Omega_{0,m}^2}{m_\chi^2} \int dz (1+z)^3 \frac{\Delta^2(z)}{h(z)} \frac{dN_\gamma(E_0(1+z))}{dE} e^{-\tau(z,E_0)}, \quad (99)$$

with

$$\Delta^2(z) = \int dM \frac{\nu(z,M) f(\nu(z,M))}{\sigma(M)} \left| \frac{d\sigma}{dM} \right| \Delta_M^2(z,M) \quad (100)$$

and

$$\Delta_M^2(z,M) = \int dc' P(c(M,z),c') \frac{\Delta_{vir}}{3} \frac{I_2(x_{\min}, c')}{I_1^2(x_{\min}, c')} (c')^3 dc'. \quad (101)$$

$\Delta_M^2(z,M)$ represents the enhancement in the gamma-ray flux due to the presence of a DM halo with a mass M at a redshift z. In $\Delta^2(z)$ all these contributions are integrated over the halo

mass function. Therefore $\Delta^2(z)$ quantifies how much the annihilation signal is boosted up by the existence of virialized DM halos. Finally, the concentration parameters are not uniquely defined by the halo mass. Rather, they follow a lognormal distribution with dispersion $\sigma_c = 0.24$ (Bullock et al. 2001*b*) and mean $\bar{c}(M)$:

$$P(\bar{c}(M), c) = \frac{1}{\sqrt{2\pi}\sigma_c c} \, e^{-\left(\frac{\ln(c)-\ln(\bar{c}(M))}{\sqrt{2}\sigma_c}\right)^2}. \tag{102}$$

In the case of a Moore profile, integrating over halos more massive than 10 M$_\odot$ and with a concentration parameter that follows the line labeled as 'Bullock et al.' in Figure 38, a boost factor is still required to match the EGB estimated by EGRET for m_χ ranging from 50 to 500 GeV (Ullio et al. 2002). In Ando (2005) the same calculation has been repeated also for a NFW profile and the results are compared to the prediction that the same scenario would assign to a signal from the GC: in fact, one cannot boost the extra-galactic DM flux as much as he wants in order to reproduce EGRET data, since the constraints towards the GC should also be respected (see Figure 39). In general the GC is a more optimistic target, in the sense that it would require a smaller boost factor in order to explain the data in terms of DM.

The situation can improve if the effect of BHs is taken into account: spikes around SMBHs would only slightly affect the signal from the GC, because even if the spike were present in the past for the SMBH of the MW, it would already be destroyed. While, for the EGB, spikes will be important since the background receives contributions from halos at high redshift, at a time when astrophysical and particle physics effects do not have time yet to damp the enhancement. In Ahn et al. (2007) an empirical relation links the mass of the halo M to the mass of the SMBH $M_\bullet$ today:

$$\frac{M_\bullet}{10^8 M_\odot} = a\left(\frac{M}{10^{12} M_\odot}\right)^b, \tag{103}$$

where three pairs of values (a, b) were considered to bracket theoretical uncertainties. Given a DM halo with a mass M, the corresponding SMBH mass $M_\bullet$ is derived and the a SMBH with that mass is placed in the halo at the redshift of formation $z_\bullet$. The halo is then let evolve till the present value M while the SMBH is supposed to maintain its mass unchanged. Assuming that halos are described by a NFW profile, the spike will be described as:

$$\rho_\chi(r, t) = \rho_{\text{NFW}}(r_{sp}(t))\left(\frac{r}{r_{sp}(t)}\right)^{-\gamma_{sp}} e^{-\tau/2}. \tag{104}$$

The spike has the usual power-law profile (see Section 14 and Equation (85), $\gamma_{sp} = 7/3$ in the case of NFW) but its amplitude decreases with time under the effect of interactions with baryons: τ is the time since spike formation in units of the *heat timescale* t_{heat}:

$$t_{\text{heat}} = 1.25 \text{ Gyrs}\left(\frac{M_\bullet}{3 \times 10^6 M_\odot}\right)^{0.5}\left(\frac{r_h}{2 \text{ pc}}\right)^{3/2}\left(\frac{M_\odot}{\bar{m}_\star}\right)\left(\frac{15}{\ln \Lambda}\right), \tag{105}$$

with $\bar{m}_\star$ an effective stellar mass $\sim 1.8 M_\odot$ (Ahn et al. 2007). Also the size of the spike changes with time since $r_{sp}(t) = e^{-\tau/2(\gamma_{sp}-\gamma_c)}r_{sp}(0)$ (γ_c is the inner slope of the DM profile before the formation of the spike). Thus, finally, the DM spike profile evolves as:

$$\rho_{sp}(r, t) = \begin{cases} \rho_s \left(\frac{r_{sp}(0)}{r_s}\right)^{4/3}\left(1 + \frac{r_{sp}(0)}{r_s}\right)^2 e^{-\tau/2}\left(\frac{r}{r_s}\right)^{-7/3} & r \geq r_{min} \\ m_\chi/\langle\sigma_{\text{ann}}v\rangle(t - t_f) & r < r_{min} \end{cases}, \tag{106}$$

Figure 39. (a) Annihilation gamma-ray energy spectrum from the GC for a DM mass of 50 GeV or 2 TeV, evaluated with a NFW or a Moore profile. Data from EGRET and from CANGAROO-II are also plotted. The H.E.S.S. result is shown as a solid line. (b) EGB intensity from DM annihilations. EGRET data point are also plotted. Taken from (Ando 2005).
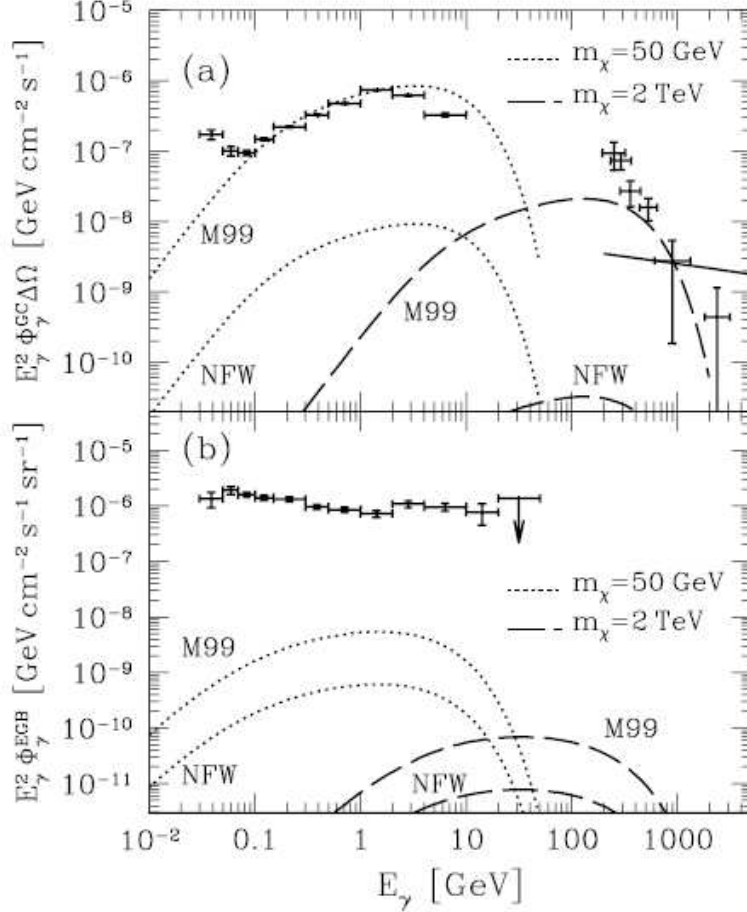
where $\rho_\chi(r_{sp})$ has been related to the density normalization ρ_s of the NFW profile and the r_{min} indicates the minimum distance where the DM reaches its maximum value. As a consequence the total profile of the halo is:

$$\rho_\chi(r,t) = \begin{cases} \rho(r)_{\text{NFW}} & (z > z_\bullet) \\ \rho(r)_{\text{NFW}} & (z \leq z_\bullet, r > r_0) \\ \rho(r)_{\text{NFW}} + \rho_{sp}(r,t) \approx \rho_{sp}(r,t) & (z \leq z_\bullet, r \leq r_0) \end{cases} \quad . \tag{107}$$

In Figure 40 the results are shown, when the integration over the mass of the halos is operated in the range $10^5 M_\odot - 10^{14} M_\odot$: we can see an improvement of more than an order of magnitude with respect to the case without SMBHs (dotted line in the figure). The main contribution comes from low-energies, due to the annihilations at high redshift in the still-present spikes. The energy of the produced photons is then redshifted till now.

The EGB from DM annihilation in mini-spikes around IMBHs has been calculated in Horiuchi & Ando (2006).

The results are shown in Figure 41 for a neutralino of 100 GeV and both the formation

Figure 40. Gamma-ray background produced by DM annihilation in DM halos with spikes (solid lines), compared to the halo-only contribution (dotted). The EGRET diffuse flux limits are shown for comparison. Three choices for the parameters in the relation between tha mass of the BH and the mass of the halo are used: $(a, b) = (0.027, 1.82)$ in red, $(0.10, 1.65)$ in blue and $(0.67, 1.82)$ in green. The DM parameters adopted are $m_\chi = 100$ GeV, $\sigma_{\text{ann}}v = 10^{-26}$cm^{3}s^{-1}. Taken from Ahn et al. (2007).
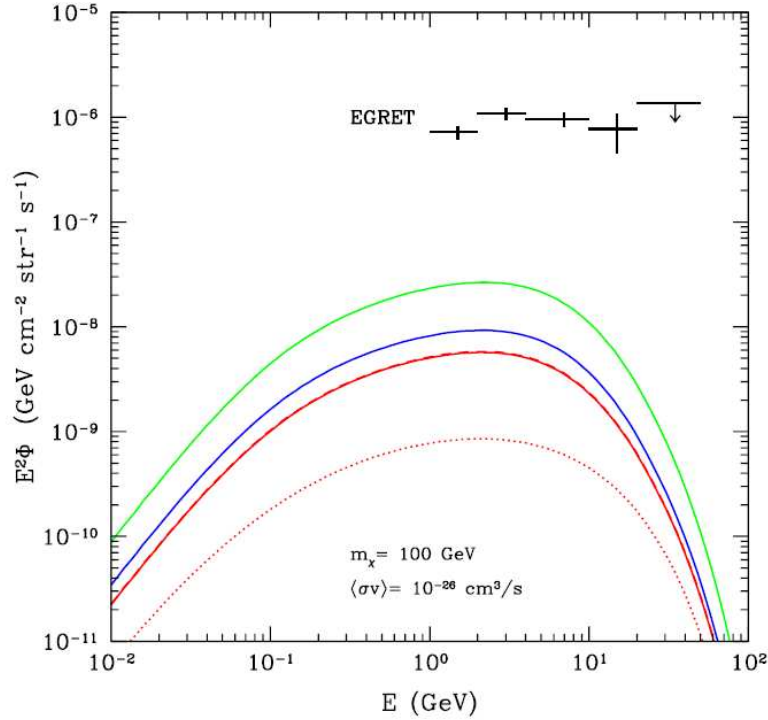

scenarios. As before, the main contribution is at low energies, but now the predictions from scenario B are able to account for the amplitude of the EGB, and the same is true if one consider the line spectrum.

This model is sensitive to the average of the halos properties, whereas, in the case of annihilations from, e.g., the GC, one has to deal with a single realization that may differ significantly from the average, so that the study of the gamma-ray background and the way DM contributes is, for indirect searches, an interesting alternative to the study of unidentified sources.

As a conclusive remark about IMBHs, Figure 42 shows the constraining power of the different detection strategies discussed above:

- the dotted line refers to the population of IMBHs in our Galaxy (Bertone, Zentner & Silk 2005) discussed before. For each value of the mass of the DM candidate, the corresponding value of the averaged cross section σv is deduced for which all the 200 realizations of the MW have at least one IMBH that can be detectable according to EGRET 5σ point source sensitivity above 4 GeV as in Bertone, Zentner & Silk (2005). In other words, if none of the EGRET unidentified sources can be interpreted as IMBH, a model described by a point in the $(m_\chi, \sigma v)$ that is above the line, will be compatible

Figure 41. Contribution to the CGB from scenario A and scenario B IMBH mini-spikes. Also shown are the EGRET data and predictions of minimal host halo only scenario (i.e. no spikes or mini-spikes). We see that mini-spikes increase DM contribution to the CGB of 1-3 orders of magnitude. For the meaning of the 1σ scatter lines see Horiuchi & Ando (2006). $m_\chi = 100$ GeV and $\sigma_{ann}v = 3 \times 10^{-26}$cm^{3}s^{-1}. Note that, in Horiuchi & Ando (2006), scenario A means a BH with a mass $10^2 M_\odot$ and a mild $r^{-3/2}$ mini-spike. Taken Horiuchi & Ando (2006).
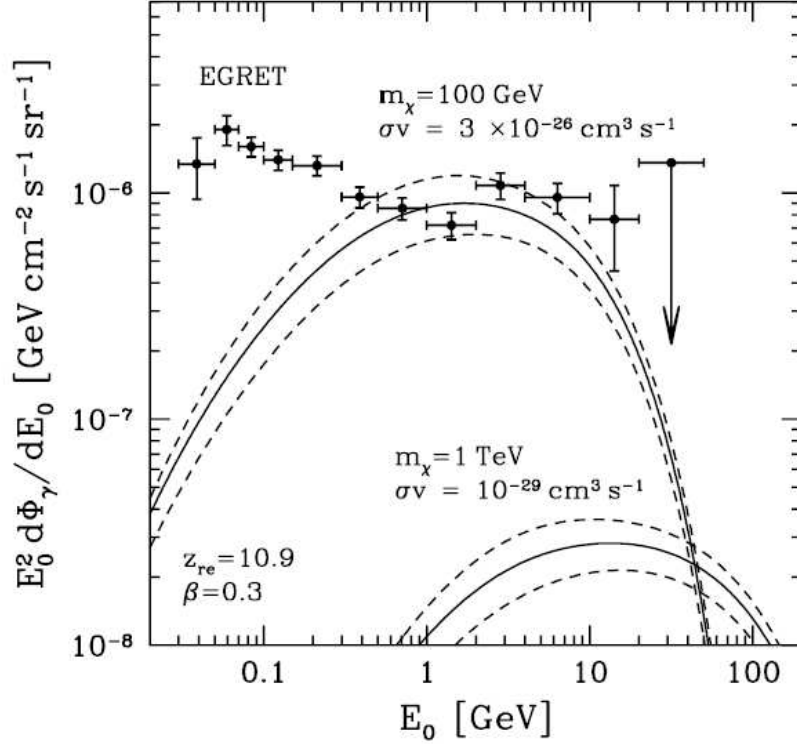
with the data with a probability less than 0.5%. If Fermi LAT detection capability is considered (with a sensitivity two order of magnitude lower than EGRET) the line goes down to the solid one.

- the thin solid line refers to the population of IMBHs in M31 (Fornasa et al. 2007). For each value of m_χ we looked for the value of σv for which all the 200 realizations of M31 have at least one IMBH with an annihilation flux larger than the 5σ sensitivity of Fermi LAT (parametrized as in Fornasa et al. (2007)) for an exposure of 2 months and integrated above 4 GeV. A null detection of IMBHs in Andromeda will excluded the region above the thin line, at least for a WIMP DM candidate.

- the dashed line takes into account the contribution of IMBHs in the computation of EGB (Horiuchi & Ando 2006). Each point above the line corresponds to a DM candidate for which annihilations in IMBHs mini-spikes at high redshift can account for the EGB values as measured by EGRET in Sreekumar et al. (1998).

- the empty dots represent particular SUSY models (generated and studied by DarkSUSY)

Figure 42. Thick solid (dotted) line: indicates the region in the parameter space above which all the realizations of the MW as in Bertone, Zentner & Silk (2005) contain at least one IMBH with an annihilation flux larger than the estimated point source sensitivity for Fermi LAT (EGRET) in 2 months. Thin solid line: indicates the region above which all the realizations of Andromeda galaxy as in Fornasa et al. (2007) have at least one IMBH with an annihilation flux larger than $10^{-10}\text{cm}^{-2}\text{s}^{-1}$. The dotted line indicated the region above which the contribution from DM annihilation in the IMBHs halos at high redshift can account for the EGB as measured by EGRET. The empty (full) dots $\circ$ ($\bullet$) represent SUSY models (studied by DarkSusy) where the neutralino density is within 3 (5)σ from the WMAP value of DM density. Taken from Fornasa et al. (2007).
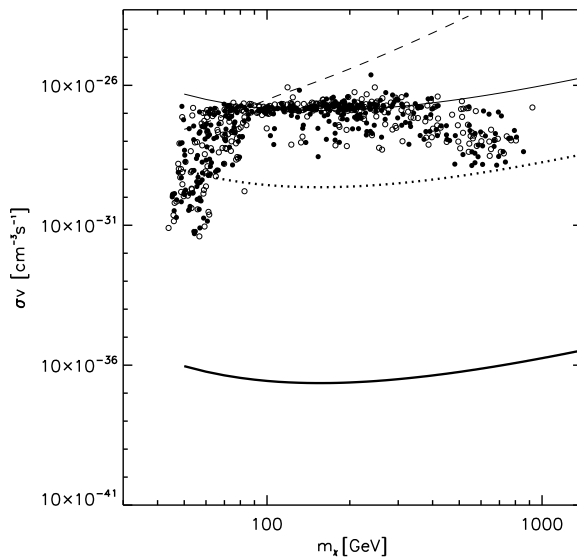
for which the neutralino can account for all the DM density measured by WMAP within 3σ.

- the full dots represent SUSY models where the neutralino density is within 5σ from the WMAP value for DM density.

Fermi LAT predictions live in regions of the parameter space at very low cross section, so the detection of IMBHs, clearly will be soon confirmed or ruled out from its data: if none of these sources is detected by the satellite in our Galaxy, it is very unlikely than such scenario will survive, at least for a WIMP DM candidate.

Chapter VI:
Anisotropy probe of
Galactic and extra-galactic
annihilation signals

19. The use of angular power spectrum of anisotropies

As I said in the abstract of this thesis, the main goal of this work is to propose two main alternatives to the indirect detection of DM towards the GC or from the dSphs in our Galaxy. These are the natural and most studied sources to detect an annihilation signal, but available data from these regions in the sky does not present a clear indication in favour of a DM contribution. Therefore in Chapters IV and V, the possibility of considering the gravitational effect of BHs (both SMBHs and IMBHs) on the distribution of DM was considered, studying under which conditions they can be considered Annihilation Boosters and trying to understand how large these DM o verdensities can be. The result is that it will be more likely to detect the gravitational effects of BHs around IMBHs or as a contribution (at high redshift) to the EGB.

In this last Chapter, I am going to present the second possibility: the analysis of the correlation properties of the gamma-ray emission. The same kind of analysis that was operated for the anisotropies of the CMB radiation can be applied to the high-energy gamma-ray map of the sky and the angular power spectrum of anisotropies in the gamma-ray emissivity can be computed looking for distinctive features due to the presence of DM.

Apart from point-like sources like, e.g., pulsars or blazars, the gamma-ray flux is dominated by the Dalactic foreground, due to the interactions of cosmic-rays with the interstellar medium and modelized, e.g. in Strong et al. (2000). This contribution, which is larger along the Galactic plane and decreases with galactic latitude, does not contain interesting informations to us and it will have to be removed. The result of the subtraction is the EGB for which an estimate is available starting from the EGRET data. Using the soon available Fermi LAT data, a new and more precise determination of the EGB will be possible. In Section 18 I have already seen that a population of common, astrophysical sources can contribute to the EGB but also gamma-rays from DM annihilations can play a significant role. In Section 18 only the contribution of extra-galactic DM halos have been considered and it has been computed how the presence of SMBHs and IMBHs can boost the signal up.

To account for all terms, the annihilation signal along a given direction in the sky is contributed by four different sources:

- the smooth MW halo, that is expected to contribute most towards the GC where the DM density enhancement is expected to be very large (see references above),
- resolved and unresolved substructures within the MW halo (see (Pieri et al. 2008) and references therein).
- extra-galatic DM halos at all redshifts (Ullio et al. 2002), including
- their substructures.

The possibility of detecting DM annihilating in Galactic substructures has been studied in Pieri et al. (2008) and will be reviewed in Section 22.1. Anyway, the main goal of this Chapter is to consider the analysis of the gamma-ray angular power spectrum. A similar analysis has already conducted for the extra-galactic DM halos and subhalos by Ando & Komatsu (2006) and Ando et al. (2007*b*) with results that will be presented in Section 23.2. On the contrary Siegal-Gaskins (2008) focused on a Monte Carlo realization of the MW and computed the

angular spectrum of anisotropies due to Galactic substructures (see Section 23.1). In the recent Fornasa et al. (2009), we used our hybrid model (analytic and Monte Carlo) based on Pieri et al. (2008) to simulate the MW and self-consistently we determined and compared the extra-galactic DM contribution, showing that none of these two terms can be neglected. In the analysis of the angular spectrum we also take into account the unresolved blazars population so that our approach aims at predict precisely the results from a similar anaysis conducted on the soon-available Fermi LAT data.

20. Simulation of Galactic substructures

The Cold DM scenario predicts the formation of a large number of DM halos, virialized structures with masses possibly as small as $\sim 10^{-6} M_\odot$ (Green et al. 2004, Green et al. 2005). Such halos merge into larger and larger systems, leading to the formation of today halos of galaxies and clusters of galaxies. A fraction of the small halos survives to dynamical interactions with the stellar and dark components until the present epoch. Earth-size substructures have indeed been found in numerical simulations within DM halos of mass $\sim 0.1 M_\odot$ at a redshift of 74 (Diemand et al. 2005).

Resolving such small structures within a galaxy-sized halo today is out of computational reach, so that their spatial distribution, mass function and internal structure can only be estimated upon a rather uncertain extrapolation from the properties of higher mass satellites. In Fornasa et al. (2009) we worked under the following hypotheses:

- we assumed that substructures trace the mass of the MW, i.e that their radial distribution follows the mass density profile of the parent halo (as found, e.g., in Diemand et al. (2005), see however the discussion below on the results of the most recent numerical simulations),

- we assumed that the substructures mass function is well approximated by a power-law $dn(M)/d\ln(M) \propto M^{-1}$, normalized so that 10% of the MW mass lies in objects within the mass range $10^{-5} M_{MW} - 10^{-2} M_{MW}$, as found in Diemand et al. (2006).

Under these assumptions, the number density of subhalos per unit mass at a distance R from the GC can be written as:

$$\rho_{sh}(M, R) = A M^{-2} \frac{\theta(R - r_{min}(M))}{(R/r_s^{MW})(1 + R/r_s^{MW})^2} M_\odot^{-1} \text{kpc}^{-3}, \tag{108}$$

where r_s^{MW} is the scale radius of our Galaxy and the effect of tidal disruption is accounted for by the Heaviside step function $\theta(R - r_{min}(M))$. The tidal radius, $r_{min}(M)$, is found by using the Roche criterion to decide whether a subhalo of mass M survives tidal interaction with the host halo (Pieri et al. 2008). According to our normalization about 53% of the MW mass is condensed within $\sim 1.5 \times 10^{16}$ subhalos with masses in the range $10^{-6} - 10^{10} M_\odot$. Their abundance in the solar neighborhood turns out to be ~ 100 subhalos pc^{-3}.

As far as the smooth component of the Galactic halo is concerned, we assume that the MW halo follows a NFW profile, with a scale radius $r_s^{MW} = 21.7$ kpc and that the total mass enclosed in a radius r_{200}, corresponding to the radius where the halo density is 200 times the

critical density of the universe, is $M_{\mathrm{MW}} = 10^{12} M_\odot$. An NFW fit to the DM halo of our Galaxy is consistent within 10% with the results of the *Via Lactea I* simulation (Diemand et al. 2007). A popular way to characterize the mass distribution within the DM halo is using the so-called *concentration*, a shape parameter defined as the ratio between the virial radius and the scale radius, $c \equiv r_{200}/r_s$.

Subhalos are also assumed to follow an NFW profile, with a concentration that depends on their mass (Diemand et al. 2005). To determine the dependence of concentration on the mass, we followed the prescription proposed in Bullock et al. (2001*b*) (hereafter B01) in which the concentration parameter is found to depend on both the subhalo mass M_h and on its collapse redshift, z_c, defined as the epoch in which a mass scale M_h enters the non-linear regime. The collapse occurs when $\sigma(M_h)D(z_c) \sim 1$, where $\sigma(M_h)$ is the present linear theory amplitude of mass fluctuations on the scale M_h and $D(z_c)$ is the linear theory growth factor at the redshift z_c. In an attempt to bracket our theoretical uncertainties in modeling $c(M_h, z_c)$ and its extrapolation at low masses we have implemented two rather extreme models chosen among those considered in Pieri et al. (2008), namely:

- $B_{z_0,ref}$: that extrapolates the $c(M_h, z_c)$ relation of B01 below $10^4 M_\odot$ with a simple power-law,

- $B_{z_f,ref}$: which assumes that surviving subhalos do not change their density profile since their formation. Thus the concentration parameter at z_c can be obtained from the one at $z = 0$ through $c(M_h, z_c) = c(M_h, z = 0)/(1 + z_c)$. The values of $c(M_h, z = 0)$ corresponds to those of the $B_{z_0,ref}$ case and the collapse redshift z_c is obtained by extrapolating the expression proposed by B01 below $10^4 M_\odot$.

20.1. Recent highlights from numerical simulations

Two new sets of very high resolution numerical experiments have been recently released, namely the *Via Lactea II* (Diemand et al. 2008) and the *Aquarius* (Springel et al. 2008*a*, Springel et al. 2008*b*) simulations. The main characteristics of the MW subhalo population in these two simulations are summarized in Table 8 and compared to those of our subhalos. Among the main differences, we noted that the mass fraction in substructures is a factor 2-6 smaller than that used in our model. Another difference is in the subhalo distribution which, in our case, trace the smooth mass distribution of the MW halo, $\rho_{\mathrm{MW}}(r)$, while Springel et al. (2008*a*) and Springel et al. (2008*b*) suggest to use an Einasto profile (Einasto 1965) and in *Via Lactea II* the innermost regions are best fitted by a power-law $(1 + r)^{-2}$.

The concentration parameter of subhalos in the two simulations depends from the distance from the GC and, in the *Aquarius* case, follows the prescription in Neto et al. (2007) (N07) rather than the B01 model. Finally, in *Aquarius*, the subhalo density profile is also parametrized as an Einasto, rather than an NFW, profile.

These differences, in particular the fact that neither in *Via Lactea II* nor in *Aquarius* the spatial distribution of subhalos trace the mass of the parent halo, do have a significant impact on the angular power spectrum of the gamma-ray flux, as we will show in an upcoming publication. In Fornasa et al. (2009), we performed all calculations under the assumptions

Table 8. The main characteristics of the subhalo model considered in Fornasa et al. (2009) compared with those measured in the recent *Aquarius* and *Via Lactea II* *N*-body simulations. The clumpiness is defined as the fraction of the dark mass in substructures within the virial radius of the MW r_{200} = 210 kpc. $N_{subhalos}$ is the total number of substructures within r_{200}. dn/dM is the subhalo mass function, $n_{sh}(r)$ their radial distribution and $c(M, z)$ is the model used for the concentration. ρ_{MW} and ρ_{halo} represent the mass density profile of the host halo and its substructures, respectively.

	Fornasa et al. (2009)	*Aquarius*	*Via Lactea II*
clumpiness ($< r_{200}$)	53%	8%	26%
$N_{subhalos}(< r_{200})$	1.5×10^{16}	2.3×10^{14}	7×10^{15}
dn/dM	$\propto M^{-2}$	$\propto M^{-1.9}$	$\propto M^{-2}$
$n_{sh}(R)$	NFW	Einasto ($\alpha_{\text{Einasto}} = 0.68$)	$\propto (1 + R)^{-2}$
$c(M, z)$	B01	N07	B01
$\rho_{\text{MW}}(r)$	NFW	Einasto ($\alpha_{\text{Einasto}} = 0.21$)	NFW
$\rho_{halo}(R)$	NFW	Einasto ($\alpha_{\text{Einasto}} = 0.16$)	NFW

listed above, and discuss how the differences among the subhalo models in Table 8 are expected to affect the angular power spectrum (Section 25).

21. Modeling the gamma-ray flux

21.1. Gamma-ray flux from Galactic subhalos

The gamma-ray flux expected from the annihilation of DM particles can be written as:

$$\frac{d\Phi_\gamma}{dE_\gamma}(E_\gamma, l, b) = \frac{d\Phi^{\text{PP}}}{dE_\gamma}(E_\gamma) \times \Phi^{\text{cosmo}}(l, b) \tag{109}$$

where the term

$$\frac{d\Phi^{\text{PP}}}{dE_\gamma}(E_\gamma) = \frac{1}{4\pi} \frac{\sigma_{\text{ann}} v}{2m_\chi^2} \cdot \sum_f \frac{dN_\gamma^f}{dE_\gamma} B_f \tag{110}$$

contains the dependence on particle physics parameters, while

$$\Phi^{\text{cosmo}}(\psi, l, b) = \int_M dM \int_c dc \int \int_{\Delta\Omega} d\theta d\phi \int_{\text{l.o.s}} d\lambda [\rho_{sh}(M, R(r_\odot, \lambda, l, b, \theta, \phi)) \times$$
$$P(c) \times \Phi_{halo}^{\text{cosmo}}(M, c, r(\lambda, l, b, \theta, \phi)) \times J(x, y, z | \lambda, \theta, \phi)] \tag{111}$$

represents the contribution to the foreground emission from the subhalo population and

$$\Phi_{halo}^{\text{cosmo}}(M, c, r) = \int \int_{\Delta\Omega} d\phi' d\theta' \int_{\text{l.o.s}} d\lambda' \left[\frac{\rho_{halo}^2(M, c, r(\lambda, \lambda', l, b, \theta', \phi'))}{\lambda^2} \right.$$
$$\left. J(x, y, z | \lambda', \theta', \phi') \right] \tag{112}$$

is the contribution from a single subhalo.

The total galactic flux is obtained by adding to Equation (111) the contribution of DM annihilations in the smooth NFW halo of the MW.

In Equation (110), m_χ is the DM particle mass, $\sigma_{ann}v$ the annihilation cross section, and dN_γ^f/dE_γ the differential photon spectrum per annihilation relative to the final state f, with branching ratio B_f that we took from Fornengo et al. (2004). A rather optimistic particle physics scenario is adopted (in the sense that it provides large annihilation fluxes), in which the DM particle has a mass $m_\chi = 40$ GeV, a cross section $\sigma_{ann}v = 3\times10^{-26}$cm^{3}s^{-1} and particles annihilate entirely in $b\bar{b}$.

In Equation (111), $\Delta\Omega = 9.57 \times 10^{-6}$sr is the solid angle considered for the integration, corresponding to the angular resolution of the Fermi LAT satellite, (l, b) are the Galactic coordinates of the direction of observation, and J is the Jacobian determinant of the transformation between polar and cartesian coordinate systems. The galactocentric distance, R, can be written as a function of the coordinates inside the observation cone (λ, θ, ϕ) and of (l, b) through the relation $R = \sqrt{\lambda^2 + r_\odot^2 - 2\lambda r_\odot C}$, where $r_\odot$ is the distance of the Earth from the GC, and C is the cosinus of the angle between the direction of observation and the direction of the GC.

21.2. Gamma-ray flux from extra-galactic structures

The contribution to the annihilation flux from all the structures at all redshift along the line of sight has already being computed in Section 18 following the formalism of Ullio et al. (2002). The only difference compared to what is done in Section 18 is that in order to be self-consistent to the prescriptions used for the Galactic substructures, models $B_{z0,ref}$ and $B_{zf,ref}$ are used also to describe the concentration of extra-galactic DM halos.

To account for the presence of substructures in extra-galactic halos, in Fornasa et al. (2009) we assumed that a given fraction of the halo mass is concentrated in substructures with the same properties as the Galactic subhalos described in Section 20. For consistency with the MW case, we required 10% of the parent halo mass M to be in subhalos in the mass range $10^{-5}M - 10^{-2}M$. Following this requirement the mass fraction $f(M)$ in substructures within a host halo of mass M can be fitted as

$$f(M) \equiv \frac{M_s^{tot}}{M} = \frac{1}{6} + \frac{\log_{10}(M/M_\odot)}{30}. \tag{113}$$

With the above definition, the presence of substructures is taken into account replacing Δ_M^2 in Equation (101) with the following expression:

$$\Delta_M^2(M) \rightarrow (1 - f(M))^2\Delta_M^2(M) + \frac{1}{M} \int dM_s M_s \frac{dn}{dM_s}(M_s, z)\Delta_{M_s}^2(z, M_s). \tag{114}$$

22. Mapping the gamma-ray annihilation signal

22.1. Galactic contributions

The gamma-ray flux from local substructures receives contributions from all the subhalos along the line of sight, typically $\sim 10^9$ subhalos when integrating over a a solid angle $\sim 10^{-5}$sr. A brute-force integration with a Monte Carlo approach is therefore impossible even on high-speed computers. To circumvent this problem, Pieri et al. (2008) have proposed a hybrid

approach that consists in splitting the integral into two different contributions. The first one, which we regard as due to unresolved subhalos, is the average contribution of a subhalo population distributed according to Equation (111), which can be estimated analytically. The second one comes from the nearest subhalos, that one may hope to resolve as individual structures, and it is estimated by numerical integration of 10 independent Monte Carlo realizations. To determine the number of individual subhalos in each Monte Carlo realization it is assumed that their contribution to the gamma-ray flux represents a Poisson fluctuation to the mean gamma-ray annihilation signal. Following this criterion, we only considered, in each mass decade, subhalos with $\Phi^{cosmo} > \langle \Phi^{cosmo}_{B_{z_0,ref}} (\psi = 180°) \rangle \sim 10^{-5} \text{GeV}^2 \text{cm}^{-6} \text{kpc sr}$, where the brackets indicate the mean annihilation flux. For a given halo mass, this requirement corresponds to generate all subhalos within a maximum distance $d_{max}(M)$. More than 500 subhalos are found within d_{max} for each mass decade from $10\ M_\odot$ to $10^7 M_\odot$ and their positions are simulated according to Equation (111). For less massive subhalos, if less than 500 subhalos are found, d_{max} is increased to include all the nearest 500 subhalos in that mass range.

Pieri et al. (2008) have checked that the predicted gamma-ray flux does not depend on d_{max}. Here we need to perform a similar robustness test to check that the choice of d_{max} does not introduce spurious features in the angular power spectrum. For this purpose different Monte Carlo realizations have been generated simulating subhalos up to $n \times d_{max}$ with n from 2 to 5. It has been checked that convergence in the power spectra is obtained already for $n = 2$. Since the convergence depends weakly on the model concentration parameter adopted, in our paper we adopted a more stringent criterion and set our maximum simulation distance at $3 \times d_{max}(M)$ to guarantee that the convergence is reached in both subhalo models considered.

To summarize, in our model we considered three sources of gamma-ray annihilation within the MW: the smooth Galactic halo (which we refered to as NFW), the unresolved subhalos (UNRES), and the resolved substructures (RES). Since the total annihilation depends on the square of the DM density, for the purpose of computing the angular correlation signal we also needed to consider the double products NFW × RES and NFW × UNRES. We neglected RES × UNRES since a resolved subhalo at a given location excludes the presence of unresolved substructures.

It is important to stress that the subhalos labelled as "resolved" do not correspond to those substructures that will be detected by Fermi LAT. Instead they merely represent the nearest subhalos that we generated to account for the discreteness of the subhalo spatial distribution. Moreover, considering the population of RES subhalos also accounts for the pixel-to-pixel variation in the annihilation flux that would be neglected focusing only on the smooth UNRES signal.

The possibility of detecting Galactic DM substructures is discussed in details in Pieri et al. (2008): in this paper additional prescriptions to perform the extrapolation for the subhalos concentration from higher to lower masses are considered and for each model they predict the detectability, on one hand, of the diffuse UNRES contribution and, on the other hand, of single subclumps appearing as isolated gamma-ray sources. Changing the particle physics factor so that each model does not overcome the EGRET data (Galactic foreground

plus EGB), the number of detectable subclumps ranges from zero to ~ 130. The model with the highest number of detectable subclumps is $B_{z_f,ref}$, while for the more conservative $B_{z_0,ref}$ Fermi LAT is expected to detect only an handful of substructures.

In Fornasa et al. (2009) we were interested in the correlation properties of the diffuse gamma-ray emission and these detectable sources should be masked. However, we checked that the angular spectrum does not significantly depend on the exclusion of these point-like sources.

In Figure 43 the different contributions to the differential annihilation flux at 10 GeV as a function of the angle Ψ from the GC is shown, in model $B_{z_0,ref}$ (right panel) and $B_{z_f,ref}$ (left panel).

For $B_{z_0,ref}$ the flux from Galactic substructures (red curve) dominates over the smooth NFW profile (black curve) at angular distances from the GC larger than about 3° and it remains the dominant contribution at larger angles. The blue line labeled 'EGRET' represents the EGB inferred from EGRET measurements, equal to $1.10 \times 10^{-8}\mathrm{cm}^{-2}\mathrm{s}^{-1}\mathrm{GeV}^{-1}\mathrm{sr}^{-1}$ at 10 GeV, that can be used as a generous upper bound (the Fermi LAT satellite will impose more stringent constraints, see Section 22.2).

Note that the NFW curve in Figure 43 exceeds the EGRET EGB in the central degree, but not the flux of the bright gamma-ray source (J1746-2851) that has been identified by EGRET to be near - possibly coincident with - the GC, and it is thus consistent with observations.

For $B_{z_f,ref}$, Galactic substructures dominate the NFW signal at even smaller angular separations form the GC. In this case, the average flux for Galactic substructures is larger than in the $B_{z_0,ref}$ case and almost matches the EGRET background.

22.2. *Extra-galactic contribution*

The green line in Figure 43 represents the average extra-galactic flux contributed by DM annihilation in extra-galactic halos, and their substructures, calculated with Equation (99). In model $B_{z_0,ref}$ this flux turns out to be $2.20 \times 10^{-11}\mathrm{cm}^{-2}\mathrm{s}^{-1}\mathrm{GeV}^{-1}\mathrm{sr}^{-1}$, significantly smaller than in model $B_{z_f,ref}$ (for which it is $1.45 \times 10^{-10}\mathrm{cm}^{-2}\mathrm{s}^{-1}\mathrm{GeV}^{-1}\mathrm{sr}^{-1}$) but still well below the Galactic contribution and the EGRET constraint.

I stress the fact that in Fornasa et al. (2009) we considered the EGRET background since it constitutes the best observational constraint available to date. This background is likely to be dominated by unresolved extra-galactic sources like blazars. Using the blazars Gamma-ray Luminosity Function derived from the blazars detected by EGRET, Ando et al. (2007*b*) and Ando et al. (2007*a*) have shown that these sources should contribute only to 25-50% of the total EGB. One therefore expects that, thanks to its superior sensitivity, Fermi LAT will be able to resolve a significant fraction of these sources (Ando et al. 2007*a*). As a result, the amplitude of the unresolved gamma-ray background will decrease, effectively lowering the blue line in Figure 43 in the case of Fermi LAT. This will have three advantages. First of all, a fainter gamma-ray background will increase the probability of detecting the gamma-ray annihilation signal produced by individual structures. Second, the background from Fermi LAT will provide tighter constraints to our model for the DM annihilation, telling us if our

Figure 43. Different contributions to the differential flux $d\Phi/dEd\Omega$ [cm^{-2}s^{-1}GeV^{-1}sr^{-1}] at 10 GeV as a function of the angle Ψ from the GC, in model $B_{z_0,ref}$ (left panel) and $B_{z_f,ref}$ (right panel). The blue line corresponds to the EGRET estimate of the EGB as parametrized in Sreekumar et al. (1998). The contribution from DM annihilation in the smooth host halo and its substructures are represented by the black and red curves, respectively. The latter is obtained by averaging over 10 different Monte Carlo realizations of the subhalos population. Bumps and wiggles are due to the contribution of the individual subhalos of the RES population. The green line represents the extra-galactic flux contributed by DM annihilation within extra-galactic halos and their substrutures. We have assumed $m_\chi = 40$ GeV, $\sigma_{ann}v = 3\times10^{-26}$cm^{3}s^{-1} and annihilations to $b\bar{b}$. Taken from Fornasa et al. (2009).
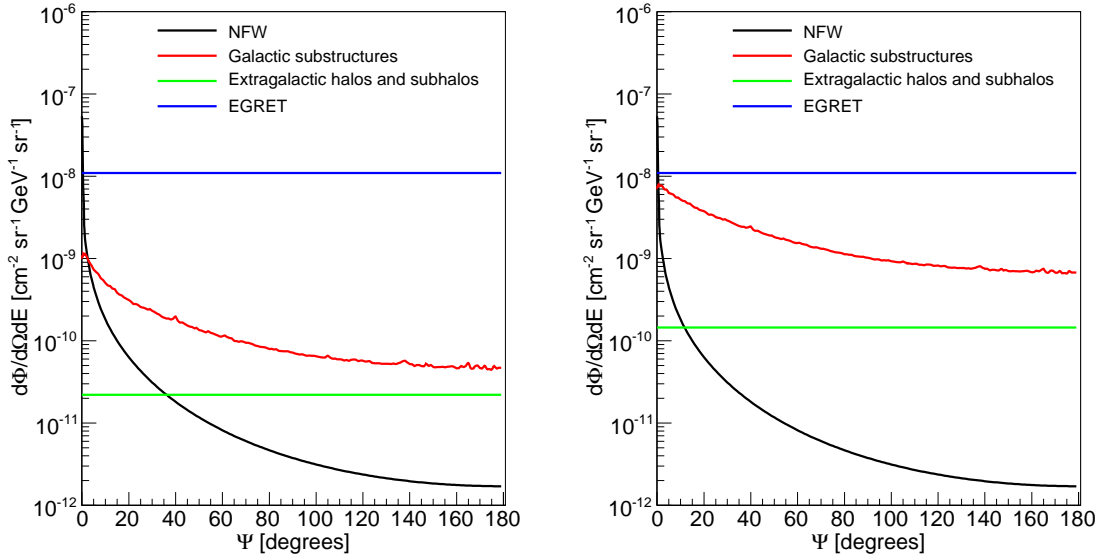
description is too optimistic. Finally, with a larger number of resolved astrophysical sources, Fermi LAT will provide a better estimate of the blazar luminosity function.

The fact that the extra-galactic flux is contributed by both DM annihilation and blazars and because of the uncertainty on the latter contribution, one has the freedom of modifying the relative importance of blazars emission to the total EGB, keeping a good agreement with the data. Different choices for these relative contributions have been proposed in Ando et al. (2007b). They are listed in the first two columns of Table 9. The same DM annihilation flux leads to a different value of f_{DM}^{EGRET} for EGRET and Fermi LAT, due to the lower Fermi LAT EGB.

It is particularly important to note that not all of the scenarios in Table 9 are physically plausible when implemented in our model. For example, boosting the average galactic and extra-galactic DM annihilation flux so that it will account for more than 61% of the Fermi LAT EGB, leads to a flux that exceeds the EGRET constraint towards the GC (even excluding the central degree). Thus, for $B_{z_0,ref}$ we will only consider f_{DM}^{Fermi} as large as 0.61, restricting to the last two rows in Table 9. For the model $B_{z_f,ref}$, a similar argument rules out cases with $f_{DM}^{Fermi} > 0.80$.

Table 9. $f_{\text{blazars}}^{\text{EGRET}}$ and $f_{\text{DM}}^{\text{EGRET}}$ indicate the contribution of gamma-ray from blazars and from DM annihilation respectively, to the EGB as measured by EGRET. $f_{\text{blazars}}^{\text{Fermi}}$ and $f_{\text{DM}}^{\text{Fermi}}$ represent the same quantities estimated for the Fermi LAT satellite in Ando et al. (2007*b*) using the blazar luminosity function derived from EGRET data. The last two rowes indicates the corresponding boost factors needed to bring the average annihation flux (Galactic plus extra-galactic) to the relative percentage of the EGB value.

$f_{\text{blazars}}^{\text{EGRET}}$	$f_{\text{DM}}^{\text{EGRET}}$	$f_{\text{blazars}}^{\text{Fermi}}$	$f_{\text{DM}}^{\text{Fermi}}$	boost factor $B_{z_0,ref}$	boost factor $B_{z_f,ref}$
0.1	0.9	0.03	0.97	ruled out	ruled out
0.3	0.7	0.20	0.80	ruled out	5.9
0.5	0.5	0.39	0.61	49.8	4.2
0.7	0.3	0.61	0.39	29.9	2.6

23. Angular power spectrum of the gamma-ray unresolved signal

23.1. Galactic contribution

To compute the Galactic gamma-ray angular power spectrum and investigate the relative importance of the different contributions, in Fornasa et al. (2009) we separately analized the five maps of Φ^{cosmo} corresponding to the NFW, RES, UNRES, NFW×RES and NFW×UNRES contributions. In the maps, the value of Φ^{cosmo} is specified within angular bins of $\Delta\Omega = 9.57 \times 10^{-6}$sr.

Since we were interested in the contributions of DM halos and subhalos, we masked out the region close to the GC and the Galactic plane in which the signal is dominated by gamma-rays produced by cosmic rays interacting with the interstellar galactic medium (Strong et al. 2000). This background rapidly decreases with galactic latitude. For this reason we used a composite mask consisting in a strip of 10° above and below the Galactic plane and the squared area around the GC with coordinates $|b| \leq 30°$ and $|l| \leq 30°$. Outside the mask, the average galactic annihilation flux turns out to be $\langle d\Phi/dEd\Omega \rangle = 8.79\times10^{-11}\text{cm}^{-2}\text{s}^{-1}\text{GeV}^{-1}\text{sr}^{-1}$ in the case of $B_{z_0,ref}$ and $\langle d\Phi/dEd\Omega \rangle = 1.16 \times 10^{-9}\text{cm}^{-2}\text{s}^{-1}\text{GeV}^{-1}\text{sr}^{-1}$ for $B_{z_f,ref}$, and it is dominated by the UNRES term.

To characterize the angular correlation signatures of the various contributions we computed the angular power spectrum of the different maps with the **HEALPix** 2.01 package (Gorski et al. 1999). Five `Healpix_Map` objects are created covering the whole sky with 786432 pixels of constant area (corresponding to `N_side` = 2^8). Each pixel of the `Healpix_Map` is filled with the corresponding flux $d\Phi/dEd\Omega$ from the simulated maps. The number of pixels is determined from the requirement that the area of the single bin is smaller than $\Delta\Omega$.

The angular power spectrum, C_ℓ, is computed from the spherical harmonic coefficients $a_{\ell,m}$ of the gamma-ray flux angular fluctuation map as follows:

$$\left\langle \frac{d\Phi}{dEd\Omega} \right\rangle a_{\ell,m} = \int d\Omega \left(\frac{d\Phi(\theta,\phi)}{dEd\Omega} - \left\langle \frac{d\Phi}{dEd\Omega} \right\rangle \right) Y_{\ell,m}(\theta,\phi)^*, \tag{115}$$

$$C_\ell = \frac{\sum_{m=0}^{\ell} |a_{\ell,m}|^2}{2\ell + 1}, \tag{116}$$

where $Y_{\ell,m}(\theta, \phi)$ are the spherical harmonics and the integration in Equation (115) extends to the unmasked area. The angular spectra of the RES and NFW×RES maps have been obtained by averaging the spectra of the 10 independent maps corresponding to the different Monte Carlo realizations of resolved subhalos.

I note in passing that the angular correlation signal does not depend on the particle physics scenario since it is evaluated with respect to the average flux (aside from a weak dependence on the minimum subhalo mass, which, in turn, depends on the properties of the DM particle). However, for the purpose of comparing the gamma-ray angular spectrum due to DM annihilation to that of extra-galactic astrophysical sources, a particular particle physcis scenario has to be specified. In this case we refer to the reference values presented in Section 21. The angular spectrum is computed at the energy of 10 GeV where Fermi LAT exhibits its best angular resolution of $\sim 0.1°$.

The masking procedure induces spurious features in the spectra of the NFW, UNRES and NFW×UNRES maps: they have been smoothed out by averaging over 18 multipoles.

The total angular spectrum is obtained by performing a sum of the aforementioned contributions and the cross-correlation terms:

$$\left\langle \frac{d\Phi^{\text{tot}}}{dEd\Omega} \right\rangle^2 C_\ell^{\text{tot}} = \sum_i \left\langle \frac{d\Phi^i}{dEd\Omega} \right\rangle^2 C_\ell^i + \sum_{i,j} \left\langle \frac{d\Phi^i}{dEd\Omega} \right\rangle \left\langle \frac{d\Phi^j}{dEd\Omega} \right\rangle \sum_m a_{\ell,m}^i a_{\ell,m}^{*j}, \tag{117}$$

with $i, j \in$ [NFW, RES, UNRES, NFW×RES, NFW×UNRES].

The results for model $B_{z_0,ref}$ and $B_{z_f,ref}$ are plotted in Figure 44, for which we also took into account the pixel window function for the corresponding resolution of our maps (Gorski et al. 1999). The different curves in the plot represent the angular spectrum of each component weighted by the square of its relative contribution to the total annihilation flux $\langle d\Phi^i/dEd\Omega \rangle^2 / \langle d\Phi^{\text{tot}}/dEd\Omega \rangle^2$. Cross-correlations are taken into account in the computation of the total spectrum but are not shown in Figure 44. Black crosses represent the spectrum of the total flux and the shaded areas show the 1σ error boxes. These are obtained by summing in quadrature the uncertainties related to the finite binsize and, if applicable, the scatter among the different Monte Carlo realizations of resolved subhalos. The first contribution dominates at lower multipoles ℓ while the second becomes the main source of error at larger multipoles where the power spectrum is mainly due to the RES contribution. Poisson errors are not accounted for since they depend on the observational setup and they will be discussed in the next Section for the case of the Fermi LAT satellite.

The main contribution to the total flux is provided by the autocorrelation of the resolved (red curve) and unresolved (blue curve) subhalos. The former dominates at large multipoles while the latter dominates at $\ell < 30$. The interplay between these two components is responsible for the minimum at $\ell \sim 30$ in the total spectrum. All components involving the smooth DM distribution provide a negligible contribution to the total spectrum.

The total spectrum and the different contributions for model $B_{z_f,ref}$ are very similar to model $B_{z_0,ref}$. The only difference is represented by the position of the minimum which is

Figure 44. The curves represent the angular power spectrum $C_\ell\ell(\ell+1)/2\pi$ of the different contributions to the Galactic annihilation flux in the framework of model $B_{z_0,ref}$ (left panel) and $B_{z_f,ref}$ (right panel). The labels identify the different contributions. Black crosses represent the angular spectrum of the total annihilation signal together with its 1σ error (shaded areas). Taken from Fornasa et al. (2009).
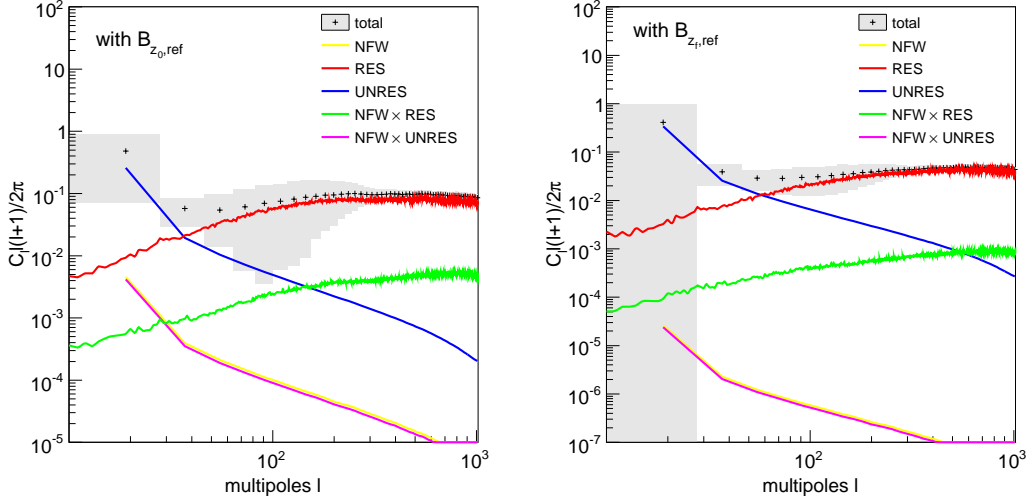
now around $\ell \sim 50$. This is due to the contribution of the resolved subhalos (red curve) which is smaller than in the previous case: subhalos in the $B_{z_f,ref}$ model are less concentrated than in $B_{z_0,ref}$ and consequently they contribute less to the spectrum at small angular scales. We conclude that changing the concentration parameter significantly affects the mean annihilation flux but not the angular power spectrum of the signal.

Our model predictions depend on the assumption about the minimum subhalo mass, for which the theory does not provide very strong constraints. In order to check the dependence of our results on the minimum subhalo mass, we have re-simulated the resolved subhalos excluding all structures below a given mass threshold. The spectrum does not change when excluding subhalos with a mass below $10^4 M_\odot$, showing that the angular correlation is mainly contributed by massive subhalos.

To check the reliability of our hybrid model, we have compared our results with those of a similar study recently carried out by Siegal-Gaskins (Siegal-Gaskins 2008) who used a pure Monte Carlo approach to compute the power spectrum of the annihilation signal produced by a population of subhalos in the MW above $10 M_\odot$ and $10^7 M_\odot$, hence neglecting the contribution of smaller subhalos. To compare our simulation approach to hers, we have modified our subhalo model to match that of Siegal-Gaskins (2008). In particular we re-simulated our Galactic subhalo using a shallower mass function $dn/dM \propto M^{-1.9}$, assuming an Einasto density profile ρ_{halos} for subhalos, adopted a simplified power-law model for the concentration parameter with $c(M) \propto M^{-0.138}$ and normalized the number of subhalos in the MW with a mass larger that $10^8 M_\odot$ to be $N(M > 10^8 M_\odot) = 0.0064(10^8 M_\odot/M_{MW})^{-0.9}$ (this normalization forces the number of MW subhalos to be five times smaller than with the normalization assumed in

Section 20 for the $B_{z_0,ref}$ and $B_{z_f,ref}$ cases).

The only residual difference between our model and that of Figures 5 and 6 of Siegal-Gaskins (2008) is the spatial subhalo distribution in the MW which is more similar to the anti-biased model of Siegal-Gaskins (2008).

The result of this exercise is shown in Figure 45. The curves shows the spectra normalized at $C_\ell = 150$ for the various cases explored. The spectra of the subhalos *a la* Siegal-Gaskins are consistent with Fig. 5 and 6 of Siegal-Gaskins (2008) for both the two mass thresholds considered (10 $M_\odot$ (black curve) and $10^7 M_\odot$ (red curve)). The agreement is valid at the same time for the shape and the amplitude of the signals.

The comparison with the spectrum of our subhalos in the case of $B_{z_0,ref}$, shows that, for the same mass cut, our spectrum is steeper than in Siegal-Gaskins (2008). This can be explained by noting that small mass halos are more concentrated in Siegal-Gaskins (2008) than in our case, resulting in a larger power at small scales (i.e. at large multipoles).

Also the amplitude of the angular spectra predicted in models $B_{z_0,ref}$ and $B_{z_f,ref}$ results to be different than the same quantity in Fig. 5 of Siegal-Gaskins (2008), even when the different subhalo spatial distribution is considered: our spectra are characterized by a lower amplitude, the result of having considered subhalos with masses lower than 10 $M_\odot$. They contribute to the total annihilation flux but their distribution is almost homogeneous around the observer, hence decreasing the spectral amplitude.

Finally, as I have already pointed out, the results presented here are robust to the choice of the maximal simulation distance. We have checked that resolving halos at distances larger than $3 \times d_{max}(M)$ has very little impact on the angular power spectrum.

23.2. Extra-galactic contribution

For the analysis of the angular spectrum of the extra-galactic annihilation flux in Fornasa et al. (2009) we referred to the approach used originally by Ando & Komatsu (2006) and extended by Ando et al. (2007*b*) to account for substructures.

For the description of extra-galactic DM halos, (Ando & Komatsu 2006) followed an analytical approach, using thet fact that the angular multipoles C_ℓ are related to the three dimensional power spectrum $P_f(k)$ of $f = \delta^2 - \langle\delta\rangle^2$ with $\delta = d\Phi/dEd\Omega - \langle d\Phi/dEd\Omega\rangle$:

$$\left\langle\frac{d\Phi}{dEd\Omega}\right\rangle^2 C_\ell = \int d\frac{dr}{r^2} W^2([1+z]E_\gamma, r) P_f\left(k = \frac{\ell}{r}; r\right), \qquad (118)$$

where $W([1+z]E_\gamma, r)$ contains the particle physics parameters, while the way DM is distributed is encoding in the power spectrum $P_f(k)$, which is itself the Fourier transform of the two-point correlation function of f: $\xi_f^{(2)}(\vec{x} - \vec{y}) = \langle f(\vec{x})f(\vec{y})\rangle$.

The two-point correlation function of f is then re-written as two-point and four-point correlation function of δ:

$$\xi_f^{(2)}(\vec{x} - \vec{y}) = \xi^{(4)}(\vec{x}, \vec{x}, \vec{y}, \vec{y}) + 2\xi^{(2)}(\vec{x} - \vec{y})^2. \qquad (119)$$

This is equivalent to decomposing the power spectrum in two parts $P_f(k) = P_{f,2}(k) + P_{f,4}(k)$, the first depends on the non-linear power spectrum of density fluctuations and is

Figure 45. Angular power spectrum C_ℓ, normalized to C_{150} for the resolved subhalos modeled as in Siegal-Gaskins (2008). The black (red) curve shows the case of a $10M_\odot$ ($10^7 M_\odot$) mass cutoff. The green (blue) curve indicates the spectrum for the resolved subhalos in model $B_{z0,ref}$ for a mass cut-off of $10M_\odot$ ($10^7 M_\odot$). Taken from Fornasa et al. (2009).
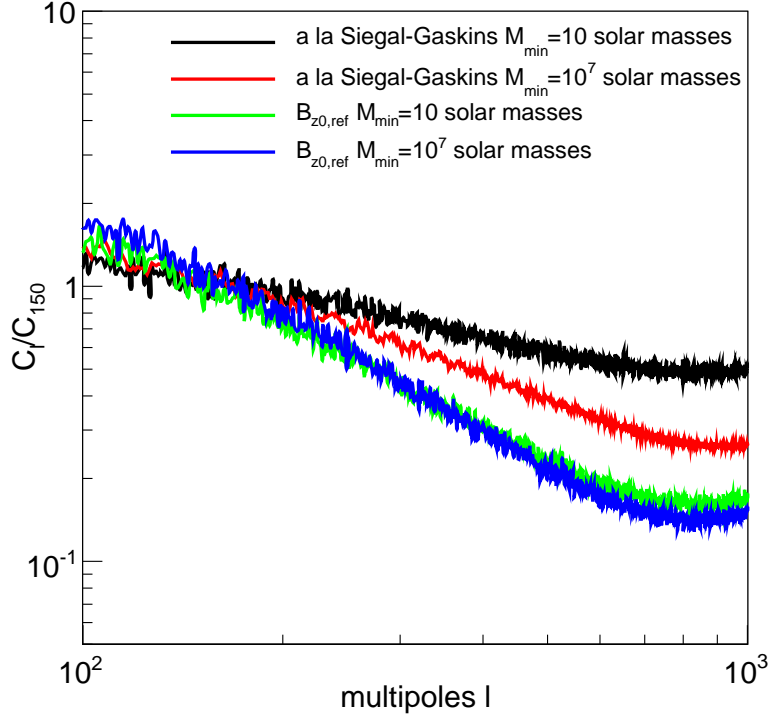

always sub-dominant. On the contrary the second part $P_{f,4}(k)$ receives contribution from the so-called *1-halo* term, relative to the case where both $\vec{x}$ and $\vec{y}$ belong to the same DM halo and from the *2-halo* term when $\vec{x}$ and $\vec{y}$ belong to different halos. The computation of $P_{f,4}$ contains also the Fourier transform of the DM density profile of the single halo, which it is assumed by Ando & Komatsu (2006) to be a described by a NFW profile.

The final result can be seen in Figure 46 (panels (c) and (d)) for a WIMP DM with $m_\chi = 100\,\text{GeV}$ and $\langle\sigma_{ann}v\rangle = 3\times 10^{-26}\text{cm}^{-3}\text{s}^1$: the 2-halo term dominates at low multipoles while the relevance of the 1-halo term depends on the low end of the mass integration. If the integration is extended to low mass halos (lower panel) the 1-halo significantly contribute only at very high multipoles while, on the contrary, with a minimal halo mass of $10^6 M_\odot$ its contribution is relevant at all scales.

Ando et al. (2007b) is instead devoted to the effect of extra-galactic DM subhalos: like in our model, their DM halos and subhalos are described by NFW density profiles and subhalos trace the smooth underlying mass distribution of the host halo. Moreover they assumed that the mean number of subhalos within a host halo of mass M, $\langle N|M\rangle$, scales as $\propto M^\alpha$ and they considered two extreme cases, $\alpha = 1$ and $\alpha = 0.7$ (Ando et al. 2007b) (in Fornasa et al. (2009) we only considered the first case to match the subhalo mass function of our model).

Figure 46. Angular power spectrum $C_\ell \ell(\ell + 1)/2\pi$ of DM annihilating in extra-galactic substructures with (a) $\alpha = 1$ and (b) $\alpha = 0.7$. The (c) and (d) panels refers to the angular spectrum of DM annihilating in extra-galactic halos (with no subhalos) with two different mass cut. The dotted and dashed line show the contribution from the 1-halo and 2-halo terms, respectively, and the solid line is the total. Taken from Ando et al. (2007*b*).
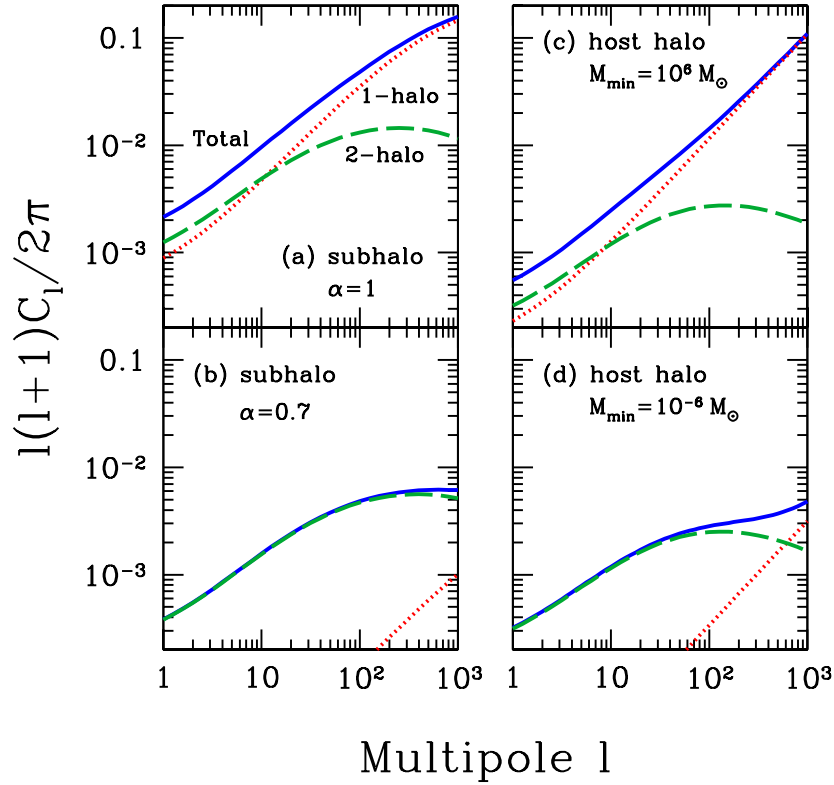
It should be noticed that Ando et al. (2007*b*) did not account for the contribution of subhalos by integrating over their mass function, as in the second term of Equation (114). Instead, they considered a gamma-ray subhalo spectrum averaged over its mass function and multiplied by the mean comoving density of subhalos. Their approach remains analytical, computing the angular spectrum as Fourier transform of the correlation function and distinguishing 1-halo and 2-halo contribution. The results for the case of "subhalos-only" can be seen in Figure 46.

These model details hardly affect the angular power spectrum since one considers fluctuations over the mean flux. While we will quantify the differences between the two approaches in a future work in which the angular power spectrum and the mean flux will be computed self-consistently, for the purpose of discussing the angular power spectrum, we adopted the same approach as in Ando et al. (2007*b*) and we used their very same angular power spectra shown in Fig. 5 of their paper for both the DM annihilation and the blazars contribution to the extra-galactic flux.

We did not plot the contribution of the DM and blazars to the angular spectrum of the

extra-galactic gamma-ray background in Figure 44 to avoid confusion. Instead, in the next section I show how well these spectra will be measured by Fermi LAT and compare them to the Galactic contributions.

24. Fermi LAT gamma-ray angular spectra

I want now to apply the model described in the last sections to predict the angular power spectrum that Fermi LAT is expected to observe and discuss the possibility of indirect DM detection through characteristic signatures in the spectrum.

The contribution of the different components to the total angular spectrum of the gamma-ray flux is shown in Figure 47 for the $B_{z0,ref}$ case. The red histogram indicates the angular spectrum of anisotropies in the blazar emissivity (see Fig. 5 of Ando et al. (2007b)). Black crosses represents the contribution of Galactic substructures that, as we have shown, dominate over the smooth NFW signal. Open diamonds indicate the contribution of extra-galactic halos and their substructures. All the different contributions are normalized to the square of the ratio between the average flux of that particular contribution to the average total flux $\langle d\Phi^i/dEd\Omega\rangle^2/\langle d\Phi^{\text{tot}}/dEd\Omega\rangle^2$.

Poissonian errors in each bin of the sky maps are due to the small statistics, i.e. the limited number of gamma-ray photons from annihilation collected during observations. The 1σ error is computed, following Ando et al. (2007b), as follows:

$$\delta C_l = \sqrt{\frac{2}{(2l+1)\Delta l f_{\text{f.o.v.}}}\left(C_l + C_l^b + \frac{C_N}{W_l^2}\right)}, \tag{120}$$

where $\Delta l = 18$ and $4\pi f_{\text{f.o.v.}} = 9.706$ sr is the area outside the mask. C_N is the power spectrum of the photon noise $C_N = 4\pi f_{\text{f.o.v.}}/N_{\text{EGB}}$ that depends on the instrument characteristics and integration time (N_{EGB} is the number of photons of the EGB) and is independent from ℓ. We have assumed an effective area constant with energy of 10^4cm^2 and an exposure time of 1 year. W_ℓ is the window function of a Gaussian point spread function $W_\ell = \exp(-\ell^2\sigma_b^2/2)$ that we computed for the Fermi LAT angular resolution $\sigma_b = 0.115°$.

The angular spectrum of the background C_ℓ^b is not uniquely defined but depends on the signal one wants to detect: for the extra-galactic DM component, the background is represented by blazars and by the Galactic annihilations. While, viceversa, for the Galactic DM component, blazars and extra-galactic annihilations play the role of background.

The total signal (shown as crosses in Figure 47 and Figure 48) is obtained by adding all components weighted by their relative contribution to the total gamma-ray flux $\langle d\Phi^i/dEd\Omega\rangle^2/\langle d\Phi^{\text{tot}}/dEd\Omega\rangle^2$ including the cross-correlation term involving extra-galactic halos and blazars. We ignored the cross-correlation between the Galactic subhalos and the blazars since they have independent spatial distributions. The total errors (blue boxes) account for the Poisson noise of both the Galactic and extra-galactic DM component, to which we summed the binsize and scatter among Monte Carlo realizations. The Poissonian noise becomes the main source of errors only al large multipoles. Finally, we assumed that the angular power spectrum of blazars is known without errors.

In the particle physics scenario considered here and for the $B_{z_0,ref}$ model, the average flux $\langle d\Phi/dEd\Omega \rangle$ produced by DM annihilations within and outside our galaxy is less than 1% of the EGB estimated for Fermi LAT. We can therefore boost up this contribution by increasing the cross section of the DM candidate. This has the effect of changing the values of $f_{\text{blazars}}^{\text{Fermi}}$ and $f_{\text{DM}}^{\text{Fermi}}$, i.e. the relative contribution of blazars and DM to the total EGB. The two panels in Figure 47 refer to $f_{\text{DM}}^{\text{Fermi}} = 0.61$ (left) and $f_{\text{DM}}^{\text{Fermi}} = 0.39$ (right). The corresponding boosting factors are shown in the plots. Larger boosting factors (corresponding to larger $f_{\text{DM}}^{\text{Fermi}}$) are excluded since they would correspond to models already excluded by the current EGRET constraint.

In both plots the contribution of the Galactic signal to the angular power spectrum largely dominates the extra-galactic component at all multipoles. As a consequence, the two main contributions to the angular spectrum are provided by the blazars and the Galactic annihilation signal. The former dominates at large multipoles whereas the latter dominates at low ℓ. The position of the cross-over depends on the boosting factor, but even in the less favourable case of $f_{\text{DM}}^{\text{Fermi}} = 0.39$ the DM annihilation signature can be clearly seen as a turn-over in the power spectrum at $\ell < 30$.

These considerations remain valid for the $B_{z_f,ref}$ model whose angular power spectrum is shown in Figure 48. In this case, however, the cross-over is found at smaller multipoles, making more difficult to detect the contribution for DM annihilation when $f_{\text{DM}}^{\text{Fermi}} = 0.39$ because of the large errorbars. On the other hand, with the $B_{z_f,ref}$ model one can increase the boost factor up to $f_{\text{DM}}^{\text{Fermi}} = 0.80$ without ending up with an unphysical scenario already excluded by EGRET.

25. Discussion and results

In Fornasa et al. (2009) we modeled for the first time the angular power spectrum of the diffuse gamma-ray signal at high Galactic latitude taking into account both the DM annihilation in substructures within our Galaxy and annihilation within extra-galactic halos and their subhalos, also including the contribution from extra-galactic objects like blazars. The purpose is to understand whether the gamma-ray satellite Fermi LAT will be able to unambiguously detect the signature of DM annihilation that, in the ΛCDM scenario, preferentially takes place in the central regions of DM halos and in their hierarchically-nested substructures.

For this purpose we developed an hybrid approach in which the annihilation signal is computed using two different techniques. First, we performed a numerical integration to compute the contributions to the gamma-ray flux from the smooth Galactic halo, from the unresolved Galactic substructures and, finally, from extra-galactic DM halos and their substructures. Second, we used Monte Carlo techniques to account for the nearest Galactic subhalos, that show up in the mock gamma-ray maps as individual gamma-ray sources.

We explored two different subhalo models corresponding to different prescriptions for the mass concentration within the halo, $B_{z_0,ref}$ and $B_{z_f,ref}$.

The EGB is computed by adding the annihilation signal from DM halos and subhalos and that from high-energy astrophysical sources like blazars. The relative contributions of the two

Figure 47. Angular power spectrum of gamma-ray anisotropies in the case that DM annihilations contribute to 61% (left) and 39%(right) of the total average flux of the CGB as estimated for the Fermi LAT satellite. The plus signs + indicate the Galactic component following the $B_{z_0,ref}$ model (see Figure 44). The diamonds $\diamond$ refer to DM annihilating in extra-galactic, unresolved DM halos and subhalos and the spectrum is taken from Ando et al. (2007*b*). The red line represents the angular spectrum of blazars as described in Ando et al. (2007*b*). All these three components are normalized to their average contribution to the total flux $\langle d\Phi^i/dEd\Omega\rangle^2/\langle d\Phi^{tot}/dEd\Omega\rangle^2$. The 1σ error of the total spectrum is indicated by the blue boxes and it is obtained propagating the errors from the Galactic and the extragalactic DM components, assuming no errors for the blazars. Taken from Fornasa et al. (2009).
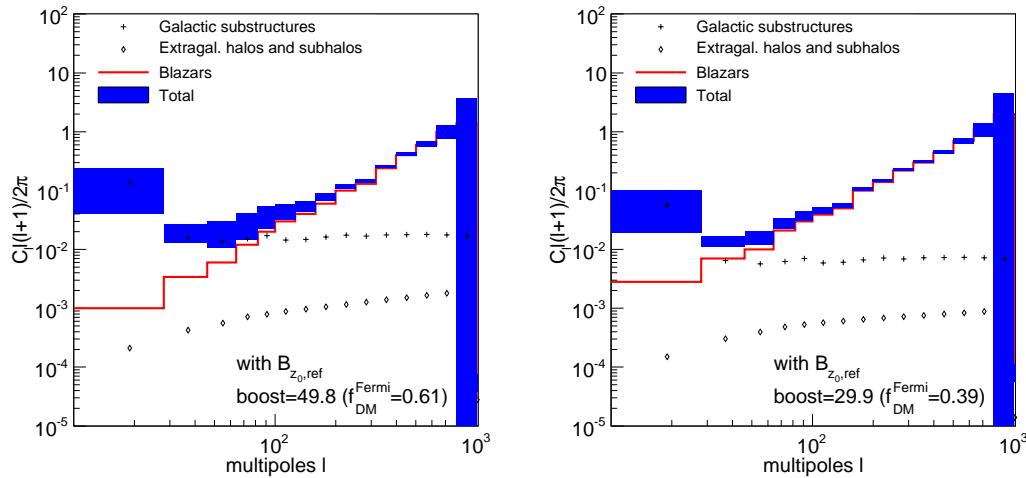

signals is treated as a free parameter. The only constraint is that the total gamma-ray signal, Galactic annihilation foreground and CGB, does not exceed the current limit of EGRET.

Our main conclusions are:

- The annihilation of the NFW smooth Galactic halo dominates over that of Galactic substructures only within a few degrees from the GC. The exact value depends on the subhalos concentration and ranges from $< 1°$ in model $B_{z_f,ref}$, to $\sim 3°$ in model $B_{z_0,ref}$. Moreover, the gamma-ray flux from extra-galactic halos is fainter than the Galactic signal at all angles. This is true both for $B_{z_0,ref}$ and $B_{z_f,ref}$.

- To predict the annihilation flux we have assumed a favourable particle physics setup, with a mass of 40 GeV, a cross section $\sigma_{ann}v = 3 \times 10^{-26}$cm^{-3}s^{-1}, and annihilations to $b\bar{b}$. With this choice, model $B_{z_0,ref}$ accounts for only 0.8% of the total unresolved EGB that will be measured by Fermi LAT. Larger fluxes are possible for smaller masses and larger cross sections, provided that the total flux does not exceed the current measurement of the EGB by EGRET and still allowing blazars to contribute to a significant fraction of the flux. Similar considerations also apply to model $B_{z_f,ref}$. The largest boost factor compatible with the data is of order 100, and it could be achieved e.g. through the so-called Sommerfeld enhancement or in some rather fine-tuned supersymmetric scenarios (Profumo 2005, Sommerfeld 1931).

Figure 48. Angular power spectrum of gamma-ray anisotropies in the case that DM annihilations contribute to 80% (upper left), 61%(upper right) and 39% (lower center) of the total average flux of the EGB as estimated for the Fermi LAT satellite. The curves and the error boxes have the same meaning of Figure 47 but refer here to the $B_{z_f,ref}$ case. Taken from Fornasa et al. (2009).
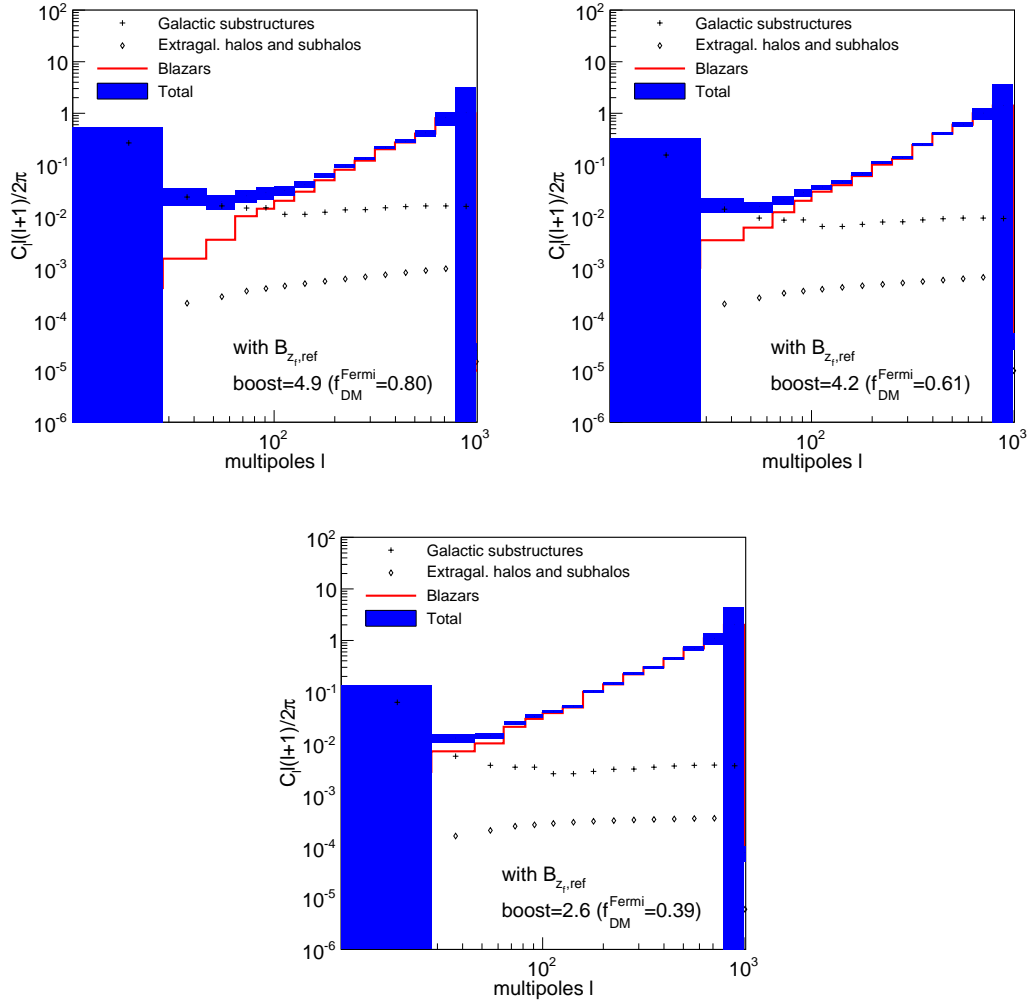
- The angular power spectrum predicted by our model is reliable and robust. To test its reliability we compared our results with those recently published in Siegal-Gaskins (2008), who performed a similar analysis considering, however, only Galactic substructures and using a full Monte Carlo approach. When the same halo model is considered, we found fair agreement with Siegal-Gaskins (2008). To test the robustness of our method we verified that our results do not change significantly when we increase the volume within which we simulate the distribution of Galactic subhalos beyond a well defined reference value.

- The angular power spectrum of the Galactic gamma-ray photons produced by DM annihilation is dominated by subhalos. Contributions involving the DM particles in

the smooth Galactic halo are negligible at all multipoles. At low multipoles (large angles) the spectrum is dominated by unresolved halos whose annihilation flux appear in the gamma-ray sky map as a smooth foreground (see e.g. Figs. 6 and 7 of Pieri et al. (2008)). On the other hand, nearby resolved clumps dominate the power at small angular separations (large multipoles). These results are robust in the sense that they do not change appreciably when adopting different prescriptions for the concentration parameters. This is not surprising since the power spectrum, which refers to fluctuations about the mean flux, should not depend appreciably on the subhalo structure.

- Subhalos of masses below $10^4 M_\odot$ give a small contribution to the angular spectrum of the Galactic annihilation flux.

- The signature of DM annihilations in the angular power spectrum can be found only for an optimistic particle physics setup. In fact, for our benchmark particle physics scenario (without any boost factor) the power spectrum of the unresolved gamma-ray background would be completely dominated by blazars. However, boosting up the particle physics factor without exceeding the background that EGRET has estimated, we find that the power spectrum is dominated by the DM component at low multipoles while blazars determine the spectrum at small angular scales. The turn-over depends on the prescription for the concentration of subhalos, occuring at smaller scales in the case of $B_{z0,ref}$.

- The angular power spectrum of DM annihilations is largely dominated, at all scales, by the Galactic signal. It depends mostly on the relative importance of the average Galactic flux compared to the extra-galactic DM signal which, in our models, favours the first term, both for $B_{z0,ref}$ and $B_{zf,ref}$.

- We found that a 1-year all-sky survey with Fermi LAT, now operational, may be able to spot the annihilation signature of DM in the angular power spectrum of the unresolved gamma-ray flux. This signature is provided by the up-turn in the power spectrum which, at low multipoles, is dominated by the DM annihilation signal. Our results partially contradict those of Ando et al. (2007*b*) who did not account for the Galactic contribution to the angular power spectrum which, instead, completely obliterate the one provided by annihilations in extra-galactic halos.

- Our results seem to confirm those of Siegal-Gaskins (2008) since the angular spectrum measured by Fermi LAT should indeed provide a detection of DM annihilation within our Galaxy, although it is doubtful that such measurement will be able to constrain the properties of the subhalo population. However, we should point out that the subhalo description adopted in Siegal-Gaskins (2008) would boost up the extra-galactic DM annihilation flux to a value of $3.60 \times 10^{-10} \mathrm{cm}^{-2}\mathrm{s}^{-1}\mathrm{GeV}^{-1}$ comparable to, if not larger than, the Galactic annihilation flux. On one side this fact increases the possibility of detecting the DM contribution to the angular spectrum. On the other hand it will be hard to disentangle Galactic and extra-galactic contributions.

As a remark I want to stress that the results of the recent *Via Lactea II* (Diemand et al. 2008) and the *Aquarius* (Springel et al. 2008*a*, Springel et al. 2008*b*) numerical

experiments, both with improved resolution, have now updated our knowledge on the subhalo distribution function and concentration parameters. The differences in the subhalos extracted from these simulations, whose main characteristics are listed in Table 8, may change the angular spectrum of the DM annihilation flux although we have shown that changing subhalo model significantly affects the gamma-ray flux but has less impact on the spectral analysis. We will investigate this issue thoroughly in a forthcoming paper. Here I just report the result of a preliminary analysis in which we computed the angular power spectrum of the Galactic annihilation signal obtained when subhalos are modeled according to *Via Lactea II* and *Aquarius*. In both cases we found that the angular spectrum is flatter, especially at small ℓ. This is not surprising since, in both experiments, the mass distribution is less clumpy and the subhalo radial distribution is flatter than in the model adopted in the present paper. A flatter spectrum, combined with a fainter annihilation flux due to the reduced number of substructures, would reduce the up-turn in the angular spectrum, making it more challenging to detect the DM annihilation feature. The significance of this effect depends on the boosting factors that, because of the dimmer flux, could be further increased without exceeding the measured gamma-ray background.

I also want to stress that our analysis of the angular spectrum focused on a particular energy range ($E > 10$ GeV) hence ignoring the different energy dependence of the variuos contributions to the correlation signal. Indeed it has recently argued that a multiwavelength analysis of the angular power spectrum could discriminate between astrophysical and annihilation signal and, if the statistics is good enough, would constrain the DM properties (Siegal-Gaskins & Pavlidou 2009).

25.1. Angular power spectrum of IMBHs

Being tuned to the results of *N*-body simulations, our description of the Galactic and extra-galactic subhalos population does not account for the effect of baryons in the evolution of DM structures. As a consequence our computation of the angular spectrum does not account for the effect, e.g., of IMBHs, which may be present in extra-galactic DM halos and contribute, to some extent, to the EGB. The correlation properties of the IMBHs predicted to populate extra-galactic DM halos have been recently studied in Taoso, Ando, Bertone & Profumo (2008). To report their results, each DM halo at $z = 0$ is assumed to host a number of IMBHs proportional to the mass of the host halo (as it was done in Fornasa et al. (2007) and Horiuchi & Ando (2006)), so that the today comoving number density of unmerged IMBHs is:

$$n(z = 0) = \int_{M_{min}}^{\infty} dM \frac{dn}{dM}(M, z = 0) N_{\text{IMBH}} \frac{M}{10^{12.1} h^{-1} M_{\odot}}, \tag{121}$$

where dn/dM is the halo mass function (parametrized following Sheth & Tormen (1999) and Eisenstein & Hu (1997)), M_{min} is the critical mass for a DM halo to host an IMBH (see Equation (87)) and the comoving number density is normalized to the prediction for the number N_{IMBH} of IMBHs harbored today in the MW halo of mass $10^{12.1} h^{-1} M_{\odot}$. On the contrary, at the redshift of formation, it is assumed that all DM halos with a mass larger than M_{min} host one (and only one) IMBH so that $n(z = z_f) = \int_{M_{min}}^{\infty} dn/dM(M, z = z_f) dM$.

At intermediate redshifts, the comoving number of IMBHs is assumed to depend on the redshift by a simple power-law, linking the two different regimes at $z = 0$ and $z = z_f$ (Horiuchi & Ando 2006):

$$n(z) = n(z_f)\left(\frac{1+z}{1+z_f}\right)^\beta.\tag{122}$$

β is taken to be 0.3 (Horiuchi & Ando 2006) and the implementation of the new cosmological WMAP parameters (Komatsu et al. 2008) has the consequence of modifying the prediction for the number of Galactic IMBHs today from 101 (Bertone, Zentner & Silk 2005) to around $N_{\mathrm{IMBH}} = 40$.

The DM halo around each IMBH is described by a mini-spike with slope equal to $-7/3$, independent from redshift (except than in the cut radius). Regarding the spatial distribution of IMBHs within the host halo, the shape is assumed to be steeper than a NFW profile and the size is rescaled proportionally to the virial radius of the host halo.

Following these prescriptions, the annihilation flux predicted for mini-spikes around IMBHs results to be at the same level of the EGRET data for the EGB, at least for a DM candidate with a mass of 100 GeV, a cross section of $\sigma_{\mathrm{ann}}v = 3 \times 10^{-26}\mathrm{cm}^{-3}\mathrm{s}^{-1}$ and annihilating, alternatively, in $b\bar{b}$ or $\tau\bar{\tau}$.

The computation of the angular spectrum of anisotropies is done analytically, modifying Equation (118) (taken from Ando & Komatsu (2006)) and the results are shown in Figure 49. The description of the blazar population is different in the two panels of Figure 49 (see Taoso, Ando, Bertone & Profumo (2008) for details) so that DM annihilating around IMBHs contribute to a different percentage of the EGB (the quantity f_{DM} indicated in the figures). The spectrum is computed at an energy of 10 GeV with the same particle physics parameters than above and the contribution of blazars is also shown as a background. The spectrum of DM annihilation around extra-galactic IMBHs results to be detectable over the background by Fermi LAT after two years of data in both the cases of Figure 49. The power spectrum due to the presence of extra-galactic subhalos (as in Figure 46) is also shown for comparison and it results that the IMBHs signal is characterized by a larger power at high multipoles, as a consequence of the different spatial distribution of IMBHs compared to that of subhalos.

In Taoso, Ando, Bertone & Profumo (2008) they finally show how the signal changes if the spectrum is computed at a different energy (increasing the energy increases also the amplitude of the spectrum even if the statistics is worse) or if the annihilation channel or the mass of the DM candidate is changed (softer energy spectra correspond to a lower amplitude in the angular spectrum while changing m_χ basically modifies the amplitude of the error bars).

Figure 49. Angular power spectrum of the EGB from DM annihilations around IMBHs at the photon energy of $E = 10$ GeV. Dashed line shows the contribution from the DM annihilation ($f_{\mathrm{DM}}^2 C_\ell^{\mathrm{DM}}$), dotted line is for blazars ($f_B^2 C_\ell^B$) and the dot-dashed line is the cross-correlation term ($2 f_{\mathrm{DM}} f_B C_\ell^{\mathrm{Cr}}$9. The total signal C_ℓ^{tot} is shown as a thick, black solid line. Errors bars are for 2 years of Fermi LAT data. The thin blue solid line shows the DM signal for DM annihilations in subhalos (Ando et al. 2007*b*). Taken from Taoso, Ando, Bertone & Profumo (2008).

Acknowledgments

References

Aaronson M 1983 *Astrophys. J.* **266**, L11.

Abazajian K N et al. 2008 The Seventh Data Release of the Sloan Digital Sky Survey.

Aharonian F et al. 2005 *Astron. Astrophys.* **430**, 865–875.

Aharonian F et al. 2006*a* *Nature* **439**, 695–698.

Aharonian F et al. 2006*b* *Phys. Rev. Lett.* **97**, 221102.

Aharonian F et al. 2008 *Phys. Rev.* **D78**, 072008.

Ahn E J, Bertone G & Merritt D 2007 *Phys. Rev.* **D76**, 023517.

Albert J et al. 2006 *Astrophys. J.* **638**, L101–L104.

Albert J et al. 2008 *Astrophys. J.* **679**, 428–431.

Aliu E et al. 2008 MAGIC upper limits on the VHE gamma-ray emission from the satellite galaxy Willman 1.

Allen S W, Schmidt R W & Fabian A C 2002 *Mon. Not. Roy. Astron. Soc.* **334**, L11.

Ando S 2005 *Phys. Rev. Lett.* **94**, 171303.

Ando S & Komatsu E 2006 *Phys. Rev.* **D73**, 023521.

Ando S, Komatsu E, Narumoto T & Totani T 2007*a* *Mon. Not. Roy. Astron. Soc.* **376**, 1635–1647.

Ando S, Komatsu E, Narumoto T & Totani T 2007*b* *Phys. Rev.* **D75**, 063519.

Aparicio A, Carrera R & Martinez-Delgado D 2002 *Astronom. J.* **123**, 2511.

Appelquist T, Cheng H C & Dobrescu B A 2001 *Phys. Rev.* **D64**, 035002.

Bahcall J N & Wolf R A 1976 *Astrophys. J.* **209**, 214–232.

Baltz E A, Taylor J E & Wai L L 2006 Can Astrophysical Gamma Ray Sources Mimic Dark Matter Annihilation in Galactic Satellites?

Barbieri R, Hall L J & Rychkov V S 2006 *Phys. Rev.* **D74**, 015007.

Barbieri R & Strumia A 1999 *Phys. Lett.* **B462**, 144–149.

Barth A J, Martini P, Nelson C H & Ho L C 2003 *Astrophys. J.* **594**, L95–L98.

Battaglia M et al. 2001 *Eur. Phys. J.* **C22**, 535–561.

Battaglia M et al. 2004 *Eur. Phys. J.* **C33**, 273–296.

Baumgardt H, Makino J & Ebisuzaki T 2004 *Astrophys. J.* **613**, 1143–1156.

Begeman K G, Broeils A H & Sanders R H 1991 *Mon. Not. Roy. Astron. Soc.* **249**, 523.

Berezinsky V S 1991 *Phys. Lett.* **B261**, 71–75.

Bergström L 1989 *Phys. Lett.* **B225**, 372.

Bergström L, Bringmann T, Eriksson M & Gustafsson M 2005*a* *Phys. Rev. Lett.* **95**, 241301.

Bergstrom L, Bringmann T, Eriksson M & Gustafsson M 2005*b* *Phys. Rev. Lett.* **94**, 131301.

Bergstrom L, Bringmann T, Eriksson M & Gustafsson M 2005*c* *JCAP* **0504**, 004.

Bergström L, Edsjö J, Gondolo P & Ullio P 1999 *Phys. Rev.* **D59**, 043506.

Bergstrom L, Edsjo J & Ullio P 2001 *Phys. Rev. Lett.* **87**, 251301.

Bergstrom L & Hooper D 2006 *Phys. Rev.* **D73**, 063510.

Bergstrom L, Ullio P & Buckley J H 1998 *Astropart. Phys.* **9**, 137–162.

Bernabei R et al. 2008 *Eur. Phys. J.* **C56**, 333–355.

Bernloehr K, Carmona E & Schweizer T 2007 *in* 'Proc. of the 30th ICRC' Merída, Mexico.

Bertone G, Hooper D & Silk J 2005 *Phys. Rept.* **405**, 279–390.

Bertone G & Merritt D 2005 *Phys. Rev.* **D72**, 103502.

Bertone G, Servant G & Sigl G 2003 *Phys. Rev.* **D68**, 044008.

Bertone G, Zentner A R & Silk J 2005 *Phys. Rev.* **D72**, 103517.

Biland A 2008 *in* 'Proc. of IDM 2008' Stocholm, Sweden.

Binney J & Tremaine S 1987 *Galactic dynamics* Princeton Univ. Press.

Borzumati F, Bringmann T & Ullio P 2008 *Phys. Rev.* **D77**, 063514.

Bringmann T, Bergstrom L & Edsjo J 2008 *JHEP* **01**, 049.

Bringmann T, Doro M & Fornasa M 2009 *JCAP* **0901**, 016.

Bringmann T & Hofmann S 2007 *JCAP* **0407**, 016.

Bryan G L & Norman M L 1998 *Astrophys. J.* **495**, 80.

Bullock J S et al. 2001*a* *Astrophys. J.* **555**, 240–257.

Bullock J S et al. 2001*b Mon. Not. Roy. Astron. Soc.* **321**, 559–575.

Burkert A 1996 *IAU Symp.* **171**, 175.

Carmona E et al. 2007 Monte Carlo Simulation for the MAGIC-II System.

Cembranos J A R, Feng J L, Rajaraman A & Takayama F 2005 *Phys. Rev. Lett.* **95**, 181301.

Cerdeno D G, Munoz C & Seto O 2008 Right-handed sneutrino as thermal dark matter.

Cesarini A, Fucito F, Lionetto A, Morselli A & Ullio P 2004 *Astropart. Phys.* **21**, 267–285.

Chamseddine A. H. A R L & P. N 1982 *Phys. Rev. Lett.* **49**, 970.

Cheng H C & Low I 2003 *JHEP* **09**, 051.

Cheng H C, Matchev K T & Schmaltz M 2002 *Phys. Rev.* **D66**, 056006.

Chertok M et al. 2006 *AIP Conf. Proc.* **842**, 995–997.

Clowe D, Gonzalez A & Markevitch M 2004 *Astrophys. J.* **604**, 596–603.

Clowe D et al. 2006 *Astrophys. J.* **648**, L109–L113.

Cohn H & Kulsrud R M 1978 *Astrophys. J.* **226**, 1087.

Colafrancesco S, Profumo S & Ullio P 2007 *Phys. Rev.* **D75**, 023513.

Cote P et al. 2004 *Astrophys. J. Suppl.* **153**, 223.

Cote P et al. 2006 The ACS Virgo Cluster Survey. VIII. The Nuclei of Early- Type Galaxies.

Da Costa G S 1999 *in* 'The Third Stromlo Symposium: The Galactic Halo' p. 165.

de Austri R R, Trotta R & Roszkowski L 2006 *JHEP* **05**, 002.

de Blok W J G 2005 *Astrophys. J.* **634**, 227–238.

de Blok W J G & Bosma A 2002 *Astron. Astrophys.* **385**, 816.

Diemand J, Kuhlen M & Madau P 2006 *Astrophys. J.* **649**, 1–13.

Diemand J, Kuhlen M & Madau P 2007 *Astrophys. J.* **657**, 262.

Diemand J, Moore B & Stadel J 2005 *Nature.* **433**, 389–391.

Diemand J et al. 2008 Clumps and streams in the local dark matter distribution.

Dienes K R, Dudas E & Gherghetta T 1998 *Phys. Lett.* **B436**, 55–65.

Dodelson S 2003 *Modern Cosmology* Academic Press.

Driscoll D D et al. 2007 Search for Dark Matter Annihilation in Draco with STACEE. preprint, arXiv:0710.3545.

Einasto J 1965 *Trudy Inst. Astroz. Alma-Ata* **51**, 87.

Eisenstein D J & Hu W 1997 *Astrophys. J.* **511**, 5.

Eke V R, Navarro J F & Steinmetz M 2001 *Astrophys. J.* **554**, 114–125.

Faber S M & Gallagher J S 1979 *Ann. Rev. Astron. Astrophys.* **17**, 135–183.

Falk T, Olive K A & Srednicki M 1994 *Phys. Lett.* **B339**, 248–251.

Fan X et al. 2001 *Astron. J.* **122**, 2833.

Feng J L, Rajaraman A & Takayama F 2003 *Phys. Rev. Lett.* **91**, 011302.

Ferrarese L & Ford H 2004 Supermassive Black Holes in Galactic Nuclei: Past, Present and Future Research.

Flanagan E E & Hughes S A 1998*a Phys. Rev.* **D57**, 4535–4565.

Flanagan E E & Hughes S A 1998*b Phys. Rev.* **D57**, 4566–4587.

Fornasa M & Bertone G 2008 *Int. J. Mod. Phys.* **D17**, 1125–1157.

Fornasa M, Pieri L, Bertone G & Branchini E 2009 Anisotropy probe of galactic and extra-galactic Dark Matter annihilations.

Fornasa M, Taoso M & Bertone G 2007 *Phys. Rev.* **D76**, 043517.

Fornengo N, Pieri L & Scopel S 2004 *Phys. Rev.* **D70**, 103529.

Frank J & Rees M J a C U 1976 *Mon. Not. Roy. Astron. Soc.* **176**, 633.

Freitag M, Amaro-Seoane P & Kalogera V 2006 *Astrophys. J.* **649**, 91–117.

Fryer C L & Kalogera V 2001 *Astrophys. J.* **554**, 548–560.

Gaisser T K, Stanev T, Honda M & Lipari P n.d. Prepared for 27th International Cosmic Ray Conference (ICRC 2001), Hamburg, Germany, 7-15 Aug 2001.

Geha M et al. 2008 The Least Luminous Galaxy: Spectroscopy of the Milky Way Satellite Segue 1. preprint, arXiv:0809.2781.

Gehrels N & Michelson P 1999 *Astropart. Phys.* **11**, 277–282.

Gentile G, Burkert A, Salucci P, Klein U & Walter F 2005 *Astrophys. J.* **634**, L145–L148.

Genzel R et al. 2003 *Astrophys. J.* **594**, 812–832.

Gilmore G et al. 2007 The Observed properties of Dark Matter on small spatial scales. preprint, arXiv:0703308.

Gondolo P, Edsjö J, Bergström L, Ullio P, Schelke M, Baltz E, Bringmann T & Duda G 2005 'Darksusy 5.0.1'.
    URL: *http://www.physto.se/ edsjo/darksusy*

Gondolo P & Silk J 1999 *Phys. Rev. Lett.* **83**, 1719–1722.

Gondolo P et al. 2004 *JCAP* **0407**, 008.

Gorski K M, Wandelt B D, Hansen F K, Hivon E & Banday A J 1999.

Graham A W & Guzman R 2003 *Astron. J.* **125**, 2936.

Green A M, Hofmann S & Schwarz D J 2004 *Mon. Not. Roy. Astron. Soc.* **353**, L23.

Green A M, Hofmann S & Schwarz D J 2005 *JCAP* **0508**, 003.

Griest K & Seckel D 1991 *Phys. Rev.* **D43**, 3191–3203.

Gualandris A & Merritt D 2007*a* Dynamics around supermassive black holes.

Gualandris A & Merritt D 2007*b* Ejection of Supermassive Black Holes from Galaxy Cores.

Gustafsson M, Lundstrom E, Bergstrom L & Edsjo J 2007 *Phys. Rev. Lett.* **99**, 041301.

Hagelin J S, Kane G L & Raby S 1984 *Nucl. Phys.* **B241**, 638.

Haisch U & Weiler A 2007 *Phys. Rev.* **D76**, 034014.

Halpern J P, Gezari S & Komossa S 2004 *Astrophys. J.* **604**, 572–578.

Hayashi E & Navarro J F 2006 *Mon. Not. Roy. Astron. Soc.* **373**, 1117–1124.

Hillas A M 1985 *in* 'Proc. of the 19th ICRC' La Jolla.

Hofmann W 2006 Performance limits for Cherenkov instruments.

Hooper D, de la Calle Perez I, Silk J, Ferrer F & Sarkar S 2004 *JCAP* **0409**, 002.

Hooper D & Dingus B L 2004 *Phys. Rev.* **D70**, 113007.

Hooper D & March-Russell J 2005 *Phys. Lett.* **B608**, 17–23.

Hooper D & Profumo S 2007 *Phys. Rept.* **453**, 29–115.

Horiuchi S & Ando S 2006 *Phys. Rev.* **D74**, 103504.

Hubble E 1929 *Proceedings of the National Academy of Sciences* **15**.

Hunter S D et al. 1997 *Astrophys. J.* **481**, 205–240.

Ibanez L E 1984 *Phys. Lett.* **B137**, 160.

Islam R R, Taylor J E & Silk J 2003 *Mon. Not. Roy. Astron. Soc.* **340**, 647.

Islam R R, Taylor J E & Silk J 2004 *Mon. Not. Roy. Astron. Soc.* **354**, 629.

Jeltema T E & Profumo S 2008 Searching for Dark Matter with X-ray Observations of Local Dwarf Galaxies.

Jungman G, Kamionkowski M & Griest K 1996 *Phys. Rept.* **267**, 195–373.

Kaplinghat M 2005 *Phys. Rev.* **D72**, 063510.

Kazantzidis S et al. 2004 *Astrophys. J.* **608**, 663–3679.

Keshet U, Waxman E & Loeb A 2004 *JCAP* **0404**, 006.

Kildea J et al. 2007 *Astropart. Phys.* **28**, 182–195.

Klypin A A, Kravtsov A V, Valenzuela O & Prada F 1999 *Astrophys. J.* **522**, 82–92.

Kolb E W & Turner M S 1990 *Early Universe* Addison-Wesley.

Komatsu E et al. 2008 Five-Year Wilkinson Microwave Anisotropy Probe (WMAP) Observations: Cosmological
    Interpretation. preprint, arXiv:0803.0547.

Komossa S et al. 2003 *Astrophys. J.* **582**, L15–L20.

Komossa S et al. 2004 *Astrophys. J.* **603**, L17–L20.

Kormendy J & Ho L C 2000 Supermassive Black Holes in Inactive Galaxies.

Koushiappas S M, Bullock J S & Dekel A 2004 *Mon. Not. Roy. Astron. Soc.* **354**, 292.

Koushiappas S M & Zentner A R 2006 *Astrophys. J.* **639**, 7.

Koushiappas S M, Zentner A R & Walker T P 2004 *Phys. Rev.* **D69**, 043501.

Li T P & Ma Y Q 1983 *Astrophys. J.* **272**, 317–324.

Lokas E L, Mamon G A & Prada F 2005 *Mon. Not. Roy. Astron. Soc.* **363**, 918.

Lopez Honorez L, Nezri E, Oliver J F & Tytgat M H G 2007 *JCAP* **0702**, 028.

Ma E 2006 *Phys. Rev.* **D73**, 077301.

Mack G D, Jacques T D, Beacom J F, Bell N F & Yuksel H 2008 *Phys. Rev.* **D78**, 063542.

MacMillan J D & Henriksen R N 2002 *Astrophys. J.* **569**, 83–90.

Martin N F, Ibata R A, Chapman S C, Irwin M & Lewis G F 2007 A Keck/DEIMOS spectroscopic survey of faint Galactic satellites: searching for the least massive dwarf galaxies. arXiv:0705.4622.

Martin S P 1997 A Supersymmetry Primer.

Mashchenko S, Sills A & Couchman H M P 2006 *Astrophys. J.* **640**, 252–269.

Mateo M 1998 *Ann. Rev. Astron. Astrophys.* **36**, 435–506.

Matsubayashi T, Shinkai H & Ebisuzaki T 2004 *Astrophys. J.* **614**, 864–868.

Mayer-Hasselwander H A et al. 1998 *Astron. Astrophys.* **335**, 161–172.

McConnachie A W, Penarrubia J & Navarro J F 2006 Multiple components and the interpretation of velocity dispersion profiles in dwarf spheroidals. preprint, arXiv:astro-ph/0608687.

McGaugh S S & de Blok W J G 1998 *Astrophys. J.* **499**, 41.

Merritt D 2003 Single and Binary Black Holes and their Influence on Nuclear Structure.

Merritt D 2006*a Rept. Prog. Phys.* **D69**, 2513–2579.

Merritt D 2006*b Astrophys. J.* **648**, 976.

Merritt D & Ferrarese L 2001 *Mon. Not. Roy. Astron. Soc.* **320**, L30.

Merritt D, Harfst S & Bertone G 2007 *Phys. Rev.* **D75**, 043517.

Merritt D, Milosavljevic M, Verde L & Jimenez R 2002 *Phys. Rev. Lett.* **88**, 191301.

Merritt D, Navarro J F, Ludlow A & Jenkins A 2005 *Astrophys. J.* **624**, L85–L88.

Merritt D & Szell A 2006 *Astrophys. J.* **648**, 890.

Miller M C & Colbert E J M 2004 *Int. J. Mod. Phys.* **D13**, 1–64.

Moore B, Quinn T R, Governato F, Stadel J & Lake G 1999 *Mon. Not. Roy. Astron. Soc.* **310**, 1147–1152.

Moore B et al. 1999 *Astrophys. J.* **524**, L19–L22.

Munoz R R et al. 2005 *Astrophys. J.* **631**, L137–L142.

Murphy B W, N. C H & H. D R 1991 *Astrophys. J.* **370**, 60.

Nakano T & Makino J 1999 On the Cusp around Central Black Holes in Luminous Elliptical Galaxies.

Navarro J F, Frenk C S & White S D M 1996 *Astrophys. J.* **462**, 563–575.

Navarro J F, Frenk C S & White S D M 1997 *Astrophys. J.* **490**, 493–508.

Navarro J F et al. 2004 *Mon. Not. Roy. Astron. Soc.* **349**, 1039.

Navarro J F et al. 2008 The Diversity and Similarity of Cold Dark Matter Halos.

Neto A F et al. 2007 The statistics of LCDM Halo Concentrations.

Pagels H & Primack J R 1982 *Phys. Rev. Lett.* **48**, 223.

Paige F E, Protopopescu S D, Baer H & Tata X 2003.

Peebles P J E 1972 *Gen. Rel. and Grav.* **3**, 63.

Peskin M E & Schroeder D V 1995 *An introduction to Quantum Field Theory* Addison-Wesley.

Piatek S, Pryor C, Armandroff T E & Olszewski E W 2002.

Pieri L, Bertone G & Branchini E 2008 *Mon. Not. Roy. Astron. Soc.* **384**, 1627.

Pohl M 1997 *Astron. Astrophys.* **317**, 441–447.

Press W H & Schechter P 1974 *Astrophys. J.* **187**, 425–438.

Preto M, Merritt D & Spurzem R 2004 *Astrophys. J.* **613**, L109.

Profumo S 2005 *Phys. Rev.* **D72**, 103521.

Pulhofer G et al. 2003 *in* 'Proc. of the 28th ICRC' Tsukuba, Japan.

Raffelt G G 2007 *J. Phys.* **A40**, 6607–6620.

Reed D et al. 2005 *Mon. Not. Roy. Astron. Soc.* **357**, 82–96.

Rodriguez C et al. 2006 *Astrophys. J.* **646**, 49–60.

Salucci P & Burkert A 2000 *Astrophys. J.* **537**, 9.

Sanchez-Conde M A et al. 2007 *Phys. Rev.* **D76**, 123509.

Schodel R et al. 2007 The structure of the nuclear stellar cluster of the Milky Way.

Segall M, Ibata R, Irwin M, Martin N & Chapman S 2007 *Mon. Not. Roy. Astron. Soc.* **375**, 831–842.

Sersic J L 1968 *Atlas de galaxiss australes* Cordoba, Argentina: Observatorio astronomico.

Servant G & Tait T M P 2003 *Nucl. Phys.* **B650**, 391–419.

Shapiro S L & Teukolski S A 1983 *Black Holes, White Dwarfs and Neutron Stars, the physics of compact objects*

John Wiley & sons.

Sheth R K & Tormen G 1999 *Mon. Not. Roy. Astron. Soc.* **308**, 119.

Shetrone M, Cote P & Sargent W L W 2001 *Astrophys. J.* **548**, 592–608.

Siegal-Gaskins J M 2008 *JCAP* **0810**, 040.

Siegal-Gaskins J M & Pavlidou V 2009 Robust identification of isotropic diffuse gamma rays from Galactic dark matter.

Siegel M H, Shetrone M D & Irwin M 2008 Trimming Down the Willman 1 dSph. arXiv:0803.2489.

Sigurdsson S, Hernquist L & Quinlan G D 1994.

Sikivie P 2006 *AIP Conf. Proc.* **805**, 23–29.

Simon J D & Geha M 2007 *Astrophys. J.* **670**, 313–331.

Sommerfeld A 1931 *Annalen der Physik* **403**, 257.

Spitzer L J 1987 *Dynamical evolution of Globular Clusters* Princenton series in Astrophysics.

Springel V et al. 2008*a* A blueprint for detecting supersymmetric dark matter in the Galactic halo.

Springel V et al. 2008*b* The Aquarius Project: the subhalos of galactic halos.

Sreekumar P et al. 1998 *Astrophys. J.* **494**, 523–534.

Strigari L E et al. 2007*a* *Phys. Rev.* **D75**, 083526.

Strigari L E et al. 2007*b* Redefining the Missing Satellites Problem. preprint, arXiv:0704.1817.

Strigari L E et al. 2007*c* The Most Dark Matter Dominated Galaxies: Predicted Gamma- ray Signals from the Faintest Milky Way Dwarfs. preprint, arXiv:0709.1510.

Strigari L E et al. 2008 *Nature* **454**, 1096–1097.

Strong A W, Moskalenko I V & Reimer O 2000 *Astrophys. J.* **537**, 763–784.

Swartz D A, Ghosh K K, Tennant A F & Wu K W 2004.

Taoso M, Ando S, Bertone G & Profumo S 2008.

Taoso M, Bertone G & Masiero A 2008 *JCAP* **0803**, 022.

Tegmark M et al. 2004*a* *Phys. Rev.* **D69**, 103501.

Tegmark M et al. 2004*b* *Astrophys. J.* **606**, 702–740.

Thorne K S & B. B V 1976 *Astrophys. J.* **204**.

Tremaine S & Gunn J E 1979 *Phys. Rev. Lett.* **42**, 407–410.

Trotta R, Feroz F, Hobson M P, Roszkowski L & Ruiz de Austri R 2008 *JHEP* **12**, 024.

Tyler C 2002 *Phys. Rev.* **D66**, 023509.

Ullio P, Bergstrom L, Edsjo J & Lacey C G 2002 *Phys. Rev.* **D66**, 123502.

Ullio P, Zhao H & Kamionkowski M 2001 *Phys. Rev.* **D64**, 043504.

Volonteri M, Haardt F & Madau P 2003 *Astrophys. J.* **582**, 559–573.

Walker M G et al. 2007 Velocity Dispersion Profiles of Seven Dwarf Spheroidal Galaxies.

Wang J X & Merritt D 2004 *Astrophys. J.* **600**, 149–161.

Willman B et al. 2005 *Astrophys. J.* **626**, L85–L88.

Willman B et al. 2006 Willman 1 - A Galactic Satellite at 40 kpc With Multiple Stellar Tails. preprint, arXiv:astro-ph/0603486.

Willott C J, McLure R J & Jarvis M J 2003 *Astrophys. J.* **587**, L15–L18.

Wilson A G 1954 *in* 'Publications of the Astronomical Society of the Pacific' Vol. 67 Chicago Journals p. 27.

Wood M et al. 2008 A Search for Dark Matter Annihilation with the Whipple 10m Telescope. preprint, arXiv:0801.1708.

Yao W M et al. 2006 *J. Phys.* **G33**, 1–1232.

York D G et al. 2000 *Astron. J.* **120**, 1579–1587.

Young P 1980 *Astrophys. J.* **242**, 1232.

Zentner A R, Berlind A A, Bullock J S, Kravtsov A V & Wechsler R H 2005 *Astrophys. J.* **624**, 505–525.

Zentner A R & Bullock J S 2003 *Astrophys. J.* **598**, 49.

Zhao H 1996 *Mon. Not. Roy. Astron. Soc.* **278**, 488–496.

Zwicky F 1933 *Helv. Phys. Acta* **6**, 110–127.

Zwicky F 1937 *Astrophys. J.* **86**, 217–246.